DISSERTATION

SENSING VIA SIGNAL ANALYSIS, ANALYTICS, AND CYBERBIOMETRIC

PATTERNS

Submitted by

Wesley Anderson

School of Biomedical Engineering

In partial fulfillment of the requirements

For the Degree of Doctor of Philosophy

Colorado State University

Fort Collins, Colorado

Fall 2022

Doctoral Committee:

    Advisor: Steve Simske

    Kevin Lear
    John Volckens
    Ellison Carter

ABSTRACT

SENSING VIA SIGNAL ANALYSIS, ANALYTICS, AND CYBERBIOMETRIC PATTERNS

Internet-connected, or Internet of Things (IoT), sensor technologies have been increasingly incorporated into everyday technology and processes. Their functions are situationally dependent and have been used for vital recordings such as electrocardiograms, gait analysis and step counting, fall detection, and environmental analysis. For instance, environmental sensors, which exist through various technologies, are used to monitor numerous domains, including but not limited to pollution, water quality, and the presence of biota, among others.

Past research into IoT sensors has varied depending on the technology. For instance, previous environmental gas sensor IoT research has focused on (i) the development of these sensors for increased sensitivity and increased lifetimes, (ii) integration of these sensors into sensor arrays to combat cross-sensitivity and background interferences, and (iii) sensor network development, including communication between widely dispersed sensors in a large-scale environment. IoT inertial measurement units (IMU's), such as accelerometers and gyroscopes, have been previously researched for gait analysis, movement detection, and gesture recognition, which are often related to human-computer interface (HCI). Methods of IoT Device feature-based pattern recognition for machine learning (ML) and artificial intelligence (AI) are frequently investigated as well, including primitive classification methods and deep learning techniques.

The result of this research gives insight into each of these topics individually, i.e., using a specific sensor technology to detect carbon monoxide in an indoor environment, or using accelerometer readings for gesture recognition. Less research has been performed on analyzing the systems aspects of the IoT sensors themselves. However, an important part of attaining overall situational awareness is authenticating the surroundings, which in the case of IoT means the individual sensors, humans interacting with the sensors, and other elements of the surroundings. There is a clear opportunity for the systematic evaluation of the identity and performance of an IoT

sensor/sensor array within a system that is to be utilized for "full situational awareness". This awareness may include (i) non-invasive diagnostics (i.e., what is occurring inside the body), (ii) exposure analysis (i.e., what has gone into the body through both respiratory and eating/drinking pathways), and (iii) potential risk of exposure (i.e., what the body is exposed to environmentally). Simultaneously, the system has the capability to harbor security measures through the same situational assessment in the form of multiple levels of biometrics.

Through the interconnective abilities of the IoT sensors, it is possible to integrate these capabilities into one portable, hand-held system. The system will exist within a "magic wand", which will be used to collect the various data needed to assess the environment of the user, both inside and outside of their bodies. The device can also be used to authenticate the user, as well as the system components, to discover potential deception within the system. This research introduces levels of biometrics for various scenarios through the investigation of challenge-based biometrics; that is, biometrics based upon how the sensor, user, or subject of study responds to a challenge. These will be applied to multiple facets surrounding "situational awareness" for living beings, non-human beings, and non-living items or objects (which we have termed "abiometrics"). Gesture recognition for intent of sensing was first investigated as a means of deliberate activation of sensors/sensor arrays for situational awareness while providing a level of user authentication through biometrics. Equine gait analysis was examined next, and the level of injury in the lame limbs of the horse was quantitatively measured and classified using data from IoT sensors. Finally, a method of evaluating the identity and health of a sensor/sensory array was examined through different challenges to their environments.

ACKNOWLEDGEMENTS

TABLE OF CONTENTS

LIST OF TABLES

LIST OF FIGURES

Chapter 1
Introduction

Over the past few years, network-enabled (Internet of Things, or IoT) sensors have been increasingly adopted for a wide variety of purposes. Sensors for air quality monitoring, movement and gait analysis, and location services have been increasingly adopted. In fact, the International Data Corporation (IDC) estimated that there will be 41.6 billion connected IoT devices by the year 2025 [1]. This is five for every human on the planet. These sensors include, but are not limited to, gas sensors, pressure sensors, temperature and humidity sensors, miniaturized microphones, GPS units, and inertial measurements units (IMU), such as accelerometers and gyroscopes. The need for more comprehensive environmental monitoring due to a quickly changing climate is becoming more apparent, and the technological advancements in the field of IoT have made high-level monitoring more feasible.

Implementation of environmental monitoring sensors, along with inter-network communication with other IoT devices for combined analyses, has yet to be widely executed to my knowledge. Error-free readings are important in usage such as (i) smart home systems, (ii) at-home medical diagnostics, and (iii) environmental exposure analysis for individuals and whole communities. Over time, degradation of sensor accuracy has been noted, and methods to compensate for this have been theorized and tested, which will be discussed in Chapter 2. A reliable, robust description of a sensor's health, however, has yet to be defined, and a systematic method to periodically evaluate it has yet to be developed. To do this, further model development in both hardware and software must be considered for short and long-term implementation of this technology. Ease of activation of these sensors for users of all ages and technological backgrounds is also important to consider when developing such a system.

The vast amount of data collection available with this system may require security measures such as multi-factor authentication to protect the individual's privacy rights, and thereby ensure data security for the system. Without such protection, there are envisioned scenarios in which the data collected may reveal directly or through inference information that might violate

the Health Insurance Portability and Accountability Act (HIPAA). Therefore, if the dataset is de-identified, the number of threats to the data producer (e.g., the user) decreases [2]. Patients in assisted care living, who are frequently less technologically grounded, would benefit from a form of system activation that concurrently provides security and privacy for the acquired data. Three important considerations for privacy include the frequency of data upload, the user focus (e.g., the anonymization, or lack thereof, of the user), and the proactivity of the user with the device (e.g., the control of collection frequency by the user) [3]. Recently, physical and continuous biometrics have been increasingly incorporated for multi-factor authentication through human-computer interface (HCI) in cellular devices, personal computers, and elsewhere. These methods can be simultaneously employed as biometrics; either individually as continuous biometrics, or in combination as hybrid biometrics [4]. This form of authentication is able to eliminate a level of identification (or at least reduce the exposure to a single type of biometric) while simultaneously adding user focus to the situation.

A proposed method of combining the components of this system is through the use of a "magic wand", which will harbor multiple IoT sensor technologies that will (i) include ease of activation through gesture recognition with intent of sensing, (ii) implement the appropriate sensor/sensor array and predictive modeling technique to give accurate and precise readings for analysis, (iii) simultaneously provide security through authentication with multiple levels of personal and "sensor biometrics" while also evaluating the "health", or performance, of the utilized sensors to determine if replacement of these sensor(s)/sensor arrays is necessary. Potential components of the system will be analyzed for their practicality, cost, size, power consumption, and accuracy when combined with ML/AI methods. Ultimately, a more general system optimization can be formulated for different applications of interest. An extra example of an application of interest is demonstrated through a system to evaluate the health status of a horse through gait analysis and model development.

This dissertation is organized as follows. In Chapter 2 a background on general IoT sensor technology and machine learning approaches is presented. Chapter 3 provides general details on the current implementation of these sensors into technology, and the potential for a meta-analytic

system for full "situational awareness" while providing security through user biometrics and "sensor biometrics" in the form of a "magic wand" system. Chapter 4 outlines improvements to the field of gesture recognition through the use of an optimized objective function that is combined with a support vector machine (SVM) and binary comparisons through assigned hamming codes and distances, along with a deep learning technique through the conversion of 1-D signals to 3-D images in combination with AlexNet. Finally, it covers a biometric authentication system design in which a "biometric VPN" (virtual private network), which will be described in detail, is maintained through multiple levels of classification and data partitioning of the user authentication. Chapter 5 describes how a similar process can be utilized to develop a model for gait analysis and prediction of multiple metrics of lameness through wearable sensors. Chapter 6 will outline the forensic identification and potential anomaly detection of different IoT environmental sensors (namely, MOS sensor technologies) through different environmental and analyte exposures. The dissertation concludes with a summary conclusion and identifies future research in Chapter 7.

Chapter 2
Background

To develop and assess approaches and classification methods for so-called "abiometrics" (application of biometric approaches to abiotic elements and systems) of Internet of Things (IoT) sensors, an understanding of the various technologies and related features are required. The following sections describe the origins of biometrics and IoT technologies, followed with general characteristics, functions, and important performance parameters associated with (i) gas sensors and (ii) inertial measurement units (IMU's), such as accelerometers and gyroscopes, and their components. The sections continue with a description of the previous work in the fields of Human Activity Recognition (HAR) and gesture recognition; gait characterization and analysis for equine animals; and modeling, calibration, and processing for environmental sensors.

2.1 Biometrics Overview

Biometrics refer to the assignment of identity through the measurement of physical attributes or behavior. Within the traditional triad of security, which includes knowledge, possession, and identity [5], biometrics would be considered a part of the identity category. Biometrics can be separated into three categories, which include physical, or physiological, biometrics; behavioral, or continuous, biometrics; and innate, or chemical, biometrics. Common forms of each are highlighted in Table 2.1 [4]. An example is an iris/retina scan, which is a form of a physical biometric. Selection of the type of biometric used depends on a number of factors, including the level of sensitivity of the information being accessed through the authentication or verification, whether authentication (1:N matching) or verification (1:1 matching) is of interest for access to the system, the recognition accuracy of the biometric trait, and the availability and embeddability of the technology required for measurement.

Table 2.1: Comparison between forms of biometrics [4].

TYPE	FORM
PHYSICAL	Face, fingerprint, hand, iris, retina
BEHAVIORAL	Arm sweep, handwriting, gesture, heartbeat, keystroke, voice, walking
INNATE	Genetic, tissue assay, mass spectroscopy

According to Dahia et. al [6], the three main biometric recognition tasks include enrollment, verification, and identification (Figure 2.1). The authors describe enrollment as "the template extracted from the input sample that is stored together with an identity reference". Verification is the "identity reference that is used to retrieve a specific template from the gallery, which is then matched against the template extracted from the input sample to decide whether they belong to the same subject". Finally, identification is when "the template extracted from the input sample is matched against all templates in the gallery to retrieve its identity reference" [6].

(a)　　　　　　　　　(b)　　　　　　　　　(c)
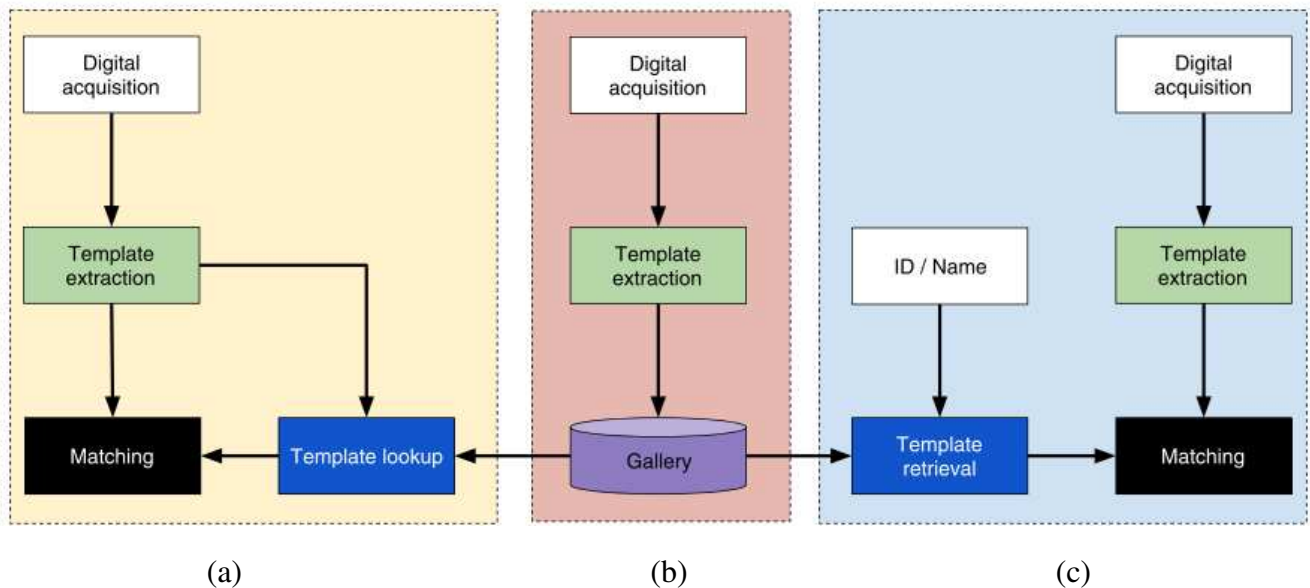
Figure 2.1: Three main biometric recognition tasks: (a) Identification, (b) enrollment, and (c) verification. Taken from Dahia et. al. (2019).

Biometric recognition is based on the fundamental premise of distinctiveness and permanence of these physical and behavioral characteristics [7]. For behavioral biometrics, such as gait and handwriting, distinctiveness and permanence are weak, and thus very few systems have incorporated this type of biometric to date because of lack of adequate recognition accuracy as a result [8]. Fingerprints, face, and iris detections, however, have been incorporated into many commercial systems because of their strong distinctiveness and exceeding permanence compared to the former. Nevertheless, each of these modalities has a risk of spoof (including replay and replication) attacks, as well as issues for large-scale deployments. For instance, it was reported that 2% of the population does not have usable fingerprints for enrollment in fingerprint identification systems [7]. As physical biometrics are mostly one-time measurements, it is also important to consider that once access from an outsider is gained, there are no other roadblocks to get through. Admittance into a system with all the access rights and privileges of the user whose device has been infiltrated are then available until any sort of time-out is reached or the access is willingly released by the hacker. The deployment combination of different biometric modalities can ensure a desired level of security and flexibility in applications where spoof attacks are an issue, as it is difficult to spoof multiple modalities simultaneously. Combining more than one modality can also address problems like high error rate and can enhance recognition accuracy [9].

Multi-modal biometrics refer to the combination of different forms of biometrics. Multi-modal systems are often implemented to overcome limitations of each of the individual methods and to decrease or reduce the time in which no measurement is available for authentication or validation. An example of a multi-modal system is described in [10], in which a database of 10 fingerprints, two iris scans, and a photograph of the face is used for biometric identification. In this reference, it is claimed that this system achieves de-duplication accuracy of more than 99% while also ensuring total inclusion, or the ability of every user to utilize the biometric system. However, as mentioned previously, even accuracy as high as this can still lead to misidentifications on the order of millions in countries like India, where the population far exceeds one billion people, and thus a robust system that allows for verification of the output in order to achieve even higher accuracy while also being able to recognize flaws is potentially greatly beneficial. Other

improvements include, but are not limited to, i) ease of use and ii) increase in overall distinctiveness and universality [11].

Applications of biometrics to living beings, specifically humans, have been widely studied, yet there has been little research into the application of similar ideas and techniques to other living beings, such as equine animals, or to non-living objects/items in the case of environmental gas sensors and other IoT devices. The following sections will describe the general characteristics, functions, and important performance parameters associated with Internet of Things (IoT) sensors (specifically, gas sensors and inertial measurement units (IMU's)), and how these lead to the potential for implementation of biometric techniques in the field. These techniques are then applied through challenge-based biometrics (which shall be described in detail in Chapter 2) to humans, non-human living beings (specifically, equine animals), and non-living items and objects (in this case, IoT sensors in the form of environmental sensors).

2.2 Internet of Things Sensor Technology Overview

Internet of Things (IoT) sensors refer to "an open and comprehensive network of intelligent objects that have the capacity to auto-organize, share information, data and resources, reacting and acting in face of situations and changes in the environment" [12]. The basic purpose of IoT is to combine a set of diverse sensors, such as accelerometers and gyroscopes, gas and environmental sensors, microphones, among others, as well as devices such as Global Positioning Systems (GPS), RS, Radio-Frequency Identification (RFID), laser scanner, and networks to comprehend the information sharing of global things.

IoT can encompass millions of networked embedded smart devices, or smart things; these smart things are capable of accumulating information about themselves, their environment, and associated smart devices and interconnect this information to other devices and systems via the Internet [12]. IoT devices have been applied in healthcare [13]–[15], agricultural and environmental analyses [16], [17], as well as flood monitoring and mapping [18], [19], transportation [20], and construction automation [21]. The key objective of the IoT paradigm is to enable users to "uniquely identify, signify, access, and control things at anytime and anywhere via

the internet". For the construction of these systems, a focus in improvement in sensor design, along with advances in micro- and nano-fabrication technology, leads to development of high-performance sensors [22].

IoT architecture has been discussed by many, including by Burhan et. al. [20]. According to these authors, there is no consensus on the architecture of IoT; many authors argue on whether the architecture should be broken into three-, four-, or five-layer schemes (Figure 2.2). In general, the potential architectures share commonalities with regard to the application and perception layers. The perception layer, or the sensor layer, is where identification and collection of information sources is accomplished. Sensors are selected based on the need of the user(s) within the system. The application layer consists of all applications that use, or have been deployed by, the IoT system. Examples of applications include, but are not limited to, smart homes, smart cities, and smart health, among others.
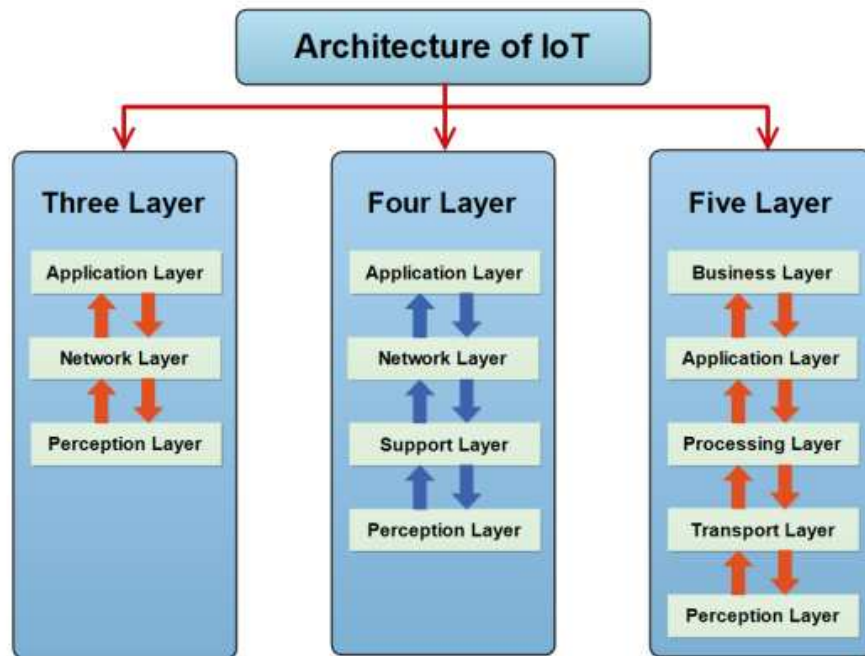
Figure 2.2: Three-, four-, and five-layer architectures of IoT networks. Taken from Burhan et. al. (2018).

Within the three- and four- layer architectures is the network layer, or the transmission layer, that is the connection between the perception and application layer. As is in the name, the network layer is meant to transmit information collected by the perception layer to the application

layer, while also connecting the individual smart thing applications (e.g., the previously mentioned smart homes and smart devices) to each other. The four-layer architecture also includes a support layer, which is intended for secure computing (both locally, and in the cloud) and anti-virus protection for the network layer. In contrast, while the five-layer architecture includes the original three layers of the three-layer architecture, the network layer is often called the transport layer in this structure, it also includes a processing and business layer. This architecture is meant to add even more security to the system. Here, the processing layer (or the middleware layer) collects and processes big data while removing extra information and extracting the useful information. The business layer is utilized to manage and control the applications within the IoT system of interest with business and profit models while also maintaining the privacy of the many users within the network.

Within the architecture of the IoT system, there are many potential opportunities for outside attack [20], [23]. Attacks can come at all levels or layers. In the perception layer, for instance, attacks can be in the form of eavesdropping, or the interception of private communications; node capture, or the gain of control of a key node; replay attacks, or the use of eavesdrop to steal authentic information that is later used in an attack between the intruder and victim with the proof of their identify and authenticity; timing attacks, or attacks that are used to determine the time it takes the system to respond to different queries; and fake or malicious nodes, where an extra node is added to the system to input fake data meant to mimic the existing real data. These attacks often come in a form that is mis-identified as an anomaly, or a pattern that does not conform to the expected behavior [23]. This is especially common with malicious attacks, where the attacker attempts to make the data appear normal, which can not only be difficult to detect, but also will skew the ability the define "normal" sensor behavior.

With potential adversaries in mind, many have attempted to implement measures that would secure and protect the data, as well as the transmission and storage of that data, within an IoT system. The authors in [24] reviewed research that has examined equipping smart devices in smart city ecosystems, in which data is collected by IoT sensors, with biometric authentication services. Their review focuses on the perception layer, which in this instance is focused on the

interaction between the user and the device for authentication. Once the user has gained access to the services, they are within the application layer, as defined by the authors, and can access applications such as those for smart utilities, smart mobility, smart healthcare services, smart governance, and a smart economy. This review, however, did not consider malicious attacks on the sensors themselves.

In [25], Intrusion Detection Systems (IDS's) within IoT systems are reviewed as a method of detecting and mitigating IoT-related security attacks. IDS systems, which are tools for monitoring data to identify and protect against intrusions, can be divided into three stages. The first stage, the monitoring stage, is made up of network-based and host-based sensors. The second, the analysis stage, relies on feature extraction and pattern recognition methods. The third and final stage, the detection stage, relies on anomaly or misuse intrusion detection. In this process, the IDS is able to detect potentially harmful activities. The types of methods reviewed by the authors include, but are not limited to, host-based, or single system, and network-based, or network traffic system, intrusion detection, as well as anomaly-based intrusion detection. Specifically, the methods of anomaly-based intrusion detection include the use of data mining, machine learning, statistical models, rule and payload models, and signal processing models. The performance of IDS's is often characterized using true positive rates, false positive rates, precision, F-score, error rate, and energy consumption and processing time of the method utilized. The authors note that it is important to search for these attacks, as they can degrade the usability of the many IoT applications.

Increasing numbers of sensors are being employed in IoT networks. In fact, it is estimated that there will be approximately 42 billion IoT devices in use by the year 2025 [1] With this increasing popularity of these sensors and devices, there is an ever-growing opportunity for everyday citizens to participate in collection of data that can benefit themselves, as well as their constituents. The participation of a population in such a manner is known as popular epidemiology using citizen science, which is a population understanding, responding to, and reducing pollutant concentrations and health patterns to which people are exposed using a mobile IoT sensor information system. Such a platform would not only provide a means for collecting this important

10

data, but also engage and educate members in the community about pollution, associated adverse health effects, and their exposure environment. In addition, by linking the local pollutant measurements taken by community members with health-related information, it may be possible for environmental and health-care scientists to make associations between pollutant levels and local illness patterns. These associations would, in turn, provide closer to optimal responses to health hazards in real-time, including potential municipal, policy, or business responses.

In this sense, through the capabilities of IoT sensors, it is possible for everyday citizens to measure what's going on inside of their bodies, what's going into their bodies, and what is occurring around them in both indoor and outdoor environments through measurements made with the same technology. Activation of the correct sensor/sensor array allow the users to make each of these measurements in this way. A device that allows for the incorporation of different sensor technologies for situational awareness, along with the ability to activate the correct sensors while forensically identifying the user is proposed here. This device will be further discussed in Chapter 3. Before discussing such a system, however, it is important to understand the underlying theories of the existing technologies, and how their characteristics and previous assessments can lead to such an application.

2.2.1 Overview of Gas Sensor Technologies

To develop and assess biometric applications towards gas sensors, an understanding of sensor technology and related theories is required. The following section describes the general characteristics, functions, and performance parameters associated with gas sensor systems and their individual components.

In many cases, gas sensors comprise a transducer and an active layer. The purpose of these sensors is to convert a desired chemical reaction into a measurable electronic signal [22]. This is done through changes in resistance, frequency, current, and voltage. Different gas sensor technologies include, but are not limited to, electrochemical sensors (e.g., metal oxide semiconductors (MOS), chemiresistive sensors, amperometric sensors, among others), carbon nanotube (CNT) sensors, acoustic gas sensors (e.g., quartz crystal micro-balance (QCM), surface

acoustic waves (SAW), flexural plate wave (FPW) and thin rod sensors, among others), and optical gas sensors (e.g., fiber optic, photonic crystal, among others). The selection of the sensor technology is chosen based on the application of the technology and environment in which it will be used [22], [26], [27]. Each sensor type is developed to improve upon:

- *Sensitivity*, or the smallest volume concentration of the target gas that can be sensed in the time of detection (R_g/R_a for oxidizing gases, and R_a/R_g for reducing gases, where R_a is the resistance in the reference gas, and R_g is the resistance in the target gas);

- *Selectivity,* or the ability of the gas sensors to detect a specific gas in a mixture of gases;

- *Response time,* or the period from the time when a gas concentration reaches a specific value to that when a sensor generates a corresponding signal;

- *Reversibility,* or the ability of a gas sensor to return to its original state once the surrounding environment is at a normal state, and

- *Recovery time,* or the time required for a sensor signal to return to its initial value after a change from a concentration value to zero [27].

Accuracy and precision, or the ability of the sensor to output a recognized ideal value at a given concentration of gas (or the amount of shift from the true value) and have an acceptable amount of agreeability between repeated measurements (which can be measured through the width of the distribution of said measurements), respectively, are also important considerations when developing various gas sensor technologies [28]. Table 2.2 provides a comparison of characteristics of each sensor technology to highlight the strengths and weaknesses of each. Several authors [27], [29] have observed that devices based on electrochemical technologies, specifically semiconductor metal oxide thin films, are the most promising among solid-state gas sensors due to their small size, low cost, real-time operation, and high compatibility with microfabrication processing. For the purpose of this dissertation, the focus will be on the technology behind electrochemical sensors (specifically, MOS sensors).

Table 2.2: Performance characteristics of various gas sensor technologies. Reprinted from Materials Science and Engineering: B, "Semiconductor metal oxide gas sensors: A review", Pages No. 206-217, Copyright 2018, with permission from Elsevier.

Parameters	Types of Gas Sensors				
	SMO Gas Sensors	Catalytic Combustion Gas Sensors	Electro Chemical Gas Sensors	Thermal Conductivity Gas Sensors	Infrared Absorption Gas Sensors
Sensitivity	E	G	G	P	E
Accuracy	G	G	G	G	E
Selectivity	F	P	G	P	E
Response Time	E	G	F	G	F
Stability	G	G	P	G	G
Durability	G	G	F	G	E
Maintenance	E	E	G	G	F
Cost	E	E	G	G	F
Suitability to portable instruments	E	G	F	G	P

E: excellent, G: good, F: Fair, P: Poor.

The MOS gas-sensing mechanism consists of a Micro-Electrical Mechanical System (MEMS)-fabricated substrate that the sensor is fabricated on, a MOS sensing layer, an electrode, and a microheater. Figure 2.3 provides a general cross-sectional diagram of the basic setup for a MOS sensor. The technology is based on the change in conductivity of the device-sensing component in the presence of reducing or oxidizing gases [22]. The design of these sensors allows for the sensing layer to be directly exposed to the target analyte(s). There is a correlation between the resistance and energy barrier which changes by charge carrier density at the grain boundaries, and this correlation is directly proportional to the concentration of the exposed analytes.
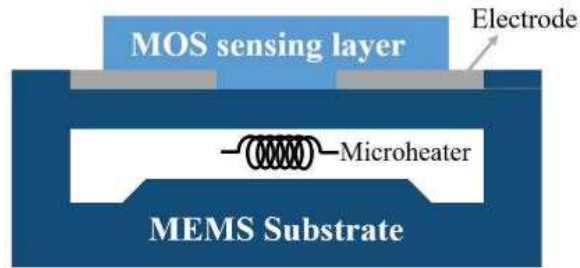
Figure 2.3: MOS sensor cross-sectional view, which includes the Micro-electrical Mechanical System (MEMS) substrate that the sensor is fabricated on, the MOS sensing layer, the electrode, and the microheater. Taken from Nazemi et al (2019).

There are two types of MOS sensors: n-type and p-type. The n-type sensors, which are most commonly fabricated using TiO_2, ZnO, SnO_2 and WO_3, are dependent on electrons as charge carriers, while the p-type sensors, which are most commonly fabricated using NiO, Mn_2O_4 and Cr_2O_3, are dependent on "positive holes", or lack of electrons, as the charge carriers. The MOS sensor's sensitivity relies on the thickness of receptor layer, the catalytic metal particles placed in it, and the temperature of the receptor layer (which is generated by the microheater component of the sensor), and the resultant changes in resistance are dependent on whether the sensor is n- or p-type. The attributes of MOS sensors are simplicity and durability, as well as and ease and low cost of fabrication, while the limitations include high operating temperature (150°C-400°C), power consumption, susceptibility to temperature and humidity changes, and drift over the lifetime of use.

The material, production, and design of the core components of the MOS sensor are selected to achieve specific performance goals [27]. Specific sensor fabrication, dynamic range, and calibration are selected and fulfilled based on the desired interaction and reaction with the analyte(s) of interest. Within the same technology, these ranges can be tweaked, or modulated, to sense many different analytes. This is advantageous for portable sensing systems, as fewer sensors are necessary to sense the complexity of the environment within a setting.

2.2.2 Overview of Inertial Measurement Units

To develop and assess the application of intent of sensing with biometric applications towards the human-computer interface-based control of the aforementioned device in which full situational awareness can be measured, an understanding of sensor technology and related theories is required. The following section describes the general characteristics, functions, and performance parameters associated with inertial measurement unit (IMU) technologies.

IMU's consist of accelerometers, gyroscopes, and magnetometers. Accelerometers are instruments used for measuring forces generated by acceleration from movements, vibrations, or gravity of objects. Their uses range from detecting the actions of a user, such as measurements of sedentary time, physical activity, physical activity energy expenditure (PAEE), shaking or palsies, gait types and behaviors, and sleep-related behaviors, all the way to image stabilization in cameras, measuring the orientation of a device relative to Earth's gravitational pull (e.g. to enable automatic display rotation between landscape and portrait mode, and detection of orientation for device activation in smart phones). Similarly, gyroscopes are instruments used to measure forces that generate rotational velocity with respect to the reference position of the device. They are used in automotive, defense, industrial, smart technology, and medical applications [30].

Two forms of accelerometers are currently utilized in today's technology, including piezoelectric/piezoresistive and capacitive accelerometers. Capacitive accelerometers, however, are the most commonly used sensors in micro technologies [31]. Figure 2.4 depicts a capacitive-based accelerometer.
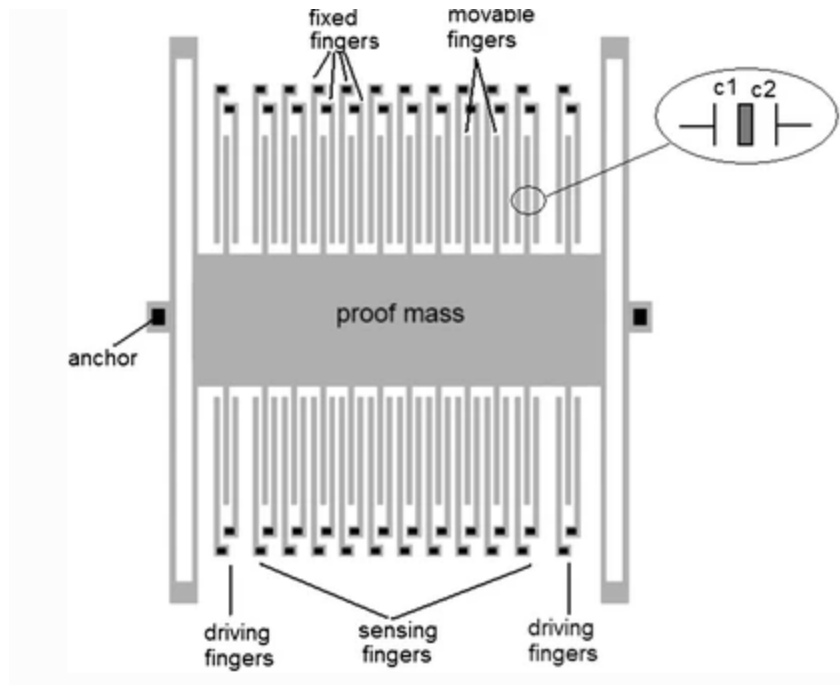
Figure 2.4: Diagram of capacitive accelerometer technology. Taken from Sharma et. al. (2012).

The different forms of gyroscopes include mechanical, optical, and quartz, among others. The theory behind gyroscopes is based on the Coriolis Effect, which describes the transfer of energy between two vibration modes. Put simply, the Coriolis acceleration, which is proportional to the angular velocity of the object, is an apparent acceleration that is observed in a rotating frame of reference. In Figure 1 in [32], the relationships between sense direction, drive direction, and angular velocity are shown . Modern accelerometers and gyroscopes, particularly in the MEMS form, are known for their low cost, low power consumption, and ease of use, among others.

2.3 Machine Learning Overview

With the advancements and reduction in size and cost of sensor development and implementation, as well as data acquisition, cloud communication, and storage, there exists the ability to collect copious amounts of data on from the aforementioned IoT sensor technology. Sensor developers and manufacturers collect data that must be calibrated, and features must be selected and utilized to give the most salient and accurate information for a useful output. Sensor outputs include, but are not limited to, specific gas concentrations from gas sensors, three-

dimensional acceleration and rotation data from accelerometers and gyroscopes, and voice recordings from microphones. Given the availability of this information, the opportunity exists to apply machine learning, deep learning, and classification methods to improve the different outputs of each IoT sensor technology. These approaches could be utilized to provide information about the user, the users' surroundings, and the environment in which they are being deployed, as well as biometric/abiometric information about the sensor, sensor system, and the user. Feature selection and generation are also possible through data mining, analysis, and dimension reduction techniques, and this all can allow the user to evaluate the level of selectivity of gas sensors and the patterns and types of movements for IMU's. The following section describes literature review on general machine learning information.

Machine learning can be categorized into three different forms: (i) clustering, (ii) classification, and (iii) regression. Clustering is defined as a method in which data is divided into groups in a way that objects in a group share more similarity than with objects in other groups. It is utilized in data mining, bioinformatics, energy studies, machine learning, networking, and pattern recognition [33]. Classification is the allocation of objects into either initially undefined classes so that the individual objects in that class are close to one another and can be recognized as such and classes can be defined based off of the results [34], or into pre-defined classes [35]. Regression is the estimation of relationships between a dependent variable and one or more independent variables [36]. Each form of machine learning model is developed through datasets that are split into training and testing sections, in which the training data is used to train the model (and is often split itself into training and validation data to validate and produce the model), and the testing data is used to test the model.

There are multiple forms of training for the different types of machine learning models. Training can be in the form of supervised, unsupervised, and reinforced learning [37]. Firstly, supervised learning is an approach that utilizes labeled training data using a mapping function (e.g., classification or regression). The data is utilized to generate models that are verified with the training data and then correctly assign the testing data. Unsupervised learning is an approach that attempts to identify inherent patterns within unlabeled data through underlying patterns (e.g.,

clustering) in hopes of determining the correct output for testing data. Finally, reinforced learning is an approach that updates based on rewards or penalties for the actions it performs in a sequence of decisions to train the model.

A literature review [35]–[44] on germane machine learning identified several common high-level learning and modeling techniques for imaging and signal-based classification. Elementary classification methods, or methods that can be built upon or combined, include but are not limited to Support Vector Machines (SVM), k-Nearest Neighbors (kNN), Decision Trees, and Naïve Bayes. SVM [38], [41] classify between two or more classes using an N-dimensional hyperplane boundary. The training samples this method focuses on are those closest in the feature space to the optimal boundary between the classes, and these samples are the "support vectors". The aim is to find the optimal boundary between two classes, and it can be used in the problem of more than two classes by repeatedly applying the classifier to each possible combination of classes while being combined with ensemble approaches (e.g., decision tree, voting) in order perform higher level classifications. For nonlinear class boundaries, the feature space can be projected into a higher dimension through the use of kernel tricks, such as polynomial kernels or radial basis function (RBF) kernels.

k-Nearest Neighbors (kNN) [35] models compare each unknown sample directly against the original training data, and that sample is assigned to the most common class of k training samples that are nearest in the feature space to the unknown sample. The object is assigned to the class that is most common to its surrounding neighbors. The model is developed by utilizing training data that has been pre-classified to points within an n-dimensional Euclidean space. The selection of k is dependent on the training data that is available; a low k will mean a very complex decision boundary, and a higher k will result in greater generalization. Decision tree classification [41] models utilize a recursive split of the input data, where "trees" represent repeated splits, branches represent the paths through the splits, and leaves are the ultimate target values. The splits could be based off of a certain band or feature being above or below a threshold, or simply a "yes" or "no" decision, depending on the problem being addressed. Naïve Bayes [45] is an algorithm that utilizes Bayes' rule while under the assumption that the attributes are conditionally

independent, which can be considered to be naïve, hence the name. Compared to the aforementioned classification techniques, it usually requires less data to train the necessary parameters for accurate classification. It operates under the assumption that the presence (or absence) of a particular feature of a class is unrelated to the presence (or absence) of any other feature.

Outside of the elementary classification models, neural network (NN) models [40] are an approach that uses a network of nodes to derive and emulate relationships within complex datasets. In the same regard that the biological neural system has an organization of neurons, axon, and dendrites that carry and relay information from generated electrical impulses, neurons (or nodes) in neural networks are formed through training to create weight connections between inputs and outputs. These models can be trained through supervised, unsupervised, or reinforced learning techniques. Deep learning models are NN models that have more than a few layers within the network. Artificial neural networks (ANN's), which are a form of NN, are structured so that neurons are organized in layers of varying size in the NN model. Convolutional neural networks (CNN's), another form of NN, have a network architecture with convolution, sub-sampling, and classification layers. Different forms of CNN's, which are commonly used in image classification problems, are LeNet, AlexNet, ZFNet, and GoogLeNet, among others.

Dynamic Time Warping (DTW) is an important tool in supporting various efforts, including but not limited to speech recognition, handwriting and signature matching, sign language recognition, amino acid sequence alignment, gesture recognition, biometrics, and time series clustering, among others [42], [43]. It is used to align signals whose features experience effects of temporal distortion or phase-shifting, which are common artifacts in the efforts listed above, and measure similarity between the two sequences. The algorithm attempts to minimize the effects of shifting and distortion in time while measuring similarity by allowing "elastic" transformation of time series to detect similar shapes with different phases, which occurs as the cost function is minimized, along with the optimal warping path, or the minimal path of the distance matrix built between the two signals.

Similarly, Hidden Markov Models (HMM's) have been widely used in speech recognition, bioinformatics, facial expression and gesture recognition, and gene sequencing prediction [44]. They are statistical models designed using a Markov process with hidden states, and the likelihood of transitions between states depend only on the current state, as they are a memory-less algorithm. HMMs are well equipped for sequences of data, as well as data of variable-length inputs, and thus have similar strengths and applications as DTW.

Principle Component Analysis (PCA) and Linear Discriminant Analysis (LDA) [39], [46] are similar techniques used for dimensionality reduction of high-dimension datasets and feature extraction, which allows for ease of interpretation and computation while maintaining information and algorithm performance. PCA, which is commonly used in pattern recognition and data visualization tasks, looks to reduce dimensionality while preserving as much variability, or statistical information, as possible by finding new variables that are linear functions of those in the original dataset that maximize variance and are uncorrelated with each other; these are known as the "principal components". In this sense, the principal components are then representative of the most variance of the data while eliminating variables removing variables that add no new information to the classification task or model. LDA utilizes a linear combination of features to classify two or more groups or events. The ratio of between-class to within-class variance is maximized in LDA to maximize separability, and an optimized decision boundary is created using the covariance and probability of classes within the dataset. It is especially useful for class definition and data classification tasks.

To determine which classification technique to use with the task at hand, it is important to note that the selection of the classification algorithm is case specific. How the classes are mapped, the nature of the training data, and the predictor variables determine the optimal algorithm for the problem of interest. Therefore, the analyst of a specific task should experiment with multiple classifiers to determine which provides the optimal classification for a specific task [38]. There is also the potential for multiple classification methods to be used together to improve the accuracy of a classification problem. Meta-algorithmics [47] refers to the "pattern-driven means of combining two or more algorithms, classification engines, or other systems". Algorithms can be

combined through first-, second-, or third-order means, and oftentimes it is true that the combination of poorly-performing classification algorithms can be useful when combined with others.

2.4 Implementation, Modeling, and Machine Learning/Artificial Intelligence with Respect to IoT Sensor Applications and Biometrics

Previous literature has applied modeling, machine learning, and deep learning techniques to i) human activity recognition (HAR), including gesture recognition and gait analysis, ii) gait analysis and activity recognition in other living beings, such as equine animals, and iii) environmental sensor monitoring. Machine learning and modeling in these spaces has yet to reach the accuracy and robustness desired for the mass implementation imagined, which can lead to undesired rates of misclassification and error in any envisioned space. Given this, it is important to be able to determine the current and future performance of these techniques in each field, and how biometrics/abiometrics can be applied. The following sections describe information collected through literature reviews related to the use of machine learning and modeling techniques for the aforementioned fields.

2.4.1 IMU's and Machine Learning for Human Activity Recognition, Including Gesture Recognition

Human activity recognition (HAR) can be categorized into several forms, including walking, running, sitting, stair ascent and descent, and movement and gesture recognition. American Sign Language recognition, upper limb protheses, and capacitive touch are of similar interest in the application and processes that they follow. Data for HAR can be captured through computer vision- or video-based methods [48]–[50], as well as sensor-based methods [49]–[52] (e.g., IMUs, electrocardiogram (ECG), electromyogram (EMG), and combinations of these). Video-based methods often suffer from partial image occlusion and background clutter, lighting issues, change in scale and viewpoint, and detecting and extracting human location from image sequences, as well as expense of the system, privacy issues, and difficulty in implementation of cameras into different settings [48]. Therefore, sensor-based HAR data capture, which include

sensors embedded in smart phones, wearable devices, and home settings [51], has been growing in popularity due to its ease of use and implementation without affecting daily lifestyle, low cost and power, and miniaturized nature, as well as lack of issues with different environments (such as lighting) and the ability to communicate through wireless sensor networks.

Multiple authors [48], [52] have described the methods for the current "state of the art" approaches for robust and accurate classification of different forms of human activity recognition (HAR). Forms of activity can be categorized into static and dynamic. Static activities include, but are not limited to, sitting, standing, and sleeping, while dynamic activities include walking, running, going up and down stairs, and gesturing, among others. There are also activities with postural transitions, which are activities that shift between static and dynamic, or between dynamic and dynamic or static and static. Examples include, but are not limited to, a jog to a stand or a walk to a jog.

The process behind HAR includes data acquisition, pre-processing (including noise filtering and distortion removal), followed by feature extraction, feature selection, and classification. The authors in [50] summarize common machine learning techniques in HAR when data is collected through wearable sensors and smartphones. They include Decision Trees, k-Nearest Neighbors (kNN's), Hidden Markov Models (HMM's), and Support Vector Machine (SVM) techniques. While each of these techniques have their respective strengths, the weaknesses include the challenges with extraction of principal features that will be effective for classification, as well as overfitting when less training data is available (in the case of SVM, this situation conversely leads to underfitting). The authors in [50] and [52] summarize the common deep learning techniques in HAR, and they include Convolutional Neural Networks (CNN's) applied to images formed from raw sensory data (e.g., virtual images and frequency images), CNN's applied to raw time series signals, Long-Short Term Memory (LSTM) Models for raw signals, and hybrid models that include multiple deep-learning techniques (e.g., an LSTM model with convolutional and global pooling layers). Challenges for deep learning techniques include, but are not limited to, the tradeoff between computational complexity and accuracy and the optimization of hyperparameters (e.g., convolutional layers, filters and filter sizes, neurons, epochs, etc.).

Gesture recognition, a subset of HAR, can be used to express emotion, aide or replace speech (through sign language), and control the activation of different smart devices or technology through human-computer interface (HCI). Specifically, it has been used in the past to interact with smartphones, gaming systems (e.g., the Wii) and virtual reality/augmented reality (VR/AR), and other smart technologies [53]. A review [54] highlighted the commonly used processing technique, which is similar to that used in HAR; data must be denoised and segmented in the pre-processing phase, features can be extracted in the time-,frequency, or wavelet transform-domains, and wrapper, filter, or embedded methods are often utilized for feature selection.

Several authors [55]–[59] have used different machine learning and modeling techniques for gesture recognition. In [55], the authors used a Hidden Markov Model (HMM) for gesture recognition with a handheld device. With seven participants, there were 10 gestures studied and 20 samples per gesture. The authors removed the effect of gravity through orthogonal normalization, as well as the effect of variable duration and the magnitude of the observed accelerations that depend on the rate of the gestures. A left to right HMM with continuous normal output distributions was used with 8 states, two transition probabilities, and one Gaussian output distribution with great effect. The method achieved 96.76% accuracy when using user dependent training, and 99.76% accuracy when using user independent training.

In [56], the authors recognized that gestures, along with other forms of human recognition, are likely to be performed at different speeds, and therefore implemented a Dynamic Time Warping (DTW) algorithm with a time series template optimization that looked to find a set of small distances to the templates of the respective class of the gesture while having large distances to the templates of the classes of other gestures. In other words, the authors looked to define a target function as a measure for class separability of a template and look to optimize that function to maximize the spread between intraclass and interclass distributions. Multiple methods were utilized as potential target functions, including (i) calculating the difference between minimal interclass distance and maximal intraclass distance(s), (ii) calculating the difference of center points of distributions, (iii) calculating the Kullback-Leibler divergence, which is a measurement of dissimilarity for probability distributions that accounts for deviations of the distributions that

the other two methods do not take into account, and finally (iv) error function integrals, which minimizes the threshold classification error and calculates the classification error through the Gauss error function. To test the different target functions, the authors had seven participants complete a set of fifteen instances of nine different classes of hand gestures, and it was seen that the first two target functions achieved higher precision and recall than the latter two. With the optimized templates, the algorithm yielded a precision rate of 97.35% and a recall rate of 85.86% with user-dependent classification.

The authors in [57] used a Frame-based Descriptor and multi-class SVM (FDSVM) to classify the 12 gestures recorded from ten individuals over two weeks using the existing IMU in a Wii remote. Here, the Frame-based descriptor was used to reduce the effect of the intra-class variation and noise seen in feature extraction, and the SVM was used to deal with the highly non-linear gesture space issue and the limited sample size of the study. Frequency- and temporal-based input features were used by the authors, including mean frequency, energy, frequency-based entropy, standard deviation of the amplitude, and temporal correlation among axes. The SVM was a multi-class SVM, as more than two types of gestures are recognized. It was converted to a multi-class problem through the use of several binary-class problems. The experiments by the authors here were aimed at determining the optimal frame number for the frame-based descriptor, as well as evaluating the recognition performance for user-dependent and user-independent gesture recognition. The user-independent recognition accuracy for this study was 98.23% when only 4 of the gestures were examined, and 89.29% when all 12 gestures were examined, while the user-dependent recognition accuracy was 99.38% for 4 gestures and 95.21% for all 12 gestures.

Deep learning techniques have also been considered for recognizing and classifying different gestures for gesture recognition by several authors. The authors in [58] used a multi-layered feed forward artificial neural network (ML-FFNN) to recognize and classify gestures made through recordings made with an IMU attached to the users' wrist. The 26 gestures used were each recorded 50 times, and the authors split those recordings into training, validation, and testing data (560 samples for training, 260 samples for validation, and 560 samples for testing for each user). The authors took steps to remove high-frequency noise generated from involuntary muscle

movement with a rolling average function and used a 3.5 second window for segmentation to remove inconsistencies and high variance of the signals. The ML-FNN included a bipolar logistic as an activation function and underwent supervised training using back-propagated stochastic gradient descent with Least Squared Error (LSE) as the cost function. The study examined inter- and intra-class variance, as well as the optimization of parameters such as the input vector dimensions, the number of classes, and the number of hidden neurons when the number of input and output nodes were held constant. Using this method, the authors were able to achieve 99.42% recognition accuracy after the optimization of the network parameters was done successfully, and variance was reduced.

Similarly, in [59], the authors utilized a feedforward neural network and similarity matching (FNN and SM) model on a dictionary of 24 gestures that included 8 "basic" and 16 "complex" gestures. The authors collected data from five participants using a pen-like sensing device that included an IMU attachment. The FNN recognition algorithm was employed for the basic gestures here, and the algorithm for the complex gestures included the SM algorithms. A segmentation algorithm, which was used to identify the starting and ending points of each basic gesture automatically, both in their own respects and within the construct of the complex gestures, was also developed in this study. Following raw data collection, the authors used a moving average filter for preprocessing, and the zero-crossing points of the smoothed signals were used as indications of beginning and ending points for segmentation. The features extracted from the filtered and segmented signals included mean absolute value (MAV) of the x- and y-axes of acceleration (which encompassed most of the movement, as the gestures were generated by movements in the x- and y-axes of the accelerometer), the ratio of the MAV of the x-axis over the MAV of the y-axis, the absolute value of the differences in MAV_x and MAV_y, the value of the maximum absolute acceleration point, and the correlation coefficient between the x- and y- axis, among others.

The FNN was constructed with three layers, and each node included a non-linear logistic function. Each basic gesture was assigned a corresponding 4-bit Johnson code, and a Hamming distance between the codes were utilized to measure the similarity between recognized basic

gestures within a complex gesture and pre-defined gesture "templates", or the sequence of basic gestures within a complex gesture, that the participants were supposed to complete. The authors conducted both user-dependent and user-independent experiments, and the overall recognition accuracy for the user dependent experiments was reported as 99.88%, while the user-independent recognition accuracy was reported as 98.88%. Both results were measured using 5-fold cross-validation, where the data from four participants were used to create a training set and the fifth was used to create a test set.

Additional considerations for gesture recognition first include incorporating meta-algorithmics and analytics, which have been shown to improve similar systems using the strength of individual classification methods [47]. Another matter is the intent of the gestures being considered, which can be applied to the activation of sensing options within a device, similar to the activation of different smart devices seen in [53]. This activation can trigger certain sensors within an array, the algorithm or model necessary for a desired analyte, or the temperature modulation necessary for that analyte, which gives options and the power of decision-making to the user. Finally, although computer vision or image-based gestures suffer from lighting or occlusion issues, among others, the image recognition algorithms that have been developed recently, such as AlexNet and GoogLeNet [60], [61], are powerful classification tools.

Alternatively, incorporation of these considerations to biometrics techniques, including the conversion of 1-D signals generated from IMUs to 3-D images for improved recognition accuracy and 2nd and 3rd order meta-algorithmics to combine different classification methods for increased accuracy may be beneficial, and will be examined below.

2.4.2 Machine Learning and Modeling for Equine Activity Recognition, Including Gait Analysis and Lameness Detection

Equine activity recognition, including gait and lameness detection, is often a combination of analysis of the equine animal in question's stride frequency and length in combination with the distinction of gait between one of the potential symmetrical or asymmetrical gaits. The symmetrical gaits of interest of an equine animal include walking, trotting, and pacing, while

asymmetrical gaits include cantering and galloping. Similarly, footfall sequence and lameness detection are of equal importance when examining the activity recognition of an equine animal.

Methods of gait measurement exist in different forms, which include kinetic and kinematic measurements. Kinetic measurements are measurements taken by force plates to measure ground reaction force (GRF), as exerted on a limb during the stance phase, in three dimensions. Common methods of kinetic data capture include, but are not limited to, force-measuring horseshoes, treadmills, and ground-based plates. While they are a commonly used data collection method, force-based measurements can suffer from limited, laborious, and time-consuming data collection (mostly in the case of force plates and treadmills).

Kinematic measurements are measurements taken through visual- and sensor-based means to measure gait characteristics, such as optical motion capture (OMC) and inertial measurement unit (IMU). In OMC, markers are attached to the body of the equine animal, and multiple cameras are distributed that track the 3-D position of the markers in space. With IMU sensors, kinematic measurements are taken using strategically placed sensors to measure displacement and orientation of the area of interest on the body of the equine animal. While OMC suffers from issues such as image occlusion, lighting issues, and the restriction of data collection to indoor environments, IMU-based measurements have been noted to have ease of use, low cost and power, among other advantages, and thus have been increasingly employed to for kinematic measurements of gait. The focus in this dissertation, therefore, will be on IMU-based gait measurement techniques.

Several authors [62]–[64] have employed different machine learning and modeling techniques to distinguish locomotion types of equine animals, as well as to score lameness. In [62], the authors used stride timing, limb angle parameters, upper body symmetry and vertical displacement patterns, as well as a symmetry index as inputs to compare IMU-based data to OMC-based data for lameness scoring of seven Warmblood clinic-owned mares. Bland-Altman analysis was used here to study the agreement between measurements of the IMU and OMC systems using the protraction, retraction, abduction, and adduction angles of the limbs in both the sagittal and coronal planes of the horse as it progressed through its gait during trotting. Similarly, statistical analyses of the limb angle parameters were calculated to show per horse variation and between

horse variation. The authors utilized eight ProMove-mini wireless IMU sensors and eighteen infrared cameras that tracked the position of reflective markers, three of which were on the poll (head), three on the girth, three on the pelvis of the horse, and one on each of the attached IMU sensors, for data collection. Data from the IMUs was collected at a rate of 200 Hz. Two experiments were performed for each of the ten horses at walk and trot. Bland-Altman analysis showed that there was a small bias between the two systems of measurement, excluding the coronal angles for the forelimbs, which the authors speculated was likely due to poor depth perception of the OMC system. Also, the authors noted that while the per-horse variation is low, a large variation is noticeable between horses in all calculated limb parameters. It is important to note that the authors observed the need for the biological significance to be investigated with respect to their correlation with lameness.

In [63], the authors utilized LDA using stride timings to find criteria that are optimal for discriminating between the different gaits of an Icelandic equine animal. In this study, the right and left foot timings (e.g., the varied stance and swing times), as well as the ratios of foot-contact times, for all four limbs were inputs to the generated model. Speed was measured throughout the experiment using a GPS receiver attached to the rider's hat, and IMUs were attached to the dorsal portion of the hoof. The samples collected from the IMUs were collected at a rate of 200 Hz. The extracted features were checked using cross-validation, and the LDA generated seven functions, the first three of which cumulatively explained over 95% of the variance between the different gaits and classified 95% of the original and cross-validated cases correctly. Specifically, for the symmetrical gaits, 99% of walk strides, 96% of tolt strides, 99% of trot strides and 77% of pace strides were correctly classified, and for the asymmetric gaits 76% of left canter strides were correctly classified, as were 97% of left gallop, 99% of right canter and 70% right gallop. The variability in classification was mostly due to misclassification between gaits that shared the same lead limb, according to the authors (i.e. left canter instead of left gallop).

To distinguish between sound and lame horses during galloping and trotting gaits, the authors in [64] used a supervised neural network. Single IMU sensors were placed on the head, pelvis, and each limb of the Thoroughbred racehorses utilized in this study. A sound horse was

exercised through both trot and gallop trials, and then lameness of either the forelimb or hind limb was induced using increased sole pressure; the limb selected was based off a coin flip. Variable increases in sole pressure were utilized to collect data from three levels of lameness, including an approximate score of 1 or 2, a 3, and a score of greater than 3. The maximum, minimum, range, and time indices of the vertical head and pelvic acceleration, head rotation in the sagittal plane, pelvic rotation in the frontal plane, limb contact intervals, stride durations, and limb lead preference were inputs to the neural network.

Misclassification rate was between 0.2 and 0.65 for classifications between sound and lame limbs, as well as lameness between individual limbs (e.g., sound vs. left forelimb lame, and forelimb lame vs. hind limb lame, respectively). The authors also examined stride frequency differences between sound and lame horses and found that stride frequency was significantly less for the right limb lead during galloping after induction of lameness in the right forelimb, but this was not true of the left limb lead before and after induction of lameness in the left forelimb, or any other timing variables used to distinguish between sound and lame states. It was also noted by the authors that, against their desire, they created a least one case of residual mild lameness in the right forelimb at the time of the second induced lameness, which may have influenced their results.

When examining further research into characterizing and modeling equine gait and lameness, there are multiple considerations. First, when developing ground truthing for class and model development for the different stages and levels of lameness, as well as the type of lameness, it is important to consider that lameness scoring is dependent on the observer. The authors of [62] noted a lack of consistency between different levels of experience of observers, as well as a limitation of human visual symmetry perception and the bias effect. In other words, visual perception of lameness has been shown to be influenced by the horse, the gait of the horse, and the type of lameness it is experiencing. It is also important not to create or increase any existing variability in the gait of the horse through sensor placement while also considering the position of the sensor with respect to any prospective rider. In the same sense, it is important to consider the variability in gait imposed by the rider themselves, as well as the surface on which the horse is exercising on, and the familiarity that the horse has with the environment that it is exercising in.

Finally, it is of particular interest of researchers to minimize the potential for variability caused by sensor placement and presence, and therefore models and approaches developed for sensors in areas such as the head and sacrum, where extra equipment is commonly required to place the sensors, must be reconsidered, and adjusted accordingly. It is also notable that models developed around the individual horse of interest may be of benefit to the model performance for that horse, as gait is likely varied between individual horses, and lameness is likely to be expressed and measured in different manners that cannot be considered on a larger scale.

2.4.3 Implementation of Environmental Sensors

As was stated previously, environmental sensors are designed to convert a chemical reaction into a measurable electronic signal to respond to changes in their environments. This occurs through the technologies themselves, the different methods of fabrication within those technologies, and the connection to other sensors within networks and sets of networks. Implementation of environmental IoT sensors, namely MOS sensors, involve several common areas of interest using machine learning and modeling techniques. Calibration and re-calibration models are produced to ensure that sensors generate and maintain accurate readings, and improvement in these processes can occur through data pre-processing and robust feature selection. Similarly, correction for variations in measurements are also a common occurrence that requires modeling, including but not limited to environmental differences (e.g., temperature, humidity), interference gases, and aging (or more commonly known as drift) of individual sensors. Improvement in sensitivity and selectivity (outside of technology selection and fabrication) through machine learning models that distinguish between background analytes and the analyte of interest. Reproducibility and inherent variability are commonly examined as well, as sensors of the same technology and makeup often output differing responses to environmental challenges. Topics similar to these will be reviewed and discussed in this section.

Several authors have employed different machine learning and modeling techniques for data pre-processing, feature selection and extraction, and classification of sensed analytes. The

authors in [65]–[67] discuss these topics in relation to electronic-nose (e-nose) sensor arrays, but similar theories can be applied elsewhere.

Modeling techniques have also been employed to correct for issues such as sensor drift, aging, and correction. Data pre-processing techniques were examined in [65]. Here, the authors split pre-processing into i) baseline manipulation, ii) compression, and iii) normalization. The methods of baseline manipulation, or the attempts to reduce the effects of sensor drift, include differential, fractional, and subtractive. Compression, or operations used to reduce the number of measurements per example to a reasonable number, was examined through steady-state, transient integral, and windowed time slicing. Normalization, or the set of operations for smoothing between variations, was examined by the authors using vector normalization, vector auto-scaling, and dimension auto-scaling. In total, this led to the possibility of 48 different combinations of techniques. To measure the performance of the different pre-processing techniques, the authors utilized predictive accuracy, and a classification method involving a combination of LDA as a feature extraction tool and kNN voting rule as a classifier, which was evaluated using 5-fold cross-validation. The results showed substantial differences in the transformation and compression techniques, but no great effect from normalization techniques. The greatest improvement in classification was seen through differential baseline manipulation, compression through transient response, and dimensional auto-scaling normalization.

In [66], the authors propose the use of embedded PC technology with a GNU/Linux operating system and appropriate pattern recognition or regression software in an electronic nose (e-nose) prototype to examine different processing methods. E-nose instruments, according to the authors, include nonspecific sensors in combination with a pattern recognition system. The sensor design included three sensor modules, which each contained four metal oxide sensors, one temperature sensor and signal conditioning electronics on a printed circuit board. The sensor fabrication contained internal structure based on micro-beads of sensing material that was deposited over a coil, and this was meant to provide the ability for fast thermal response to a modulating heater voltage. In this study, sequential forward floating selection (SFFS) was used for feature selection, and feature extraction was done using linear discriminant analysis (LDA) and

principal component analysis (PCA). To test the performance of the feature extraction and selection, both a kNN classifier and Gaussian mixture model (GMM) classifier were utilized. The data set was collected over three days, and the dataset consisted of odors from coffee, tobacco, and cedar-wood. 16 samples were taken for each odor in random order. It was observed that, when using classification rate and boundary stability as metrics of performance, the GMM outperformed the kNN model slightly (86.4% and 85% accuracy using the validation data, respectively). The authors also noted that there was a significant dependence of the performance of the GMM on the number of principal components found using PCA, and that this could be improved by instead using LDA during dimension reduction.

The authors in [67] attempted to address issues of calibration of metal oxide semiconductors due to their inherent high correlation among features, sensor drift, scattering at different concentrations, and lack of reproducibility. This is largely due to the fact that calibration models are only robust to the environmental conditions in which they are constructed, and thus cross-sensitivity is highly present in varied conditions. It is also noted that a similar effect is seen through the inherent differences in manufacturing of sensors of similar types, as they also require specific calibration models with less generalization. This applies not only to the calibration of the original sensors within a system, but also replacement sensors of the same Stock Keeping Unit (SKU). In their study, the authors used five replicas of a 24-sensor array that included eight sensors within three different MOX gas sensor SKUs. The arrays were exposed to a total of 48 different conditions, which included changes in the analyte being exposed to the sensors, the concentration of the analytes, and the humidity level (e.g., six gases at eight humidity and gas concentration combinations). This study examined four different scenarios of calibration of sensor arrays:

- An individual calibration model obtained with data from one sensor array that is then tested with data from the same sensor array;

- An individual calibration model obtained from data with one sensor array that is tested with the other sensor arrays;

- A calibration model that is generalized through collection and training from multiple replicas of the sensor array, and is applied to different sensor arrays, and

- A calibration model that is again generalized through collection and training from multiple replicas of the sensor array, but features are extracted and selected through various sensor types and operating temperatures.

The authors used partial least squares-discriminant analysis (PLS-DA) in combination with kNN in the latent variable (LV) subspace as a model for calibration, as well as feature selection using a genetic algorithm. In the first scenario, the classification rate was 100% when the calibration model was used on the same sensor array that the model was trained on, but in scenario two, the classification rate dropped significantly to 91% when the model was applied to other sensor arrays. The third scenario saw a classification rate of 99% when the models generated from four of the sensor array replicas were tested on the fifth sensor array, and in the fourth scenario, the addition of feature selection resulted in a classification rate of 97.5%, which is a drop from the first generalized model, but still an improvement from the non-generalized models.

When examining further research into modeling and correcting sensor readings, there are considerations that have yet to be examined. First, raw signals require complex analysis that is not easily interpretable. Most methods require optimization, and the success of optimization is dependent on the quality and quantity of the data. Sensor variability and the constrained conditions of calibration models hinder their generalization capacity, and this, along with the inherent variability of similar sensor and sensor array constructs, mean that there are real-world implementation issues. However, the inherent sensor variability can potentially be utilized for other purposes related to biometrics, and this will be an important aspect of examination in this dissertation.

2.4.4 Implementation of Biometric Techniques

As mentioned above, biometrics are biological measurements that are used to refer to the authentication or verification of a person by measuring and assessing physical and behavioral characteristics. They are implemented in unimodal methods, where individual biometrics are assessed, as well as multi-modal methods, where multiple biometrics are combined. Data utilized

for biometric problems is collected in both sensor- and image-based fashions. In-depth reviews of the different stages of biometric implementation will be examined in this section.

Several authors [68]–[70] have reviewed the implementation of biometric techniques. In [68], the authors reviewed sensor-based biometric recognition techniques through the examination of the acquisition of biometric data from a sensor, data pre-processing and potential dimensionality reduction, feature extraction, recognition and/or classification, clustering, and validation. Data acquisition is split between physiological, behavioral, and biosignal-based data. The authors identified several issues with sensor-based data acquisition, including varying presentation of the signals, irreproducible presentation of the signals, defective signal acquisitions, and sensor technology inconsistency (e.g., differing sensor data changes between technologies and manufacturers). To extend information between different biometric sensors with different characteristics and data types, data pre-processing is an important step. The authors describe pre-processing as a "process of selecting different constraints that are expressive of the sensor data", which can take different forms depending on the type of biometric. For physiological and behavioral biometrics, the stages are described as i) cropping or resizing, ii) normalization and segmentation, and iii) filtering. Biosignal-based sensor data, while often requiring similar cropping, normalization, and segmentation, also require different filtering methods.

Feature extraction and selection with respect to sensor-based biometric techniques can account for the issue of dimensionality reduction, where the likely high-dimensional data is not appropriate to be handled, according to the authors. Extraction of the features conserves the maximum amount of information as the original filtered data, while selection then selects the best features to categorize classes of the data. Feature extraction can be categorized as non-transformed or transformed descriptors, structural, or graph descriptors, while feature selection is categorized into exhaustive searches, branch and bound algorithms, sequential selections, and bidirectional searches. According to several authors, features can also be used from several biometric sensors through feature fusion, and each feature can respectively have an assigned weight that determines its impact on the final decision of the respective output of the biometric decision. Fusion can also

occur at the algorithm and biometric level, as it is possible to combine both various feature algorithms and biometric sources (e.g., a combination of a fingerprint and facial recognition).

In classification, the authors note commonly used algorithms in biometric problems, such as k-Nearest Neighbors, Bayesian Classifiers, Support Vector Machines, and deep learning methods, which include neural networks that include an appropriate architecture selection and regularization. When considering clustering, the authors also note multiple steps and techniques. The steps include specifying i) a variation in measurement among the samples, ii) a clustering principle, and iii) a search algorithm to assign the data to various clusters after the variation and principle have been determined. Clustering methods discussed include hierarchical, density-based, grid-based, and partition-based. Finally, the authors discuss validation, which is meant to report the performance and issues with a choice of process and model. Considerations the authors noted here include proper model and algorithm selection, constraint settings, and over and underfitting the training of the model. Validation methods here include k-fold cross-validation, leave-one-out-cross-validation, random subsampling cross-validation, and boot-strapping methods. After parameter settings and the model have been selected and optimized, testing data should be utilized to estimate the performance with new data.

In [69], the authors discuss Multiple Classifier Systems (MCS), and their application in the field of biometrics. An MCS is categorized by classifier dependencies, or the outputs of the classification based on the different parameters and methods; type of classifier outputs, which include abstract, rank, and measurement; aggregation procedures, which include trainability and adaptivity; and architecture, which is the grouping of the multiple classifiers into hierarchical, cascading, and parallel configurations. In the case of multi-modal biometrics, the fusion of information can also occur at the pre-classification level or post-classification level. In the pre-classification level, fusion can occur either through sensor or feature level fusions. Sensor level fusion combines raw data from sensors, while feature level fusion combines feature vectors either from different sensors or different extraction algorithms on the same data. In the post-classification level, fusion occurs through abstract-level fusion, which is the combination of decisions already taken by individual biometric systems (i.e., majority and weighted voting); rank-level fusion,

which allows for a system to provide possible matches ranked according to the output of the full classification; and measurement-level fusion, which provides probabilities of the rankings between different classifiers.

Gawande et. al. [70] reviewed both unimodal and multimodal biometric techniques, as well as some of the evaluations of performance and limitations associated with biometric problems. According to the authors, the accuracy of biometric systems are not static, but are dependent on several factors, including but not limited to biometric quality of the data, size of the database, the time interval between enrollment and verification, variations in the operating environment, distinctiveness of biometric modality, and robustness of the employed algorithm(s). The common performance metrics include, but are not limited to, false acceptance rate, or the rate of accepting an imposter as a legitimate user; false rejection rate, or the rejection of authorized individuals; failure to enroll, or the lack of required biometric trait from the user; and equal error rate, or the number of both false rejections and false acceptances. Other metrics of biometric algorithms include cost, interoperability, user convenience, and security.

The authors continue to discuss the issues with unimodal biometric systems, which include (i) noisy data acquired by the sensor, which can greatly reduce the accuracy of the biometric system, (ii) non-universality, which refers to the lack of ability for every individual to produce the biometric trait of interest, (iii) lack of individuality, or the measure of similarity between individuals with certain biometric traits, (iv) lack of invariant representation, or the inherent variability between the user's template data and verification data, and (v) susceptibility to circumvention, or the ability of an imposter to circumvent a biometric system using spoofed traits of a user. Due to these issues, the authors propose multimodal systems, as including different types of biometrics together can improve the performance of the biometric system over unimodal systems. While this is true, multimodal systems have their own disadvantages, including high computational cost and storage, time for enrollment and verification, and risk of not combining the different modalities correctly, which can further decrease the accuracy of the system from the unimodal possibilities.

According to the authors, the methods of forming multi-modal biometric systems include (i) through multiple modalities, (ii) through similar measurements from multiple sensors (e.g., collecting data of a subject's face from both a static image and a video frame), (iii) through multiple features (usually from an image), and (iv) through repeated instances, where a measurement can be taken repeatedly for increased recognition accuracy. The authors discuss a method of fusion known as fixed rule fusion, which include maximum or minimum rule, sum rule, product rule, and mean rule. Within fixed rule fusion, matching techniques that measure the distance between the template and validation data include city block distance, Euclidean distance, Mahalanobis distance, and Hamming distance. These measurements of matching can be utilized in multimodal systems where one biometric is less informative than another, such as when a user has dry hands or is wearing facial protections in certain environments, as well as when multimodal systems have different expectations of performance, such as when a gait-based biometric is combined with a facial scan. Typically, different biometrics have greatly different authentication probabilities; for example, iris detection provides many more bits of recognition than gait analysis. This leads to the common application of gait and similar biometric recognition techniques to "auxiliary" biometrics, while facial and iris detection are commonly primary forms of recognition.

Another important consideration when examining biometric implementation is the level of biometric which is being utilized. In [4], the author discusses dynamic and challenge-based biometrics. In biometric-based security systems, once access is gained, there is oftentimes no further check into the identity of the user who has gained said access. With dynamic biometrics, the level of security changes throughout the session, and the level of authorization can be adjusted based upon the current confidence of the system based upon the previously interpreted biometric measurement. These dynamic biometrics are based upon two or more biometrics in combination and are also based upon the availability of the biometrics for said combination. These biometrics can be harvested through certain challenges, which can be asked of the user attempting to gain access to the system. The author uses this theory here to develop a biometric cepstrum, which is established through the availability and performance of the measurable biometrics. This method is

used to maintain a biometric virtual private network (VPN), which is the secured link between the user and the information being protected.

Chapter 3
Example of Sensor Implementation in At-Home Healthcare Through "Magic Wand"

As was mentioned in Chapter 2, the capabilities of IoT-enabled sensors have expanded due to increased research in the fields of non-invasive medical diagnostics and therapeutic monitoring techniques. This leads to the potential for at-home healthcare opportunities, both for those in assisted-care situations – in which frequent diagnostics may be necessary – and for those who have limited availability to proper healthcare services. All of these groups are in need of frequent diagnostics, such as for diabetes. Addressing these needs is possible through a combination of data collection, connectivity of multiple types and units of sensors, artificial intelligence (AI) and machine learning (ML) algorithms, and "smart home" environments. In developing countries, where healthcare infrastructure is often limited and the burden of disease is high, technology for the monitoring of specific biosignals will be especially beneficial. This is also true of remote locations in any locale. The most recent Personalized Medicine Coalition (PMC) report of the year (which represents innovators, scientists, patients, providers and payers, and promotes the understanding and adoption of personalized medicine concepts, services, and products to benefit patients and health systems) stated that one of the most important goals of healthcare moving forward is to implement better personalized healthcare in order to optimize medical decisions, improve medical treatments, and reduce waiting lists and financial costs while treating patients holistically [71]. Mobile diagnostics give the opportunity for both of these goals, and many others, to be met. As mentioned previously, the two main methods of mobile medical diagnostics are through sensing and imaging. This section, however, will focus on the potential for IoT (Internet of Things) based sensing capabilities in the field of mobile health diagnostics.

To describe a method of implementing the previously reported technologies in a single portable device, this chapter will examine the capabilities of these IoT enabled sensors, and their expansion into the field of non-invasive medical diagnostics and therapeutic monitoring techniques. Similarly, it will outline the capabilities of these sensing opportunities in the field of

cyber security through both (i) biometrics of the user and (ii) so-called "abiometrics" (biometric approaches applied to non-living items) of the device components. This leads to the potential for secure at-home healthcare opportunities, as reported in [72].

3.1 Environmental Gas Sensor Arrays for Non-Invasive Diagnostics and Exposure Analysis

The knowledge that breath odors can be used for diagnostic purposes goes back as far as 400 B.C, where it is mentioned by Hippocrates as a diagnostic tool [73]. In recent years, 1,765 different gases/VOC's (volatile organic compounds) have been recognized in exhaled breath (EB) [74]. The methods of measuring these components include gas chromatography (GC), mass spectrometry, laser-absorption spectroscopic techniques, and chemical sensors and sensor arrays [74]. For sensing or detection methods to be viable, they must have sufficient sensitivity, high selectivity, and system stability [75]. The cheaper and simpler alternatives to GC, which has been the most common method to this point, are chemical sensor arrays, which have shown promising results in medical diagnostics for kidney disease, diabetes, Alzheimer's, Parkinson's, and lung cancer. Multiple reviews have summarized the potential uses of sensitive materials in the form of semiconductor-based chemiresistors or sensor arrays, which include metal oxides, graphene, and carbon nanotubes, among others [74]–[76]. Chemiresistive gas sensors are reasonably applicable to the field of early disease screening through EB measurements due to their recent advancements in compact size, low power consumption, inexpensive price, and easy integration into sensor arrays [77].

Examples of VOC's and their corresponding diseases are shown in Table 3.1.

Table 3.1: Examples of verified biomarkers present in EB, and their respective diseases. © 2020 IEEE. Reprinted, with permission, from W. Anderson, S. Simske, "At-Home Healthcare through Smart-Environmental Sensing, including Biometrics for Multi-Factor Authentication", IEEE ICHI, Dec. 2020.

Gas/VOC	Corresponding Disease(s) for which the gas/VOC has relevant diagnostic value
Acetone	Diabetes[74]
Ammonia	Kidney disease[73] and renal function[74]
Carbon Monoxide	Lung inflammation[74]
Dimethyl Sulfide	Liver Disease[74]
Ethane	Schizophrenia[74]
Hydrogen Cyanide	Bacterial Infection[74]
Nitric Oxide	Asthma[74]
Methane	Irritated bowl syndrome, oxidative stress, etc.[75]
Carbon dioxide	Helicobacter pylori infection[76]

These diseases range from minor bacterial infections to major ailments, such as liver or kidney disease. Major diseases, such as lung cancer, colorectal cancer, breast cancer, and tuberculosis have biomarkers identified, but more studies are needed to verify and simplify these [78]. Saidi et al. recently discovered four new biomarkers for lung cancer through exhaled breath analysis and showed that electronic nose (e-nose) type sensor arrays are viable for not only determining the presence of lung cancer, but also the histological type of lung cancer [79]. Further studies of this sort must continue to help narrow down the most descriptive biomarkers, as many of these major diseases need early detection and diagnosis for improved treatment options and results. This

follows the rule, "the earlier detected, the better." Sensor arrays are generally useful for distinguishing the presence of a single disease from a healthy person; however, the ability to distinguish the presence of different diseases from each other is not yet possible due to the vast overlap of biomarkers between diseases [78]. The ability to distinguish patterns for distinct diseases is available; this method is analogous to a "fingerprint" measurement of a person. "Fingerprints" of biomarkers can be determined through further studies to give a more in-depth distinction between sets of biomarkers present in the state of a disease.

Lung function analysis, or finding the spot where expiration ends and the consecutive inspiration starts, is a crucial step in pulmonary function testing [80]. Changes in the respiratory cycle, including frequency and continuity of breathing, are other informative measurement made possible through sensor arrays. Individual psychological stress caused by cardiac and arterial vascular dysfunction can be monitored [77], and the presence of lung diseases and infections can be detected and diagnosed at early stages through the tracking of this cycle. The final use of EB measurements is the tracking of environmental exposure through VOC detection. Most of the VOC's found in EB are in fact due to this environmental exposure, which has practical uses in the broader area of personalized medicine, wherein measurement, diagnosis, prognosis, and therapy are customized to the individual.

3.2 Diagnostics Through Voice Recordings

Microphones have been integrated into much of the current technology used in today's world, including cellular devices, laptops, the interiors of cars, and many others. Low cost, low power devices give high-quality signals that allow for speech recognition, and the expanding research on noise cancellation creates superb results. Multiple studies have recently recognized that, because of the direct correlation between voice impairments and Parkinson's disease in 90% of patients, a voice recognition method is very useful for early detection of the disease [81]–[85], which affects seven to ten million people worldwide [84]. Similarly, speech analysis has been used by groups like Koing et al. to diagnosis mild cognitive impairment (MCI) and early stage Alzheimer's disease with as high as 87% accuracy [86]. Kaminska et al. showed that, through

speech analysis and acoustic features, the four states of bipolar disorder (mania, euthymia, depression, and normal) were able to be monitored with varied success through clustering methods (up to 80% correlation of clustering) [87]. Early diagnosis and frequent monitoring of these diseases improves treatment options for those who suffer the effects, and speech analysis through data acquisition using microphones are making this more and more possible.

Speech analysis has also been utilized for pathology detection in patients by multiple research groups [88]–[90]; in these studies, those participants who are healthy and who are sick are recognized correctly with accuracy as high as 98.23% [89]. Though this type of analysis is not specific to any certain disease: some groups are attempting to use speech analysis to diagnose specific illnesses. Brown et al. have begun studies into using recordings of both speech and coughing, along with an input of symptoms by the user, to diagnose COVID-19, where they have had mild success to date [91]. Similarly, Lei et al. used recordings of breathing sounds for both classification between healthy and pathological patients and as reliable diagnostic indicators for influenza, pneumonia, and bronchitis [92]. Detecting voice disorders -- which can occur after a lasting cold or flu, a continuing virus or bacteria, or from vocal abuse -- are important as well. Akbari et al. was able to distinguish, with varying success, between subsets of different voice disorders, including paralysis, hyperfunction, unilateral vocal fold paralysis, vocal fold polyp, vocal fold nodules, A–P squeezing, and gastric reflux [93]. Accuracy was as high as 97% in this study. From these results, it is clear that the clinical relevance of diagnostics based on voice data and speech analysis is practical for implementation in a mobile healthcare system.

3.3 Wearable Monitors for Vital Recordings, Motion, Gait, and Related Therapeutics

The ability to portably monitor heart rate and blood pressure has been made reliable in the past few decades [94] .This has been made possible through wearable monitors, such as pulse oximeters which use photoplethysmography. Wearable cuffs, which are now commonly found in many smartwatch products, such as the AppleWatch, have also proven useful. Data from these sensors are of great importance, as hypertension, or high blood pressure, is an often-undetected

health disorder that can lead to more severe diseases, such as heart disease (including congestive heart failure) and renal dysfunction [95]. This issue can be resolved through wearable monitoring systems that communicate alert messages to the patient and the healthcare provider when these sensors detect alarming measurements [96]. These wearable monitors can also be utilized to measure stress levels, as studied by Can et al., who reported 97.92% accuracy for three-level stress detection with their person-specific models [97]. When integrated into a system of other IoT's, the impact of these wearable monitors is quite likely to increase.

Inertial measurement units (IMU's) have been integrated into many of the same technologies that microphones have, including cellular devices, newer drive-assist vehicles, and various others. These IoT sensors have also been heavily studied as wearable sensors for their ability to monitor the various stages of rehabilitation for patients with cerebral palsy [98]–[100]. This is important, as the high incidence and costs associated with cerebral palsy means that improved rehabilitation strategies are necessary [100]. Rehabilitation post-stroke is a similar situation that can require high incidence and improved rehabilitation strategies [101], [102]. Laudanski et al. reported recognition of overground walking, stair ascent, and stair descent with 100% accuracy; and overground walking, stair ascent, and descent with a distinction between stepping pattern used while negotiating stairs (step-over-step (SOS) and step-by-step (SBS)) with 94% accuracy for post-stroke patients [101].

The same sensors have been utilized to monitor everyday function for signs of something out of the ordinary for elderly patients, or those at high risk for injury [103]. Similarly, these sensor systems can monitor with recognition rates above 85% the rehabilitation motions of patients suffering from frozen shoulder, knee surgery, and hip surgery [104]. While results of wearable IMU devices for different rehabilitation tracking and monitoring techniques is proven to be sufficient, the number of IMUs needed for these applications is difficult to determine because comparison between descriptions of positions of these sensors throughout the different studies is not precise enough for the comparisons to be considered uniform [105]. This does not deter from the fact that these sensors have shown their utility within their own systems and would be beneficial when included in an at-home healthcare system with other IoT sensor systems.

3.4 Effects of Environmental Pollution on Human Health Conditions

Air pollution exists in many different forms and has a major impact on the lives of those that live in its midst. Many studies agree on the major impacts that air pollution has on respiratory diseases, functions, and inflammations; as well as cardiovascular diseases and functions [106]–[109]. In 2016, the World Health Organization estimated that particulate matter (PM) air pollution contributes to approximately 800,000 premature deaths each year through these ailments; this number has likely increased over the past few years [108]. Example pollutants include particle pollution, ground-level ozone, carbon monoxide, sulfur oxides, nitrogen oxides, and lead [109]. PM pollution, which is comprised of a mixture of solid particles and liquid droplets (e.g., soot, smoke, etc.) can be readily detected through sensor arrays. This is of the utmost importance, as susceptible populations, such as the elderly, asthmatics, or those infected with COVID-19, may benefit from limiting their outdoor activity during times where pollution is at a peak, and when poor air quality days are occurring.

Changes in behavior such as outlined above may benefit individual patients in both short-term, symptomatic control and in long-term cardiovascular and respiratory complications [108]. The use of these sensor arrays, in combination with breath analysis, will be beneficial for informing public officials of the presence of such pollution spikes in hopes of mitigation, as well as for the spread of public knowledge of the timings and locations of such occurrences. It is also estimated that 4.3 million people die from household air pollution every year globally [110]; localized mitigation, therefore, is also of the utmost importance. Integration of the same sensor arrays used for breath analysis into a monitoring system is advantageous for these purposes.

3.5 Biometrics, and Multi-Factor Authentication

Biometrics, or the assignment of identity through the measurement of physical attributes or behavior [71], has recently been adopted at an extensive rate for security purposes. This is due to the fact that, when used individually, many former security measures, such as passcodes and pins, are easily stolen or lost. Thus, a recent push to use physical biometrics has taken place.

Physical biometrics include facial recognition, fingerprint or iris/retina scans [4], which are still the most popular forms [7]. When combined with other security measures, such as pin codes and passwords, multiple levels of authentication are created. This is a form of identification scheme that pairs a "who-you-are" with a "what-you-know" technique [111]. Another form of identification, "what-you-have", can also be utilized as a level of authentication; an example of this would be an RFID card, or an e-token [111]. The location of the user is an often forgotten biometric, but it can be utilized in any setting where the location data is readily available.

Similarly, biometrics can be extended to continuous forms, which include arm sweeps, finger writing, gestures, handwriting, keystroke, heartbeat, voice recordings, and gait analyses [4]. With the availability of IoT technology through mobile devices, these biometrics are all readily available for use. Recently, a study by Zhao et al. showed that recordings of intervocalic breath sounds, or sounds made through inhalation of air during speech, was successfully used as a biometric; the group was able to recognize individuals using this biometric with a CNN-LSTM method at 91.3% accuracy when testing a group of fifty speakers [112].

Biometrics are part of the continuum between inspection (or validation) and the forensic identification of a single individual, item, or process. Because of this, IoT sensors of different types also contribute a biometric of their own to the system. Therefore, to achieve multi-factor authentication, one must only select the best performing biometrics, whether that be individually or as a combination of two or more through hybrid biometrics. This decision, along with a set of sensor biometrics and a location determination using a GPS unit, provides a path to three-factor authentication, ensuring with even higher confidence the security of the system.

3.6   Integration of IoT sensors into "Magic Wand" Appliance"

A system that integrates multiple of IoT sensors for personalized medicine through expired breath analysis, voice recordings, vital monitors, and gait analysis (Figure 3.1) is able to output both 1) the status of the user, with respect to the user's body and to their surroundings; and 2) the security of the data from the system. This mobile healthcare and environmental monitoring are given through the previously described magic wand appliance (Figure 3.2) [113].

When combined with a ML/AI algorithm for classification, the system will be able to combine outputs from the sensing options mentioned and make a combined decision on the user's health status while simultaneously validating the identification of the user through multiple biometrics. When applied to specific application areas, evolutionary and agent-based models will also be employed for overall system design, deployment, test, and measurement optimization. For successful output of the system, it is likely that a Bayesian algorithm will be effective for classification of both health status and biometric validation. Communication of the system can be easily implemented through cellular devices, as over 94% of the world population-- that is, 6.8 billion people-- are subscribers of cell phone technologies, and an estimated 2.7 billion subscribers are using Internet [114]. This platform can be employed to assess all necessary health conditions of the user and help educate and empower individuals and communities to understand their local environment and associated health effects. This, in turn, allows them to actively participate in avoidance and/or remediation strategies; that is, personalized healthcare.
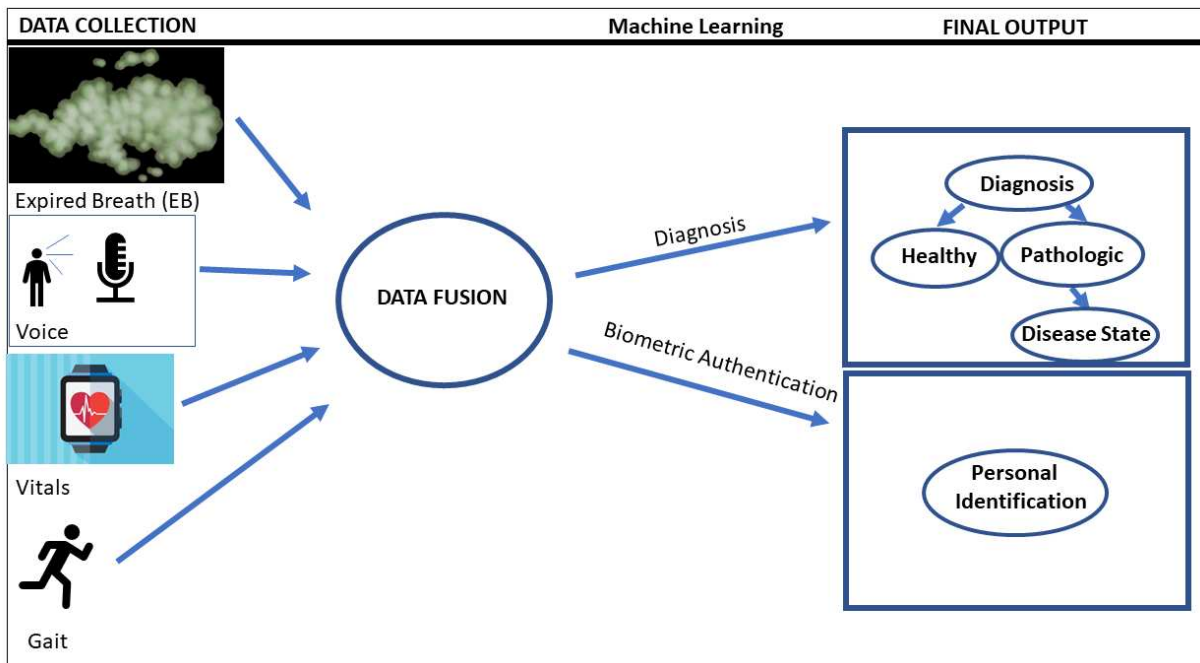
Figure 3.1: Integration of IoT sensors into one comprehensive system in which data fusion allows for biometrics and diagnostics cohesively. © 2020 IEEE. Reprinted, with permission, from W. Anderson, S. Simske, "At-Home Healthcare through Smart-Environmental Sensing, including Biometrics for Multi-Factor Authentication", IEEE ICHI, Dec. 2020.
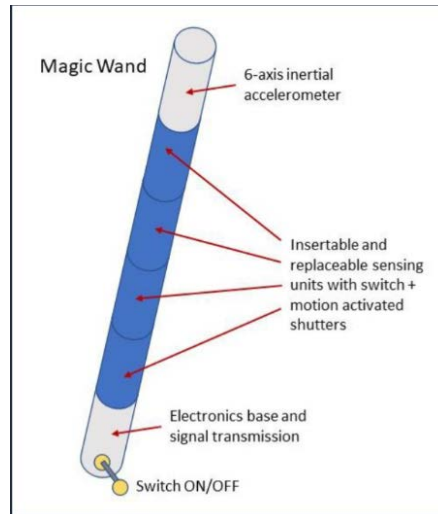
Figure 3.2: Magic wand device in which fusion allows for biometrics and diagnostics cohesively. © 2020 IEEE. Reprinted, with permission, from W. Anderson, S. Simske, "At-Home Healthcare through Smart-Environmental Sensing, including Biometrics for Multi-Factor Authentication", IEEE ICHI, Dec. 2020.

Chapter 4
Classification Examples for Gestures with Intent

In this Chapter, gesture recognition through IoT sensors in the form of inertial measurement units (IMU's) is addressed because of their ease of use, potential of added security through the potential biometric measurements of the user, and the ability of gestures to be used with intent of sensing. This is a form of Human-Computer Interface (HCI), where a user communicates its intentions with a smart technology or device (possibly within a smart system). Alternatively, activation by button pressing has been used for household appliances for generations but (i) it might be difficult for elderly users who are unable to distinguish different buttons within the control system and (ii) doesn't engage younger users like "waving a wand" might. When a movement is made for a gesture, acceleration naturally occurs, and this information can be used to determine how the movement was made along with the path of the extremity. As mentioned in Chapter 2, gesture recognition exists in both the form of video- and sensor-based recognition, and these vary in both their data collection and classification methods. However, the low cost and low power use associated with accelerometer and IMU-based gesture recognition are more desirable than vision-based detection, which can be altered by illumination differences and poor image quality. As discussed previously, there have also been many different uses for gesture recognition, including American Sign Language (ASL) detection [115]–[117], as well as recognition for static and dynamic hand gestures [118]–[120] and pens and holdable objects [59], among others. Common machine learning (ML) algorithms for gesture recognition mentioned previously include dynamic time warping [121], [122], Hidden Markov Models [117], [121], Support Vector Machine [123], [124], and Linear Discriminant Analysis [115], [125], among others.

To begin the work described in this chapter of the dissertation, it was prudent to first start with a basic method of gesture recognition through a simple set of equations, known as an objective function. These equations would use the basis of the IMU technology, the axes on which they collect data, to recognize simple movements that could later be built upon as a combination of these simple movements. These "atomic gestures" (or elementary gestures) are defined as

movements that cannot be decomposed any further and can be used in combination for complex gesture recognition [126]. Objective functions such as the ones that will be defined in this section have yet to be examined, and they will be compared to previous methods to determine their effectiveness. If possible, it will then be sensible to examine methods of improving the efficacy of the equations.

Deep learning techniques, such as Convolution Neural Networks (CNN), have also been studied extensively for such recognition. Although images from vision-based sensing are less desirable for gesture recognition due to the inconsistencies of image quality, the image processing techniques available are often more robust and accurate than many of the machine learning techniques described previously. AlexNet, a CNN, won first place in ImageNet Large-Scale Visual Recognition Competition in 2010, and has since been one of the gold standards for image recognition due to its superiority over other classification methods [60], [61]. Nakano et al. [127] noted the potential of converting 1-D signals to other forms for the purpose of improved classification, as techniques for data reduction and ease of visualization are needed for accurate classification. Representing time series data as images, therefore, is an attractive method for potential value in 1D signal classification and will be examine in this section as well.

This chapter herein describes a proof-of-concept pilot study in which multiple classification methods, including a simple optimized objective function, an SVM with that objective function as a form of initial decision through predictive selection, and through representing 1-D time series signals as 3-D images, which are then recognized using state-of-the-art image recognition algorithms such as AlexNet (the CNN used herein). Due to the limited data collection from the COVID-19 pandemic, the small sample sizes here limit the conclusiveness of the statements made in this chapter.

4.1 Methods

Classification through an Objective Function with SVM

Data was first collected from 5 participants using a LSM9DS1 9-axis accelerometer/gyroscope/magnetometer connected to an Arduino UNO at the end of a 6-inch-long

PVC pipe (Figure 4.1). The subjects were asked to hold the gesture sensing device vertically to perform the gestures depicted in Figure 4.2.
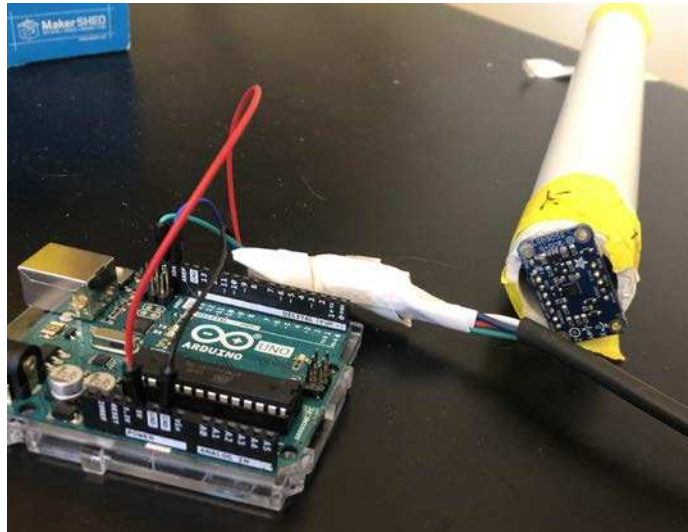
Figure 4.1: LSM9DS1 9-axis accelerometer/ gyroscope/ magnetometer attached to the end of a 6-in long PVC pipe.

For the purpose of this study, five participants (four males and one female) completed a set of pre-defined "atomic" gestures (Figure 4.2). These movements are composed of translational (Figure 4.2(a-c.)) and rotational movements (Figure 4.2(d-f)). Each participant completed a total of 50 of each gesture with each hand, for a total of 600 movements.

(a)   (b)   (c)   (d)   (e)   (f)
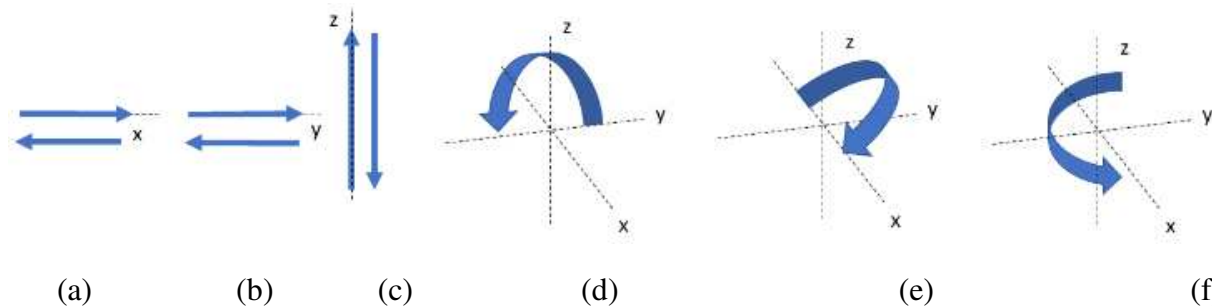
Figure 4.2: Atomic gestures; (a) x-direction, (b) y-direction, (c) z-direction, (d) yz rotation, (e) xz rotation, and (f) xy rotation.

Each trial began with a user-initiated start through the push of a button, and the respective trial ended when the user returned to their initial starting position, and no movement is detected

for a full second. Data is sampled at 50 Hz from the three axes of the accelerometer (x, y, and z-axes) and gyroscope (roll, pitch, and yaw axes). Classification is based on a 50% training and 50% testing configuration of the movement set for each user. To classify movements, data must first be separated into "movement" and "non-movement". This is performed using an adaptive threshold, which is optimized for each user based off accuracy (Figure 4.3). 20 ms windows of data with no overlapping frames are utilized to segment the data based on the beginning and ending of each movement. The mean acceleration and angular velocity are stored, along with calibration data acquired during pre-measured non-movement that is used to compensate for potential offsets of the sensor, including gravity.

The objective function equations, defined to differentiate among the six primary movement behaviors, are described below (Eqns 4.1-4.6),

$$J_x = \frac{2 * |x - x_o|}{|y - y_o| + |z - z_o|} + W_2 \frac{|p - p_o| + |q - q_o|}{|r - r_o|} \tag{4.1}$$

$$J_y = \frac{2 * |y - y_o|}{|x - x_o| + |z - z_o|} + W_2 \frac{|r - r_o| + |q - q_o|}{|p - p_o|} \tag{4.2}$$

$$J_z = \frac{2 * |z - z_o|}{|x - x_o| + |y - y_o|} + W_2 \frac{|r - r_o| + |p - p_o|}{|q - q_o|} \tag{4.3}$$

$$J_{yz} = \frac{|y - y_o| + |z - z_o|}{2 * |x - x_o|} + W_1 \frac{2 * |r - r_o|}{|p - p_o| + |q - q_o|} \tag{4.4}$$

$$J_{xz} = \frac{|x - x_o| + |z - z_o|}{2 * |y - y_o|} + W_1 \frac{2 * |p - p_o|}{|r - r_o| + |q - q_o|} \tag{4.5}$$

$$J_{xy} = \frac{|x - x_o| + |y - y_o|}{2 * |z - z_o|} + W_1 \frac{2 * |q - q_o|}{|r - r_o| + |p - p_o|} \tag{4.6}$$

where x, y, and z are accelerometer data in the x, y, and z directions, respectively, r, p, and q are angular velocity in the roll, pitch, and yaw directions, respectively, x_0, y_0, z_0, r_0, p_0, and q_0 are the respective calibration data for each axes, and W_1 and W_2 are optimized weights determining what relative amount of the gyroscope data will give the best model accuracy. Each J_n is the respective

output for each potential class of the classifier, where n is the direction of movement in each case (e.g., J_x is a movement, or gesture, in the x-direction).

The optimization algorithm for this objective function is described in Figure 4.3 below.
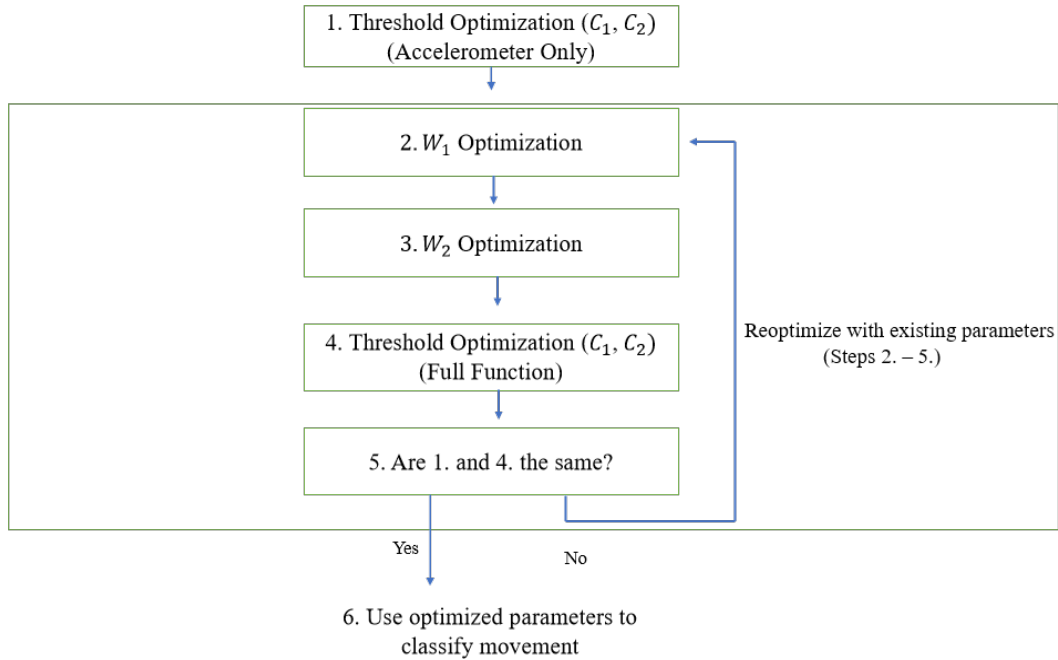
Figure 4.3: Optimization algorithm for determining the threshold and weight of gyroscope data used to achieve the highest accuracy of the model. C_1 and C_2 represent the thresholds for the accelerometer and gyroscope data, respectively, and W_1 and W_2 represent the weights applied to the gyroscope data in the objective function equations for the rotational (eqns 4.4-4.6) and translational (eqns 4.1-4.3) movements, respectively.

In this algorithm, the threshold between "movement" and "non-movement" data is first optimized (C_1 and C_2, where C_1 represents the threshold for accelerometer data, and C_2 represents the threshold for gyroscope data). After an initial optimization of just the threshold for accelerometer data, the weights for the gyroscope data for both translational and rotational movements are optimized similarly (W_1 and W_2, respectively). Once accuracy has reached a maximum value, the threshold weights are again optimized, this time including the threshold of the gyroscope data (C_1 and C_2, respectively). C_1 is examined in a range of 3 to 10 m/s2, while C_2 was examined in a range of 25 to 40 dps. If the accuracy between the initial threshold optimization and the second optimization is unchanged, classification occurs. If not, the process of optimization

of both the weights of (i) gyroscope data and (ii) thresholds of each type of data are repeated until accuracy is maximized (and error is no longer changing).

Improvement of Classification through Axis Shift

The method of improving the previously described classification (the classification through an objective function with SVM) is examined, specifically for the translational movements through an axis shift which has been presented in publication [128].

The same optimization and classification approach is used as previously described (Eqns 4.1-4.6, Figure 4.3). To improve accuracy, data manipulation can be applied through projecting the translational movement data onto the respective axis the movement was made. This is performed by finding the mean amount of acceleration data in the x-, y-, and z-directions throughout each respective movement, normalizing each vector, and placing it into a matrix (Eqn. 4.7),

$$S = \begin{bmatrix} x_{m,x} & y_{m,x} & z_{m,x} \\ x_{m,y} & y_{m,y} & z_{m,y} \\ x_{m,z} & y_{m,z} & z_{m,z} \end{bmatrix} \tag{4.7}$$

where $x_{m,x}$, $y_{m,x}$, and $z_{m,x}$ are the mean accelerometer data for an x movement; $x_{m,y}$, $y_{m,y}$, and zm,y are the mean accelerometer data for a y movement; and $x_{m,z}$, $y_{m,z}$, and $z_{m,z}$ are the mean accelerometer data for a z movement, respectively. This matrix is acquired from the training set movement data, and applied onto the test set through matrix multiplication of the inverse of the normalized matrix by the new movement data (Eqn. 4.8),

$$A = S^{-1}M \tag{4.8}$$

where S^{-1} is the inverse of the normalized matrix S, and M is the new movement data. To further analyze the user's movements, the acceleration data is transformed into distances through integration (Eqn. 4.9),

$$distance = \Delta t^2 \int_b^e \int_b^e acceleration \; dt^2 \tag{4.9}$$

where Δt is the period between samples, b is the beginning sample of the movement, and e is the ending sample. Data acquired from the three gyroscope axes cannot be similarly decomposed, as they are one integration away from being constants, and therefore they are left unmanipulated.

The distances the wand travels during each movement is analyzed by plotting them in 3-D space, and in this way the data can be visualized before and after it has been shifted by the axis projection. Finally, the number of movements each user made within 30 degrees of each axis is determined by using cosine similarities between the distance the movement traveled along its path and its respective axis. An example of this is shown (Eqn. 4.10),

$$\cos \emptyset = \frac{x \cdot x_0}{\|x\|\|x_0\|} \qquad (4.10)$$

where x0 is the x-axis. Using Eqns. 4.10-4.13, it is possible to visualize the data to better understand how to improve the results of the algorithm, as well as to determine if shifting the data to the respective axis that the user is moving on will improve the accuracy for the translational movements with this algorithm.

Classification from 1-D Signals Converted to 3-D Images
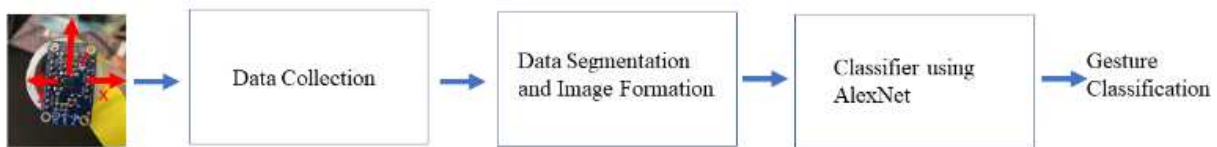
Figure 4.4: Proposed framework for gesture recognition using AlexNet.

The process for converting 1-D signals generated from IMU-based data is as follows. The data collected from the previously made atomic gestures were computationally manipulated to generate a set of complex movements comprising of the "atomic" movements completed previously (Figure 4.5). These 20 different complex movements are composed of sets of two, three, or four movements.
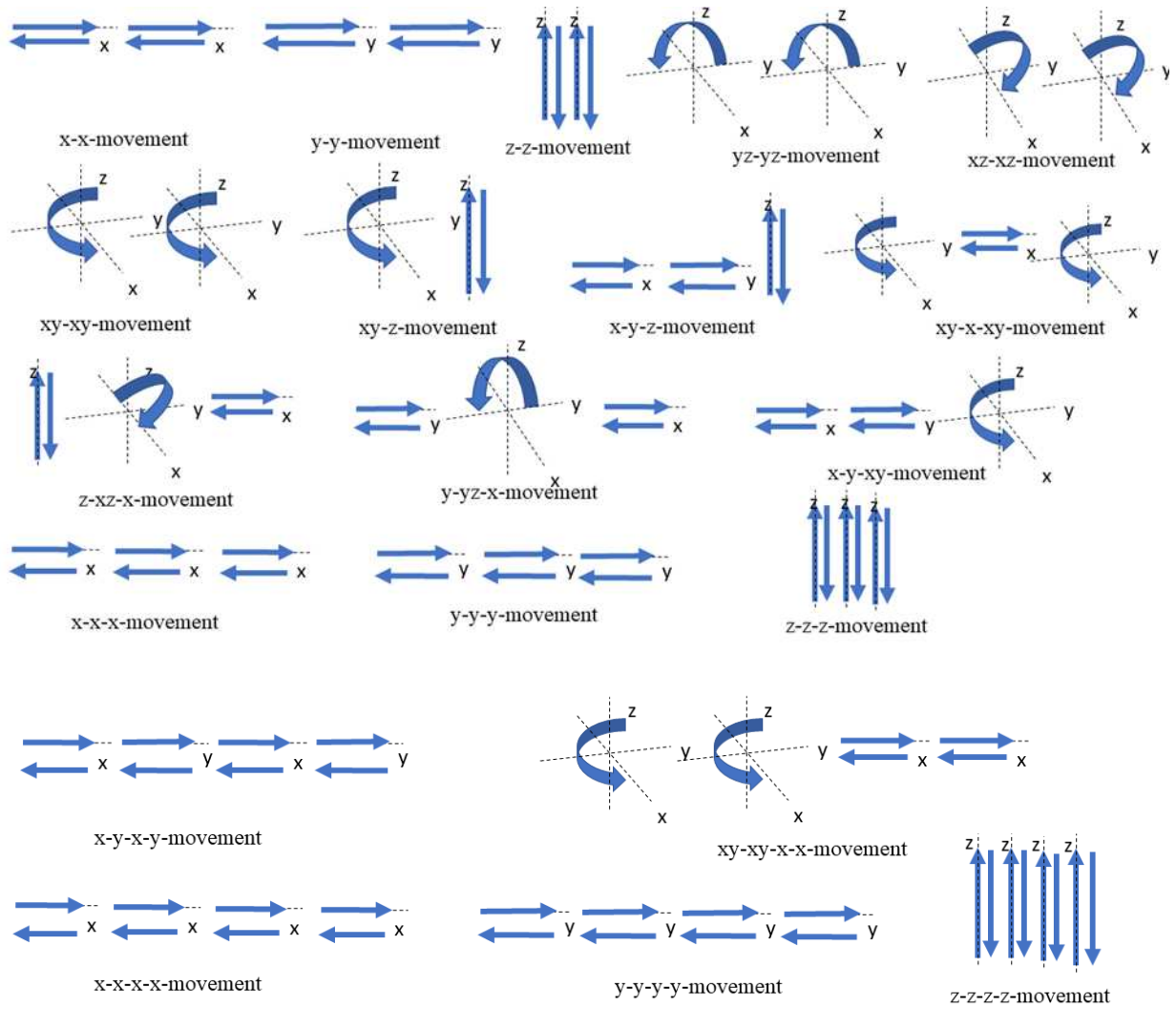
Figure 4.5: Framework of complex gestures, which are linear combinations of atomic gestures (Figure 4.2).

Post-segmented data was utilized for form 3-D images in the three following methods.

1. Arrays of data were formed with each axis in their own respective regions (Eqn 4.11),

$$
I = \begin{bmatrix}
x_1 & \cdots & x_{1,n} & y_1 & \cdots & y_{1,n} & z_1 & \cdots & z_{1,n} & \cdots \\
& \vdots & & & \vdots & & & \vdots & & \cdots \\
x_{m,1} & \cdots & x_{m,n} & y_{m,1} & \cdots & y_{m,n} & z_{m,1} & \cdots & z_{n,m} & \cdots \\
& \vdots & & & \vdots & & & \vdots & & \ddots
\end{bmatrix}
\tag{4.11}
$$

where m represents the number of rows (or samples) from one movement, and n represents the number of columns in which the data from that movement is expected to be above a minimum noise threshold below which no movement is assumed. This was extended to include the three axis of gyroscope data (roll, pitch, yaw). The data was then repeated until the dimensions of the array were 256x256 (Eqn 4.12).

$$I_{Full} = \begin{bmatrix} I & \cdots & I \\ \vdots & \ddots & \vdots \\ I & \cdots & I \end{bmatrix} \tag{4.12}$$

MATLAB's grayscale function is then used to convert the data into grayscale, and the repmat function is used to create a 3-D stack of the data to form an image of minimum dimension 227x227x3, which is required for implementation with AlexNet. An example of this image type is shown in Figure 4.6(a).

2. A similar process to 1. above is carried out, but the data generated from the 3-axis gyroscope is excluded to examine the effects of gyroscope data for this method of recognition (Eqn. 4.13).

$$I = \begin{bmatrix} x_1 & \cdots & x_{1,n} & y_1 & \cdots & y_{1,n} & z_1 & \cdots & z_{1,n} \\ & \vdots & & & \vdots & & & \vdots & \\ x_{m,1} & \cdots & x_{m,n} & y_{m,1} & \cdots & y_{m,n} & z_{m,1} & \cdots & z_{n,m} \end{bmatrix} \tag{4.13}$$

The data was again repeated until the dimensions of the array were again 227x227 (Eqn. 2), and the grayscale and repmat functions were utilized to form an image of dimension 227x227x3. An example of this image type is shown in Fig. 4.6(b).
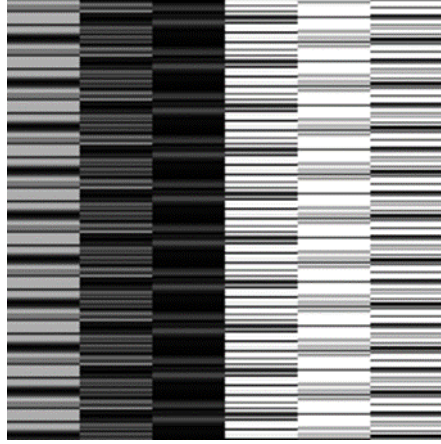
(a) x-x movement (gyroscope data included)   (b) x-x movement (no gyroscope data)
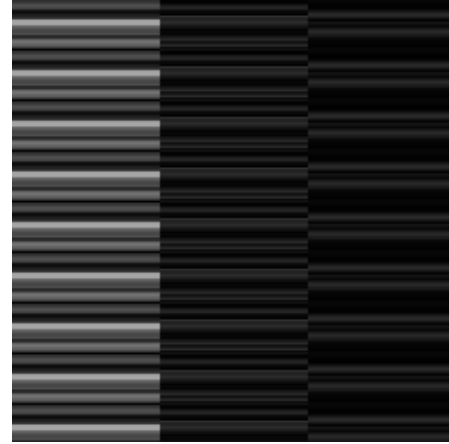
Figure 4.6: Example of gray-scaled images: (a) Type 1 and (b) Type 2.

1.   Each of the three accelerometer axes are converted from acceleration data to distance (Eqn. 4.14),

$$d = \Delta t^2 \int_{t_1}^{t_2} \int_{t_1}^{t_2} a \, dt^2 \tag{4.14}$$

where d is distance, a is acceleration, and t1 and t2 are the beginning and ending of each completed atomic gesture within a complex gesture, respectively. The three axes of data (x, y, z) are then assigned a color; red is assigned to x, green is assigned to y, and blue is assigned to z. The axes are normalized between 0 and 1 (Eqn. 4.15),

$$x_{new} = \frac{x - x_{min}}{x_{max} - x_{min}} \tag{4.15}$$

and the amount of color applied to each axis will depend on the amount of data, e.g. the distance traveled, in that axis. Examples of these "RGB images" are shown in Figure 4.7 (a) and (b).

Figure 4.7: Example of RGB images (Type 3).

With each image type, a set of training and testing data was randomly formed (50% training, 50% testing), and the training images were used to train the AlexNet image classifier (500 images for each hand) with an initial learning rate of $1x\ 10^{-4}$ seconds, a min-batch size of 10, and the max epochs at 6.

Gesture Recognition for Simultaneous Sensing and User Validation

Here, an expanded dataset was collected in a similar method described previously. Ten participants (seven males and three females) completed a set of each gesture 12 times for a total of 120 movements with their dominant hand (as previously mentioned, all participants are right-handed). The gestures were constructed from the previously described sets of "atomic" movements (Figure 4.2).

The system of networks (Figure 4.8) includes a comparison between the following two options:

Option A: A network trained by all potential gestures and all participants (global gesture set) is used to initially classify a gesture from the training set. Once that gesture is recognized, a network trained to biometrically identify a person (depicted as A.-J. in Figure 4.13) using the same image is employed, and the specific participant who made the gesture is then identified. A network trained off of only the gestures made by that specific participant (individual gesture set), which is therefore dependent on the recognized user, is then utilized to classify the gesture again. At this point, the initial classification of the gesture using the global gesture set is compared to the gesture classification of the final output, based only on the individual gesture set. The error rate here is the minimum functional error rate in the system, since it guarantees a system classification error has occurred (one of the gestures identified must be a mistake). It hides reverse errors, where the initial error (gesture ID'd against the global gesture set) is the inverse of the final error (gesture ID'd from the individual gesture set), and so the actual error rate is at least as high as the gesture comparison error.

Option B: Like Option A, the initial classification of the gesture is made using a network trained on all training data from all participants (global gesture set). In this case, the next classification is based off networks trained on clusters of the individuals, which are formed using the confusion matrix generated during training and validation of the network. Here, the confusion matrix was first made symmetrical by adding the elements with inverse indices to each other; for example, element 1-2 was added to 2-1. The matrix was then normalized based off the sum of all individual cells, and distances were forged using misclassification. It is analogous to the sum of (1 – accuracy) and is also known as the error rate (ER). Error below a certain threshold (here, 0.1) is then used to cluster classes in such a way that the ratio of mean squared error between cluster means to the mean squared error from the mean within each cluster is maximized [47]. Alternative clustering approaches could certainly have been used. As will be shown shortly, the relative value of the clustering approach can be directly tested by the systemic errors computed for Option A and Option B when comparing them for different clustering approaches.
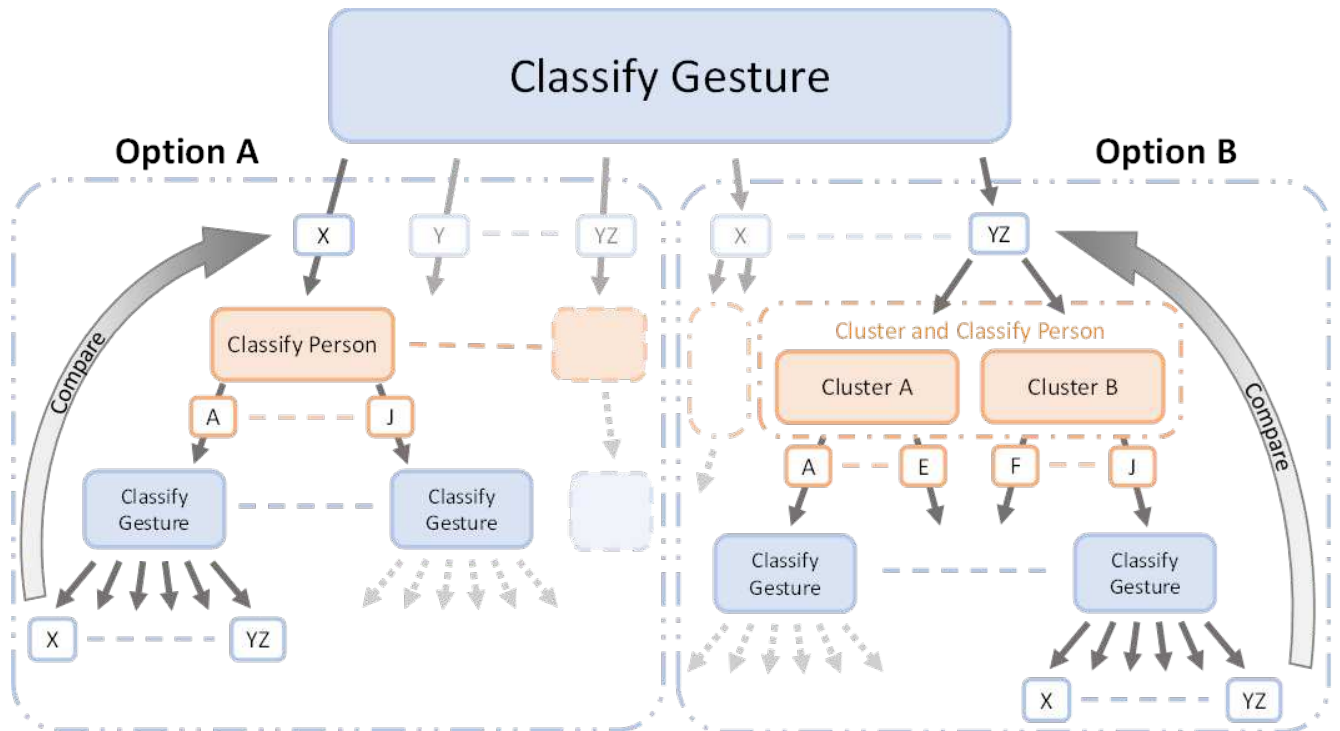
Figure 4.8: Depiction of the proposed system flow, which includes Option A and Option B.

Using this method, two independent clusters of participants were formed for each of the six individual gestures (Cluster A and Cluster B in Figure 4.8), and networks trained on these clusters were then utilized to biometrically identify the participant from which the gesture was generated from. A network trained from the gestures made by that participant individually is then utilized to classify the gesture again (individual gesture set), and finally, the initial classification of the gesture (based on the global gesture set) made by the user is compared to the gesture classification of the final output (individual gesture set). For comparison, matching percentage is also to be examined with all ten possible clusters of the five participants when grouped in sets of five and five.

A ranking difference value (RDV) computed from the difference between the ranking of the final output gestures was generated to compare between the two options. An elementary example of this is as follows:

x	y	z	yz	xz	xy
1	2	3	4	5	6
2	1	3	4	5	6
x	y	z	yz	xz	xy

In this case, the RDV is equal to 1, as the top ranking of the output of the six gestures (x in the first output ranking) was different by one position in the second output ranking (where "x" is ranked 2 instead of 1).

To test for the level of repeatability of the gestures made by the participants, a separate experiment was conducted in which the models trained from gestures made by individual people (i.e., user-dependent models) were tested with the full set of data (i.e., both the first and second half of the data was used to train and test the model in individual tests). Here, the results are indicative of how consistently, or inconsistently, the users made the individual gestures, which can be seen in the similarity/difference of the model performance when the first half of the gestures were used to train the model compared to when the second half of the gestures were used.

4.2 Results

Classification through an Objective Function with SVM

The resulting accuracies of the proposed algorithm are shown in Table 4.1.

Table 4.1: Mean accuracy for translational movements compared to one another, rotational movements compared to one another, and all six movements compared to one another with the objective function algorithm.

	LEFT HAND	RIGHT HAND
TRANSLATIONAL	78%	97%
ROTATIONAL	76%	98%
ALL 6	59%	61%

From the results of the algorithm on translational and rotational movements, it was clear that a binary classifier to discriminate these two "superclasses" computationally before a comparison algorithm is used to distinguish among the remaining two sets of three classes will benefit the results. This is a variant of the Predictive Selection meta-algorithmic pattern [47]. For its previously reported performance as a strong binary classifier [129], [130], as well as its low computational costs and storage requirements [131], a support vector machine (SVM) was used as a method of predictive selection.

Table 4.2: Mean accuracy for all six movements compared to one another using just objective function results, and mean accuracy for the objective function results after binarization into translational and rotational movements.

	LEFT HAND	RIGHT HAND
OBJECTIVE	59%	62%
OBJECTIVE + SVM	76%	92%

Movements made by all five subjects were compiled into a confusion matrix (Figure 4.9) to visualize where sources of error were present.

Figure 4.9: Confusion matrix of the objective function algorithm combined with SVM for right-handed (dominant hand) movements.

The majority of confusion (that is, the errors) was present between movements with shared axes (e.g., yz-movements were often confused with y movements, xz-movements, and xy-movements). The range of accuracies within the group of participants is shown in Table 4.3.

Table 4.3: Mean accuracy and range of accuracies from the proposed algorithm.

	Mean Accuracy	**Range**
Left Hand	77.60%	38.7%-100%
Right Hand	92.00%	85.33% - 98.67%

Precision and recall are calculated as:

$$Precision = \frac{TP}{TP + FP} \tag{4.16}$$

$$Recall = \frac{TP}{TP + FN} \tag{4.17}$$

$$F1\ Score = \frac{2 * Recall * Precision}{Recall + Precision}$$

(4.18)

The precision and recall were calculated for each movement (Appendix A.1) to show how well each movement was recognized individually.

Improvement of Classification through Axis Shift

The results of the objective function algorithm (Eqns. 4.1-4.6) combined with an SVM are shown in Table 4.3. For further visualization of the effects of the axis shift (Eqns. 4.7 and 4.8), accelerometer data was converted to distance (Eqn. 4.9) and plotted before and after shifting occurred. For further analysis of the translational movements, the mean number of movements made within 30 degrees of each axis (Eqn. 4.10) for both left- and right-handed gestures is shown (Table 4.4). A line-of-best-fit was created using a built-in search function in MATLAB known as fminsearch, which optimizes the line to find minimum error between points (Figure 4.10).
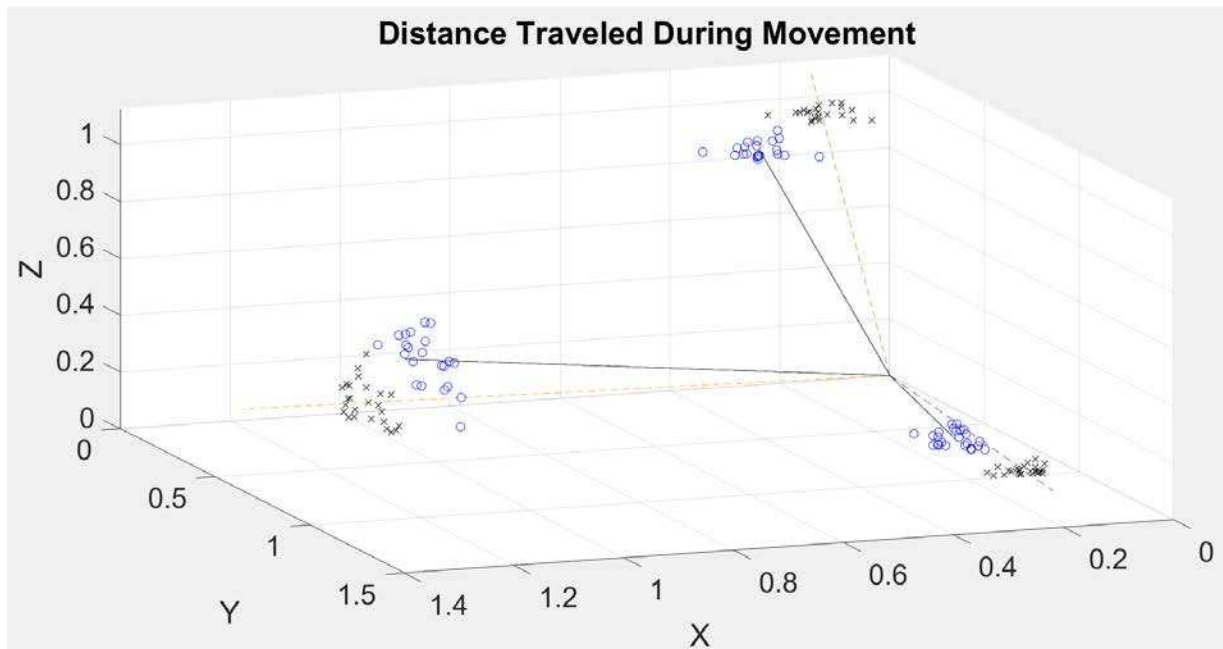
Figure 4.10: An example of mapping of data before and after the axis projection was applied. The circles represent the original mapping, and the x's represent the mapping of the shifted data. The line of best fit for each data set is included.

The mean distance traveled by the movement in each axis before and after the data manipulation (Table 4.4) further quantifies the effect of the data shift.

Table 4.4: Mean number of movements from the "test" set made within 30 degrees of each axis for both left- and right-handed gestures (out of 25).

	Mean:	
	Left	Right
x	17.4	21.8
y	19.2	23.4
z	14.6	16

The result of shifting the axis on the accuracy of the translational movements is shown in Table 4.5.

Table 4.5: Effects of the axis shift on the translational data; the boldfaced data is the axis in which the movement was supposed to be made.

		Pre-Shift			Post-Shift		
		X	Y	Z	X	Y	Z
User 1	X-movement	**0.9342**	0.2806	0.1935	**0.992**	0.0815	0.0615
	Y-movement	0.4414	**0.8928**	0.126	0.2681	**0.9498**	0.0172
	Z-movement	0.4191	0.3338	**0.8348**	0.2592	0.2171	**0.9306**
User 2	X-movement	**0.8577**	0.4523	0.1796	**0.9526**	0.2442	0.036
	Y-movement	0.2826	**0.9381**	0.1012	0.1135	**0.9797**	0.014
	Z-movement	0.3357	0.434	**0.8328**	0.1578	0.3132	**0.9361**
User 3	X-movement	**0.8922**	0.3484	0.2374	**0.9672**	0.1938	0.075
	Y-movement	0.3421	**0.9252**	0.1313	0.2259	**0.9686**	0.0121
	Z-movement	0.3416	0.2721	**0.885**	0.1989	0.165	**0.9522**
User 4*	X-movement	**0.4822**	0.2485	0.8387	**0.9917**	0.0392	0.1152
	Y-movement	0.539	**0.6499**	0.5342	0.5831	**0.6488**	0.4836
	Z-movement	0.6534	0.341	**0.6703**	0.8545	0.1354	**0.4854**
User 5	X-movement	**0.9233**	0.2511	0.2677	**0.9877**	0.1031	0.0714
	Y-movement	0.2142	**0.9668**	0.133	0.0983	**0.9945**	0.0161
	Z-movement	0.3319	0.2446	**0.9084**	0.1736	0.1104	**0.9762**

*User 4 did not make any movements within 30 degrees of the axis, so results may be skewed.

An Analysis of Variance (ANOVA) was used to analyze the ranges of accuracies before and after the axis shift was applied to determine if the change in accuracy between the two methods is significant for both dominant and non-dominant handed movements. The resulting confusion matrices from the axis shift (Eqn. 4.7 and 4.8) are shown in Figure 4.11.

(a)   (b)
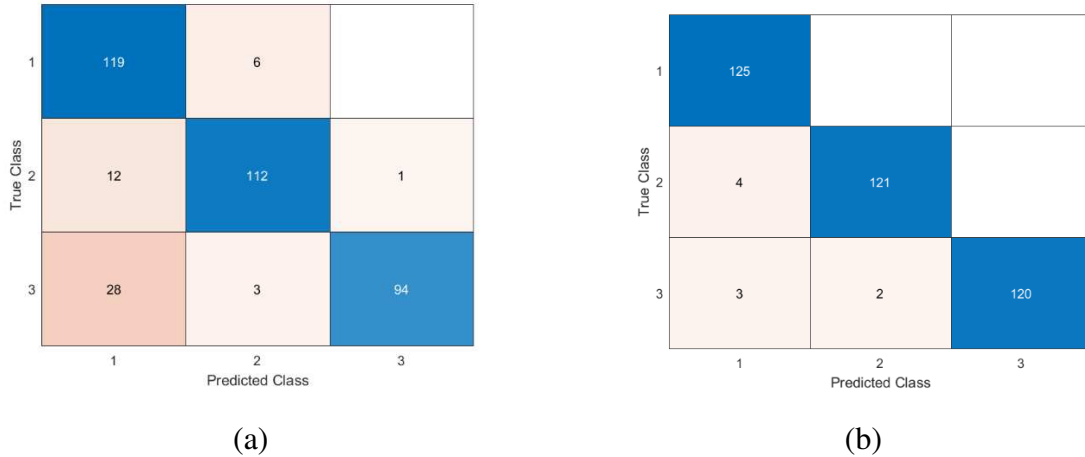
Figure 4.11: Confusion matrix for (a) left-handed translational movements and (b) right-handed translational movements after the axis-shifting algorithm.

The resulting increase in accuracy range is shown in Table 4.6, and the mean percentage increase of each axis is shown in Table 4.7.

Table 4.6: Accuracy ranges of the translational movements before and after applying the axis shift to those movements.

Accuracy Ranges		
	Pre-shift	Post-shift
Left Hand	41.3%-100%	50.667%-100%
Right Hand	89.33%-100%	93.33%-100%

Table 4.7: Mean increase of data towards correct axis for x-, y-, and z-movements, respectively (Note: data may be skewed by User 4, who did not make any movements within 30 degrees of any respective axis).

Mean Increase of Data Towards Correct Axis (%)		
X	Y	Z
27.52%	3.64%	2.27%

Classification from 1-D Signals Converted to 3-D Images

As before, precision, recall, and F1-score were used as metrics to evaluate the effectiveness of this classification method (Eqns. 4.16-4.18, respectively). The precision of each complex gesture type when formatted in the Type 1 image formation is shown in detail in Table 4.8.

Table 4.8: Precision of each individual complex movement type as a result of the Type 1. image formation (Fig. 4.6(a)) with respect to each hand the gesture was made with.

	x-x	x-x-x	x-x-x-x	x-y-x-y	x-y-z	x-y-xy	y-y
Left Hand	0.33	0.49	0.38	0.67	0.91	0.81	0.38
Right Hand	0.37	0.35	0.39	0.8	0.91	0.88	0.41
	y-y-y	y-y-y-y	y-yz-x	z-z	z-z-z	z-z-z-z	z-xz-x
Left Hand	0.42	0.43	0.91	0.4	0.36	0.46	0.93
Right Hand	0.41	0.44	0.95	0.38	0.4	0.43	0.92

	xy-z	xy-x-xy	xy-xy	xy-xy-x-x	yz-yz	xz-xz
Left Hand	0.94	0.79	0.76	0.86	0.82	0.84
Right Hand	0.92	0.92	0.82	0.85	0.94	0.93

Similarly, the precision of each complex gesture type when formatted in the previously described Type 2 image is shown in detail in Table 4.9, and the same for the Type 3 image in Table 4.10.

Table 4.9: Precision of each individual complex movement type as a result of the Type 2. image formation (Fig. 4.6 (b)) with respect to each hand the gesture was made with.

	x-x	x-x-x	x-x-x-x	x-y-x-y	x-y-z	x-y-xy	y-y
Left Hand	0.31	0.31	0.3	0.8	0.96	0.83	0.31
Right Hand	0.31	0.33	0.32	0.86	0.96	0.93	0.33
	y-y-y	y-y-y-y	y-yz-x	z-z	z-z-z	z-z-z-z	z-xz-x
Left Hand	0.31	0.32	0.96	0.32	0.32	0.32	0.89
Right Hand	0.33	0.33	0.95	0.33	0.33	0.33	0.94

	yz-yz	xz-xz	xy-z	xy-x-xy	xy-xy	xy-xy-x-x
Left Hand	0.9	0.84	0.93	0.81	0.74	0.86
Right Hand	0.93	0.93	0.92	0.86	0.85	0.89

Table 4.10: Precision of each individual complex movement type as a result of the Type 3. image formation (RGB image) with respect to each hand the gesture was made with.

	x-x	x-x-x	x-x-x-x	x-y-x-y	x-y-z	x-y-xy	y-y
Left Hand	0.85	0.89	0.9	0.97	0.9	1	0.87
Right Hand	0.94	0.96	0.944	1	0.98	0.99	0.93
	y-y-y	y-y-y-y	y-yz-x	z-z	z-z-z	z-z-z-z	z-xz-x
Left Hand	0.78	0.89	1	0.9	0.88	0.89	0.93
Right Hand	0.86	0.94	1	0.96	0.89	0.98	0.99

	yz-yz	xz-xz	xy-z	xy-x-xy	xy-xy	xy-xy-x-x
Left Hand	0.95	0.79	0.9	0.97	0.95	0.99
Right Hand	0.99	0.97	0.94	0.99	0.99	0.99

The precision, recall, and F1-score for both the left hands and right hands are shown in Figure 4.12 and Figure 4.13, respectively.
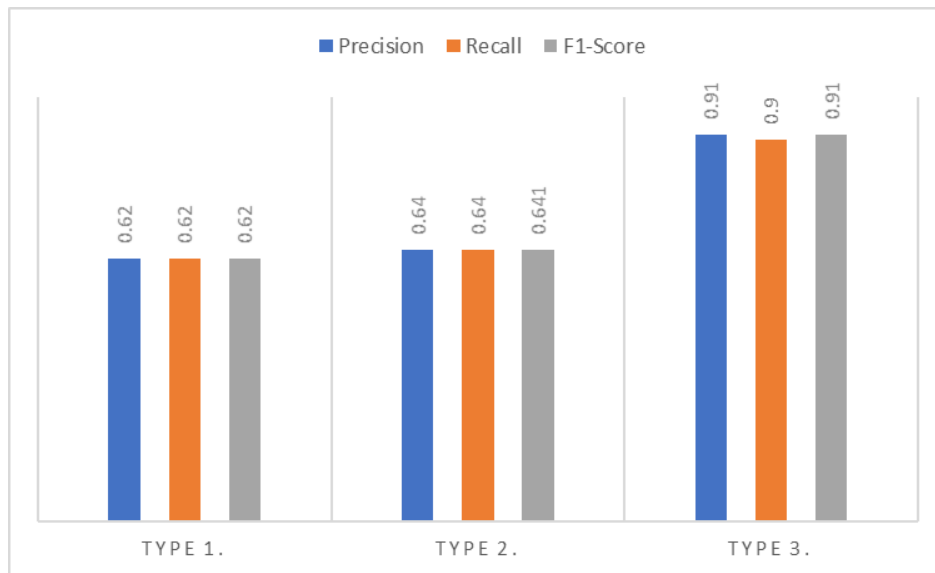
Figure 4.12: Precision, recall, and F1-score for the three types of images: left hand data.
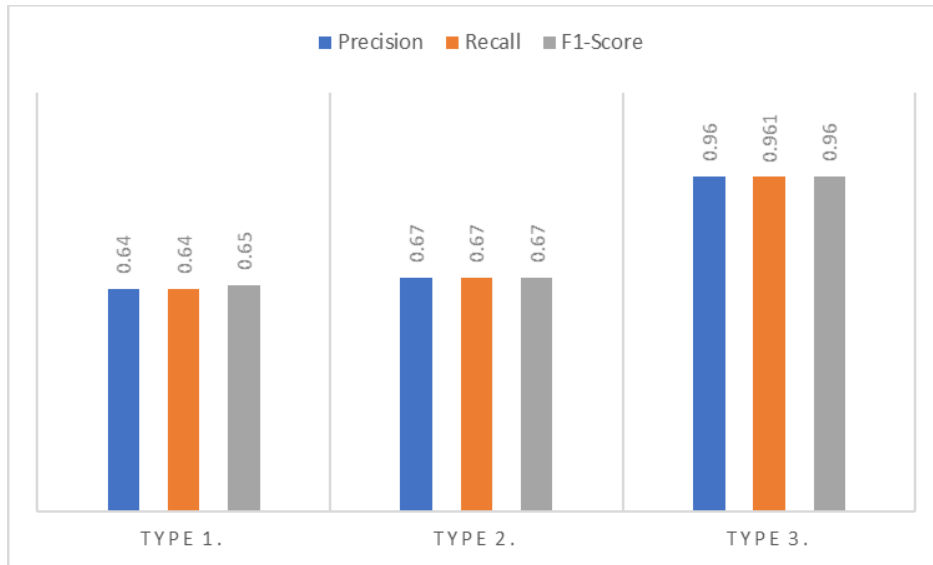
Figure 4.13: Precision, recall, and F1-score for the three types of images: right hand data.

Gesture Recognition for Simultaneous Sensing and User Validation

The percent match between the initial and final gesture classification of Option B (Fig. 4.8) for all 126 possible cluster sets when using all possible groupings of five and five is shown in Fig. 4.14.
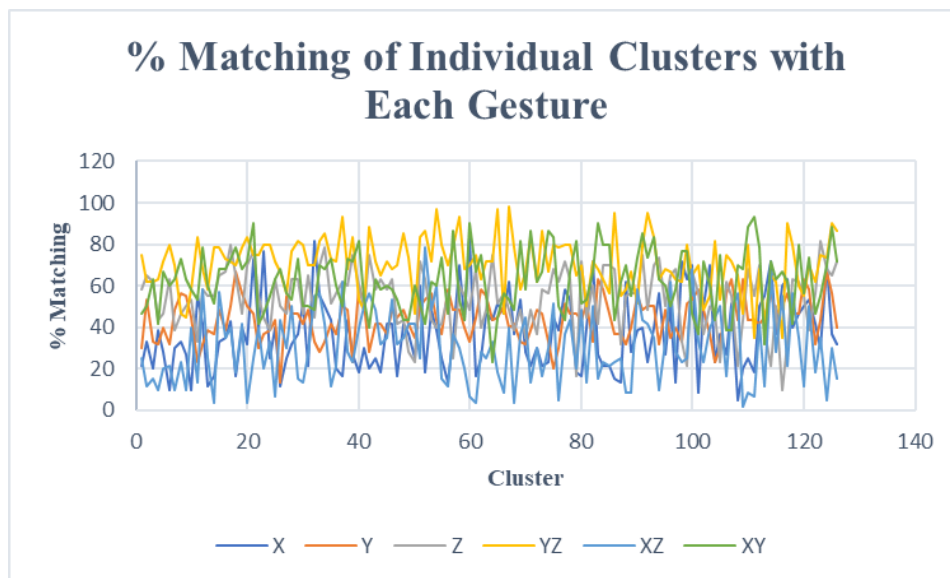
Figure 4.14: Percent matching (% matching) when different combinations of groups of 5 clusters are created (126 different combinations possible).

The percent match between the initial and final classification when comparing the clusters of participants generated using the confusion matrix method is provided in Table 4.11. The mean RDV comparing the rankings of the top-ranking gesture from the global gesture set with the ranking of this gesture in the individual gesture set was also calculated for each of the gestures in the training set. The RDV of Option A was calculated to be 0.15, while Option B was 0.13 (when using the confusion matrix method of clustering).

Table 4.11: Percent matching between the initial and final classification (Figure 4.8).

Option	% Matching
Option A	88.9
Option B	90.3

4.3 Discussions

Classification through an Objective Function with SVM

When comparing the six different movements together by the different users, the meta-algorithmic method reduced error percentage from 38.5% to 1.9%, a 36.6% reduction. However, this is only true when the user is using their dominant hand for gestures; error was only reduced by 17% when users made movements with their non-dominant hand, and 24% error is still measured with this meta-algorithmic approach.

Precision and recall, which are important measures for determining how often this classifier would activate the wrong sensing option in this "magic wand" appliance, were over 85% for most classifications (28 out of 30 times for precision, and 27 out of 30 times for recall). This statistic shows that, as a proof of concept, this meta-algorithmic approach could be suitable for a high-quality gesture recognition technique with potential to reach 100% accuracy when correctly manipulated, and particularly for the dominant hand.

Furthermore, during static calibration (i.e., the time between the start of data acquisition and the movement being made), the 9-axis IMU measures the opposing force of gravity in the

downward-pointing direction. This biometric allows for a further "super-superclass" to be made that will allow for activation of multiple sensors with high accuracy, precision, and recall.

Improvement of Classification through Axis Shift

The optimization of the objective function algorithm (Eqns. 4.1-4.6) showed that gyroscope data had no positive effect on the classifications made during this study, which is likely due to the lack of twist in any direction during the movements made during this small proof-of-concept study. The mean number of movements made outside of 30 degrees of the axis during translational movements show that (i) users in this study were able to make movements more repeatably and accurately with their dominant hand, which is agreeable with previous work [132] and (ii) that the movement in the z-direction was the most difficult to repeat accurately (Table 4.4). The change in accuracy from before and after the axis shift for non-dominant hand movements resulted in significant changes in accuracy for the translational movements ($F(1,8) = 61.47$, $p <$ 0.001). This shows promise for improving the objective function algorithm to compete with current processes mentioned previously.

The post-movement tracking of data (Figure 4.10) gives a visualization of the movement for the user to improve their motion, as visualization of movement has been shown to have a positive effect on repeatability and recognition of movements [133]. Data manipulation (Table 4.5) show that the axis shift had the desired effect of shifting the data towards the correct axis for the proposed objective function algorithm. The mean percentage increase of each axis is likely the cause in the significant improvement in the accuracy of the algorithm. Further separation of the data in this way can potentially improve other algorithms that utilize spacing between clusters of datapoints, such as k-Nearest-Neighbors (kNN's). The effect of the axis shift also allows for better performance of the objective function algorithm described here, as mathematical separation is achieved with the shift of the data.

The movements made in this section are building blocks that will allow for a set of personalized, user-dependent gestures for the activation of our "magic wand". The accuracies achieved by the algorithm are well above "guessing", even when the user does not make movements correctly.

Classification from 1-D Signals Converted to 3-D Images

The three methods of 3-D image construction from 1-D signals created during user-made gestures had varied success in classification with AlexNet. It is clear that the first two image types (Type 1 and 2) were unsuccessful at recognizing repeated gestures (e.g., x-x, y-y, etc.), but were more successful at recognizing 8 out of 20 complex gestures with over 80% precision. However, this was not true for the third type of image (Type 3); all 20 complex gestures were recognized with over 85% precision when the participants used their right hand, and 18 of those gestures were above 93% precision. There was no significant difference between the precision, recall, and F1-score of the Type 1 and 2 image types. This shows that including time series data from the gyroscope portion of the IMU has no significant effect for image recognition when the images are formed with this method. The overall system achieved 96% precision, recall and F1-score when the 1-D time series signals were converted to RGB images and classified using AlexNet which shows that this method of gesture recognition exhibits potential. Comparatively, previous studies examining classification of 1-D signals commonly use accuracy as a measure of the effectiveness of a system. Methods such as Kundu et al. [18] achieved as high as 94% accuracy through a shape-based feature extraction and Dendrogram Support Vector Machine (DSVM) classifier.

Improvement of this method may be possible if the parameters of the AlexNet neural network were fit to this model, similarly to [15], as this is a small image training dataset. It can also be noted that the structure of the complex gesture framework using atomic gestures from Figure 4.2 means that there is vast potential for personalized, user-selected gestures.

Gesture Recognition for Simultaneous Sensing and User Validation

In both instances, it is clear there is an increase in system accuracy when adopting Option B. The optimal cluster results in obvious improvement in accuracy (90.3%). System error (9.7% for the best clustering case for Option B) is still appreciable for both options, and this error represents of the minimal error of the system. However, the more robust system afforded by Option B has the potential to be applied to other similar systems in which intermediate outputs can be interpreted and vetted for system improvement.

The system presented demonstrates measurably increased effectiveness when partitioning of subjects was incorporated as an intermediate step in the overall gesture identification (specifically, there was an 18% decrease in the mean RDV as a result of the partitioning). This type of system design is fitted to the design feature of maintaining a biometric VPN until it is shown that the user has changed, since a change in gesture classification hides the details of the inner clustering from the decision, allowing challenge-based biometrics to be readily accommodated without requiring security through obscurity. In the future, such a system would need further testing that involves both i) a higher number of participants in a full study and ii) a higher number of templates to create training data for, especially when using an image recognition technique such as AlexNet. The system should also be tested for cost, which is an important metric when evaluating biometric systems, as well as an assortment of error metrics, such as false acceptance rate, false rejection rate, and equal error rate. This proposed system is meant for applications to any number of biometric techniques, and thus can be evaluated on these techniques as seen fit. Perhaps most importantly, this system provides a closed-loop verification of the biometric classification that can be used to compare the relative value of any number of different clustering algorithms in a biometric classification system. This systems engineering-based design thus obviates the need for expensive and time-consuming ground truthing of the clustering or gesture data, allowing the possibility for automated optimization of the overall system design.

Separately, the viability of using gestures as a means of biometric recognition was tested through comparing using the first and last five gestures as the training set for the AlexNet model. When the models were trained using the first five gestures, the mean accuracy was 88.8 ± 9.7 %, while the mean accuracy was 93.9 ± 5.1% when the models were trained using the second five gestures. Although these results are not statistically significantly different ($p = 0.16$, $\alpha < 0.05$), the difference still implies that there is some level of "learning" that the users experience when using the device with respect to how to make the gestures, and while the level of repeatability is not significant initially, these results will likely become more similar as users become more comfortable with the device. Also, as alluded to in Section 4.2, the hand that the user makes the gestures with can influence the results, as many of the movements can be inconsistently made with

the non-dominant hand of the user. The repeatability in this sense is something that will need further examination in future works, as it can greatly affect the results of gestures as a biometric tool.

Chapter 5
Gait Analysis and Lameness Prediction of Equine Subjects

As mentioned previously, biometric principles and techniques have yet to be implemented with non-human living beings in any application. However, as discussed in Chapter 2, there is potential to apply such principles to the different states of an animal, namely an equine animal, to assess its well-being. Gait analysis is an application in which biometric principles have the potential to be utilized to examine and potentially recognize the various "states" of gait.

Lameness is a term used to describe a horse's visual and/or measurable change in gait from the normal, usually in response to pain somewhere in a limb, but also possibly as a result of a mechanical restriction on movement. Other metrics of lameness include, but are not limited to, range of motion (ROM), or the relationship between joint contracture and soft tissue adaptive shortening with a form of lameness; synovial fluid effusion (EFF), or inflammation of the synovial membrane that lines the joints and causes an increase in severity of fluid accumulation within the joint; and flexion (FLEX), or a measurement of pain associated with a joint or soft-tissue structure during or following the flexing of the limb. This section herein describes a proof-of concept study in which a model for different metrics of lameness in an equine subject is created through biometric principles using feature extraction of signals generated from four inertial measurement unit (IMU) sensors placed strategically on the left and right fetlock, as well as just above the left and right knee (Figure 5.1).

Figure 5.1: Placement of four MoveSense IMU sensors on the left and right fetlock, as well as just above the left and right knee of the horse.

Due to the ongoing COVID-19 pandemic, the number of horses was limited to a single horse, and therefore the data was very limited in this chapter. However, the methods here are a "steppingstone" that can be further tested with a larger sample size in the future.

5.1 Methods

Quantification of Variability of Within-Day and Between-Day Exercise

Before attempting to find effective features that will be able to accurately quantify lameness, it is first prudent to measure and evaluate any underlying variability that may exist in an equine animal that is sound. These measurements characterize the baseline noise and entropy expectations. To quantify this variability, or lack thereof, of exercise within a single day, as well as between days, the following experiment and analysis took place.

A single horse with sensor attachment (shown in Figure 5.1) was exercised five to ten times per data collection episode while trotting at a constant speed of 12 km/hr. This speed was estimated and maintained by a trainer, who ran alongside the horse as it completed each individual trial. Timestamps indicating the horse reaching that constant speed, as well as slowing from that constant speed, were recorded and stored. This data was collected three times a day (in morning, mid-day, and evening, denoted as AM, MD, and PM), three days a week over two weeks. The IMU utilized for this study is the MoveSense IMU, and data was collected at a frequency of 208 Hz.

Once collected, the timestamps were utilized to segment the data, which was then standardized (Eqn 5.1)

$$X_i = \frac{x_i - \mu}{\sigma} \tag{5.1}$$

where X is the standardized datapoint, x is the raw datapoint, i is the index of the specific data features, μ is the mean of the data, and σ is the standard deviation. For within-day exercise, variability between similar signals (e.g., the x-axis of the right fetlock sensor to itself) was measured using cross correlation and Pearson Correlation coefficients between the samples taken within a day (Eqn. 5.2),

$$r = \frac{\sum(X_i - \overline{X})(Y_i - \overline{Y})}{\sqrt{\sum\left((X_i - \overline{X})\right)^2 \sum(Y_i - \overline{Y})^2}} \tag{5.2}$$

where r is the correlation coefficient, X_i and Y_i are the two samples being compared (after standardization), and $\overline{X}$ and $\overline{Y}$ are the respective standardized means of the two samples.

Modeling of Differences in Gait Over Time with Surgically Induced Lameness

A single horse with sensor attachment shown in Figure 5.1 was exercised six times per data collection while trotting a known distance of 15.5 meters. Data collection occurred before the surgical production of lameness, ten days post-surgery, and then weekly until the end of the study. The front left limb of the equine animal underwent a surgically induced osteochondral, or bone fragment, in the carpus (or knee) that induces a mild to moderate lameness. Timestamps indicating the beginning and end of that known distance were again recorded and stored.

Once collected, the timestamps were again utilized to segment the data, which was then standardized (Eqn 5.1). Features were extracted using a calculation of the Energy Spectral Density (ESD),

$$Energy\ Spectral\ Density = |FFT^2(x)| \tag{5.3}$$

where FFT is the fast Fourier Transform of each axis of acceleration data. The ESD of each axis of each sensor was then segmented into "windows" of the ESD, which are formed by dividing the signal into groups based off the peaks and valleys of the full ESD, and two different calculations were implemented:

- The percentage of signal in single, double and triple groups (or windows), and

- The ratio of percentages between singles/doubles and singles/triples (Figure 5.2).
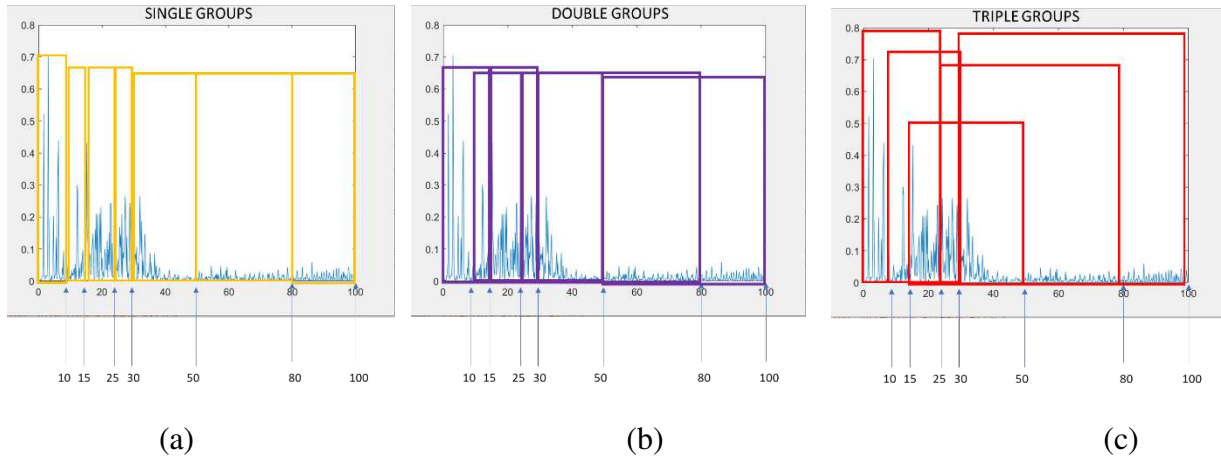
Figure 5.2: Windowing of ESD groups; (a) single, (b) double, and (c) triple groups.

Entropy was also calculated as a feature (Equation 5.4),

$$H(x) = -\sum_{i=1}^{n} P(x_i)\log(P(x_i)) \tag{5.4}$$

where H is the entropy of the signal, x is the axis of acceleration for one of the sensors, and P is the likelihood of occurrence. The number of total features was therefore 516; the list of features is shown in Table 5.1

Table 5.1: Engineered feature set used by the classifiers.

Feature Name	Description	Number of features
Entropy	Entropy of the standardized acceleration	12
Single Percentage	Percentage of ESD in each window of the "single" groups	84
Double Percentage	Percentage of ESD in each window of the "double" groups	72
Triple Percentage	Percentage of ESD in each window of the "triple" groups	60
Single-Double Ratio	Ratio of signal of each "single" group to the "double" groups that encompass them	144
Single-Triple Ratio	Ratio of signal of each "single" group to the "triple" groups that encompass them	144
Total number of features:		516

Each of these features was normalized between trials (within a single day) by a linear regression to remove the inherent variability between trials (i.e., the features were normalized around their respective mean to remove the effect of fatigue as a covariate). Once normalized, individual trials (i.e., each set of measurements taken when the horse trotted down the track) were split into 50% training and 50% testing to develop and train models. In this pilot study, four previously discussed primitive classification methods were examined, including:

- Support Vector Machine (SVM)

- k-Nearest Neighbors (KNN's)

- Decision Tree

- Naïve Bayes.

Classes for model development were generated for each of the four metrics based off of the various scoring between days of the study (Table 5.2). Scoring for each metric is as follows:

- *Synovial Effusion (EFF)*, which is a subjective measure of the severity of fluid accumulation within the joint, is scored 0 for no fluid, 1 for mild, 2 for moderate, and 3 for severe.

- *Lameness,* which is a lameness grade at a trot, is scored 0 for no lameness, 1 for mild asymmetry in limb use, 2 for occasional head nod (which is used as a compensation mechanism, as the horse lifts its head when the lame leg is about to touch the ground), 3 for consistent head nod, 4 for lame at walk, and 5 for the horse being unable to walk on the leg completely.

- *Range of Motion (ROM),* which is a description of loss of the range of motion of a particular limb, is scored 0 for normal ROM, 1 for a mild reduction, 2 for a moderate reduction, and 3 for a severe reduction.

- *Flexion,* which is a lameness grade after flexion of the joint and follows the same scoring as lameness. It is expected, therefore, that a worse than regular lameness score will be assigned, as there is an expected increase in pain after flexion.

Table 5.2: Metrics of lameness over the course of pilot study.

Limb	OA	Day	Date	Synovial Fluid Effusion (EFF)	Lame	Range of Motion (ROM)	Flexion
R	0	0	10/22/2020	0	0	0	0
L	0	0	10/22/2020	0	0	0	0
R	0	10	11/5/2020	1	0	1	0
L	1	10	11/5/2020	2	2	3	3
R	0	14	11/9/2020	1	0	0	1
L	1	14	11/9/2020	2	2	2	3
R	0	21	11/16/2020	1	0	0	0
L	1	21	11/16/2020	2	2	2	4
R	0	28	11/23/2020	1	0	0	0
L	1	28	11/23/2020	2	2	2	4
R	0	35	11/30/2020	1	0	0	0
L	1	35	11/30/2020	2	2	2	3
R	0	42	12/7/2020	1	0	0	0
L	1	42	12/7/2020	2	1	1	2
R	0	49	12/14/2020	0	1	0	0
L	1	49	12/14/2020	1	2	1	1
R	0	56	12/21/2020	0	0	0	0
L	1	56	12/21/2020	1	1	1	1
R	0	63	12/28/2020	0	0	0	0
L	1	63	12/28/2020	1	1	1	1
R	0	70	1/4/2020	0	1	0	0
L	1	70	1/4/2020	2	1	0	1

Separate models were generated for i) individual limbs (e.g., sensor data generated from the left limb was modeled separately from sensor data generated from the right limb), ii) combined limbs (e.g., a model was generated from all data collected from both limbs). Metrics used to show the results of the different algorithms are precision, recall, and F1-score.

5.2 Results

Quantification of Variability of Within-Day and Between-Day Exercise

An example of the resulting cross-correlation and Pearson Correlation coefficients between each of the five trials on the first day (specifically, the x-axis accelerometer data of the left fetlock sensor) is shown in Figure 5.3. The full set of Pearson Correlation coefficients for each

configuration of data collection during the full study is included in Appendix A (Figures A.5 – A.22).
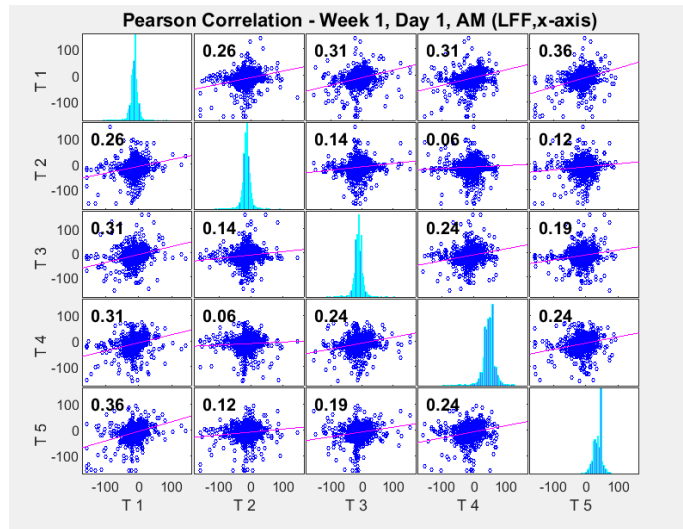
Figure 5.3: Example of Pearson Correlation coefficients on Day 1 of Week 1 between each trial (specifically, the x-axis accelerometer data of the left fetlock sensor). The individual trials are labeled as T1, T2, T3, T4, and T5, respectively.

Between day variability was quantified using a similarity score between days (Eqn 5.5),

$$simscore = \frac{(x_1 \cdot x_2)^2}{(\|x_1{}^2\| * \|x_2{}^2\|)} \tag{5.5},$$

where x_1 and x_2 are the respective arrays of energy of the two days (Eqn. 5.6)

$$Energy = \sum |FFT|^2 \tag{5.6}.$$

Examples of similarity scoring between similar signals (as before, between the acceleration data in the x-axis between the left fetlock sensor from one day to another) is shown in Figure 5.4.

(a)   (b)   (c)
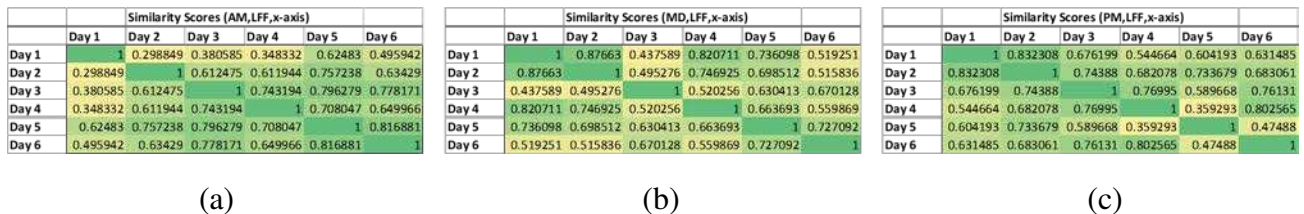
Figure 5.4: Example of similarity scores between similar times of day (specifically, the x-axis accelerometer data of the left fetlock sensor); (a) AM, (b) Mid-Day (MD), and (c) PM.

Changes in similarity scores over time over the different times of day are shown below in Figure 5.5.
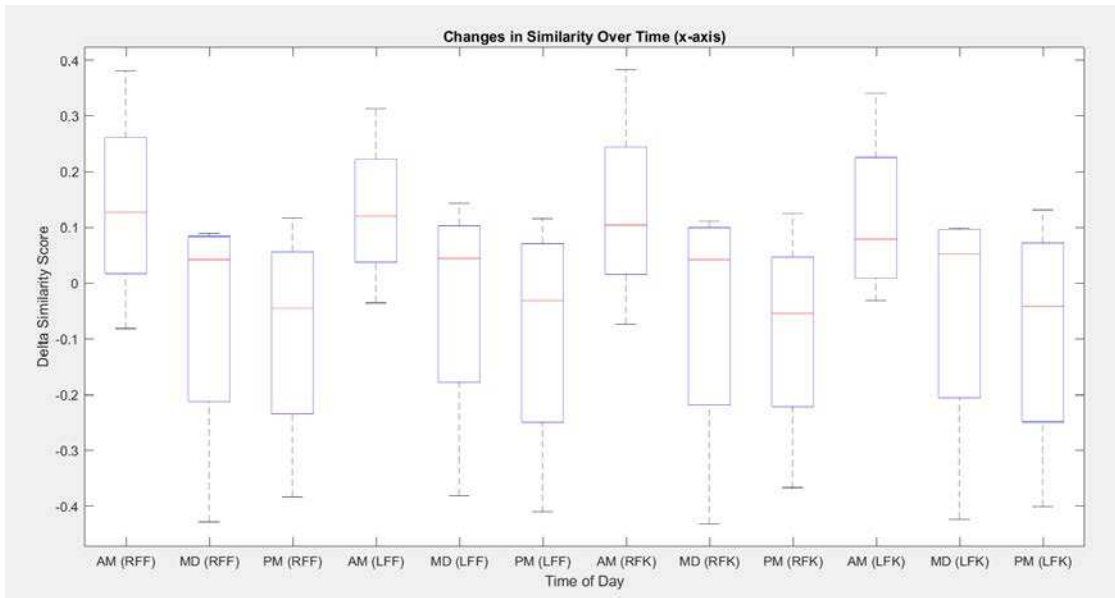
Figure 5.5: Example of changes in similarity scores between times of day over the full study (x-axis of all four sensors).

Modeling of Differences in Gait Over Time with Surgically Induced Lameness

Full results (Appendix A, Figures A.25-A.31), as well as results from the best performing algorithm (Figure 5.6, Figure 5.7) are presented.
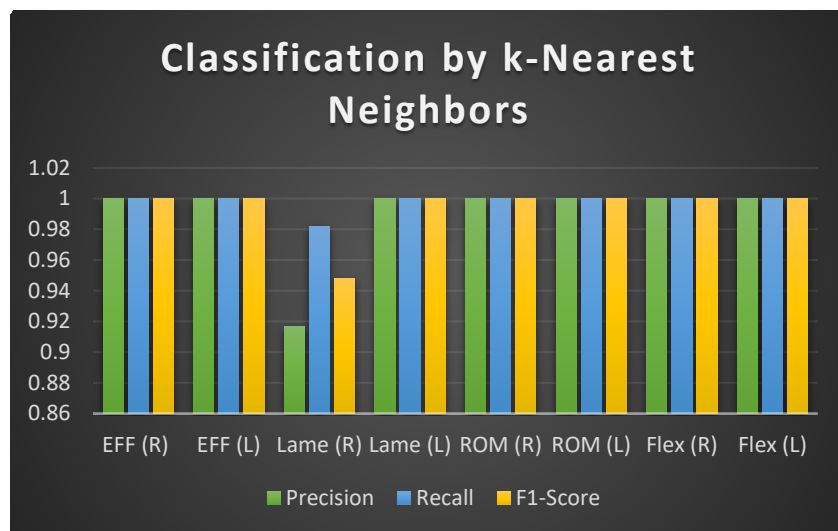
Figure 5.6: Classification results from models developed using individual limbs for each of the four metrics of lameness using kNN.
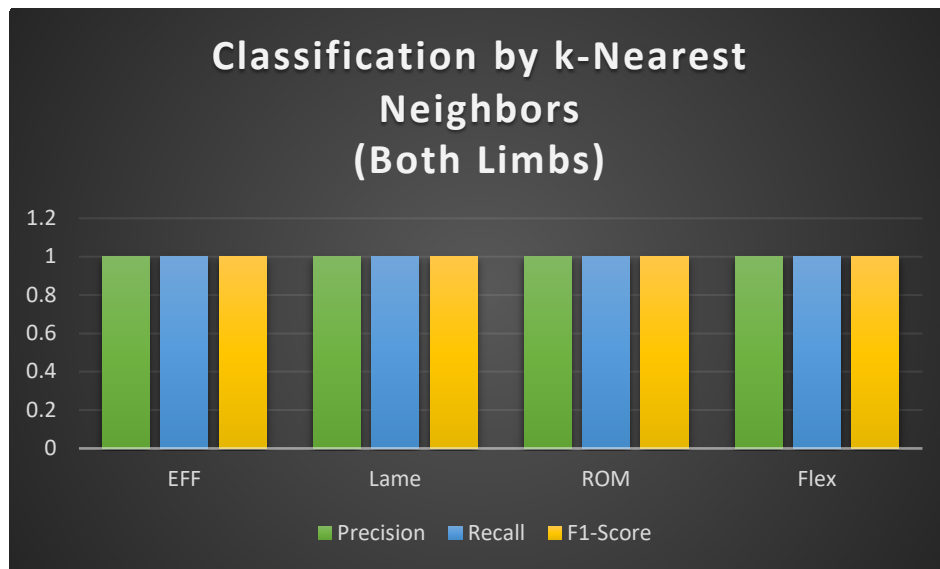
Figure 5.7: Classification results from models developed using both limbs for each of the four metrics of lameness using kNN.

To quantify the clinical relevance of the extracted features, the correlation between features and lameness metrics were measured. An example can be seen in Figures 5.8 and 5.9, where a wrapper algorithm (forward selection) was utilized to select the feature with the highest performance criterion, and this feature was plotted against the various scorings of lameness throughout the study. Figure 5.8 displays the scoring split between the left and right forelimb, and the feature selected through the wrapper algorithm was the percentage of energy in the fourth window of the x-axis of the forelimb fetlock sensors. In Figure 5.9, the means of that feature were plotted against the three measured scores (0, 1, 2), and the correlation and p-value were calculated through a linear model.
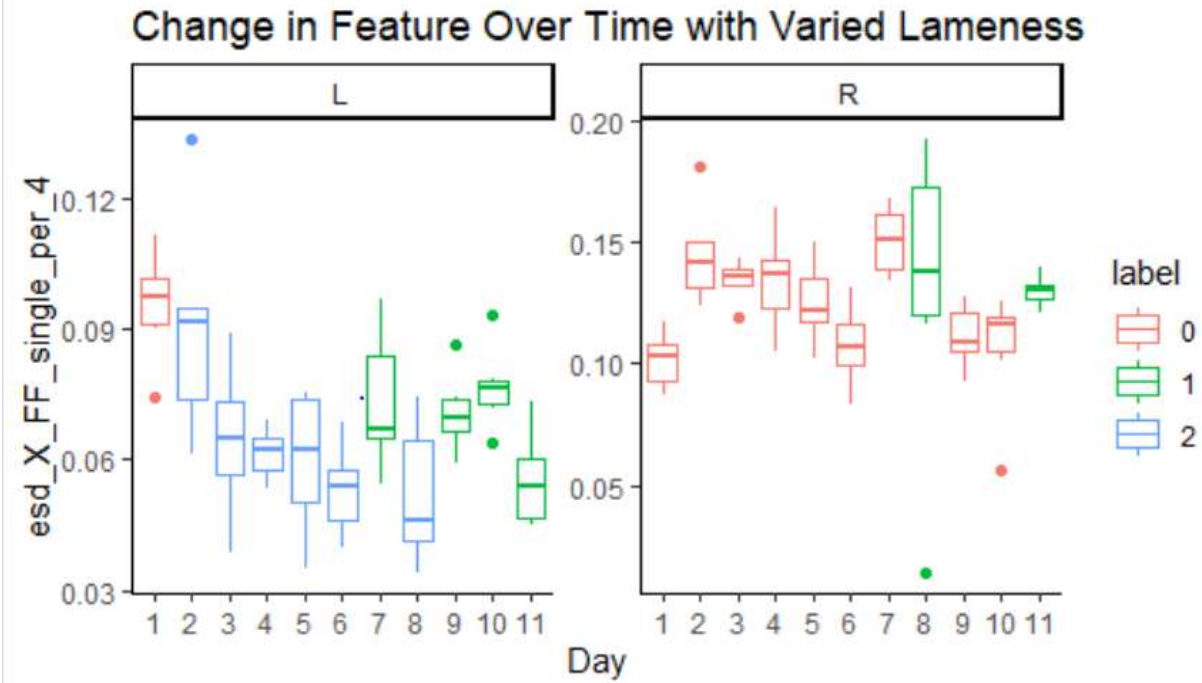
Figure 5.8: Change in feature selected through wrapper algorithm over time.
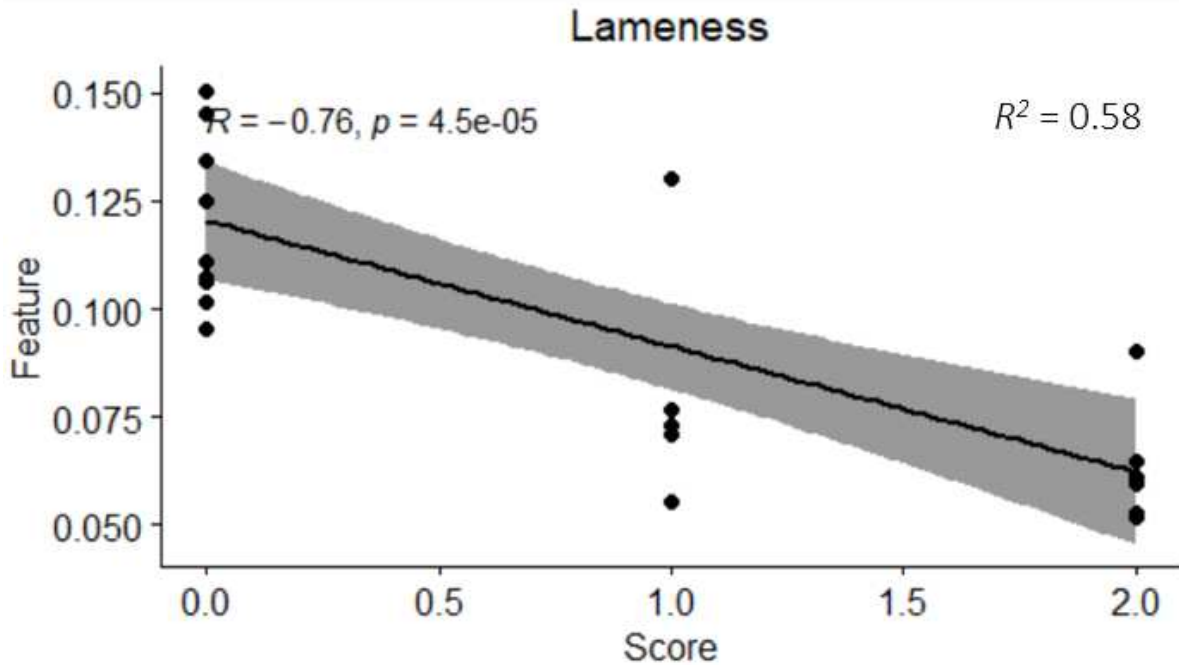
Figure 5.9: Correlation between feature selected and subjective lameness scoring.

5.3 Discussions

Quantification of Variability of Within-Day and Between-Day Exercise

The correlation between within-day measurements, or the Pearson Correlation Coefficients, are a tool used to measure the amount of correlation, or lack thereof, between the gait of the horse during each exercise. It is therefore prudent to examine the data and look for a relatively similar amount of variability between trials of exercise within a day (i.e., there is a level of symmetry, or equality, in values in the Pearson correlation table (Figure 5.3)). However, there are multiple points that are outside of the range of symmetry, meaning that these are trials that are greatly dissimilar from the others. This may be indicative of data that needs to be discarded, as it likely has a high amount of variability that is outside of the norm. Although this data is taken from a single horse, this method can be used to generally describe variability that can be corrected for when measuring differences in gait (against the norm).

Similarly, is it clear that there is a significant difference between the developed similarity scores depending on the time of day. The timing of the difference in similarity is likely indicative of the equine animal needing to "warm up", as the increase in difference is seen during trials in the morning, and it is plausible, therefore, that the horse may be stiff after a long period of non-movement or exercise. The similarity scores, while again taken from a single horse, are potentially powerful in that, when combined with more ground truthing of the horse's health and injury status, it is possible that they can be utilized to improve the level of exercise, or lack thereof, that the horse should undergo, as increases in gait variability may be indicators of underlying fatigue, injury, or illness that may be undetected beforehand. This will need to be verified statistically in the future with a much larger sample size, however, before any conclusive statements can be made.

Modeling of Differences in Gait Over Time with Surgically Induced Lameness

As shown in Figures 5.6 and 5.7, the kNN classifier correctly classified each of the four metrics with their respective scores with near 100% precision, recall, and F1-score for all but the lameness score of the right limb, wherein the model was trained on individual limbs (Figure 5.6). The difference in this performance is likely due to the lack of balance in the classes of the

individual models, as the vast majority of classes of the right limb were zeroes (as the surgery was performed on the other limb), which plausibly caused biasing towards that class. From plotting the most informative feature (as selected by the wrapper algorithm), the correlation of 0.58 is almost identical to subjective comparison of lameness among veterinarians, as described in Chapter 2. However, the data analysis techniques used here allow for more detailed correlation to other objective outcomes, such as other forms of injury and lameness, over time. It would, therefore, be prudent to have multiple professionals examine the horse, and see if performance of features matches the variability of scoring between vet professionals.

It is plausible that advanced data analytical techniques using these data also provide a possible means of further characterizing lameness and response to therapy with greater fidelity than current methods. It is important to note that, while these results are promising and warrant further studies with a larger sample size of equine animals, the current results have no statistical power, and thus conclusive statements on the performance of the models and viability of the selected features are not able to be made until further analysis is carried out on the larger dataset. However, from these results, the IMU data clearly follows trends similar to subjective scoring, which indicates that they can be used to further characterize pain and resulting lameness in horses.

Chapter 6
Forensic Identification of Environmental Sensors

Various forms of IoT environmental sensors are being examined for mass implementation into a multitude of systems and platforms. These sensors vary in size, configuration, fabrication, chemistry, and operational use. As alluded to in Chapters 2 and 3, metal oxide semi-conductors and chemiresistive sensors have shown great promise in sensing and analyzing a user's surrounding environment, the food and drink that the user is consuming, and the health status of user. However, there is a need for securing a home and/or smart environment with biometrics (i.e., a forensic environment). To show the validity of establishing biometric identity through challenging environmental sensors in a smart system (portable or stationary) with varied environments and analytes, a set of pre-selected sensors were tested in various scenarios.

6.1 Sensor and Environmentally Controlled Chamber Selection

To test the validity of establishing biometric identity through challenging environmental sensors, a set of metal-oxide semiconductor (MOS) sensors was purchased (Figure 6.1). The MQ sensor series, which includes a number of different sensors of similar build and are sensitive to specific analytes, was selected; specifically, the MQ-5, which is sensitive to liquefied petroleum gas and natural gas, the MQ-7, which is sensitive to carbon monoxide, and the MQ-135, which is sensitive to NH_3, nitric oxide, alcohol, Benzene, smoke, and carbon dioxide.

Figure 6.1: MQ sensor series used for this study, including the MQ-5, MQ-7, and MQ-135.

An environmentally controlled chamber was also purchased for the purpose of this study. The LHE-6, a benchtop-style stability test chamber, was purchased from Associated Environmental Systems (Figure 6.2). This chamber has a working volume of 4.96 cu. ft., a temperature range of -20°C to 94°C, and a humidity range of 10% to 98% relative humidity (RH).

Figure 6.2: Environmentally controlled chamber selected for this study, The LHE-6 Stability Benchtop-Style Test Chamber from Associated Environmental Systems (AES).

This chapter herein describes a study in which the aforementioned gas sensors were exposed to various environments and gases in order to evaluate the efficacy and effectiveness of applying biometric principles, specifically challenge-based biometrics, to environmental gas sensors for multiple purposes, described in Chapter 2. Specifically, the study discussed is first to test the viability of "abiometrically" validating the I.D. of environmental sensors through challenging them with different environments. Here, the hypothesis is that the raw data collected, which is data commonly used to calibrate the sensors (controlled calibration), will be distinctly different i) between sensor types (i.e., the MQ-5, MQ-7, and MQ-135) and ii) within sensor types (e.g., MQ-5 sensors will have different raw responses to other MQ-5 sensors). This will be tested

by exposing a set of each sensor type to a number of different temperature and humidity settings, which are common settings used in the calibration of these sensors. Next, the viability of "abiometrically" validating the I.D. of environmental sensors is tested through challenging them with different analytes. The hypothesis here is that the reaction of the different sensor types will be significantly different, and this in turn will allow for classification between the sensor types, and potentially the different sensors within those types, to occur with high accuracy. To test this hypothesis, the sensors will be exposed to three analytes of interest, all three of which are commonly used to calibrate the sensors of interest: hydrogen (H2), carbon monoxide (CO), and methane (CH4).

6.2 Methods

Analysis of Sensor Response to Environmental Challenges

Ten of each of the aforementioned MQ sensors (i.e., the MQ-5, MQ-7, and MQ-135) were exposed to varied combinations of temperature and humidity settings within the environmentally controlled chamber. Specifically, the temperature settings were between 20°C and 50°C in increments of 5 (e.g., 20°C, 25°C, 30°C, 35°C, 40°C, 45°C, 50°C), and these settings were in combination with a relative humidity (RH) of either 33% RH or 85% (in the case of 85%, the chamber was able to reach steady-states of 10°C and 15°C, so these temperatures were added to the original set). At each of these settings, five measurements were taken with each sensor for a total of 480 readings.

During measurements, the sensors were placed directly in the middle of the LHE-6 Stability Benchtop-Style Test Chamber, and wires were used to connect the sensor to an Arduino Uno that was placed outside of the chamber. The experimental setup is shown in Figure 6.3.

Figure 6.3: Sensor placement inside of environmentally controlled chamber.

After data collection, the changes in environmental setting were examined by first grouping the sensors by stock keeping unit (SKU) (i.e., MQ-5, MQ-7, and MQ-135). The data was then normalized by the raw output of the first setting to examine the trajectories of change between settings with each sensor without the effect of the initial offset. Finally, the differences in that normalized raw response between settings was also calculated.

Analysis of Variance (ANOVA) was then utilized to determine the statistical probability that each sensor would be recognized without confusion with another sensor of both i) the same SKU and ii) a different SKU through the following method. For all settings N (of which there are 16 total between the two RH settings), the number of comparisons between sensors is

$$C = \frac{L(L-1)}{2} \qquad (6.1)$$

where C is the total number of comparisons, and L is the number of sensors within the SKU. The probability of a false match, therefore, is

$$p(false\ match) = \frac{Q}{C * N} \qquad (6.2)$$

where Q is the number of sensors that are not statistically significantly different from one another. Here, C = 45, as L = 10. For statistical forensic purposes, the desired outcome is a probability of less than 10^{-9} of a false positive (i.e., a one in a billion chance that the recognition is not a false

positive). In an example where, when comparing sensors within the same SKU, Q = 17 (meaning there were 17 mismatches), then $p(false\ match) = \frac{17}{16*45} = 0.024$. In this case, to determine the minimum number of settings that would guarantee that a sensor is positively matched to its correct identity, then

$$(0.024)^T < 10^{-9} \tag{6.3}$$

Where T is the minimum number of settings that would be required to guarantee statistical forensics of the sensor in question. Here, solving for T would result in a T = 5.56, meaning that measurements at six settings (by rounding) would be needed to ensure this forensic identification.

To show the level of repeatability of these raw measurements with respect to each sensor, the level of repeatability of each sensor measurement at the different environmental settings was calculated by

$$R = \frac{\sigma_{ind}}{\sigma_{sample} * N} \tag{6.4}$$

where σ_{ind} is the standard deviation of the individual sensor measurements, σ_{sample} is the standard deviation of the full sample size (all 30 sensors), and N is the number of sensor within the sample size. Ideally, a value for R < 1 would be desired, as this indicates that the measurements are repeatable.

Analysis of Sensor Response to Various Gases

Ten of each of the aforementioned MQ sensors (i.e., the MQ-5, MQ-7, and MQ-135) were exposed to three calibration gases while in a constantly controlled environment of 25°C and 33% RH. Calibration gases included H_2 at a concentration of 50 parts per million (ppm), CO at a concentration of 50 ppm, and methane at a concentration of 100 ppm. Each gas was balanced with 21% oxygen in nitrogen. These calibration gases were mixed and filled by GASCO. Each sensor was exposed to each calibration gas separately five times for a total of 450 readings. Due to obscure readings from improper clearing of the gas between measurements, eleven of the CO readings were discarded.

During measurements, the sensors were placed directly in the middle of the LHE-6 Stability Benchtop-Style Test Chamber, and wires were used to connect the sensor to an Arduino Uno that was placed outside of the chamber. A hose was connected to sampling bags outside of the chamber, and for each reading, the sampling bag was filled for twenty seconds with a 0.5 L/min gas regulator for a total of 0.17 L. The gas was then released into the chamber with the hose placed strategically at 1 cm away from the sensor, and the sensors sampled the environment for one minute during each reading. The gas was then removed from the controlled environment through a fan and vent, which operated for ten minutes to properly clear the environment between each reading. The experimental setup is shown in Figure 6.4.

Figure 6.4: Experimental setup for gas exposure analysis.

The raw responses of each sensor to the three calibration gases were both corrected for the initial offset (or baseline) and aligned temporally with respect to the timing at which the gas was released into the chamber. To utilize the capabilities of the AlexNet classifier, as shown in Chapter 4, images were generated from the 1-D response signals from each sensor. To do so, the 1-D response was repeated n times to generate a matrix of sufficient dimensionality (as mentioned previously, this is at minimum 227 x 227) (Eqn 6.5),

$$I = \begin{bmatrix} x_1 & \cdots & x_{1,n} \\ \vdots & \ddots & \vdots \\ x_{m,1} & \cdots & x_{m,n} \end{bmatrix} \qquad (6.5)$$

where m represents the number of rows (or samples) from one measurement, and n is the number of columns. A moving mean was utilized to reduce the number of rows of the sample from the full amount to a number below the minimum resize requirement (for AlexNet, this is 256 x 256). Once the array was formed, the "greyscale" function in MATLAB was used to convert the data into normalized greyscale values between 0 and 1, which is based on the maximum and minimum sample reading from the full dataset. The data was then stacked three dimensionally using the "repmat" function in MATLAB, and example images resulting from this method is shown in Figure 6.5.

(a)   (b)   (c)
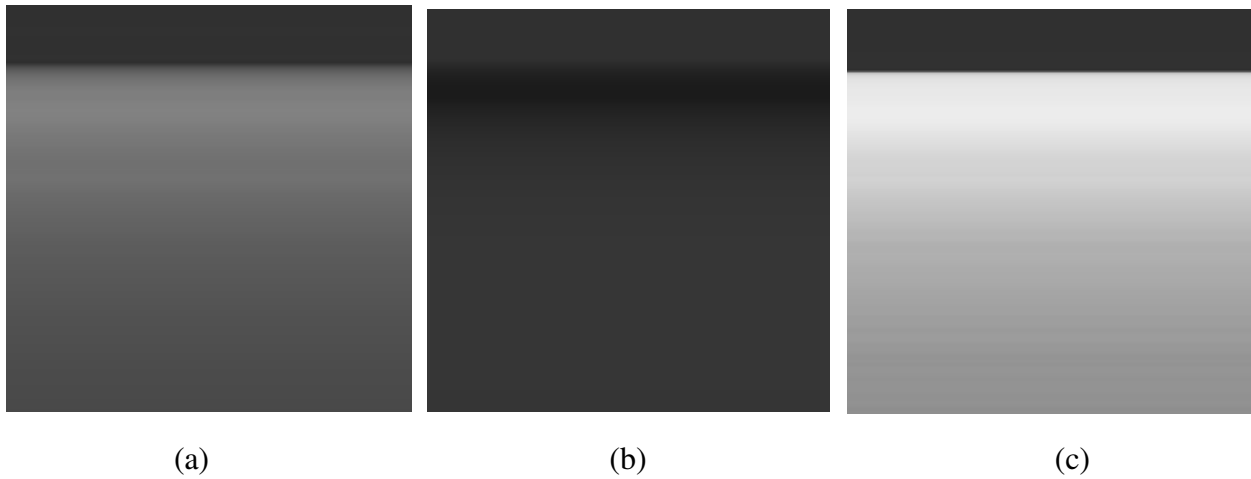
Figure 6.5: Examples of images from sensor responses to (a) H_2, (b) CO, and (c) CH_4.

The resulting images were used to train an AlexNet classifier for six different classification problems:

- Classification between the three gases,

- Classification between the three sensor types (MQ-5, MQ-7, MQ-135),

- Classification between the individual sensors (ten of each of the MQ series utilized, for a total of 30 classes) using images generated from the responses to all three gases,

- Classification between the individual sensors using only the response to H_2,

- Classification between the individual sensors using only the response to CO, and

- Classification between the individual sensors using only the response to CH_4.

The output of the classification results (namely, the classification of individual sensors from the response to the individual gases) can be utilized to determine the number of sensors which can be distinguished based on the results. To determine the number of sensors that each classification output can distinguish, the ranking of each output of the classification was recorded, and the ranking between the different classification outputs was combined through a mean. The number of sensors that the sensor in question can distinguish between is then

$$Number\ of\ sensors = \frac{N}{\mu} \tag{6.6}$$

where N is the total number of sensors, and μ is the mean of the included rankings. It is important to note that this assumes a smooth curve for N versus correct ranking.

6.3 Results

Analysis of Sensor Response to Environmental Challenges

Box plots showing the mean raw response (mV) of all sensors grouped by (SKU) at each environmental setting is shown in Figures 6.6 and 6.7.

Sensor Response to Environmental Settings (20C 33% RH)

(a)

Sensor Response to Environmental Settings (25C 33% RH)

(b)

Sensor Response to Environmental Settings (30C 33% RH)

(c)

Sensor Response to Environmental Settings (35C 33% RH)

(d)

Sensor Response to Environmental Settings (40C 33% RH)

(e)

Sensor Response to Environmental Settings (45C 33% RH)
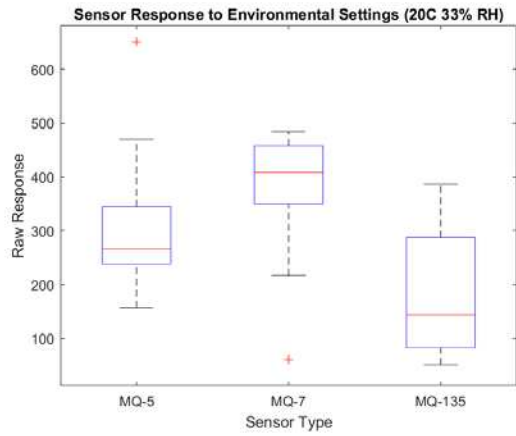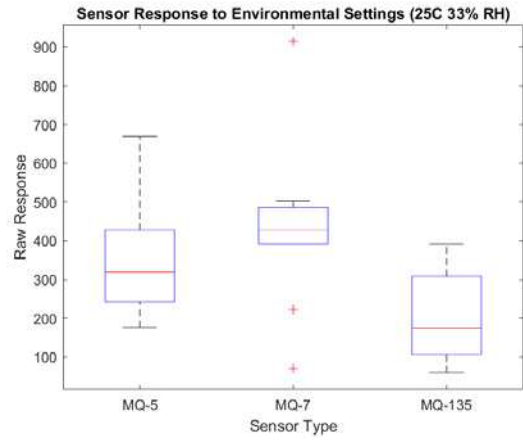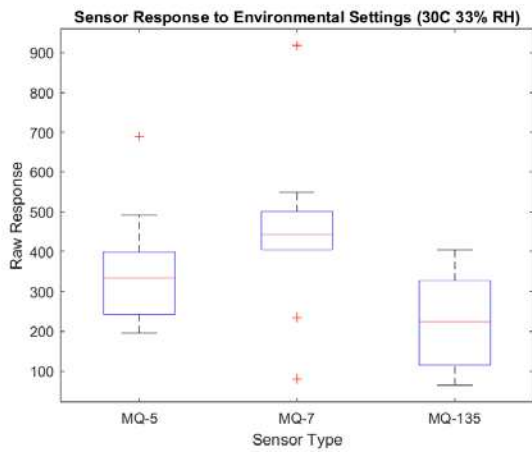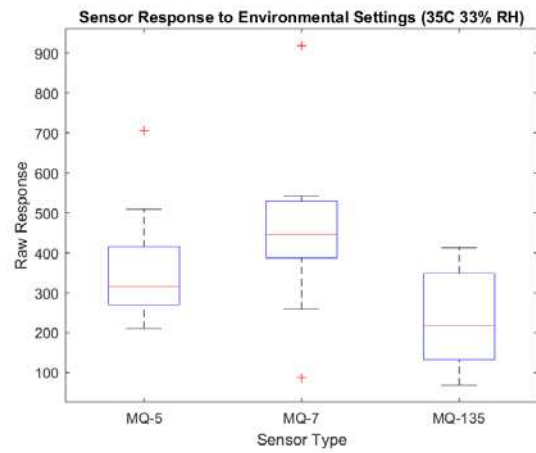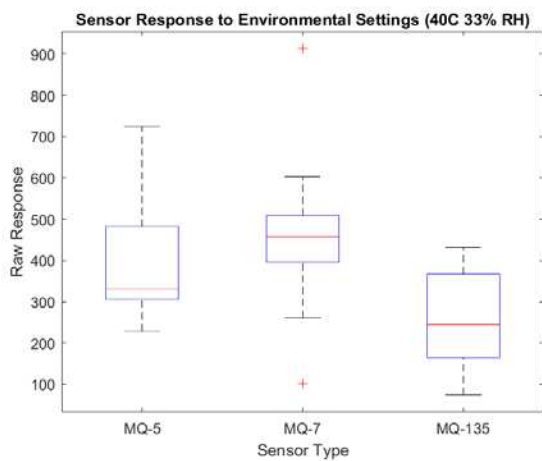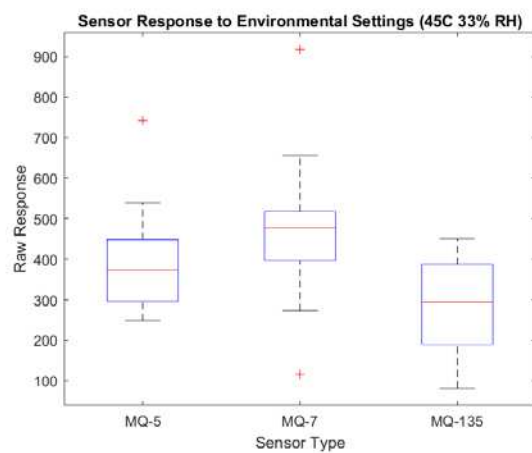
(f)
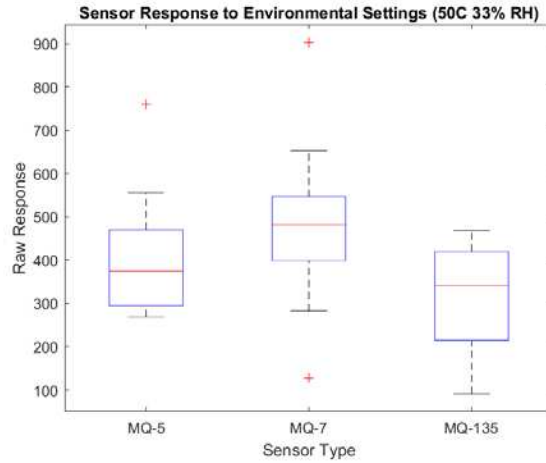
(g)

Figure 6.6: Raw response of the sensors to varied environments, including (a) 20℃ and 33% RH,(b) 25℃ and 33% RH, (c) 30℃ and 33% RH, (d) 35℃ and 33% RH, (e) 40℃ and 33% RH, (f) 45℃ and 33% RH, and (g) 50℃ and 33% RH.

(a)

(b)

(c)

(d)

(e)

(f)

(g)

(h)

Sensor Response to Environmental Settings (50C 85% RH)

(i)
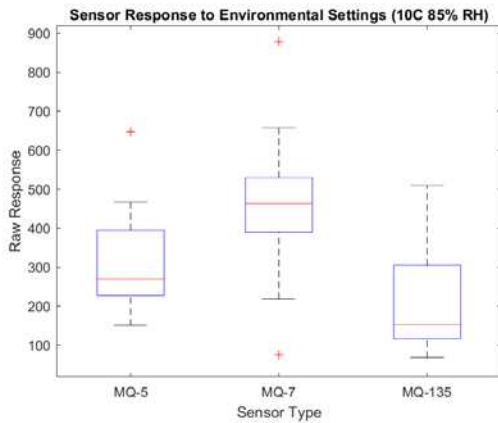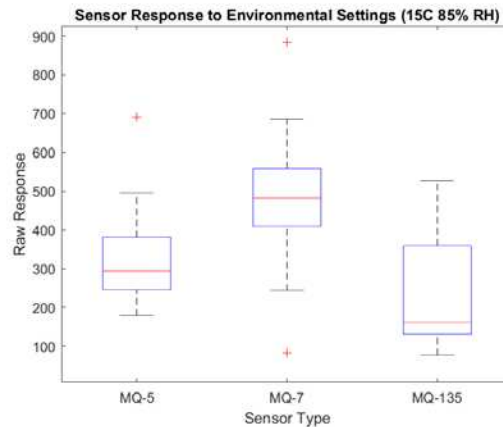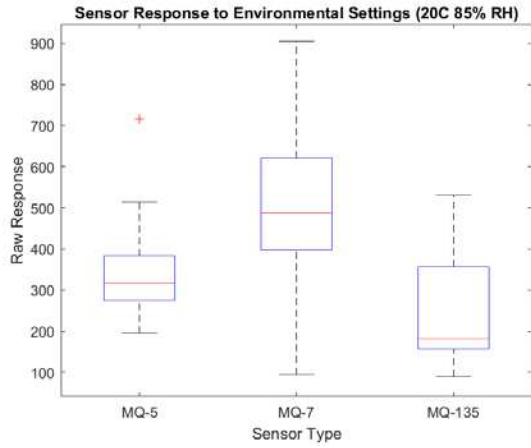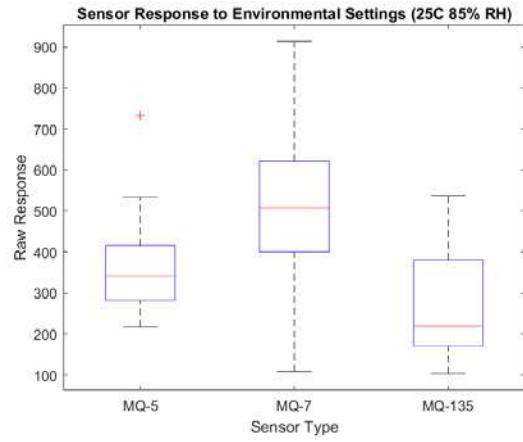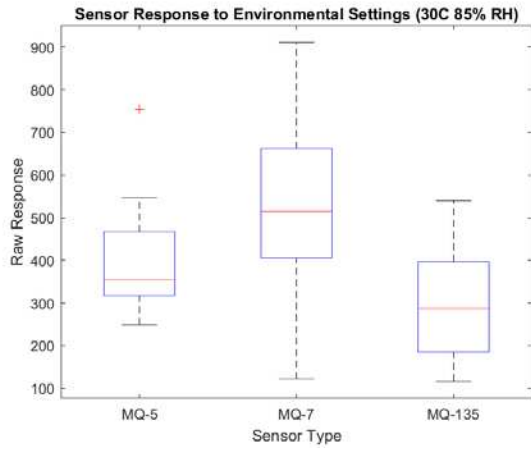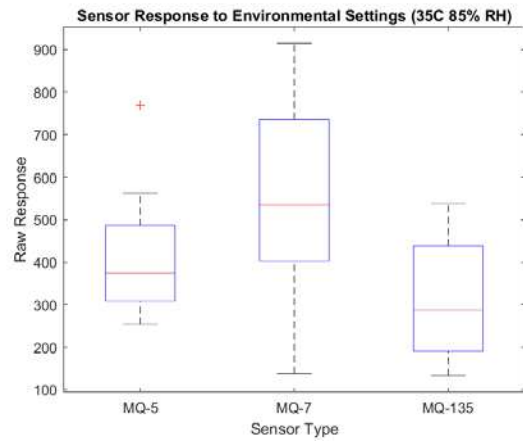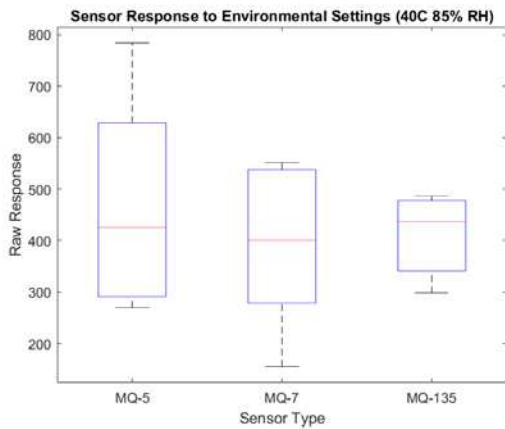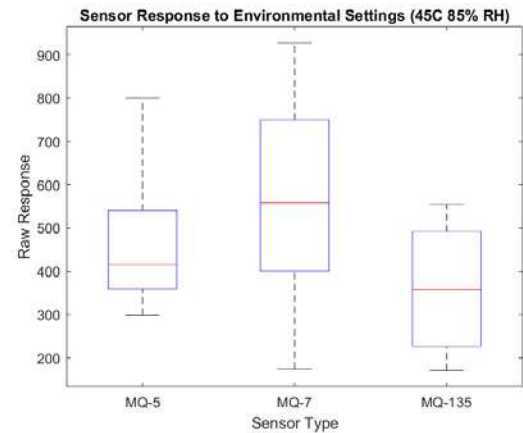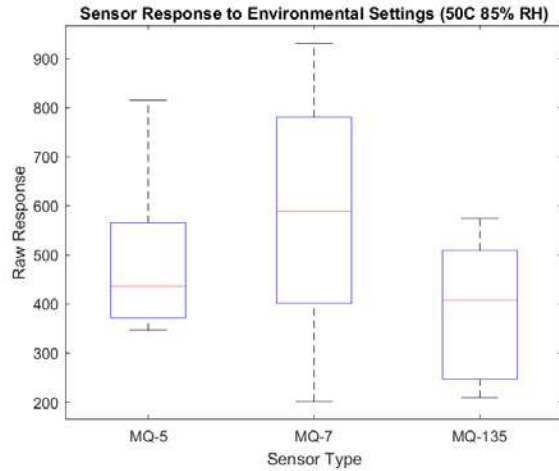
Figure 6.7: Raw response of the sensors to varied environments, including (a) 10℃ and 85% RH, (b)15℃ and 33% RH, (c) 20℃ and 85% RH, (d) 25℃ and 85% RH, (e) 30℃ and 85% RH, (f) 35℃ and 85% RH, (g) 40℃ and 85% RH, (h) 45℃ and 85% RH, and (i) 50℃ and 85% RH.

The normalized raw output of each sensor is shown in Figure 6.8, and the differences in that normalized raw response between settings are shown in Figures 6.9-6.14.

(a)

(b)
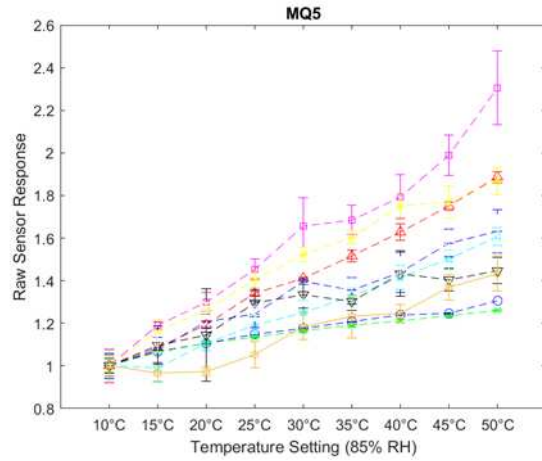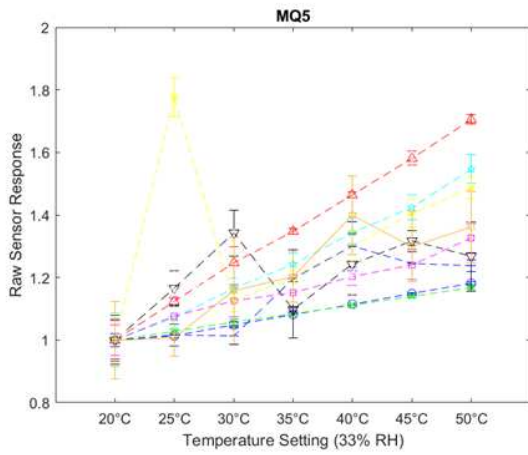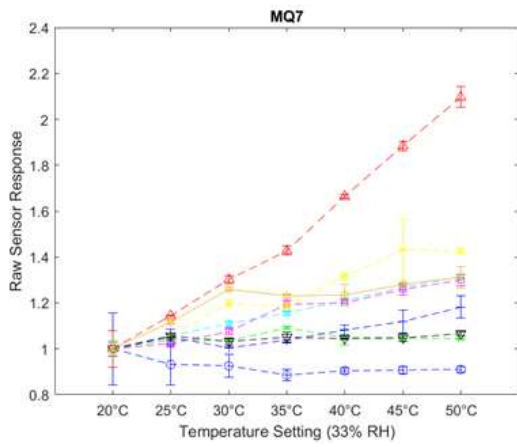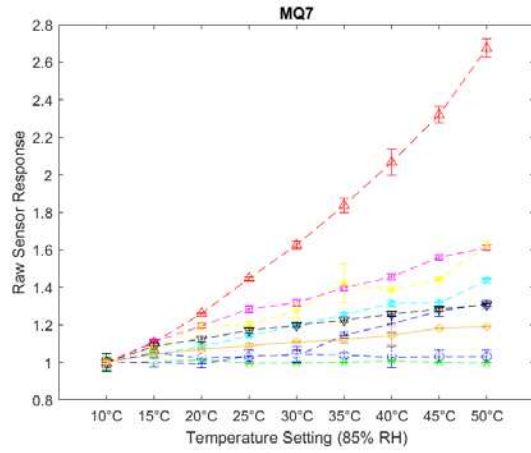
(c)   (d)
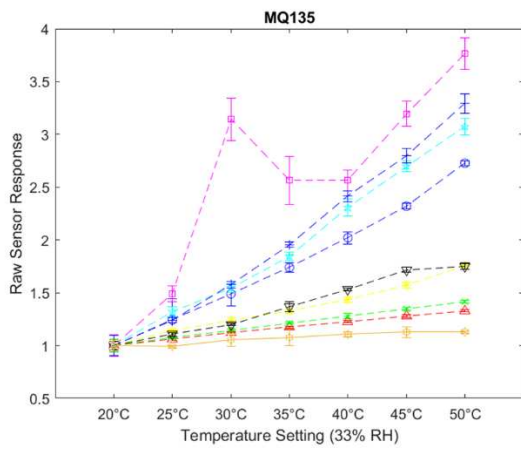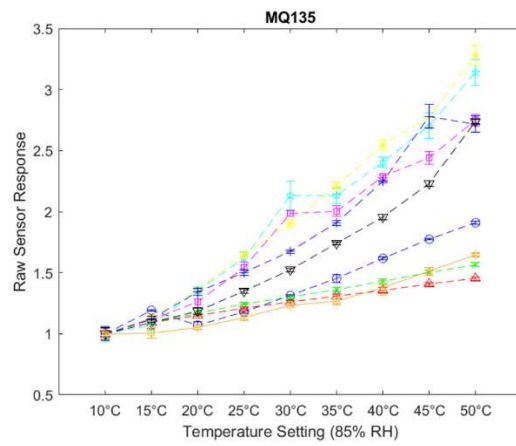
(e)   (f)

Figure 6.8: Normalized response for each sensor; (a) MQ-5 (33% RH), (b) MQ-5 (85% RH), (c) MQ-7 (33% RH), (d) MQ-7 (85% RH), (e) MQ-135 (33% RH), and (f) MQ-135 (85% RH).
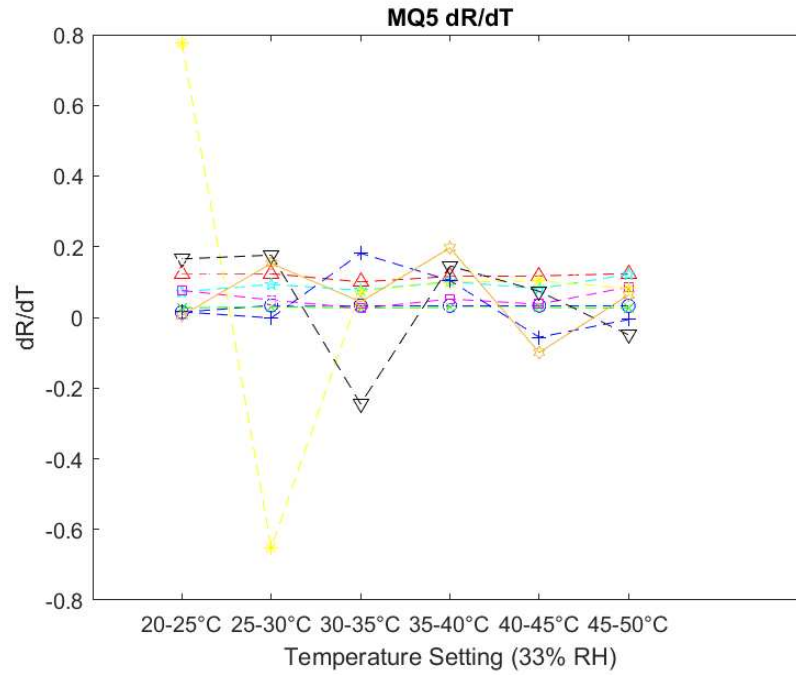
Figure 6.9: Normalized differences between temperature settings; MQ-5 sensors at 33% RH.
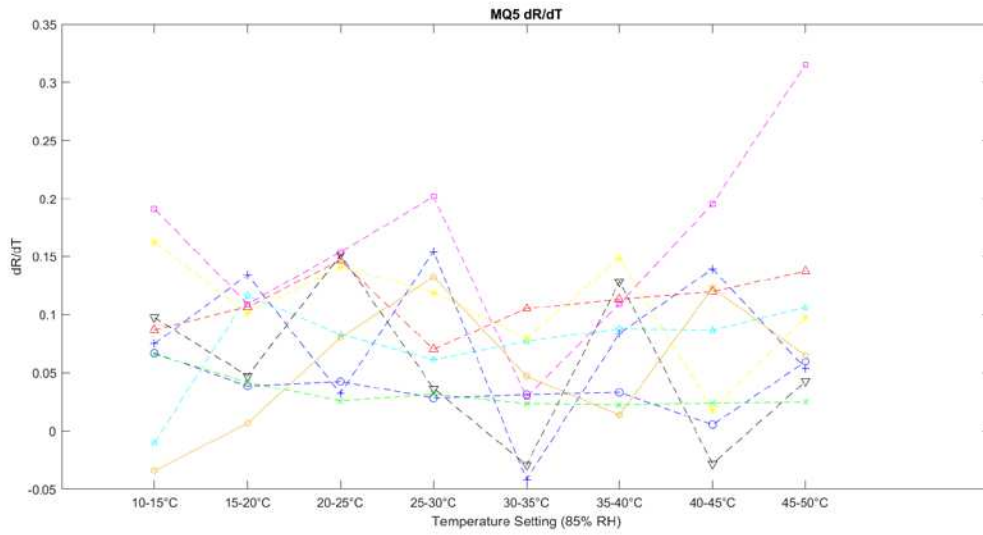
Figure 6.10: Normalized differences between temperature settings; MQ-5 sensors at 85% RH.
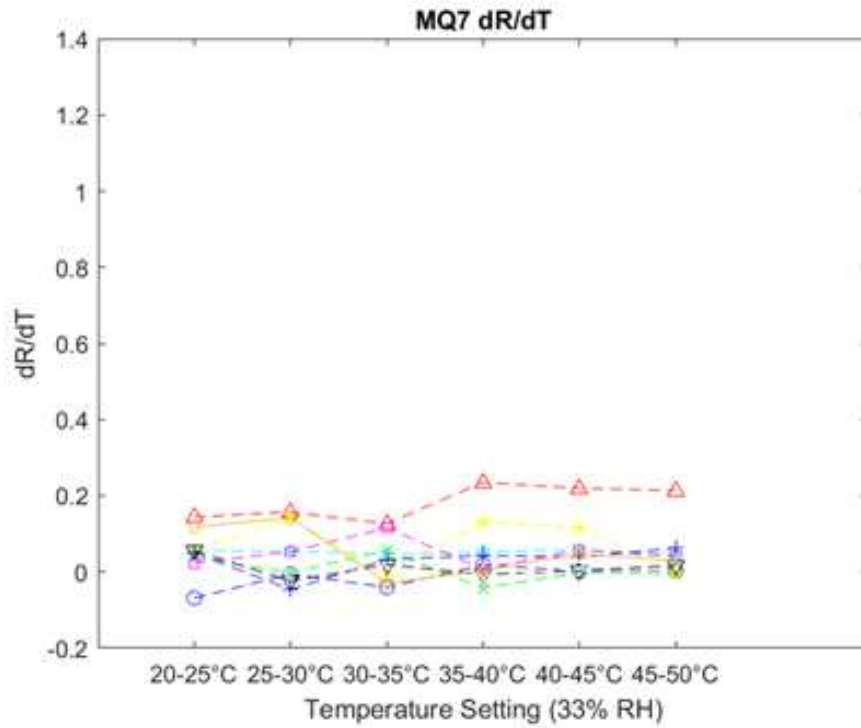
Figure 6.11: Normalized differences between temperature settings; MQ-7 sensors at 33% RH.
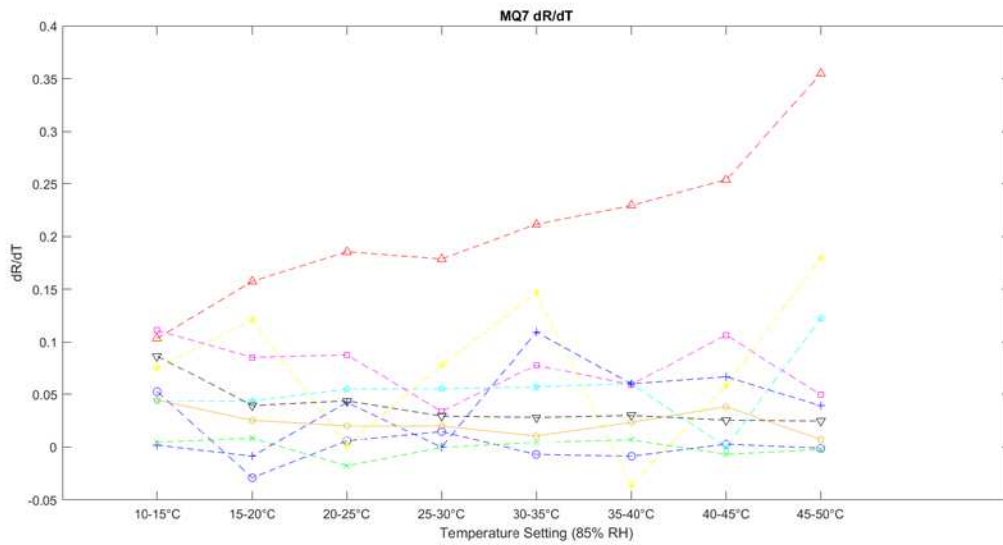
Figure 6.12: Normalized differences between temperature settings; MQ-7 sensors at 85% RH.
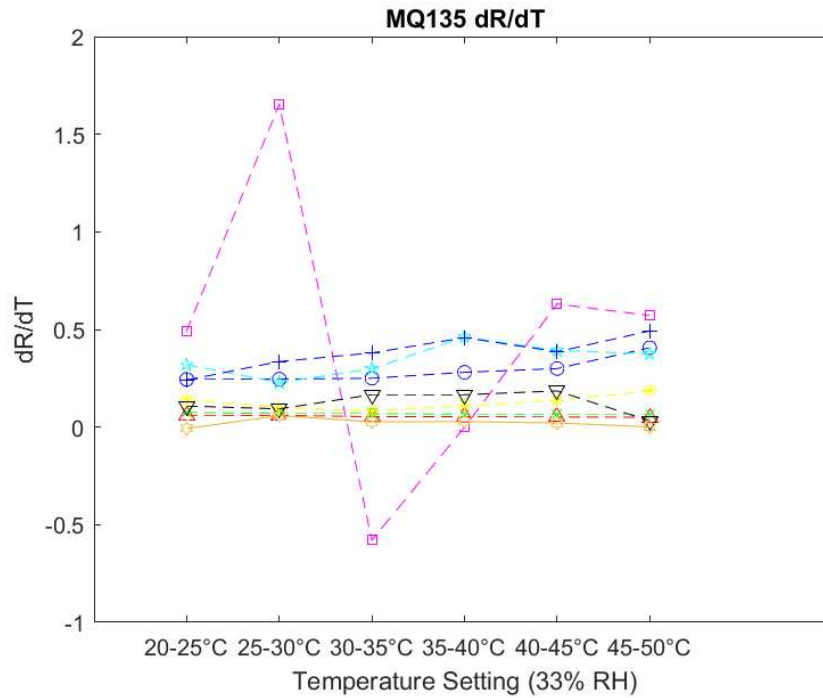
Figure 6.13: Normalized differences between temperature settings; MQ-135 sensors at 33% RH.
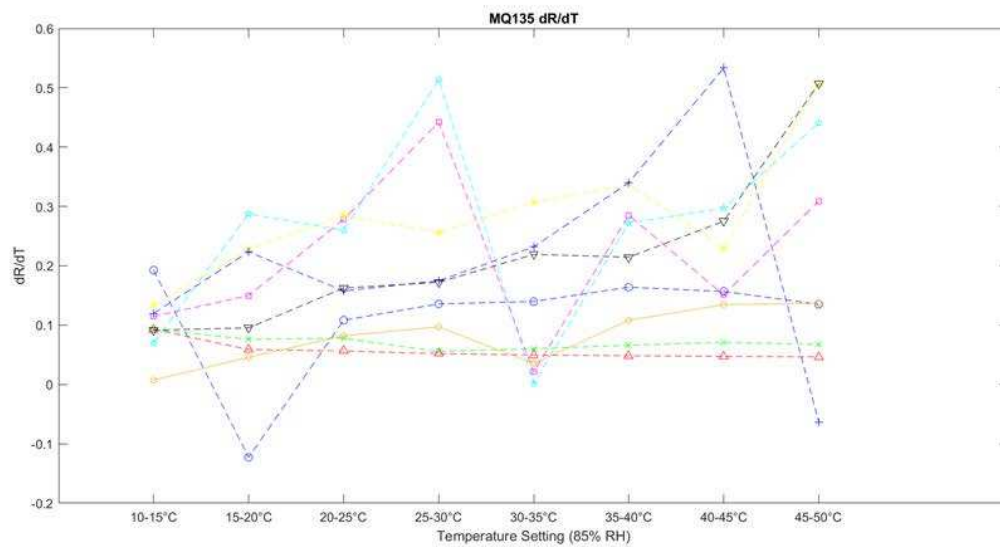
Figure 6.14: Normalized differences between temperature settings; MQ-135 sensors at 85% RH.

Analysis of Variance (ANOVA) was calculated between sensor groups and between each sensor, including both between types and within types for the latter, and the resulting F-statistics $(F_{(1,9)} = 3.36, p < 0.05)$ are included in Appendix A (Figures A.32-A.129). The number of false

matches, as well as the resulting number of required settings for forensic identification, is shown in Table 6.1.

Table 6.1: Summary of statistical forensic analysis of response to different environmental settings.

	# of Non-statistical significance	# of settings for forensic accuracy
MQ-5 - MQ-5	18	5.6 (6)
MQ-7 - MQ-7	6	4.32 (5)
MQ-135 - MQ-135	4	3.99 (4)
MQ-5 - MQ-7	30	6.52 (7)
MQ-7 - MQ-135	18	5.6 (6)
MQ-5 - MQ-135	8	4.61 (5)

The repeatability of the measurements at each environmental setting with each individual sensor of each sensor type is included in Appendix A (Figure A.130).

Analysis of Sensor Response to Various Gases

The mean response for all sensors of each type to each gas is shown in Figures 6.15 - 6.17. The mean response of the individual sensors is presented in Appendix A (Figures A.131-A.133).
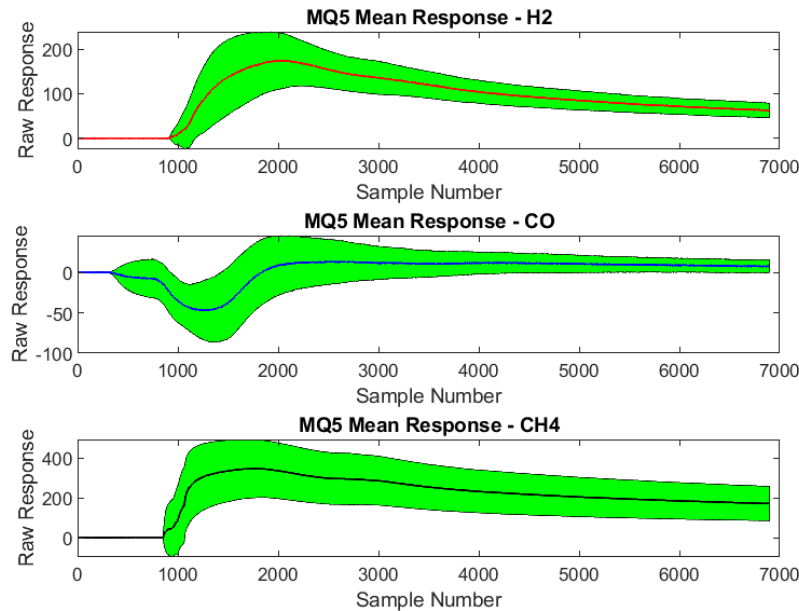
Figure 6.15: MQ-5 mean sensor response to H2, CO, and CH4.
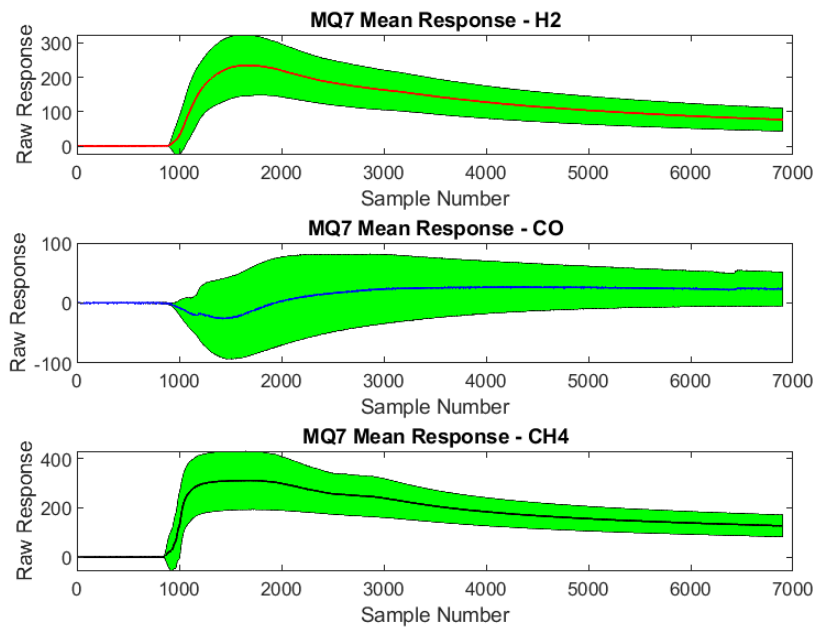
Figure 6.16: MQ-7 mean sensor response to H2, CO, and CH4.
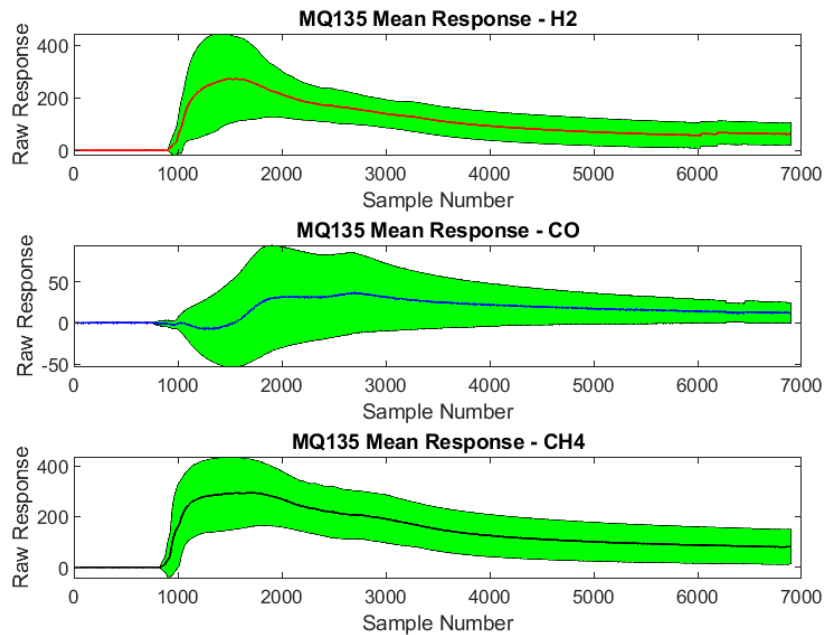
Figure 6.17: MQ-135 mean sensor response to H2, CO, and CH4.

The results of the six classification problems presented is shown in Figure 6.18.
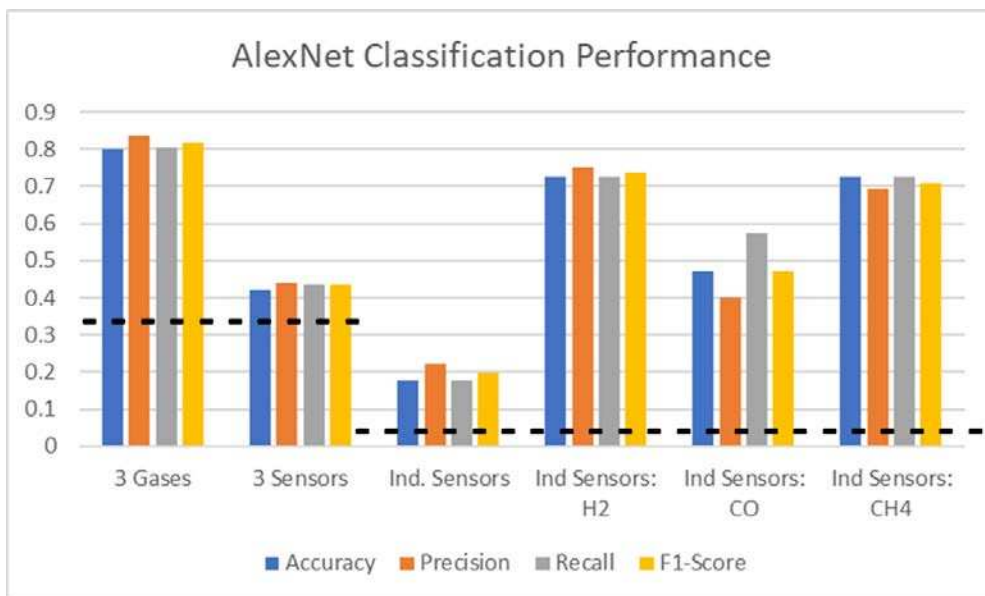
Figure 6.18: Classification performance of AlexNet for generated images.

In Figure 6.18, the dashed lines correspond to the accuracy at which "guessing" would be achieved (for three class problems, this is 1/3, and for thirty classes, this is 1/30, or 0.033). Based on the results, the rankings of the classification of H_2 and CH_4 were combined, and the calculation of the ranking of the correct classifications for each sensor, as well as the number of corresponding sensors that each sensor would be able to be distinguished from, are shown in Figures 6.19 and 6.20, respectively.
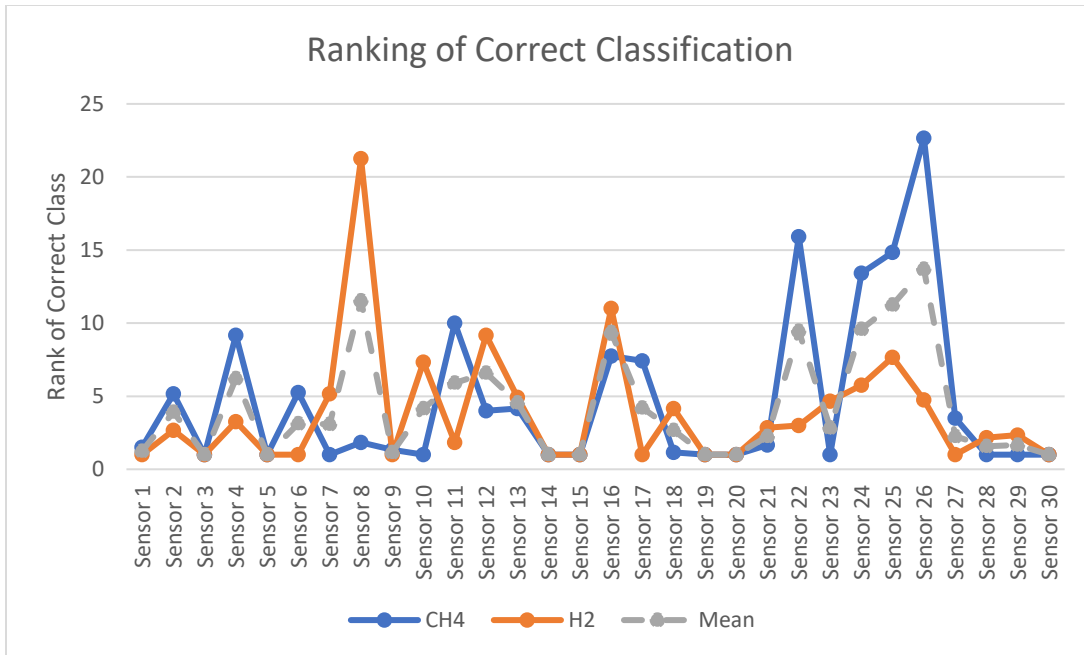
Figure 6.19: Ranking of classification for the responses to CH_4, H_2, and the mean (combination) of the two.
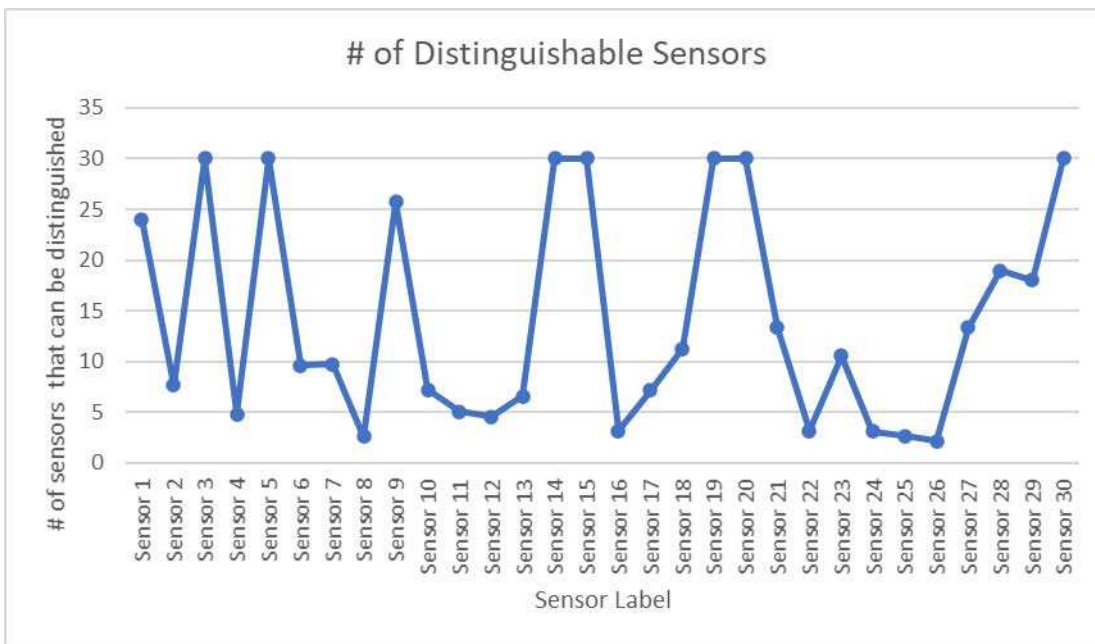
Figure 6.20: The resulting number of sensors that the combination of classifications is able to distinguish between.

6.4 Discussions

Analysis of Sensor Response to Environmental Challenges

The plots of the normalized response, as well as the normalized differences in response (Figures 6.8 – 6.14), show that there is a common trend at which each sensor increases in raw response when challenged with the different settings. There are, however, clear outliers to the trends, and these can be corrected for, but also potentially recognized as a sensor that is operating incorrectly and may need replaced, or as a set of data that does not follow with the generalized model of expected response. There is also clearly a great effect in increased humidity, which can be seen in the increase in slope between readings at 85% RH in comparison to the measurements taken at 33% RH.

The results of the ANOVA of the full set of respective SKU sensor response show that, overall, there is not a consistent statistically significant difference between the MQ-5, MQ-7, and MQ-135 sensors when grouped. The MQ-7 and MQ-135 were statistically significantly different at different settings, but overall there were only 22 instances out of 48 possibilities where this was true (i.e., 26 of the possible comparisons were not significantly different) ($F(1,9) = 3.36, p < 0.05$). However, this was not the case for the individual sensors overall. The number of mismatches in each comparison (Table 6.1) showed that there were very few instances where the raw responses to the different settings were not statistically significantly different ($F(2,29) = 2.49, p < 0.05$). Through analysis (Equations 6.1 – 6.3), examining each sensor in the range of four to seven environmental settings (e.g., exposing each sensor to four to seven different temperature and humidity settings) will be required to achieve a one in a billion chance that the sensor was forensically validated. This is a potentially important process, as these readings are taken commonly for commercial calibration purposes, and do not take extra effort to examine. These measurements are also clearly repeatable (Figure A.130), as the vast majority of the calculated ratios (Eqn 6.4) are below 1.0 (85.2%). The source of the lack of repeatability of some sensors was likely due to the lack of stability of the set environmental settings in the chamber (i.e., the environmental settings fluctuated when attempting to maintain "stable" environments). In other

words, the measurements are repeatable when tested in stable conditions. Also, while some of the raw measurements at different settings are correlated strongly within individual sensors (mean R^2 = 0.81 for 33% RH, and R^2 = 0.89 for 85% RH), the correlation is as low as 0.05 for the sensors at 33% RH and 0.07 for 85% RH. This lack of correlation is likely the cause of the "mismatches", or sensors that were not statistically significantly different from each other at the various settings, which is why the statistical analysis utilized here is necessary for statistical forensics.

Analysis of Sensor Response to Various Gases

From the results, it is clear that each classification problem was well above guessing (less so for the sensor classification problem, which was only slightly above guessing at 0.42 for accuracy, and 0.44 for precision, recall, and F1-score). Although the classification of all individual sensors using the full dataset (i.e., responses for all three gases) was approximately 20%, this is still more than six times greater than the result from guessing, and when the classification problem is split to be based only on the individual gases, the thirty-class problem increases in the different performance metrics significantly. It is also clear that, compared to the results from using H_2 and CH_4, using CO calibration gas was not as effective. This is likely due to the high polarization of CO molecules, which compared to the non-polar H_2 and CH_4, caused a great amount of variability in response, and this had an effect on the resulting classification. The performance of the classification using H_2 and CH_4, however, was further examined using the rankings of both outputs. The results show that each sensor can distinguish between a mean of 14 other sensors (and median of 10). This, when combined in a system with an initial classification of the measured analyte, can be used as a tool of dimension reduction that will require augmentation with other analyses to achieve forensic authentication within a smart IoT system. It is again important to note that this calculation assumes a smooth curve for N versus correct ranking, which is not the case for the results (which exhibit kurtosis in the distribution), so this is only an estimate. A larger dataset with more resolution with respect to different analyte concentrations will further characterize this relationship and show more definitively the relationship between classification and the ability to distinguish between sensors within the proposed smart IoT system.

Chapter 7
Conclusions and Future Work

7.1 Conclusion

The research conducted in this dissertation introduced the use of challenge-based biometrics in applications to three areas: gesture recognition for the relay of the intent of sensing to a portable hand-held device, equine gait analysis for the detection and diagnosis of lameness in an equine animal with four different metrics of lameness, and forensic authentication of sensors that have the potential to be utilized within the hand-held portable "magic wand" device through the exposure of varied environments and analytes. Two approaches were applied to gesture recognition in the effort to classify pre-determined "atomic" movements, one of which was improved upon through an axis shifting method that resulted in an increased accuracy, and the other of which the conversion of 1-D signals to 3-D images (or signal dimensional transformation) was utilized in order to employ AlexNet as a classification algorithm. Finally, the generated images, along with the AlexNet classification method, were used in a system in which the internal error was quantized through initial and final classifications of gestures, and the partitioning of subjects was able to improve the overall results, and this system was shown to be useful in the maintenance of a biometric VPN that can be established through other commonly used methods.

The method of using within and between day variability through calculation of Pearson correlation coefficients and similarity scoring was demonstrated, and the features derived from the energy spectral density of the signals demonstrated high accuracy and strong correlation to the subjective scoring of professional veterinarians seen in the literature. These objective measures of lameness in horses using wearable sensors not only provide an opportunity for more objective characterization of pain, but also provide an opportunity to use these devices at home and during training to remotely monitor equine health. However, a larger cohort of equine animals will be needed to verify these results.

Finally, the controlled exposure of MOS environmental sensors to varied environments showed promise in the forensic authentication, with as few as four measurements needed to

guarantee a one in a billion chance of a false positive, which is necessary for forensic authentication. Similarly, the exposure of the various sensors to multiple analytes showed that the modeling of the response through images generated through 1-D signals gives high enough accuracy that exposure to two analytes can distinguish one sensor from a mean of 14 other individual sensors. These challenge-based "abiometrics" give promise in anomaly detection, which in turn can be utilized to detect perception-layer attacks within IoT systems.

7.2 Future Work

In the future, multiple objectives can be accomplished that will bring further implementation of the technologies and theories discussed.

- *Objective 1:* Investigate the use of complex movements, which are linear combinations of the proposed atomic movements, that can be used as "passcodes" to gain access with the handheld system.
- *Objective 2*: Gather and develop a vast database of horse gait data with controlled sensor placement and utilization to be able to statistically verify the modeling results of this dissertation, and
- *Objective 3*: Examine similar sensor technologies and develop modeling-based techniques using the presented challenges to provide security to other perception-layer objects within an IoT system. Also, examine the layers outside of the perception layer, such as network layer attacks, to secure the system of portable-based devices presented.

This future work will provide further validation of the use of challenge-based biometrics in practice for multiple scenarios in the IoT realm, including forensic security of portable IoT devices (such as the proposed magic wand), the health and safety of non-human entities such as equine animals, and the items and objects within IoT systems, such as environmental sensors, which have multiple security risks as described here.

Bibliography

[1]   "The Growth in Connected IoT Devices Is Expected to Generate 79.4ZB of Data in 2025, According to a New IDC Forecast," *International Data Corporation (IDC Media Center)*, 2019.

[2]   A. Raij, A. Ghosh, S. Kumar, and M. Srivastava, "Privacy Risks Emerging from the Adoption of Innocuous Wearable Sensors in the Mobile Environment," *Conf. Hum. Factors Comput. Syst. - Proc.*, pp. 11–20, 2011, doi: 10.1145/1978942.1978945.

[3]   I. Krontiris, F. Freiling, and T. Dimitriou, "Location Privacy in Urban Sensing Networks: Research Challenges and Directions [Security and Privacy in Emerging Wireless Networks]," *IEEE Wirel. Commun.*, no. October, pp. 30–35, 2010.

[4]   S. J. Simske, "Dynamic biometrics: The case for a real-time solution to the problem of access control, privacy and security," *2009 1st IEEE Int. Conf. Biometrics, Identity Secur. BIdS 2009*, no. Table III, 2009, doi: 10.1109/BIDS.2009.5507535.

[5]   A. Ometov, S. Bezzateev, N. Mäkitalo, S. Andreev, T. Mikkonen, and Y. Koucheryavy, "Multi-factor authentication: A survey," *Cryptography*, vol. 2, no. 1, pp. 1–31, 2018, doi: 10.3390/cryptography2010001.

[6]   G. Dahia, L. Jesus, and M. Pamplona Segundo, "Continuous authentication using biometrics: An advanced review," *Wiley Interdiscip. Rev. Data Min. Knowl. Discov.*, vol. 10, no. 4, pp. 1–23, 2020, doi: 10.1002/widm.1365.

[7]   A. K. Jain and A. Kumar, "Biometric Recognition: An Overview," pp. 49–79, 2012, doi: 10.1007/978-94-007-3892-8_3.

[8]   N. Yusuf, K. A. Marafa, K. L. Shehu, H. Mamman, and M. Maidawa, "A survey of biometric approaches of authentication," *Int. J. Adv. Comput. Res.*, vol. 10, no. 47, pp. 96–104, 2020, doi: 10.19101/ijacr.2019.940152.

[9]   A. Mahfouz, T. M. Mahmoud, and A. S. Eldin, "Bimodal behavioral authentication framework based on decision fusion," *2017 8th Int. Conf. Inf. Commun. Syst. ICICS 2017*, pp. 368–373, 2017, doi: 10.1109/IACS.2017.7922000.

[10]   M. Kumar, M. Hanumanthappa, and T. V. S. Kumar, "Use of AADHAAR biometrie database for crime investigation - Opportunity and challenges," *Proc. 2017 Int. Conf. Innov. Information, Embed. Commun. Syst. ICIIECS 2017*, vol. 2018-Janua, pp. 1–6, 2018, doi: 10.1109/ICIIECS.2017.8276109.

[11]   V. Conti, G. Milici, P. Ribino, F. Sorbello, and S. Vitabile, "Fuzzy Fusion in Multimodal Biometric Systems The multimodal biometric systems can be classified considering the biometrics," pp. 1–8, 2007.

[12] S. Madakam, R. Ramaswamy, and S. Tripathi, "Internet of Things (IoT): A Literature Review," *J. Comput. Commun.*, vol. 03, no. 05, pp. 164–173, 2015, doi: 10.4236/jcc.2015.35021.

[13] N. Scarpato, A. Pieroni, L. Di Nunzio, and F. Fallucchi, "E-health-IoT universe: A review," *Int. J. Adv. Sci. Eng. Inf. Technol.*, vol. 7, no. 6, pp. 2328–2336, 2017, doi: 10.18517/ijaseit.7.6.4467.

[14] H. H. Nguyen, F. Mirza, M. A. Naeem, and M. Nguyen, "A review on IoT healthcare monitoring applications and a vision for transforming sensor data into real-time clinical feedback," *Proc. 2017 IEEE 21st Int. Conf. Comput. Support. Coop. Work Des. CSCWD 2017*, pp. 257–262, 2017, doi: 10.1109/CSCWD.2017.8066704.

[15] A. Rahaman, M. M. Islam, M. R. Islam, M. S. Sadi, and S. Nooruddin, "Developing iot based smart health monitoring systems: A review," *Rev. d'Intelligence Artif.*, vol. 33, no. 6, pp. 435–440, 2019, doi: 10.18280/ria.330605.

[16] H. Ping, J. Wang, Z. Ma, and Y. Du, "Mini-review of application of IoT technology in monitoring agricultural products quality and safety," *Int. J. Agric. Biol. Eng.*, vol. 11, no. 5, pp. 35–45, 2018, doi: 10.25165/j.ijabe.20181105.3092.

[17] A. D. Boursianis *et al.*, "Internet of Things (IoT) and Agricultural Unmanned Aerial Vehicles (UAVs) in smart farming: A comprehensive review," *Internet of Things*. p. 100187, 2020, doi: 10.1016/j.iot.2020.100187.

[18] J. M. Talavera *et al.*, "Review of IoT applications in agro-industrial and environmental fields," *Comput. Electron. Agric.*, vol. 142, no. 118, pp. 283–297, 2017, doi: 10.1016/j.compag.2017.09.015.

[19] S. R. Shinde, A. H. Karode, and S. R., "Review on - Iot Based Environment Monitoring System," vol. 8, no. 2, pp. 103–108, 2017.

[20] B.-S. K. Muhammad Burhan, Rana Asif Rehman, Bilal Khan, "IoT Elements, Layered Architectures and Security Issues: A Comprehensive Survey," *Nature*, vol. 388. Sensors, 2018.

[21] S. Tang, D. R. Shelden, C. M. Eastman, P. Pishdad-Bozorgi, and X. Gao, "A review of building information modeling (BIM) and the internet of things (IoT) devices integration: Present status and future trends," *Automation in Construction*, vol. 101. pp. 127–139, 2019, doi: 10.1016/j.autcon.2019.01.020.

[22] H. Nazemi, A. Joseph, J. Park, and A. Emadi, "Advanced micro-and nano-gas sensor technology: A review," *Sensors (Switzerland)*, vol. 19, no. 6, 2019, doi: 10.3390/s19061285.

[23] N. R. Prasad, S. Almanza-Garcia, and T. T. Lu, "Anomaly detection," *Comput. Mater.*

Contin., vol. 14, no. 1, pp. 1–22, 2009, doi: 10.1145/1541880.1541882.

[24] A. Ross, S. Banerjee, and A. Chowdhury, "Security in smart cities: A brief review of digital forensic schemes for biometric data," *Pattern Recognit. Lett.*, vol. 138, pp. 346–354, 2020, doi: 10.1016/j.patrec.2020.07.009.

[25] M. F. Elrawy, A. I. Awad, and H. F. A. Hamed, "Intrusion detection systems for IoT-based smart environments: a survey," *J. Cloud Comput.*, vol. 7, no. 1, pp. 1–20, 2018, doi: 10.1186/s13677-018-0123-6.

[26] G. Velmathi, S. Mohan, and R. Henry, "Analysis and review of tin oxide-based chemoresistive gas sensor," *IETE Tech. Rev. (Institution Electron. Telecommun. Eng. India)*, vol. 33, no. 3, pp. 323–331, 2016, doi: 10.1080/02564602.2015.1080603.

[27] A. Dey, "Materials Science & Engineering B Semiconductor metal oxide gas sensors : A review," vol. 229, no. January, pp. 206–217, 2018.

[28] P. Werle, "Accuracy and precision of laser spectrometers for trace gas sensing in the presence of optical fringes and atmospheric turbulence," *Appl. Phys. B Lasers Opt.*, vol. 102, no. 2, pp. 313–329, 2011, doi: 10.1007/s00340-010-4165-9.

[29] G. S. E. Comini, G. Faglia, "Stable and Highly Sensitive Gas Sensors Based on Semiconducting Oxide Nanobelts." APL Classic Papers, 2002.

[30] V. M. N. Passaro, A. Cuccovillo, L. Vaiani, M. De Carlo, and C. E. Campanella, "Gyroscope technology and applications: A review in the industrial perspective," *Sensors (Switzerland)*, vol. 17, no. 10, 2017, doi: 10.3390/s17102284.

[31] S. D. Senturia, *Microsystem Design*. Boston: Kluwer Academic Publishers, 2001.

[32] G. Zhanshe, C. Fucheng, L. Boyu, C. Le, L. Chao, and S. Ke, "Research development of silicon MEMS gyroscopes : a review," *Microsyst. Technol.*, pp. 2053–2066, 2015, doi: 10.1007/s00542-015-2645-x.

[33] A. S. Shirkhorshidi, S. Aghabozorgi, T. Y. Wah, and T. Herawan, "Big data clustering: A review," *Lect. Notes Comput. Sci. (including Subser. Lect. Notes Artif. Intell. Lect. Notes Bioinformatics)*, vol. 8583 LNCS, no. PART 5, pp. 707–720, 2014, doi: 10.1007/978-3-319-09156-3_49.

[34] R. M. CORMACK, "Review of Classification," no. iii, pp. 321–353, 1971.

[35] A. Soofi and A. Awan, "Classification Techniques in Machine Learning: Applications and Issues," *J. Basic Appl. Sci.*, vol. 13, pp. 459–465, 2017, doi: 10.6000/1927-5129.2017.13.76.

[36] C. Yu and W. Yao, "Robust linear regression: A review and comparison," *Commun. Stat.*

Simul. Comput., vol. 46, no. 8, pp. 6261–6282, 2017, doi: 10.1080/03610918.2016.1202271.

[37]   S. Sah, "Machine Learning: A Review of Learning Types," *ResearchGate*, no. July, 2020, doi: 10.20944/preprints202007.0230.v1.

[38]   A. E. Maxwell, T. A. Warner, and F. Fang, "Implementation of machine-learning classification in remote sensing: An applied review," *Int. J. Remote Sens.*, vol. 39, no. 9, pp. 2784–2817, 2018, doi: 10.1080/01431161.2018.1433343.

[39]   P. Sharma and M. Kaur, "Classification in Pattern Recognition: A Review," *Int. J. Adv. Res. Comput. Sci. Softw. Eng.*, vol. 3, no. 4, pp. 2277–128, 2013.

[40]   M. Z. Alom *et al.*, "The History Began from AlexNet: A Comprehensive Survey on Deep Learning Approaches," 2018, [Online]. Available: http://arxiv.org/abs/1803.01164.

[41]   M. Somvanshi, P. Chavan, S. Tambade, and S. V. Shinde, "A review of machine learning techniques using decision tree and support vector machine," *Proc. - 2nd Int. Conf. Comput. Commun. Control Autom. ICCUBEA 2016*, 2017, doi: 10.1109/ICCUBEA.2016.7860040.

[42]   P. Senin, "Dynamic Time Warping Algorithm Review," *Science (80-.).*, vol. 2007, no. December, pp. 1–23, 2008, [Online]. Available: http://129.173.35.31/~pf/Linguistique/Treillis/ReviewDTW.pdf.

[43]   M. Yadav and M. A. Alam, "Dynamic Time Warping (DTW) Algorithm In Speech: A Review," *Int. J. Res. Electron. Comput. Eng.*, vol. 6, no. 1, pp. 524–528, 2018.

[44]   B. Mor, S. Garhwal, and A. Kumar, "A Systematic Review of Hidden Markov Models and Their Applications," *Arch. Comput. Methods Eng.*, vol. 28, no. 3, pp. 1429–1448, 2021, doi: 10.1007/s11831-020-09422-4.

[45]   I. Rish, "An empirical study of the naive Bayes classifier," *IJCAI Work. Emperical Methods Artif. Intell.*, pp. 41–46, 2001.

[46]   I. T. Jollife and J. Cadima, "Principal component analysis: A review and recent developments," *Philos. Trans. R. Soc. A Math. Phys. Eng. Sci.*, vol. 374, no. 2065, 2016, doi: 10.1098/rsta.2015.0202.

[47]   S. Simske, *META-ALGORITHMICS*. Wiley, 2013.

[48]   M. Vrigkas, C. Nikou, and I. A. Kakadiaris, "A review of human activity recognition methods," *Frontiers Robotics AI*, vol. 2, no. NOV. 2015, doi: 10.3389/frobt.2015.00028.

[49]   O. C. Ann and L. B. Theng, "Human activity recognition: A review," *Proc. - 4th IEEE Int. Conf. Control Syst. Comput. Eng. ICCSCE 2014*, no. November, pp. 389–393, 2014, doi: 10.1109/ICCSCE.2014.7072750.

[50] C. Jobanputra, J. Bavishi, and N. Doshi, "Human activity recognition: A survey," *Procedia Comput. Sci.*, vol. 155, no. 2018, pp. 698–703, 2019, doi: 10.1016/j.procs.2019.08.100.

[51] A. Das Antar, M. Ahmed, and M. A. R. Ahad, "Challenges in sensor-based human activity recognition and a comparative analysis of benchmark datasets: A review," *2019 Jt. 8th Int. Conf. Informatics, Electron. Vision, ICIEV 2019 3rd Int. Conf. Imaging, Vis. Pattern Recognition, icIVPR 2019 with Int. Conf. Act. Behav. Comput. ABC 2019*, pp. 134–139, 2019, doi: 10.1109/ICIEV.2019.8858508.

[52] E. Ramanujam, T. Perumal, and S. Padmavathi, "Human Activity Recognition with Smartphone and Wearable Sensors Using Deep Learning Techniques: A Review," *IEEE Sens. J.*, vol. 21, no. 12, pp. 1309–13040, 2021, doi: 10.1109/JSEN.2021.3069927.

[53] C. Prandi and J. M. Marquez-Barja, *Smart Objects and Technologies for Social Good*, vol. 26, no. 5. 2021.

[54] H. M. L. Minh Dang, Kyungbok Min, Hanxiang Wang, Md. Jalil Piran, Cheol Hee Lee, "Sensor-based and vision-based human activity recognition_ A comprehensive survey _ Elsevier Enhanced Reader.pdf." Elsevier, 2020.

[55] Timo Pylvänäinen, "Accelerometer Based Gesture Recognition Using Continuous HMMs," in *Lecture Notes in Computer Science (including subseries Lecture Notes in Artificial Intelligence and Lecture Notes in Bioinformatics)*, Vol. 3522., 2005, pp. 639–646.

[56] B. Hartmann and N. Link, "Gesture recognition with inertial sensors and optimized DTW prototypes," *Conf. Proc. - IEEE Int. Conf. Syst. Man Cybern.*, pp. 2102–2109, 2010, doi: 10.1109/ICSMC.2010.5641703.

[57] S. L. Jiahui Wu, Gang Pan, Daqing Zhang, Guande Qi, "Gesture Recognition with a 3-D Accelerometer," in *International Conference on Ubiquitous Intelligence and Computing*, 2009, pp. 25–38.

[58] R. M. Stephenson, G. R. Naik, and R. Chai, "A system for accelerometer-based gesture classification using artificial neural networks," *Proc. Annu. Int. Conf. IEEE Eng. Med. Biol. Soc. EMBS*, pp. 4187–4190, 2017, doi: 10.1109/EMBC.2017.8037779.

[59] R. Xie and J. Cao, "Accelerometer-Based Hand Gesture Recognition by Neural Network and Similarity Matching," *IEEE Sens. J.*, vol. 16, no. 11, pp. 4537–4545, 2016, doi: 10.1109/JSEN.2016.2546942.

[60] S. Lu, Z. Lu, and Y. D. Zhang, "Pathological brain detection based on AlexNet and transfer learning," *Journal of Computational Science*, vol. 30. pp. 41–47, 2019, doi: 10.1016/j.jocs.2018.11.008.

[61] P. Ballester and R. M. Araujo, "On the performance of googlenet and alexnet applied to sketches," *30th AAAI Conf. Artif. Intell. AAAI 2016*, no. May, pp. 1124–1128, 2016.

[62]   S. Bosch *et al.*, "Equimoves: A wireless networked inertial measurement system for objective examination of horse gait," *Sensors (Switzerland)*, vol. 18, no. 3. 2018, doi: 10.3390/s18030850.

[63]   J. J. Robilliard, T. Pfau, and A. M. Wilson, "Gait characterisation and classification in horses," *J. Exp. Biol.*, vol. 210, no. 2, pp. 187–197, 2007, doi: 10.1242/jeb.02611.

[64]   M. A. F. Lopes *et al.*, "An attempt to detect lameness in galloping horses by use of body-mounted inertial sensors," *Am. J. Vet. Res.*, vol. 77, no. 10, pp. 1121–1131, 2016, doi: 10.2460/ajvr.77.10.1121.

[65]   R. Gutierrez-Osuna and H. T. Nagle, "A method for evaluating data-preprocessing techniques for odor classification with an array of gas sensors," *IEEE Trans. Syst. Man, Cybern. Part B Cybern.*, vol. 29, no. 5, pp. 626–632, 1999, doi: 10.1109/3477.790446.

[66]   A. Perera, T. Sundic, A. Pardo, R. Gutierrez-Osuna, and S. Marco, "A portable electronic nose based on embedded PC technology and GNU/Linux: Hardware, software and applications," *IEEE Sens. J.*, vol. 2, no. 3, pp. 235–246, 2002, doi: 10.1109/JSEN.2002.800683.

[67]   A. Solórzano *et al.*, "Multi-unit calibration rejects inherent device variability of chemical sensor arrays," *Sensors and Actuators, B: Chemical*, vol. 265. pp. 142–154, 2018, doi: 10.1016/j.snb.2018.02.188.

[68]   J. Chaki, N. Dey, F. Shi, and R. Simon Sherratt, "Pattern Mining Approaches Used in Sensor-Based Biometric Recognition: A Review," *IEEE Sens. J.*, vol. 19, no. 10, pp. 3569–3580, 2019, doi: 10.1109/JSEN.2019.2894972.

[69]   J. Fierrez, A. Morales, R. Vera-Rodriguez, and D. Camacho, "Multiple classifiers in biometrics. part 1: Fundamentals and review," *Information Fusion*, vol. 44. pp. 57–64, 2018, doi: 10.1016/j.inffus.2017.12.003.

[70]   U. Gawande and Y. Golhar, "Biometric security system: A rigorous review of unimodal and multimodal biometrics techniques," *Int. J. Biom.*, vol. 10, no. 2, pp. 142–175, 2018, doi: 10.1504/IJBM.2018.091629.

[71]   A. P. Medicine, "Moving Beyond Population Averages," no. August, 2020.

[72]   W. Anderson and S. J. Simske, "At-Home Healthcare through Smart-Environmental Sensing, including Biometrics for Multi-Factor Authentication," *2020 IEEE Int. Conf. Healthc. Informatics, ICHI 2020*, 2020, doi: 10.1109/ICHI48887.2020.9374337.

[73]   M. A. G. Wallace and J. D. Pleil, "Evolution of clinical and environmental health applications of exhaled breath research: Review of methods and instrumentation for gas-phase, condensate, and aerosols," *Anal. Chim. Acta*, vol. 1024, pp. 18–38, 2018, doi: 10.1016/j.aca.2018.01.069.

[74] M. Righettoni, A. Amann, and S. E. Pratsinis, "Breath analysis by nanostructured metal oxides as chemo-resistive gas sensors," *Mater. Today*, vol. 18, no. 3, pp. 163–171, 2015, doi: 10.1016/j.mattod.2014.08.017.

[75] A. T. Güntner, S. Abegg, K. Königstein, P. A. Gerber, A. Schmidt-Trucksäss, and S. E. Pratsinis, "Breath sensors for health monitoring," *ACS Sensors*, vol. 4, no. 2, pp. 268–280, 2019, doi: 10.1021/acssensors.8b00937.

[76] J. W. Yoon and J. H. Lee, "Toward breath analysis on a chip for disease diagnosis using semiconductor-based chemiresistors: Recent progress and future perspectives," *Lab Chip*, vol. 17, no. 21, pp. 3537–3557, 2017, doi: 10.1039/c7lc00810d.

[77] H. Tai, S. Wang, Z. Duan, and Y. Jiang, "Evolution of breath analysis based on humidity and gas sensors: Potential and challenges," *Sensors Actuators, B Chem.*, vol. 318, no. April, p. 128104, 2020, doi: 10.1016/j.snb.2020.128104.

[78] J. Pereira *et al.*, "Breath analysis as a potential and non-invasive frontier in disease diagnosis: An overview," *Metabolites*, vol. 5, no. 1, pp. 3–55, 2015, doi: 10.3390/metabo5010003.

[79] T. Saidi *et al.*, "Non-invasive prediction of lung cancer histological types through exhaled breath analysis by UV-irradiated electronic nose and GC/QTOF/MS," *Sensors Actuators, B Chem.*, vol. 311, no. February, 2020, doi: 10.1016/j.snb.2020.127932.

[80] J. Horáček, V. Koucký, and M. Hladík, "Novel approach to computerized breath detection in lung function diagnostics," *Comput. Biol. Med.*, vol. 101, no. March, pp. 1–6, 2018, doi: 10.1016/j.compbiomed.2018.07.017.

[81] L. Ali, C. Zhu, M. Zhou, and Y. Liu, "Early diagnosis of Parkinson's disease from multiple voice recordings by simultaneous sample and feature selection," *Expert Syst. Appl.*, vol. 137, pp. 22–28, 2019, doi: 10.1016/j.eswa.2019.06.052.

[82] J. H. Rhonda, J. M. Oates, J. P. Debbie, and J. H. Andrew, "Voice characteristics in the progression of Parkinson's disease," *Int. J. Lang. Commun. Disord.*, vol. 35, no. 3, pp. 407–418, 2000, doi: 10.1080/136828200410654.

[83] A. U. Haq *et al.*, "Feature Selection Based on L1-Norm Support Vector Machine and Effective Recognition System for Parkinson's Disease Using Voice Recordings," *IEEE Access*, vol. 7, pp. 37718–37734, 2019, doi: 10.1109/ACCESS.2019.2906350.

[84] L. Naranjo, C. J. Pérez, Y. Campos-Roca, and J. Martín, "Addressing voice recording replications for Parkinson's disease detection," *Expert Syst. Appl.*, vol. 46, pp. 286–292, 2016, doi: 10.1016/j.eswa.2015.10.034.

[85] A. Benba, A. Jilbab, and A. Hammouch, "Analysis of multiple types of voice recordings in cepstral domain using MFCC for discriminating between patients with Parkinson's disease

and healthy people," *Int. J. Speech Technol.*, vol. 19, no. 3, pp. 449–456, 2016, doi: 10.1007/s10772-016-9338-4.

[86] A. König *et al.*, "Automatic speech analysis for the assessment of patients with predementia and Alzheimer's disease," *Alzheimer's Dement. Diagnosis, Assess. Dis. Monit.*, vol. 1, no. 1, pp. 112–124, 2015, doi: 10.1016/j.dadm.2014.11.012.

[87] O. H. Olga Kamińska, Katarzyna Kaczmarek-Majer, Karol Opara, Wit Jakuczun, Monika Dominiak, Anna Antosik-Wójcińska, Łukasz Święcicki, "Self-organizing Maps Using Acoustic Features for Prediction of State Change in Bipolar Disorder," in *Artificial Intelligence in Medicine*, 2019, pp. 148–160.

[88] X. Wang, J. Zhang, and Y. Yan, "Discrimination between pathological and normal voices using GMM-SVM approach," *J. Voice*, vol. 25, no. 1, pp. 38–43, 2011, doi: 10.1016/j.jvoice.2009.08.002.

[89] J. D. Arias-Londoño, J. I. Godino-Llorente, N. Sáenz-Lechón, V. Osma-Ruiz, and G. Castellanos-Domínguez, "Automatic detection of pathological voices using complexity measures, noise parameters, and mel-cepstral coefficients," *IEEE Trans. Biomed. Eng.*, vol. 58, no. 2, pp. 370–379, 2011, doi: 10.1109/TBME.2010.2089052.

[90] J. D. Arias-Londoño, J. I. Godino-Llorente, N. Sáenz-Lechón, V. Osma-Ruiz, and G. Castellanos-Domínguez, "An improved method for voice pathology detection by means of a HMM-based feature space transformation," *Pattern Recognit.*, vol. 43, no. 9, pp. 3100–3112, 2010, doi: 10.1016/j.patcog.2010.03.019.

[91] C. Brown *et al.*, "Exploring Automatic Diagnosis of COVID-19 from Crowdsourced Respiratory Sound Data," pp. 3474–3484, 2020, doi: 10.1145/3394486.3412865.

[92] B. Lei, S. A. Rahman, and I. Song, "Content-based classification of breath sound with enhanced features," *Neurocomputing*, vol. 141, pp. 139–147, 2014, doi: 10.1016/j.neucom.2014.04.002.

[93] A. Akbari and M. K. Arjmandi, "An efficient voice pathology classification scheme based on applying multi-layer linear discriminant analysis to wavelet packet-based features," *Biomed. Signal Process. Control*, vol. 10, no. 1, pp. 209–223, 2014, doi: 10.1016/j.bspc.2013.11.002.

[94] J. Poore, "Calibration system for pacemaker-generated intracardiac electrogram," 5,620,473, 1997.

[95] A. Gaurav, M. Maheedhar, V. N. Tiwari, and R. Narayanan, "Cuff-less PPG based continuous blood pressure monitoring - A smartphone based approach," *Proc. Annu. Int. Conf. IEEE Eng. Med. Biol. Soc. EMBS*, vol. 2016-Octob, no. c, pp. 607–610, 2016, doi: 10.1109/EMBC.2016.7590775.

[96] P. Kakria, N. K. Tripathi, and P. Kitipawang, "A real-time health monitoring system for remote cardiac patients using smartphone and wearable sensors," *Int. J. Telemed. Appl.*, vol. 2015, 2015, doi: 10.1155/2015/373474.

[97] Y. S. Can, N. Chalabianloo, D. Ekiz, and C. Ersoy, "Continuous stress detection using wearable sensors in real life: Algorithmic programming contest case study," *Sensors (Switzerland)*, vol. 19, no. 8, 2019, doi: 10.3390/s19081849.

[98] A. Paraschiv-Ionescu, C. J. Newman, L. Carcreff, C. N. Gerber, S. Armand, and K. Aminian, "Correction: Locomotion and cadence detection using a single trunk-fixed accelerometer: Validity for children with cerebral palsy in daily life-like conditions (Journal of NeuroEngineering and Rehabilitation DOI: 10.1186/s12984-019-0494-z)," *J. Neuroeng. Rehabil.*, vol. 16, no. 1, pp. 1–11, 2019, doi: 10.1186/s12984-019-0498-8.

[99] X. Chen, S. Liao, S. Cao, D. Wu, and X. Zhang, "An acceleration-based gait assessment method for children with cerebral palsy," *Sensors (Switzerland)*, vol. 17, no. 5, pp. 1–18, 2017, doi: 10.3390/s17051002.

[100] A. Behboodi, N. Zahradka, H. Wright, J. Alesi, and S. C. K. Lee, "Real-time detection of seven phases of gait in children with cerebral palsy using two gyroscopes," *Sensors (Switzerland)*, vol. 19, no. 11, pp. 7–11, 2019, doi: 10.3390/s19112517.

[101] A. Laudanski, B. Brouwer, and Q. Li, "Activity classification in persons with stroke based on frequency features," *Med. Eng. Phys.*, vol. 37, no. 2, pp. 180–186, 2015, doi: 10.1016/j.medengphy.2014.11.008.

[102] J. J. G. Sara Garcia de Villa, Ana Jiménez Martín, "A Biomechanical Model Implementation for Upper-Limbs Rehabilitation Monitoring Using IMUs," in *Bioinformatics and Biomedical Engineering*, 2019, pp. 351–362.

[103] X. Liu, Z. Zhou, and Q. Wang, "Real-Time Onboard Human Motion Recognition Based on Inertial Measurement Units," *8th Annu. IEEE Int. Conf. Cyber Technol. Autom. Control Intell. Syst. CYBER 2018*, pp. 724–728, 2019, doi: 10.1109/CYBER.2018.8688093.

[104] C. J. Chen, Y. T. Lin, C. C. Lin, Y. C. Chen, Y. J. Lee, and C. Y. Wang, "Rehabilitation System for Limbs using IMUs," *Proc. - Int. Symp. Qual. Electron. Des. ISQED*, vol. 2020-March, pp. 285–291, 2020, doi: 10.1109/ISQED48828.2020.9137026.

[105] O. Reich, E. Hubner, B. Ghita, M. F. Wagner, and J. Schafer, "A Survey Investigating the Combination and Number of IMUs on the Human Body Used for Detecting Activities and Human Tracking," pp. 20–27, 2020, doi: 10.1109/wccct49810.2020.9170009.

[106] R. B. Hetland *et al.*, "Release of inflammatory cytokines, cell toxicity and apoptosis in epithelial lung cells after exposure to ambient air particles of different size fractions," *Toxicol. Vitr.*, vol. 18, no. 2, pp. 203–212, 2004, doi: 10.1016/S0887-2333(03)00142-5.

[107] S. Martin, L. Dawidowski, P. Mandalunis, F. Cereceda-Balic, and D. R. Tasat, "Characterization and biological effect of Buenos Aires urban air particles on mice lungs," *Environ. Res.*, vol. 105, no. 3, pp. 340–349, 2007, doi: 10.1016/j.envres.2007.04.009.

[108] J. O. Anderson, J. G. Thundiyil, and A. Stolbach, "Clearing the Air: A Review of the Effects of Particulate Matter Air Pollution on Human Health," *J. Med. Toxicol.*, vol. 8, no. 2, pp. 166–175, 2012, doi: 10.1007/s13181-011-0203-1.

[109] A. Ghorani-Azam, B. Riahi-Zanjani, and M. Balali-Mood, "Effects of air pollution on human health and practical measures for prevention in Iran," *Journal of Research in Medical Sciences*, vol. 21, no. 5. 2016, doi: 10.4103/1735-1995.189646.

[110] J. Saini, M. Dutta, and G. Marques, "Sensors for indoor air quality monitoring and assessment through Internet of Things: a systematic review," *Environ. Monit. Assess.*, vol. 193, no. 2, 2021, doi: 10.1007/s10661-020-08781-6.

[111] A. C. Weaver, "Biometric authentication," *Computer (Long. Beach. Calif).*, vol. 39, no. 2, pp. 96–97, 2006, doi: 10.1109/MC.2006.47.

[112] W. Zhao, Y. Gao, and R. Singh, "Speaker identification from the sound of the human breath," 2017, [Online]. Available: http://arxiv.org/abs/1712.00171.

[113] D. M. B. Reisfeld, S. Simske, W. Anderson, "Magic Wand Appliance to Help Engage Popular Epidemiology," USPTO assigned Application No. 62/947,956, 2019.

[114] R. B. Jones, M. N. K. Boulos, S. Wheeler, C. Tavares, and R. Jones, "Kamel Boulos , M . N ., et al .: How smartphones are changing the face of mobile and participatory healthcare : an overview , with example from eCAALYX . Biomedical Engineering Online 10 ,... How smartphones are changing the face of mobile and participato," *Biomed. Eng. Online*, no. July 2016, pp. 1–14, 2011, doi: 10.1186/1475-925X-10-24.

[115] R. Yasir, "Two-Handed Hand Gesture Recognition for Bangla Sign Language using LDA and ANN," pp. 7–11, 2014.

[116] X. Zhang, X. Chen, Y. Li, V. Lantz, K. Wang, and J. Yang, "A framework for hand gesture recognition based on accelerometer and EMG sensors," *IEEE Trans. Syst. Man, Cybern. Part ASystems Humans*, vol. 41, no. 6, pp. 1064–1076, 2011, doi: 10.1109/TSMCA.2011.2116004.

[117] T. Starner and A. Pentland, "Real-time American Sign Language recognition from video using Hidden Markov models," *Proc. IEEE Int. Conf. Comput. Vis.*, pp. 265–270, 1995, doi: 10.1109/iscv.1995.477012.

[118] F. H. K. Z. Muhammad Fawwaz Ab Hamid, "Hand Gesture Recognition Using Movidius Neural Compute Stick," in *IEEE 9th International Conference on System Engineering and Technology*, 2019.

[119] W. Lu, Z. Tong, and J. Chu, "Dynamic Hand Gesture Recognition with Leap Motion Controller," in *IEEE Signal Processing Letters*, 2016, vol. 23, no. 9, pp. 1188–1192.

[120] P. Narayana, J. R. Beveridge, and B. A. Draper, "Gesture Recognition: Focus on the Hands," *Proc. IEEE Comput. Soc. Conf. Comput. Vis. Pattern Recognit.*, pp. 5235–5244, 2018, doi: 10.1109/CVPR.2018.00549.

[121] J. M. Carmona and J. Climent, "A performance evaluation of HMM and DTW for gesture recognition," *Lect. Notes Comput. Sci. (including Subser. Lect. Notes Artif. Intell. Lect. Notes Bioinformatics)*, vol. 7441 LNCS, pp. 236–243, 2012, doi: 10.1007/978-3-642-33275-3_29.

[122] M. Kim, J. Cho, S. Lee, and Y. Jung, "IMU sensor-based hand gesture recognition for human-machine interfaces," *Sensors (Switzerland)*, vol. 19, no. 18, pp. 1–13, 2019, doi: 10.3390/s19183827.

[123] G. Serra, M. Camurri, L. Baraldi, M. Benedetti, and R. Cucchiara, "Hand segmentation for gesture recognition in EGO-vision," *IMMPD 2013 - Proc. 3rd ACM Int. Work. Interact. Multimed. Mob. Portable Devices, Co-located with ACM Multimed. 2013*, pp. 31–36, 2013, doi: 10.1145/2505483.2505490.

[124] G. R. Naik, D. K. Kumar, and Jayadeva, "Twin SVM for gesture classification using the surface electromyogram," *IEEE Trans. Inf. Technol. Biomed.*, vol. 14, no. 2, pp. 301–308, 2010, doi: 10.1109/TITB.2009.2037752.

[125] F. Moiz, P. Natoo, R. Derakhshani, and W. D. Leon-Salas, "A comparative study of classification methods for gesture recognition using a 3-axis accelerometer," *Proc. Int. Jt. Conf. Neural Networks*, pp. 2479–2486, 2011, doi: 10.1109/IJCNN.2011.6033541.

[126] J. A. P. Ari Y. Benbasat, "An Inertial Measurement Framework for Gesture Recognition and Applications," in *International Gesture Workshop:Gesture and Sign Language in Human-Computer Interaction*, 2001, pp. 9–20.

[127] K. Nakano and B. Chakraborty, "Effect of Data Representation for Time Series Classification—A Comparative Study and a New Proposal," *Mach. Learn. Knowl. Extr.*, vol. 1, no. 4, pp. 1100–1120, 2019, doi: 10.3390/make1040062.

[128] S. S. Wes Anderson, Adam Morrone, Jorge Ángel González-Ordiano, "A Handheld Device for Intentional Sensing of Environmental Analytes," in *Rocky Mountain Bioengineering Symposium*, 2020.

[129] K. B. Duan and S. S. Keerthi, "Which is the best multiclass SVM method? An empirical study," *Lect. Notes Comput. Sci.*, vol. 3541, pp. 278–285, 2005, doi: 10.1007/11494683_28.

[130] V. N. Vapnik, "An overview of statistical learning theory," *IEEE Trans. Neural Networks*, vol. 10, no. 5, pp. 988–999, 1999, doi: 10.1109/72.788640.

[131] D. Figo, P. C. Diniz, D. R. Ferreira, and J. M. P. Cardoso, "Preprocessing techniques for context recognition from accelerometer data," *Pers. Ubiquitous Comput.*, vol. 14, no. 7, pp. 645–662, 2010, doi: 10.1007/s00779-010-0293-9.

[132] H. van Meir, "Developmental differences in drawing performanceof the dominant and non-dominant hand in right-handed boys and girls," *Hum. Mov. Sci.*, vol. 25, pp. 657–677, 2006.

[133] A. E. F. Da Gama *et al.*, "MirrARbilitation: A clinically-related gesture recognition interactive tool for an AR rehabilitation system," *Comput. Methods Programs Biomed.*, vol. 135, pp. 105–114, 2016, doi: 10.1016/j.cmpb.2016.07.014.

Appendix A
Additional Figures
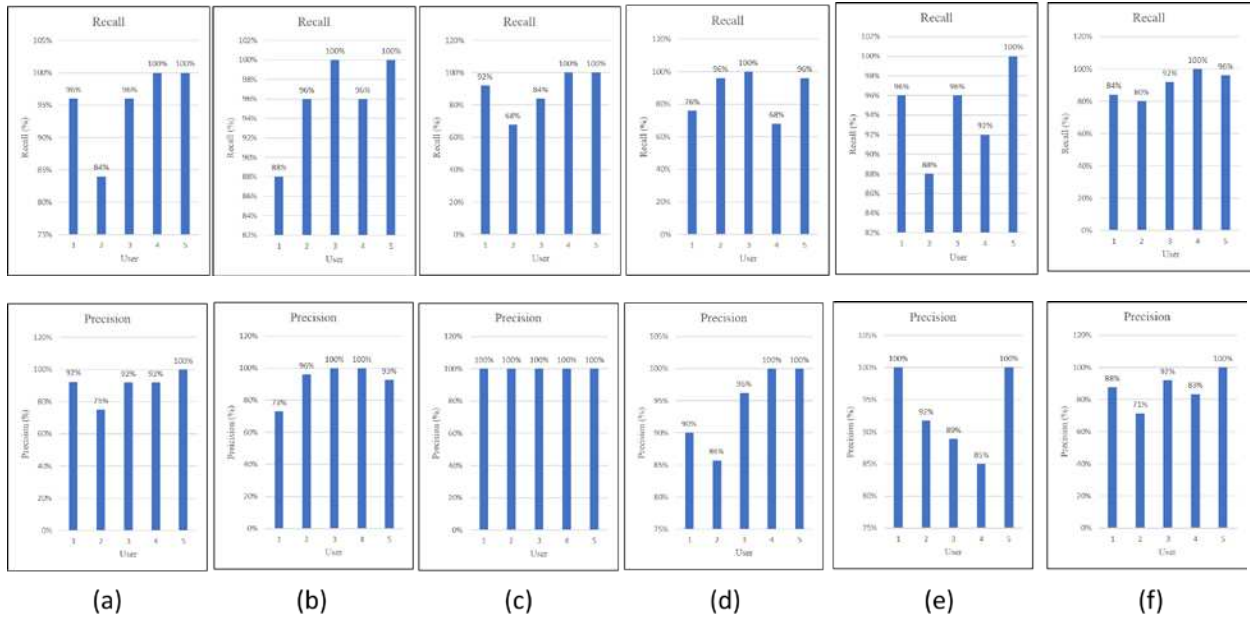
Figure A.1: Precision and recall of each gesture recognition. (a) xmovements, (b) y-movements, (c) z-movements, (d) yzmovements, (e) xz-movements, and (f) xy-movements.
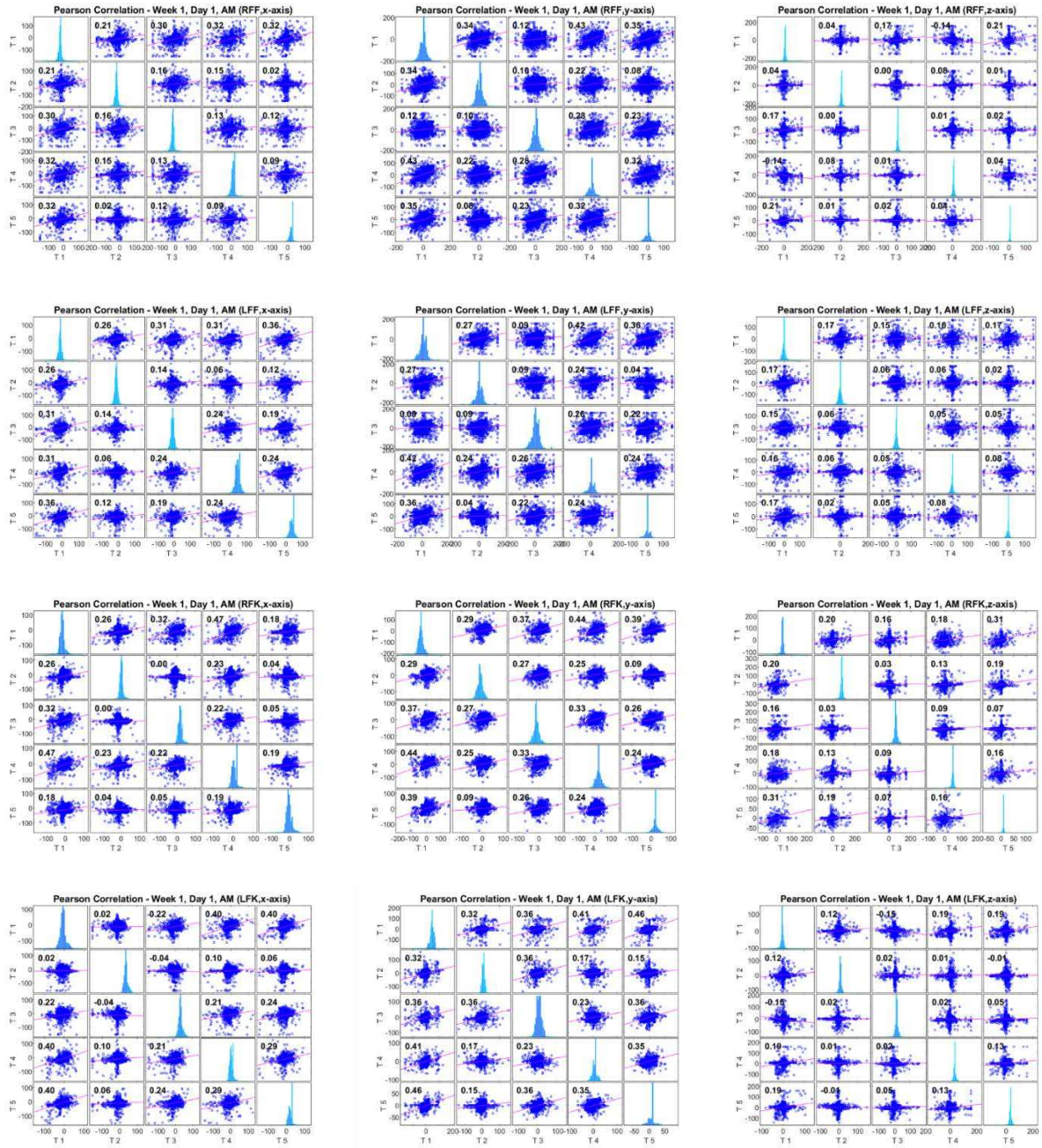
Figure A.2: Pearson Correlation Coefficients - Week 1, Day 1, AM.

Figure A.3: Pearson Correlation Coefficients - Week 1, Day 2, AM.
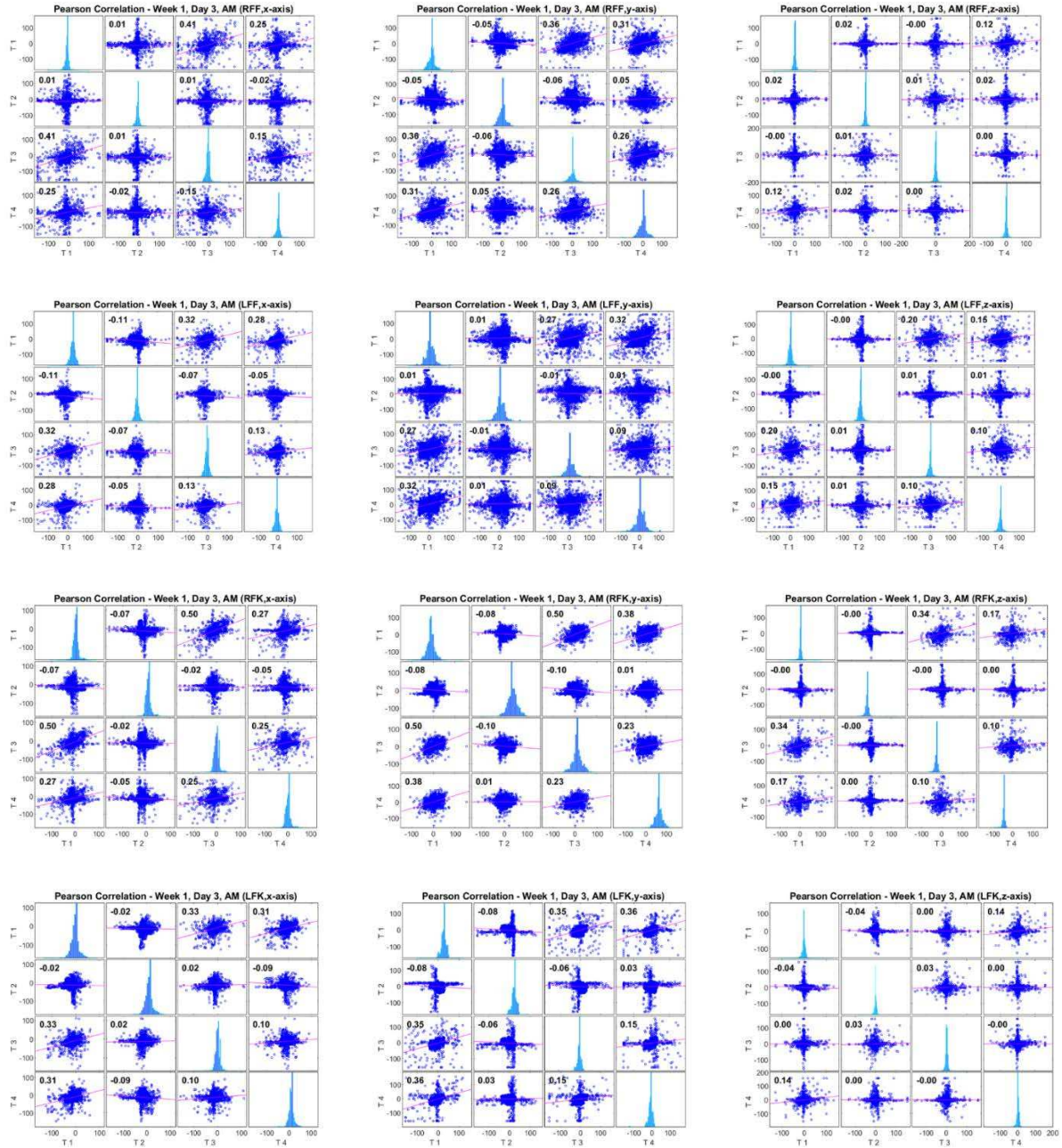
Figure A.4: Pearson Correlation Coefficients - Week 1, Day 3, AM.
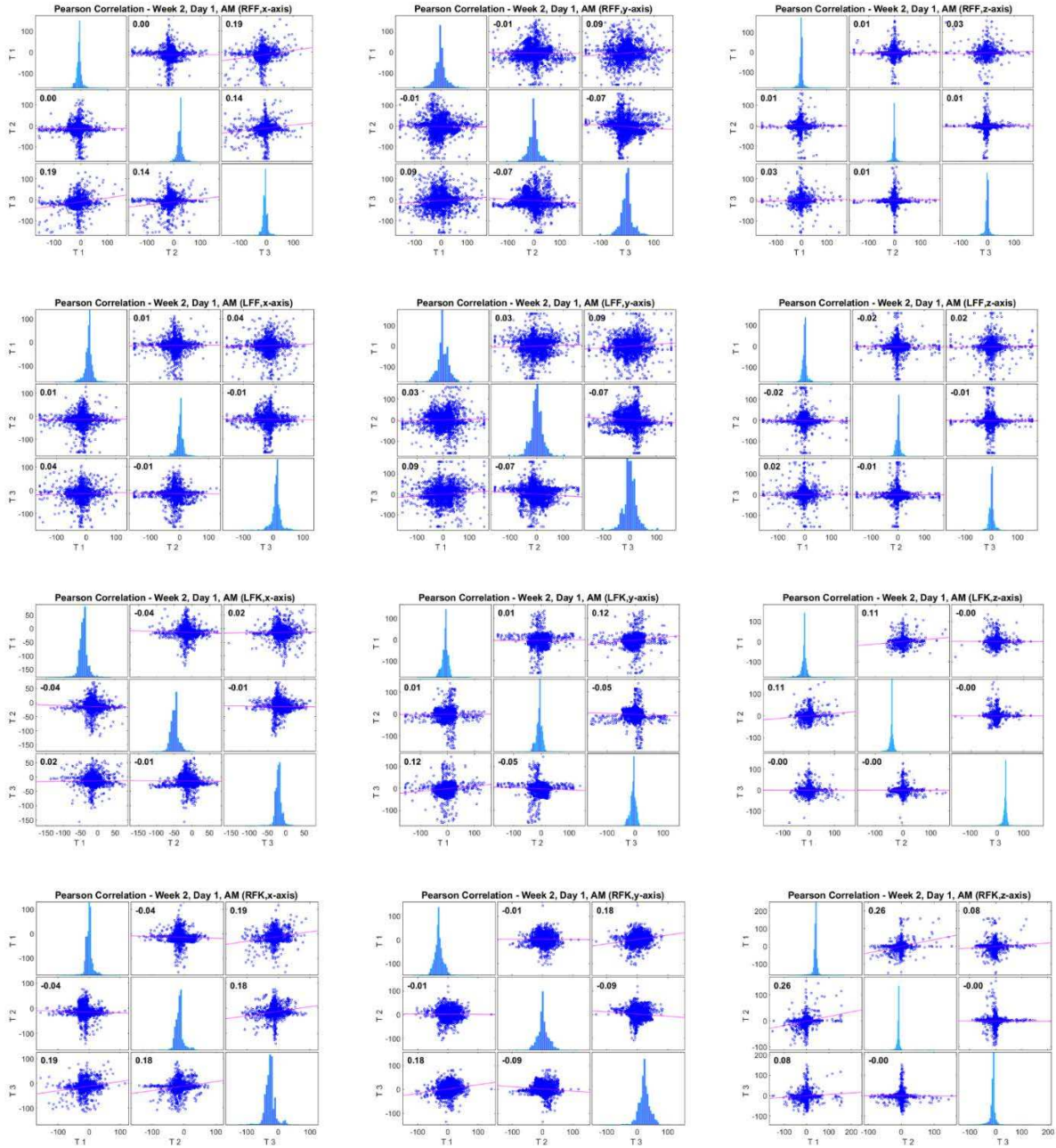
Figure A.5: Pearson Correlation Coefficients - Week 2, Day 1, AM.
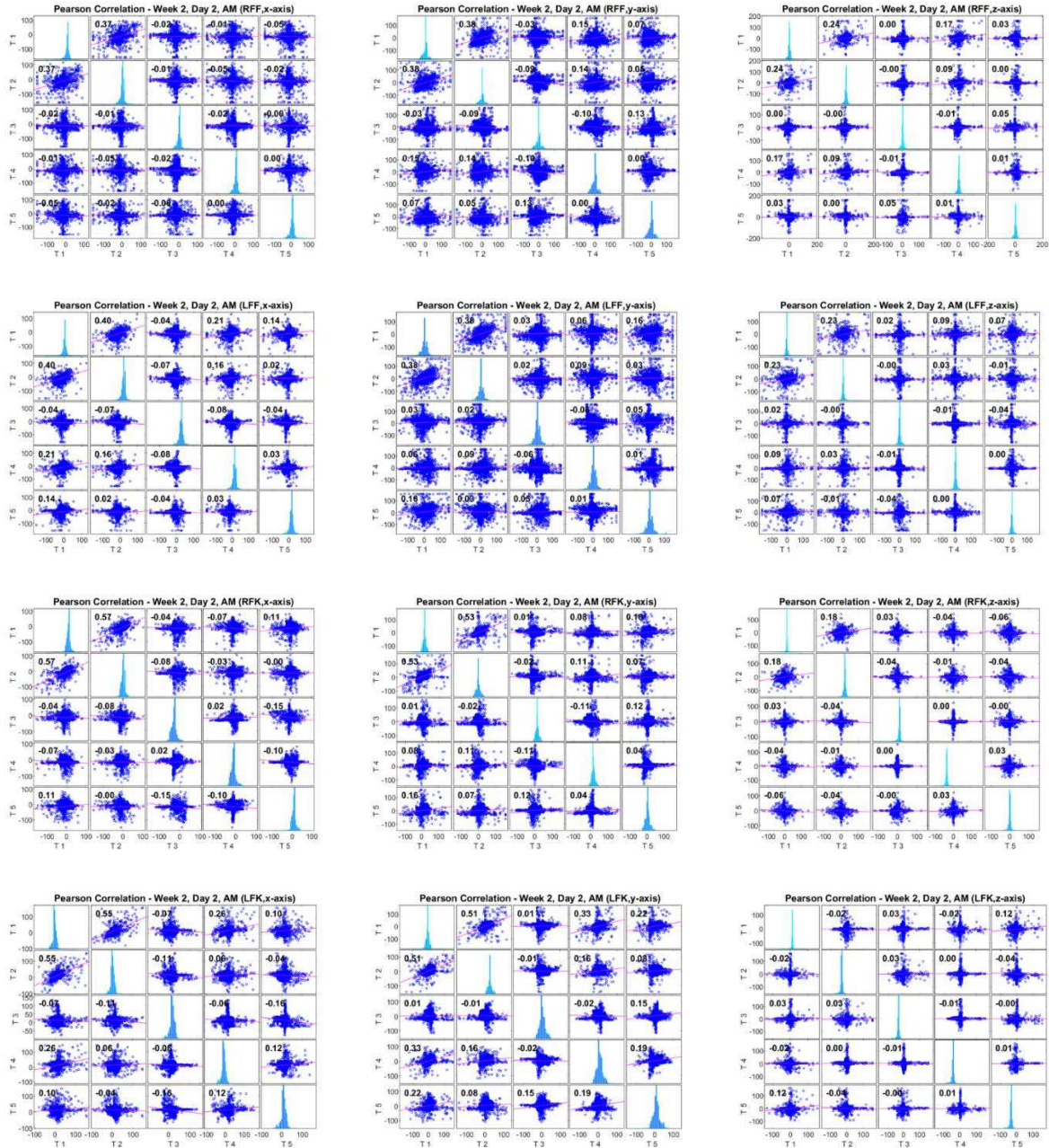
Figure A.6: Pearson Correlation Coefficients - Week 2, Day 2, AM.
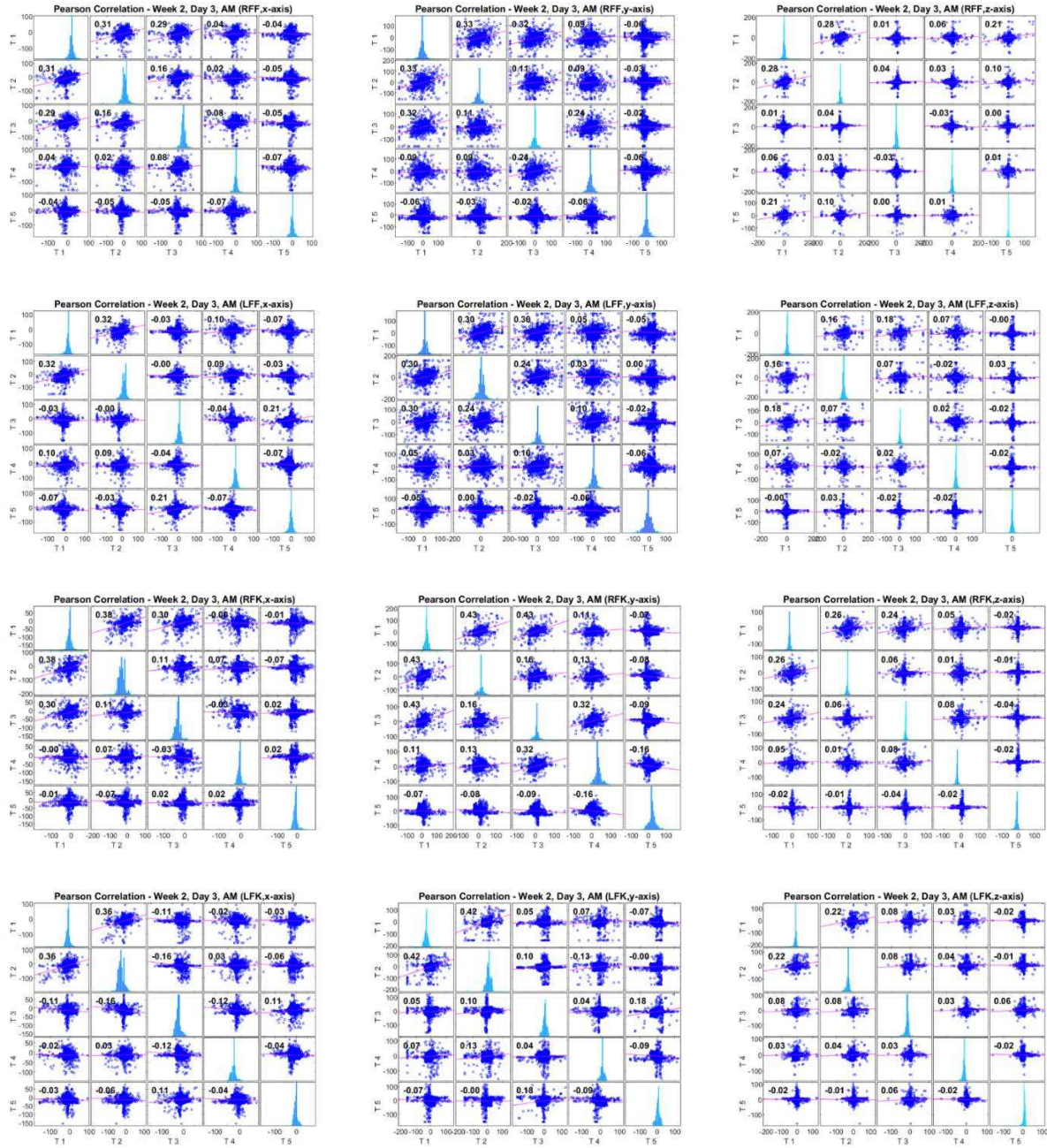
Figure A.7: Pearson Correlation Coefficients - Week 2, Day 3, AM.
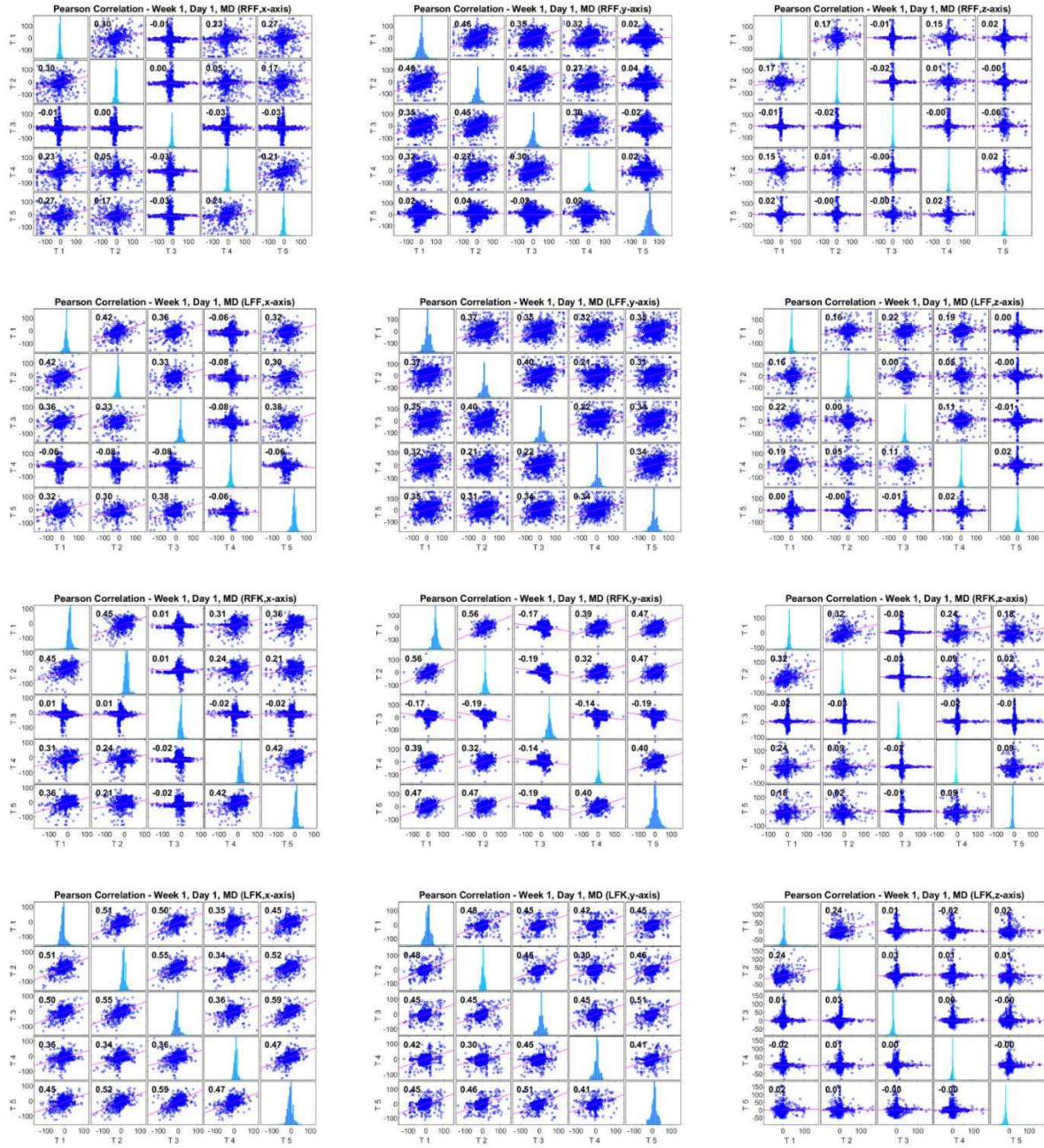
Figure A.8: Pearson Correlation Coefficients - Week 1, Day 1, MD.
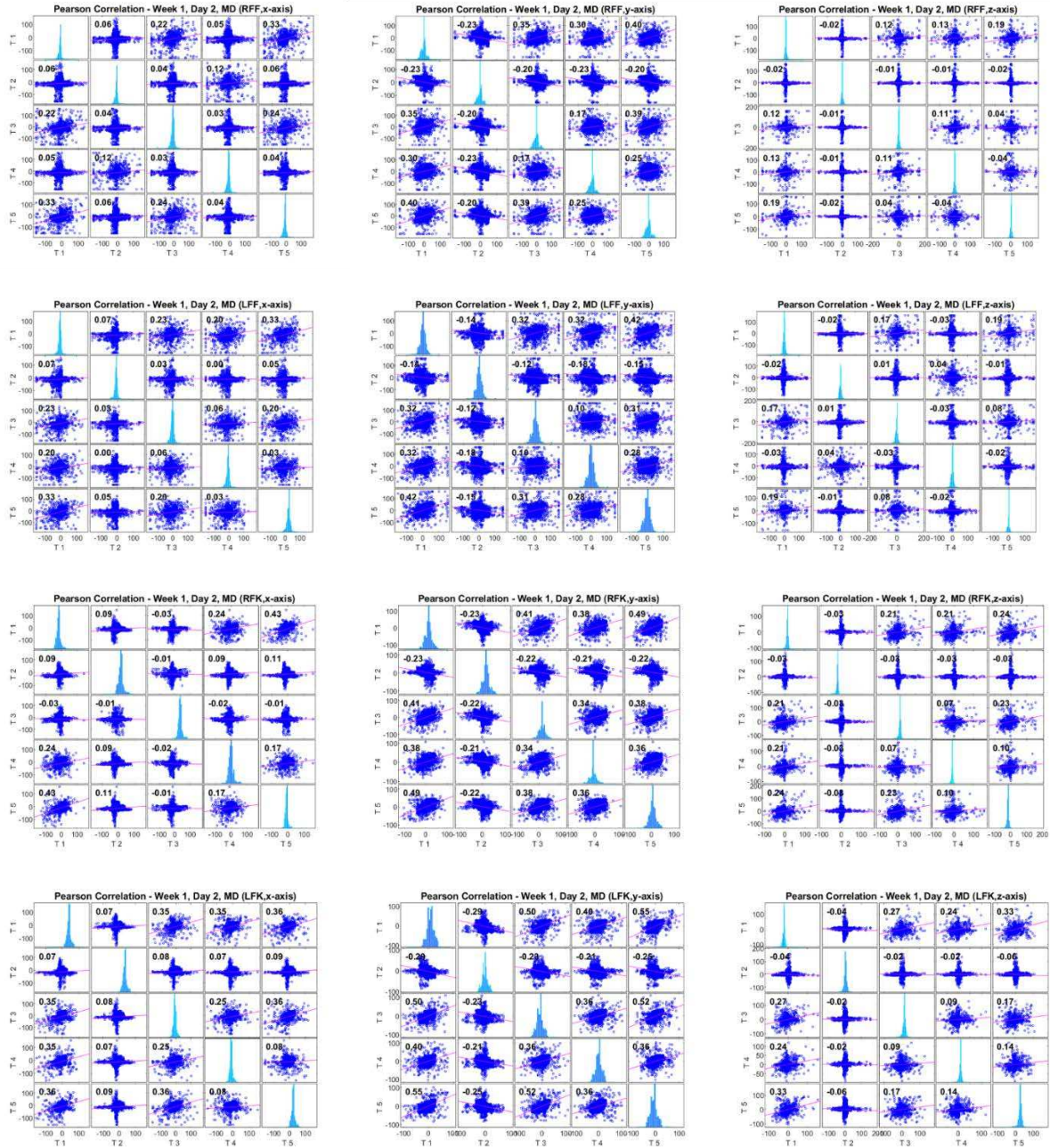
Figure A.9: Pearson Correlation Coefficients - Week 1, Day 2, MD.
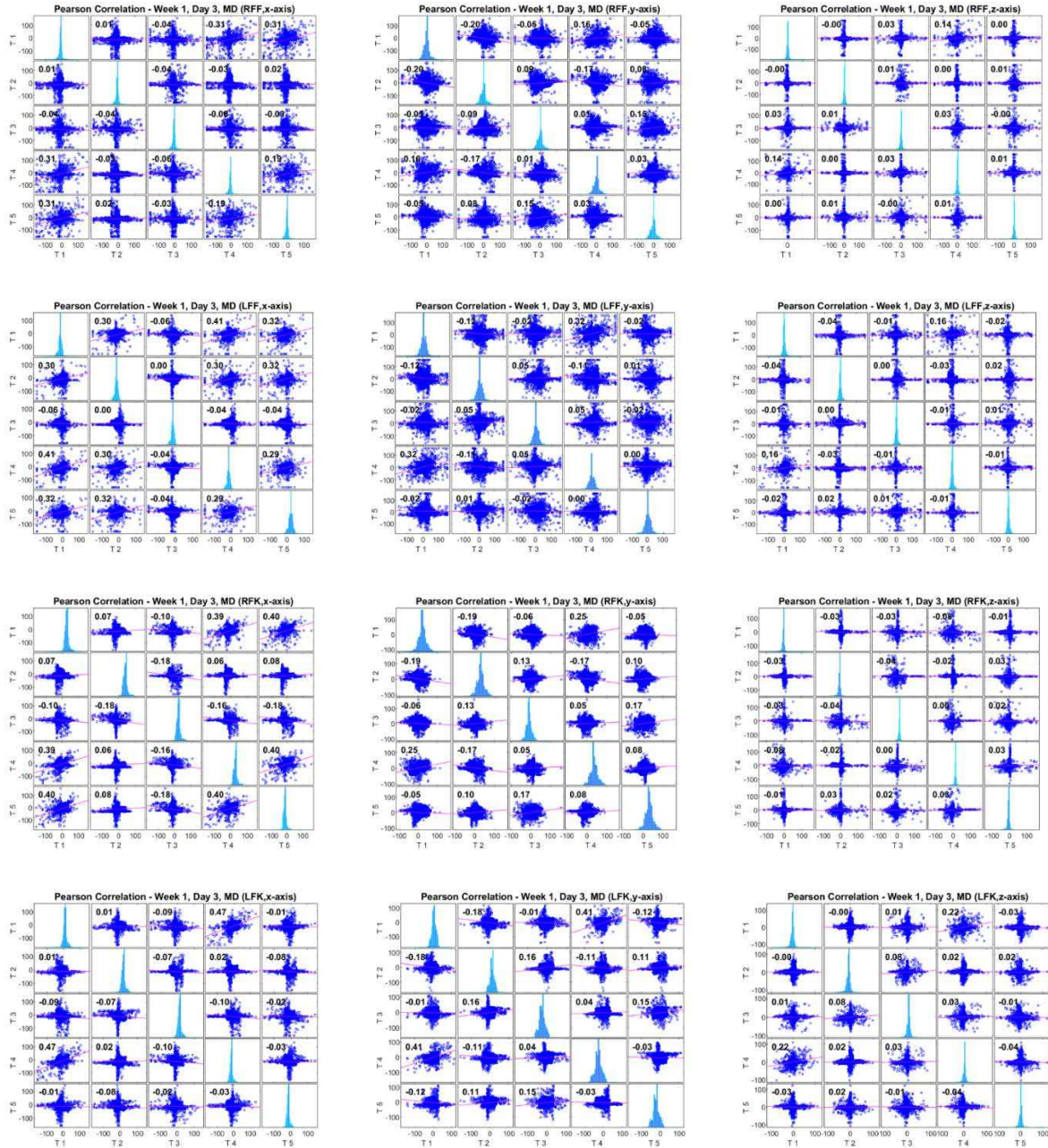
Figure A.10: Pearson Correlation Coefficients - Week 1, Day 3, MD.
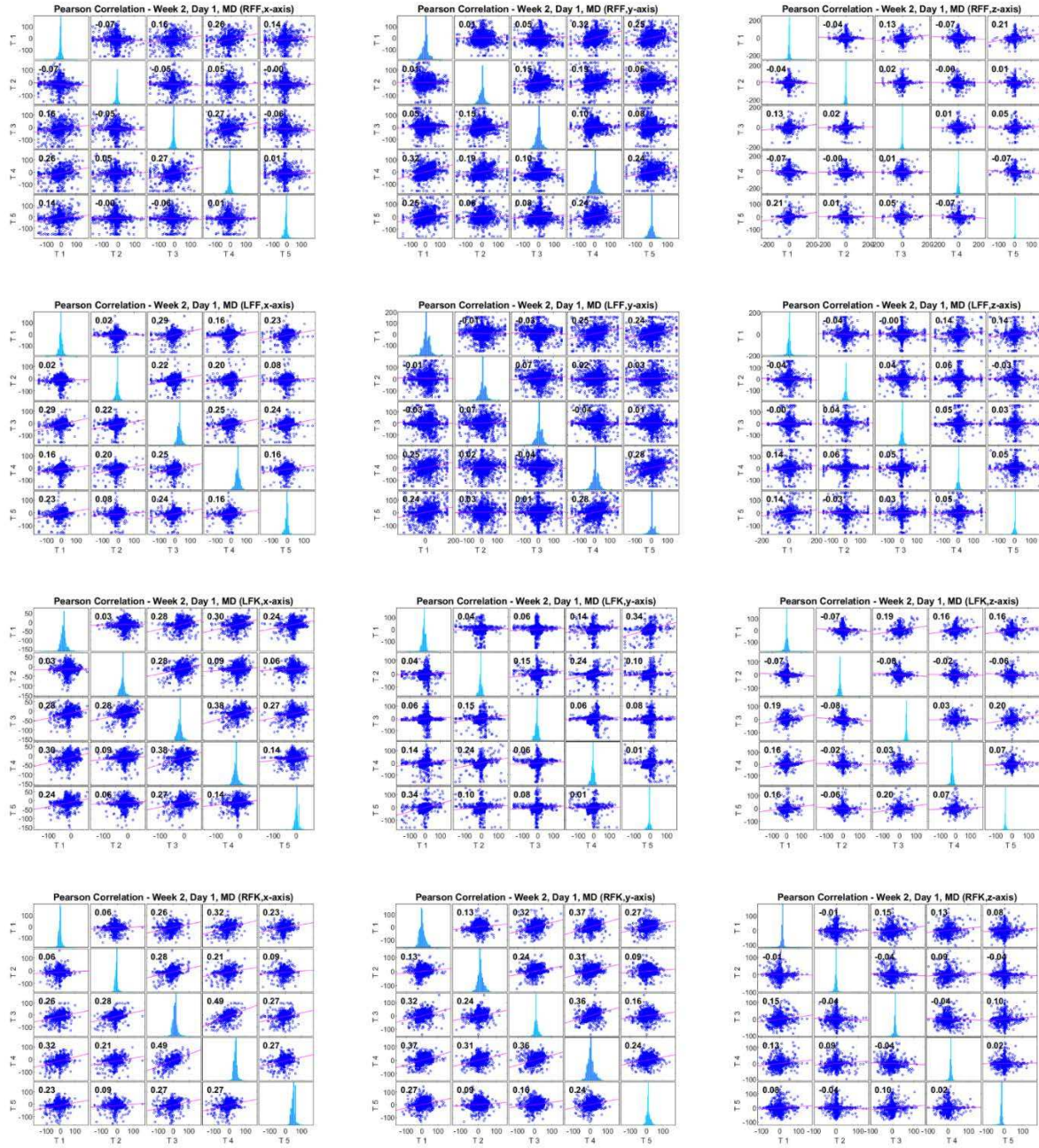
Figure A.11: Pearson Correlation Coefficients - Week 2, Day 1, MD.
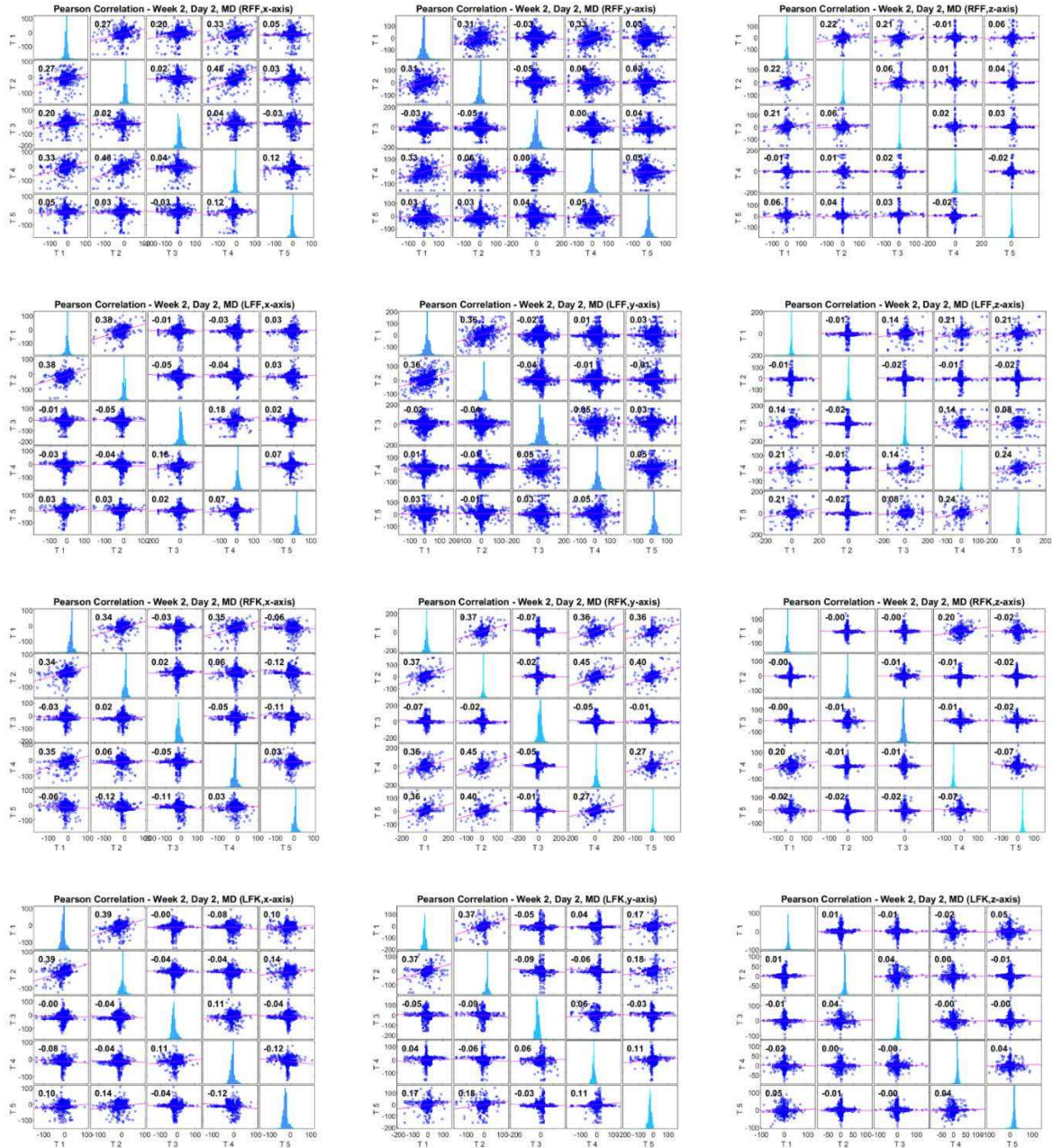
Figure A.12: Pearson Correlation Coefficients - Week 2, Day 2, MD.
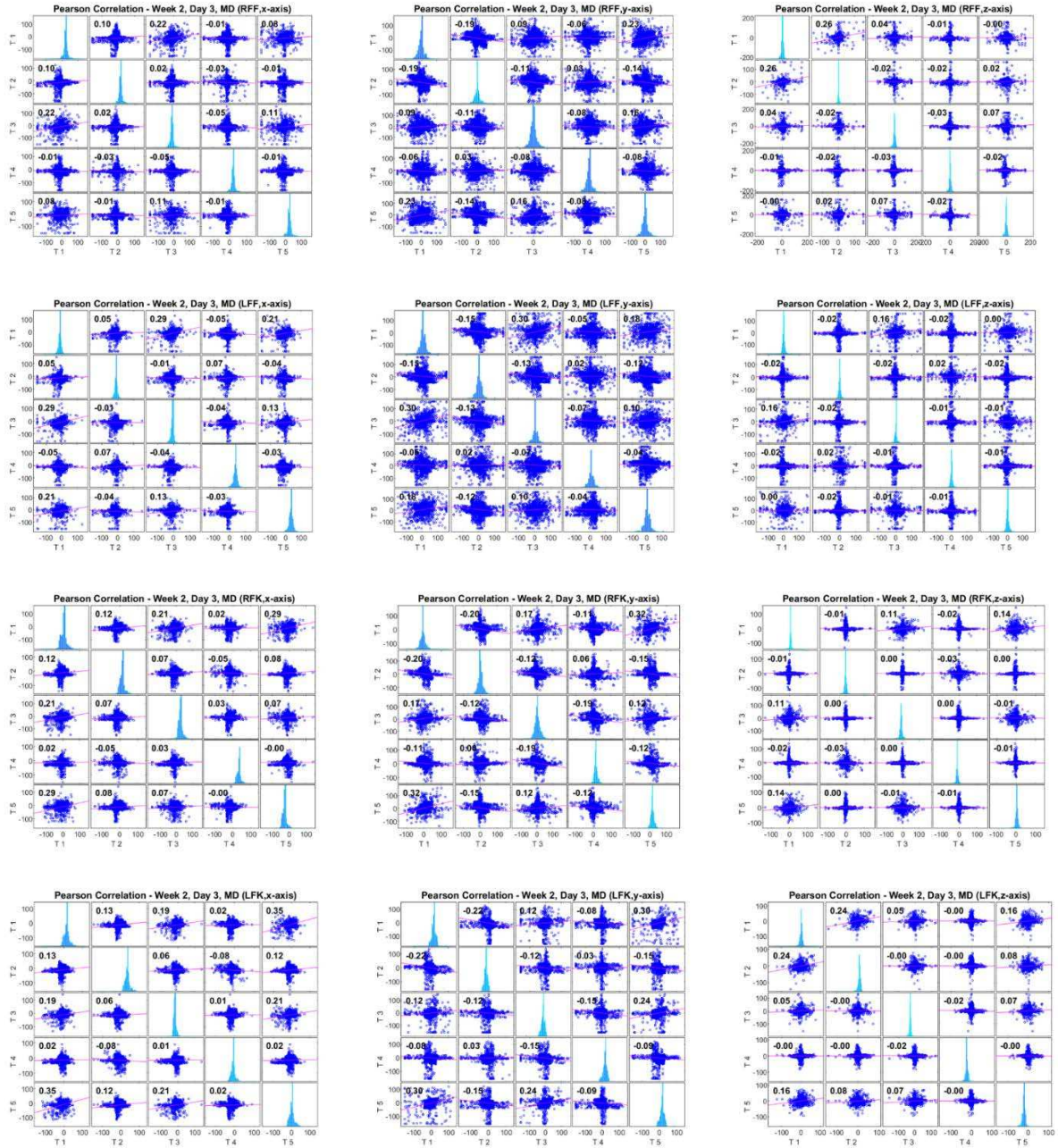
Figure A.13: Pearson Correlation Coefficients - Week 2, Day 3, MD.
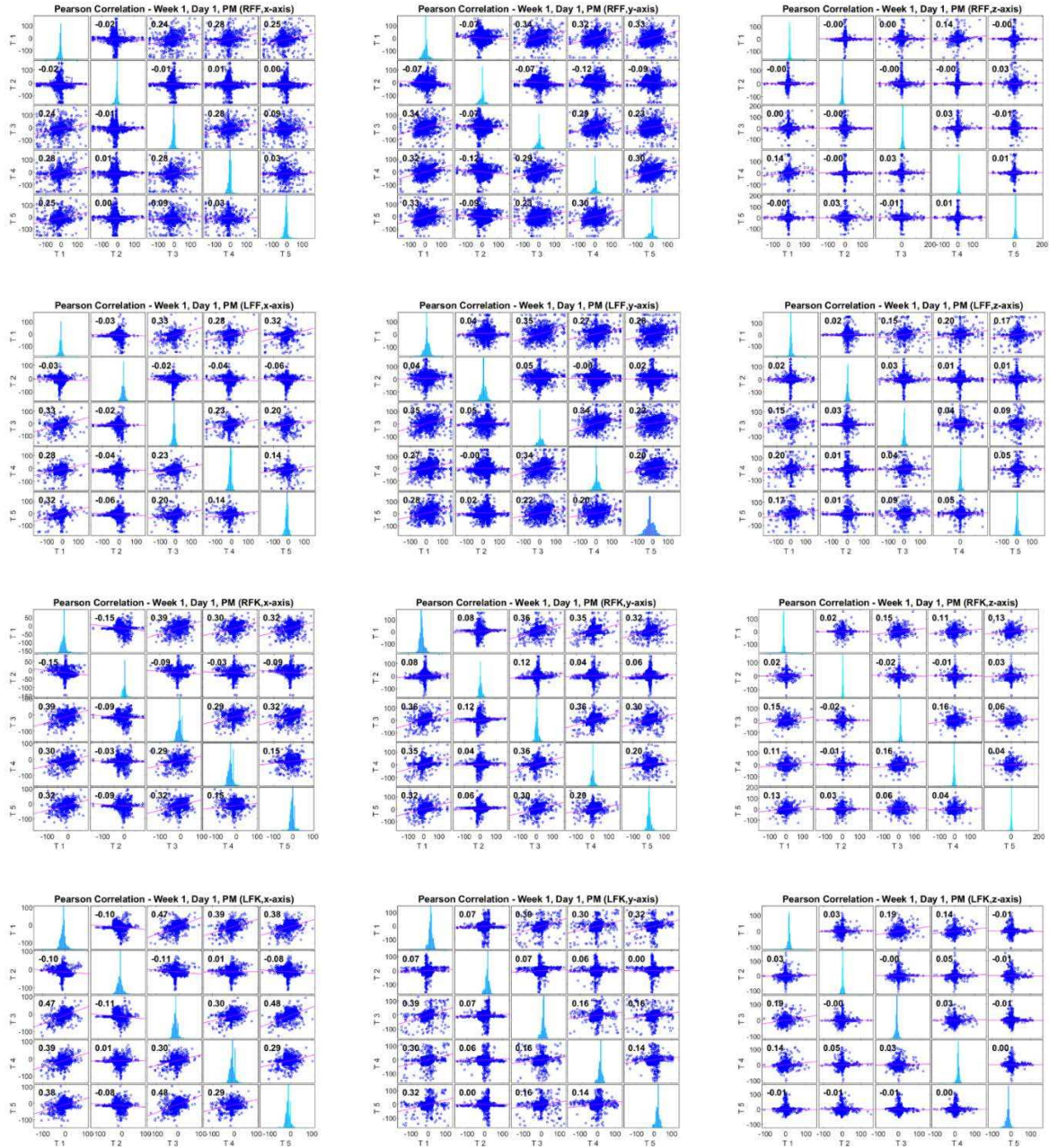
Figure A.14: Pearson Correlation Coefficients - Week 1, Day 1, PM.
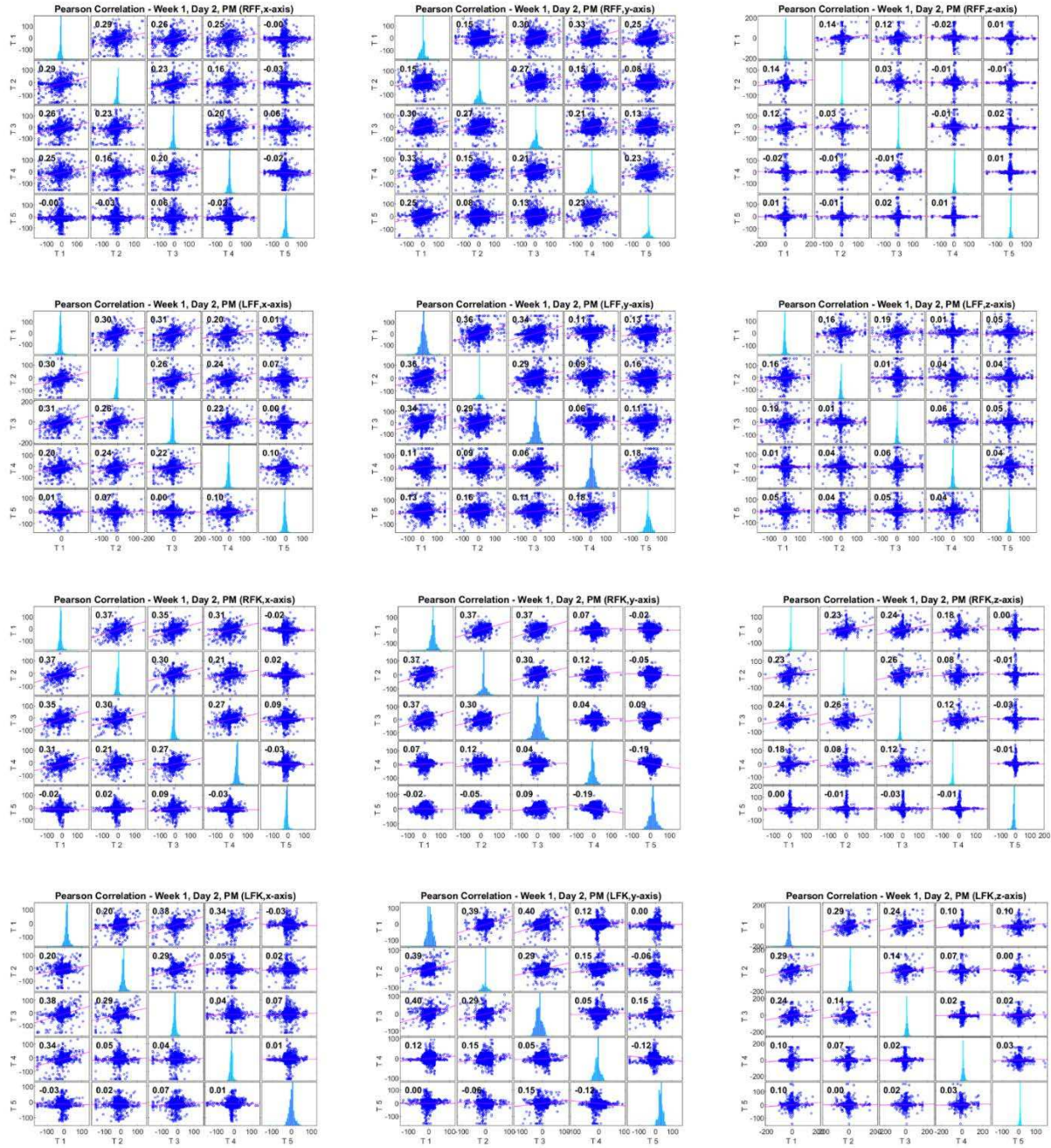
Figure A.15: Pearson Correlation Coefficients - Week 1, Day 2, PM.
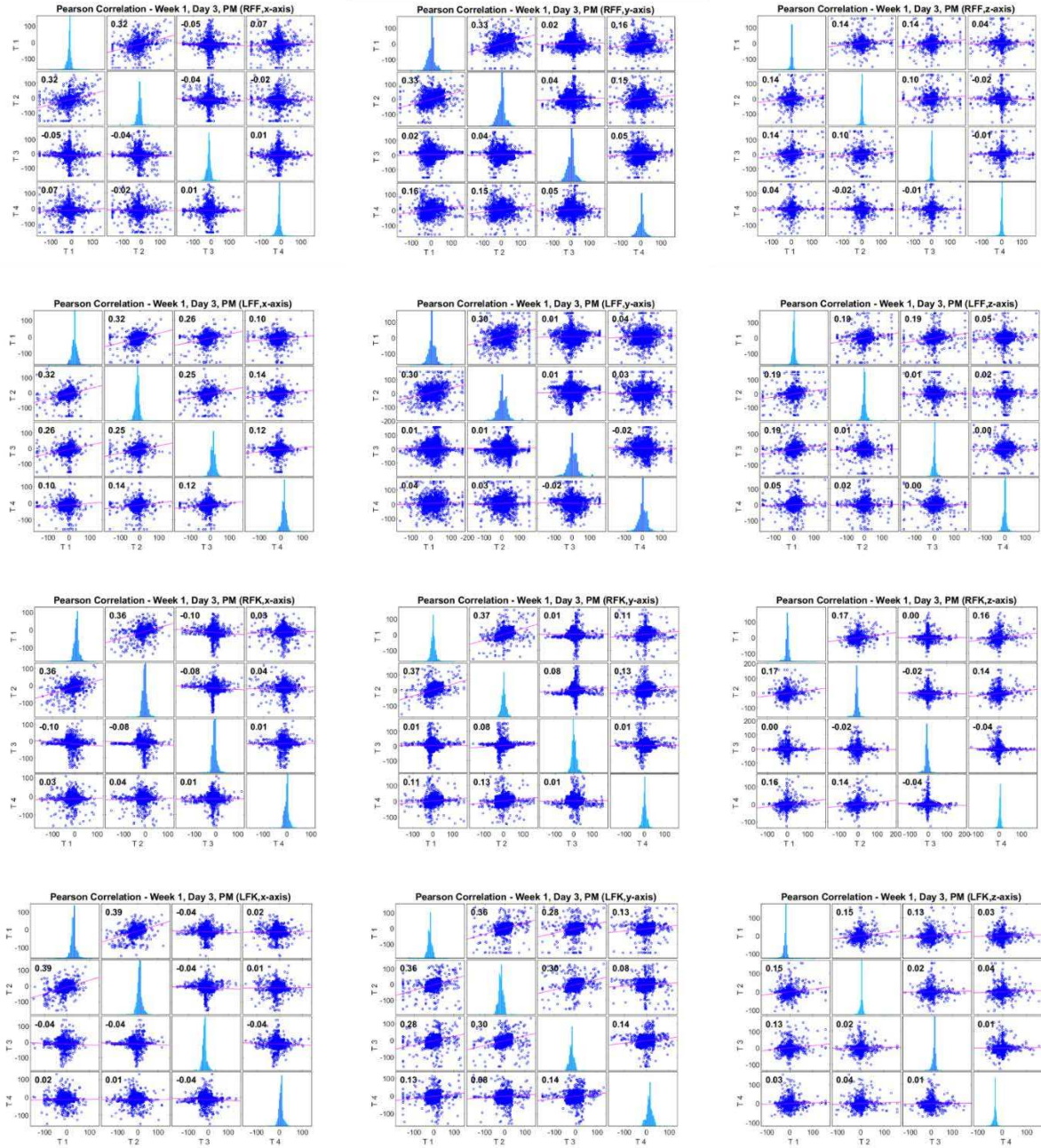
Figure A.16: Pearson Correlation Coefficients - Week 1, Day 3, PM.
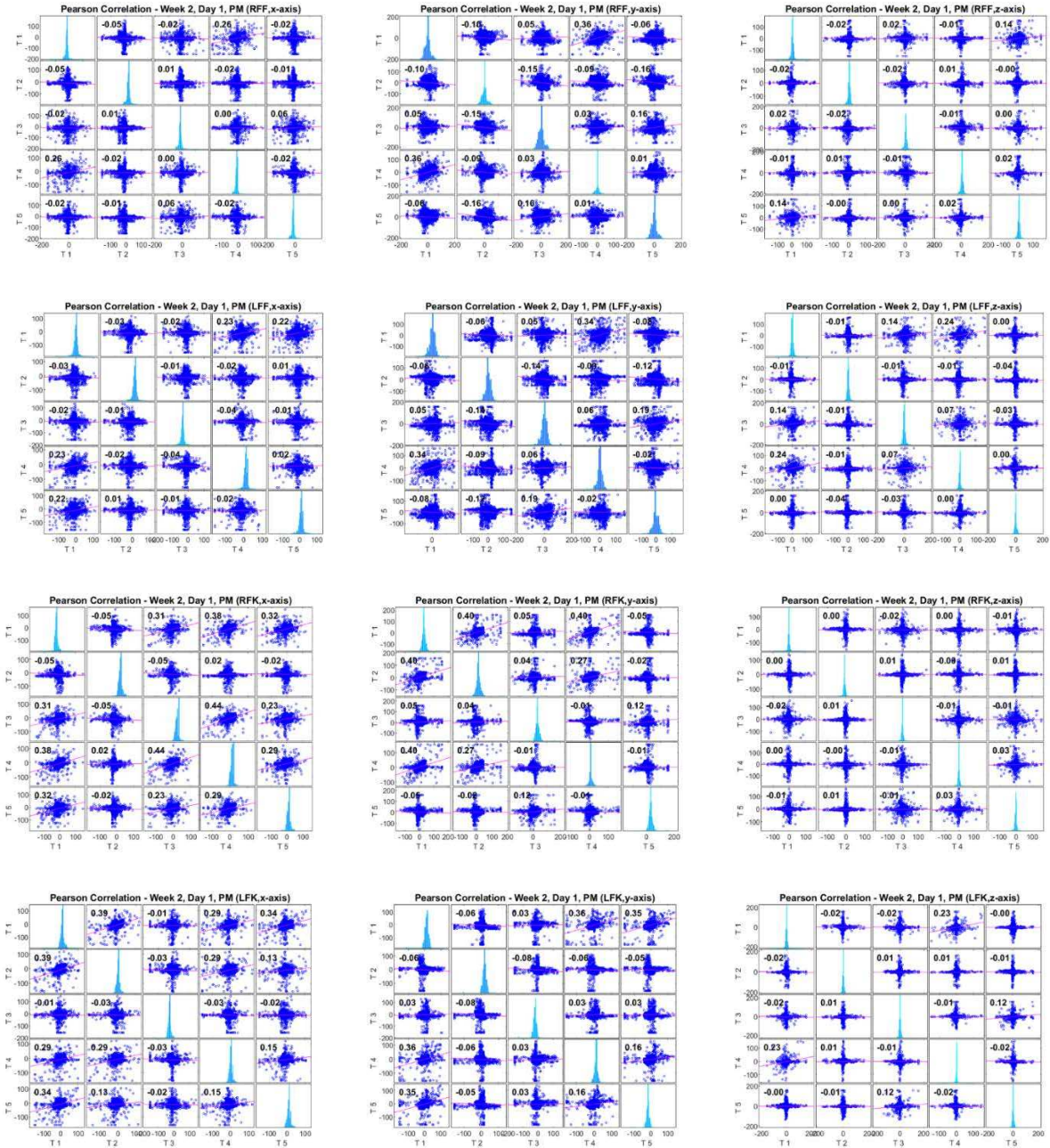
Figure A.17: Pearson Correlation Coefficients - Week 2, Day 1, PM.
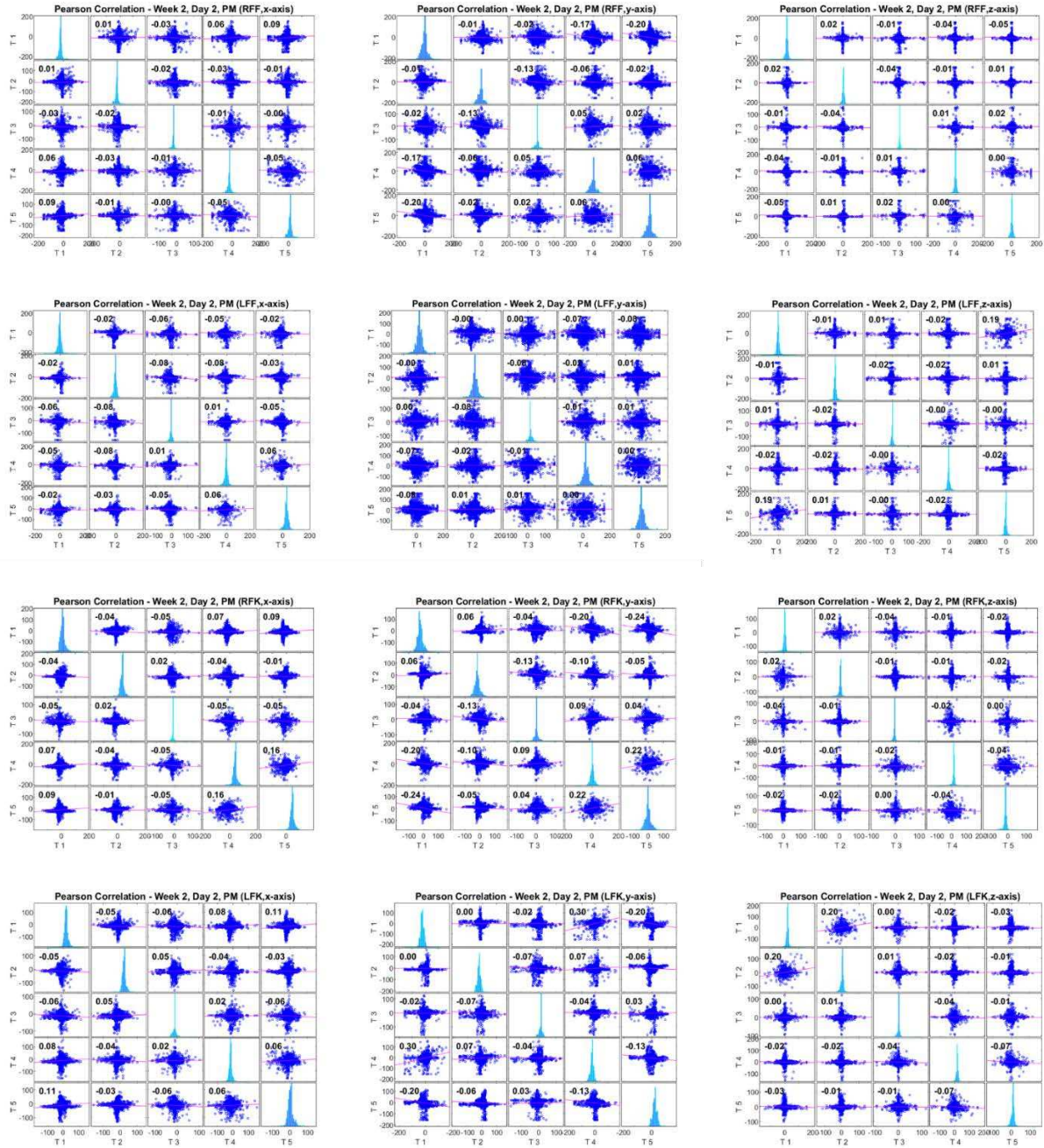
Figure A.18: Pearson Correlation Coefficients - Week 2, Day 2, PM.
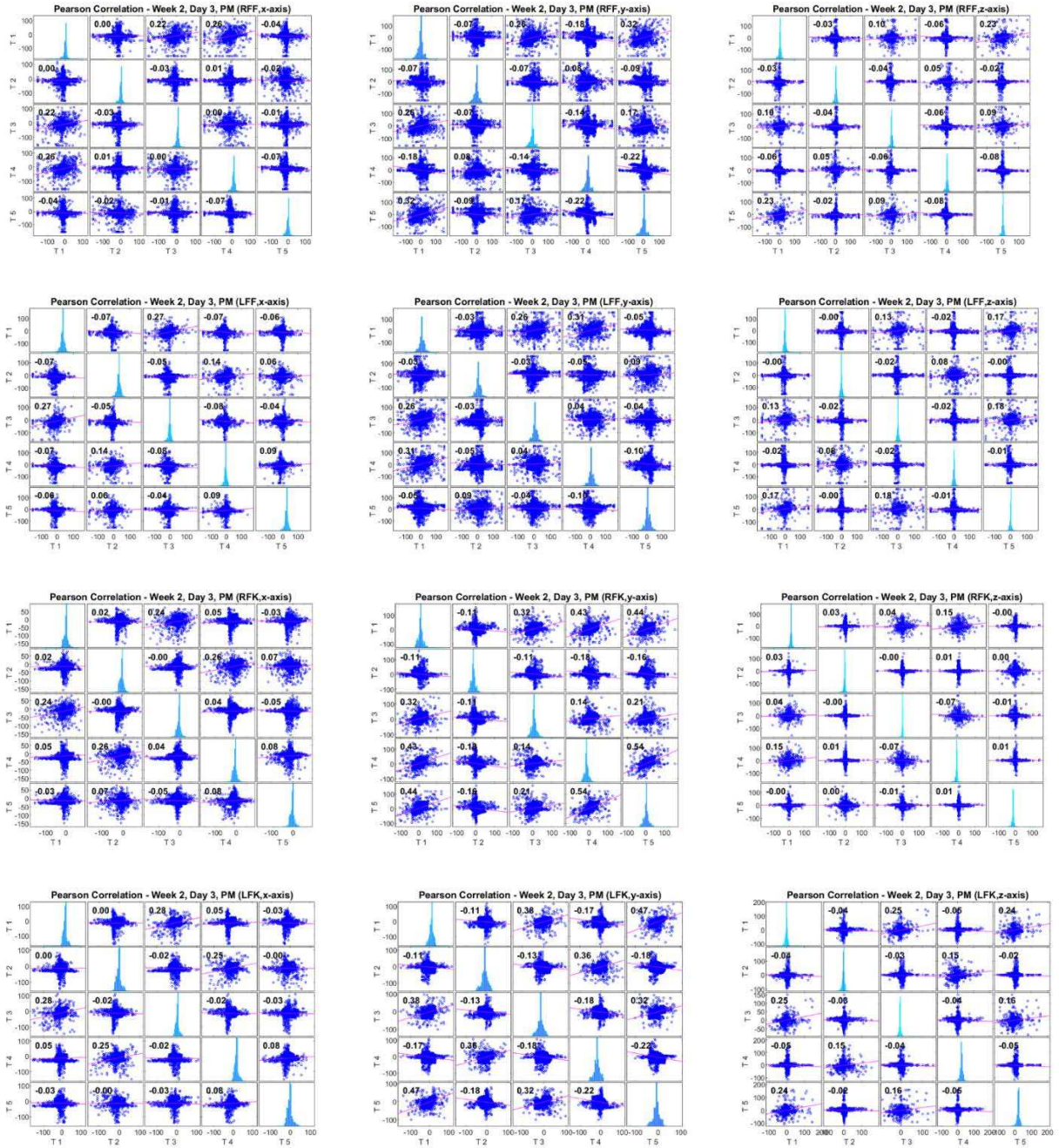
Figure A.19: Pearson Correlation Coefficients - Week 2, Day 3, PM.

Similarity Scores (AM,LFF,x-axis)

	Day 1	Day 2	Day 3	Day 4	Day 5	Day 6
Day 1	1	0.298849	0.380585	0.348332	0.62483	0.495942
Day 2	0.298849	1	0.612475	0.611944	0.757238	0.63429
Day 3	0.380585	0.612475	1	0.743194	0.796279	0.778171
Day 4	0.348332	0.611944	0.743194	1	0.708047	0.649966
Day 5	0.62483	0.757238	0.796279	0.708047	1	0.816881
Day 6	0.495942	0.63429	0.778171	0.649966	0.816881	1

Similarity Scores (MD,LFF,x-axis)

	Day 1	Day 2	Day 3	Day 4	Day 5	Day 6
Day 1	1	0.87663	0.437589	0.820711	0.736098	0.519251
Day 2	0.87663	1	0.495276	0.746925	0.698512	0.515836
Day 3	0.437589	0.495276	1	0.520256	0.630413	0.670128
Day 4	0.820711	0.746925	0.520256	1	0.663693	0.559869
Day 5	0.736098	0.698512	0.630413	0.663693	1	0.727092
Day 6	0.519251	0.515836	0.670128	0.559869	0.727092	1

Similarity Scores (PM,LFF,x-axis)

	Day 1	Day 2	Day 3	Day 4	Day 5	Day 6
Day 1	1	0.832308	0.676199	0.544664	0.604193	0.631485
Day 2	0.832308	1	0.74388	0.682078	0.733679	0.683061
Day 3	0.676199	0.74388	1	0.76995	0.589668	0.76131
Day 4	0.544664	0.682078	0.76995	1	0.359293	0.802565
Day 5	0.604193	0.733679	0.589668	0.359293	1	0.47488
Day 6	0.631485	0.683061	0.76131	0.802565	0.47488	1

Similarity Scores (AM,LFF,y-axis)

	Day 1	Day 2	Day 3	Day 4	Day 5	Day 6
Day 1	1	0.291326	0.368879	0.316462	0.660742	0.483868
Day 2	0.291326	1	0.62244	0.610764	0.742188	0.638256
Day 3	0.368879	0.62244	1	0.747363	0.815871	0.754045
Day 4	0.316462	0.610764	0.747363	1	0.665185	0.61653
Day 5	0.660742	0.742188	0.815871	0.665185	1	0.81318
Day 6	0.483868	0.638256	0.754045	0.61653	0.81318	1

Similarity Scores (MD,LFF,y-axis)

	Day 1	Day 2	Day 3	Day 4	Day 5	Day 6
Day 1	1	0.866141	0.476862	0.78727	0.67272	0.52161
Day 2	0.866141	1	0.482138	0.660694	0.60934	0.480338
Day 3	0.476862	0.482138	1	0.469653	0.510353	0.687947
Day 4	0.78727	0.660694	0.469653	1	0.551343	0.499819
Day 5	0.67272	0.60934	0.510353	0.551343	1	0.616601
Day 6	0.52161	0.480338	0.687947	0.499819	0.616601	1

Similarity Scores (PM,LFF,y-axis)

	Day 1	Day 2	Day 3	Day 4	Day 5	Day 6
Day 1	1	0.837054	0.655085	0.503044	0.598963	0.610207
Day 2	0.837054	1	0.716886	0.645892	0.728387	0.67189
Day 3	0.655085	0.716886	1	0.739558	0.604374	0.752533
Day 4	0.503044	0.645892	0.739558	1	0.351556	0.794206
Day 5	0.598963	0.728387	0.604374	0.351556	1	0.484481
Day 6	0.610207	0.67189	0.752533	0.794206	0.484481	1

Similarity Scores (AM,LFF,z-axis)

	Day 1	Day 2	Day 3	Day 4	Day 5	Day 6
Day 1	1	0.275561	0.358683	0.295785	0.702092	0.472899
Day 2	0.275561	1	0.616632	0.580222	0.706413	0.595211
Day 3	0.358683	0.616632	1	0.757158	0.777516	0.752151
Day 4	0.295785	0.580222	0.757158	1	0.630783	0.581926
Day 5	0.702092	0.706413	0.777516	0.630783	1	0.787764
Day 6	0.472899	0.595211	0.752151	0.581926	0.787764	1

Similarity Scores (MD,LFF,z-axis)

	Day 1	Day 2	Day 3	Day 4	Day 5	Day 6
Day 1	1	0.844601	0.432291	0.760696	0.737595	0.515109
Day 2	0.844601	1	0.412444	0.60782	0.607698	0.426325
Day 3	0.432291	0.412444	1	0.451542	0.583583	0.650925
Day 4	0.760696	0.60782	0.451542	1	0.585521	0.486831
Day 5	0.737595	0.607698	0.583583	0.585521	1	0.663231
Day 6	0.515109	0.426325	0.650929	0.486831	0.663231	1

Similarity Scores (PM,LFF,z-axis)

	Day 1	Day 2	Day 3	Day 4	Day 5	Day 6
Day 1	1	0.84098	0.656201	0.495658	0.567781	0.584557
Day 2	0.84098	1	0.717493	0.649867	0.684299	0.664378
Day 3	0.656201	0.717493	1	0.721269	0.598398	0.749848
Day 4	0.495658	0.649867	0.721269	1	0.331292	0.792742
Day 5	0.567781	0.684299	0.598398	0.331292	1	0.447349
Day 6	0.584557	0.664378	0.749848	0.792742	0.447349	1

Figure A.20: Similarity scores of the left forelimb fetlock sensor.

Similarity Scores (AM,RFF,x-axis)

	Day 1	Day 2	Day 3	Day 4	Day 5	Day 6
Day 1	1	0.236235	0.302292	0.26885	0.617683	0.439127
Day 2	0.236235	1	0.616674	0.582065	0.719374	0.603337
Day 3	0.302292	0.616674	1	0.731467	0.792611	0.755966
Day 4	0.26885	0.582065	0.731467	1	0.650104	0.606783
Day 5	0.617683	0.719374	0.792611	0.650104	1	0.791216
Day 6	0.439127	0.603337	0.755966	0.606783	0.791216	1

Similarity Scores (MD,RFF,x-axis)

	Day 1	Day 2	Day 3	Day 4	Day 5	Day 6
Day 1	1	0.870076	0.395926	0.75405	0.631187	0.481975
Day 2	0.870076	1	0.441641	0.65806	0.593909	0.463658
Day 3	0.395926	0.441641	1	0.445871	0.457853	0.632408
Day 4	0.75405	0.65806	0.445871	1	0.525261	0.47774
Day 5	0.631187	0.593909	0.457853	0.525261	1	0.61408
Day 6	0.481975	0.463658	0.632408	0.47774	0.61408	1

Similarity Scores (PM,RFF,x-axis)

	Day 1	Day 2	Day 3	Day 4	Day 5	Day 6
Day 1	1	0.804107	0.627228	0.484276	0.542943	0.582261
Day 2	0.804107	1	0.719154	0.66425	0.696016	0.66127
Day 3	0.627228	0.719154	1	0.715291	0.593285	0.727099
Day 4	0.484276	0.66425	0.715291	1	0.331464	0.777711
Day 5	0.542943	0.696016	0.593285	0.331464	1	0.44847
Day 6	0.582261	0.66127	0.727099	0.777711	0.44847	1

Similarity Scores (AM,RFF,y-axis)

	Day 1	Day 2	Day 3	Day 4	Day 5	Day 6
Day 1	1	0.274617	0.351334	0.32457	0.639063	0.476035
Day 2	0.274617	1	0.610138	0.600569	0.726119	0.614801
Day 3	0.351334	0.610138	1	0.763369	0.820106	0.760144
Day 4	0.32457	0.600569	0.763369	1	0.673111	0.636241
Day 5	0.639063	0.726119	0.820106	0.673111	1	0.804521
Day 6	0.476035	0.614801	0.760144	0.636241	0.804521	1

Similarity Scores (MD,RFF,y-axis)

	Day 1	Day 2	Day 3	Day 4	Day 5	Day 6
Day 1	1	0.879583	0.437265	0.735784	0.649233	0.500941
Day 2	0.879583	1	0.474329	0.656032	0.620428	0.484726
Day 3	0.437265	0.474329	1	0.477026	0.483311	0.657888
Day 4	0.735784	0.656032	0.477026	1	0.54148	0.486062
Day 5	0.649233	0.620428	0.483311	0.54148	1	0.627935
Day 6	0.500941	0.484726	0.657888	0.486062	0.627935	1

Similarity Scores (PM,RFF,y-axis)

	Day 1	Day 2	Day 3	Day 4	Day 5	Day 6
Day 1	1	0.808335	0.656933	0.500048	0.560131	0.598122
Day 2	0.808335	1	0.736774	0.673708	0.703244	0.663848
Day 3	0.656933	0.736774	1	0.742788	0.62141	0.737362
Day 4	0.500048	0.673708	0.742788	1	0.363245	0.797743
Day 5	0.560131	0.703244	0.62141	0.363245	1	0.473762
Day 6	0.598122	0.663848	0.737362	0.797743	0.473762	1

Similarity Scores (AM,RFF,z-axis)

	Day 1	Day 2	Day 3	Day 4	Day 5	Day 6
Day 1	1	0.226357	0.275835	0.230338	0.644298	0.432692
Day 2	0.226357	1	0.617615	0.577283	0.692115	0.578785
Day 3	0.275835	0.617615	1	0.759064	0.769365	0.723069
Day 4	0.230338	0.577283	0.759064	1	0.613569	0.581752
Day 5	0.644298	0.692115	0.769365	0.613569	1	0.759208
Day 6	0.432692	0.578785	0.723069	0.581752	0.759208	1

Similarity Scores (MD,RFF,z-axis)

	Day 1	Day 2	Day 3	Day 4	Day 5	Day 6
Day 1	1	0.87695	0.388439	0.722657	0.648983	0.490487
Day 2	0.87695	1	0.409751	0.612959	0.574296	0.437839
Day 3	0.388439	0.409751	1	0.429597	0.436453	0.597688
Day 4	0.722657	0.612959	0.429597	1	0.488239	0.458571
Day 5	0.648983	0.574296	0.436453	0.488239	1	0.59616
Day 6	0.490487	0.437839	0.597688	0.458571	0.59616	1

Similarity Scores (PM,RFF,z-axis)

	Day 1	Day 2	Day 3	Day 4	Day 5	Day 6
Day 1	1	0.800493	0.612565	0.481248	0.520729	0.568664
Day 2	0.800493	1	0.720502	0.677444	0.661373	0.668345
Day 3	0.612565	0.720502	1	0.697957	0.619749	0.73465
Day 4	0.481248	0.677444	0.697957	1	0.34112	0.805142
Day 5	0.520729	0.661373	0.619749	0.34112	1	0.451555
Day 6	0.568664	0.668345	0.73465	0.805142	0.451555	1

Figure A.21: Similarity scores of the right forelimb fetlock sensor.

Similarity Scores (AM,LFK,x-axis)

	Day 1	Day 2	Day 3	Day 4	Day 5	Day 6
Day 1	1	0.279862	0.34281	0.322449	0.563508	0.474372
Day 2	0.279862	1	0.62024	0.598799	0.779349	0.601802
Day 3	0.34281	0.62024	1	0.729633	0.7408	0.745181
Day 4	0.322449	0.598799	0.729633	1	0.697581	0.608588
Day 5	0.563508	0.779349	0.7408	0.697581	1	0.747073
Day 6	0.474372	0.601802	0.745181	0.608588	0.747073	1

Similarity Scores (MD,LFK,x-axis)

	Day 1	Day 2	Day 3	Day 4	Day 5	Day 6
Day 1	1	0.867627	0.428351	0.768364	0.686904	0.514086
Day 2	0.867627	1	0.444336	0.64989	0.61549	0.464945
Day 3	0.428351	0.444336	1	0.456281	0.53161	0.70231
Day 4	0.768364	0.64989	0.456281	1	0.550796	0.48466
Day 5	0.686904	0.61549	0.53161	0.550796	1	0.649726
Day 6	0.514086	0.464945	0.70231	0.48466	0.649726	1

Similarity Scores (MD,LFK,x-axis)

	Day 1	Day 2	Day 3	Day 4	Day 5	Day 6
Day 1	1	0.825151	0.629156	0.503811	0.564297	0.601336
Day 2	0.825151	1	0.728864	0.655479	0.696119	0.683754
Day 3	0.629156	0.728864	1	0.741784	0.588958	0.772435
Day 4	0.503811	0.655479	0.741784	1	0.34073	0.805423
Day 5	0.564297	0.696119	0.588958	0.34073	1	0.472223
Day 6	0.601336	0.683754	0.772435	0.805423	0.472223	1

Similarity Scores (AM,LFK,y-axis)

	Day 1	Day 2	Day 3	Day 4	Day 5	Day 6
Day 1	1	0.30624	0.401391	0.337728	0.658425	0.468454
Day 2	0.30624	1	0.638907	0.619597	0.759023	0.633982
Day 3	0.401391	0.638907	1	0.751273	0.828582	0.763088
Day 4	0.337728	0.619597	0.751273	1	0.678628	0.623427
Day 5	0.658425	0.759023	0.828582	0.678628	1	0.80224
Day 6	0.468454	0.633982	0.763088	0.623427	0.80224	1

Similarity Scores (MD,LFK,y-axis)

	Day 1	Day 2	Day 3	Day 4	Day 5	Day 6
Day 1	1	0.873411	0.506685	0.795029	0.675135	0.539681
Day 2	0.873411	1	0.556761	0.684244	0.646476	0.541422
Day 3	0.506685	0.556761	1	0.522486	0.530278	0.707158
Day 4	0.795029	0.684244	0.522486	1	0.576495	0.528855
Day 5	0.675135	0.646476	0.530278	0.576495	1	0.639046
Day 6	0.539681	0.541422	0.707158	0.528855	0.639046	1

Similarity Scores (PM,LFK,y-axis)

	Day 1	Day 2	Day 3	Day 4	Day 5	Day 6
Day 1	1	0.835227	0.664678	0.517608	0.5701	0.61444
Day 2	0.835227	1	0.753351	0.672276	0.602306	0.757055
Day 3	0.664678	0.753351	1	0.776476	0.602306	0.757055
Day 4	0.517608	0.672276	0.776476	1	0.370612	0.828247
Day 5	0.5701	0.722573	0.602306	0.370612	1	0.494957
Day 6	0.61444	0.691386	0.757055	0.828247	0.494957	1

Similarity Scores (AM,LFK,z-axis)

	Day 1	Day 2	Day 3	Day 4	Day 5	Day 6
Day 1	1	0.266223	0.326408	0.298096	0.637487	0.478681
Day 2	0.266223	1	0.616589	0.586234	0.744266	0.599441
Day 3	0.326408	0.616589	1	0.718411	0.806919	0.757458
Day 4	0.298096	0.586234	0.718411	1	0.676173	0.585709
Day 5	0.637487	0.744266	0.806919	0.676173	1	0.81751
Day 6	0.478681	0.599441	0.757458	0.585709	0.81751	1

Similarity Scores (MD,LFK,z-axis)

	Day 1	Day 2	Day 3	Day 4	Day 5	Day 6
Day 1	1	0.838739	0.442352	0.78008	0.694291	0.531228
Day 2	0.838739	1	0.42337	0.630578	0.585375	0.446213
Day 3	0.442352	0.42337	1	0.483891	0.50616	0.700571
Day 4	0.78008	0.630578	0.483891	1	0.566249	0.48936
Day 5	0.694291	0.585375	0.50616	0.566249	1	0.617071
Day 6	0.531228	0.446213	0.700571	0.48936	0.617071	1

Similarity Scores (PM,LFK,z-axis)

	Day 1	Day 2	Day 3	Day 4	Day 5	Day 6
Day 1	1	0.792292	0.621648	0.473349	0.523036	0.570595
Day 2	0.792292	1	0.732996	0.669171	0.687064	0.693602
Day 3	0.621648	0.732996	1	0.742063	0.594734	0.75276
Day 4	0.473349	0.669171	0.742063	1	0.329008	0.812033
Day 5	0.523036	0.687064	0.594734	0.329008	1	0.463516
Day 6	0.570595	0.693602	0.75276	0.812033	0.463516	1

Figure A.22: Similarity scores of the left forelimb knee sensor.

Similarity Scores (AM,RFK,x-axis)

	Day 1	Day 2	Day 3	Day 4	Day 5	Day 6
Day 1	1	0.246314	0.299135	0.264878	0.604388	0.435076
Day 2	0.246314	1	0.629158	0.588021	0.747487	0.603405
Day 3	0.299135	0.629158	1	0.734146	0.753783	0.750122
Day 4	0.264878	0.588021	0.734146	1	0.660463	0.595243
Day 5	0.604388	0.747487	0.753783	0.660463	1	0.76457
Day 6	0.435076	0.603405	0.750122	0.595243	0.76457	1

Similarity Scores (MD,RFK,x-axis)

	Day 1	Day 2	Day 3	Day 4	Day 5	Day 6
Day 1	1	0.872929	0.406749	0.733886	0.663956	0.496937
Day 2	0.872929	1	0.44116	0.629967	0.617158	0.465351
Day 3	0.406749	0.44116	1	0.43496	0.504873	0.633036
Day 4	0.733886	0.629967	0.43496	1	0.52451	0.464345
Day 5	0.663956	0.617158	0.504873	0.52451	1	0.634552
Day 6	0.496937	0.465351	0.633036	0.464345	0.634552	1

Similarity Scores (PM,RFK,x-axis)

	Day 1	Day 2	Day 3	Day 4	Day 5	Day 6
Day 1	1	0.810491	0.647268	0.481554	0.528464	0.586603
Day 2	0.810491	1	0.733595	0.667132	0.672989	0.674665
Day 3	0.647268	0.733595	1	0.701865	0.638663	0.709968
Day 4	0.481554	0.667132	0.701865	1	0.334766	0.7794
Day 5	0.528464	0.672989	0.638663	0.334766	1	0.45927
Day 6	0.586603	0.674665	0.709968	0.7794	0.45927	1

Similarity Scores (AM,RFK,y-axis)

	Day 1	Day 2	Day 3	Day 4	Day 5	Day 6
Day 1	1	0.281588	0.34272	0.311865	0.649793	0.450339
Day 2	0.281588	1	0.63151	0.617913	0.741871	0.624579
Day 3	0.34272	0.63151	1	0.751126	0.804168	0.754914
Day 4	0.311865	0.617913	0.751126	1	0.657635	0.605964
Day 5	0.649793	0.741871	0.804168	0.657635	1	0.795256
Day 6	0.450339	0.624579	0.754914	0.605964	0.795256	1

Similarity Scores (MD,RFK,y-axis)

	Day 1	Day 2	Day 3	Day 4	Day 5	Day 6
Day 1	1	0.890996	0.460806	0.72927	0.686735	0.514529
Day 2	0.890996	1	0.468811	0.641464	0.638965	0.466438
Day 3	0.460806	0.468811	1	0.479234	0.538044	0.695261
Day 4	0.72927	0.641464	0.479234	1	0.563209	0.492967
Day 5	0.686735	0.638965	0.538044	0.563209	1	0.671575
Day 6	0.514529	0.466438	0.695261	0.492967	0.671575	1

Similarity Scores (PM,RFK,y-axis)

	Day 1	Day 2	Day 3	Day 4	Day 5	Day 6
Day 1	1	0.801917	0.679397	0.509178	0.548726	0.615844
Day 2	0.801917	1	0.751091	0.667752	0.711359	0.678773
Day 3	0.679397	0.751091	1	0.72799	0.640684	0.730059
Day 4	0.509178	0.667752	0.72799	1	0.355121	0.795063
Day 5	0.548726	0.711359	0.640684	0.355121	1	0.479402
Day 6	0.615844	0.678773	0.730059	0.795063	0.479402	1

Similarity Scores (AM,RFK,z-axis)

	Day 1	Day 2	Day 3	Day 4	Day 5	Day 6
Day 1	1	0.20451	0.257303	0.219974	0.628671	0.409732
Day 2	0.20451	1	0.608114	0.564499	0.686413	0.556149
Day 3	0.257303	0.608114	1	0.719966	0.723466	0.717266
Day 4	0.219974	0.564499	0.719966	1	0.608711	0.562373
Day 5	0.628671	0.686413	0.723466	0.608711	1	0.735317
Day 6	0.409732	0.556149	0.717266	0.562373	0.735317	1

Similarity Scores (MD,RFK,z-axis)

	Day 1	Day 2	Day 3	Day 4	Day 5	Day 6
Day 1	1	0.869353	0.389946	0.726086	0.662685	0.503577
Day 2	0.869353	1	0.392786	0.605425	0.573126	0.436152
Day 3	0.389946	0.392786	1	0.432593	0.435767	0.602262
Day 4	0.726086	0.605425	0.432593	1	0.498125	0.465539
Day 5	0.662685	0.573126	0.435767	0.498125	1	0.585345
Day 6	0.503577	0.436152	0.602262	0.465539	0.585345	1

Similarity Scores (PM,RFK,z-axis)

	Day 1	Day 2	Day 3	Day 4	Day 5	Day 6
Day 1	1	0.772362	0.61891	0.442343	0.494259	0.55182
Day 2	0.772362	1	0.715539	0.653659	0.661037	0.665378
Day 3	0.61891	0.715539	1	0.677699	0.647522	0.7014
Day 4	0.442343	0.653659	0.677699	1	0.324236	0.777745
Day 5	0.494259	0.661037	0.647522	0.324236	1	0.449248
Day 6	0.55182	0.665378	0.7014	0.777745	0.449248	1

Figure A.23: Similarity scores of the right forelimb knee sensor.
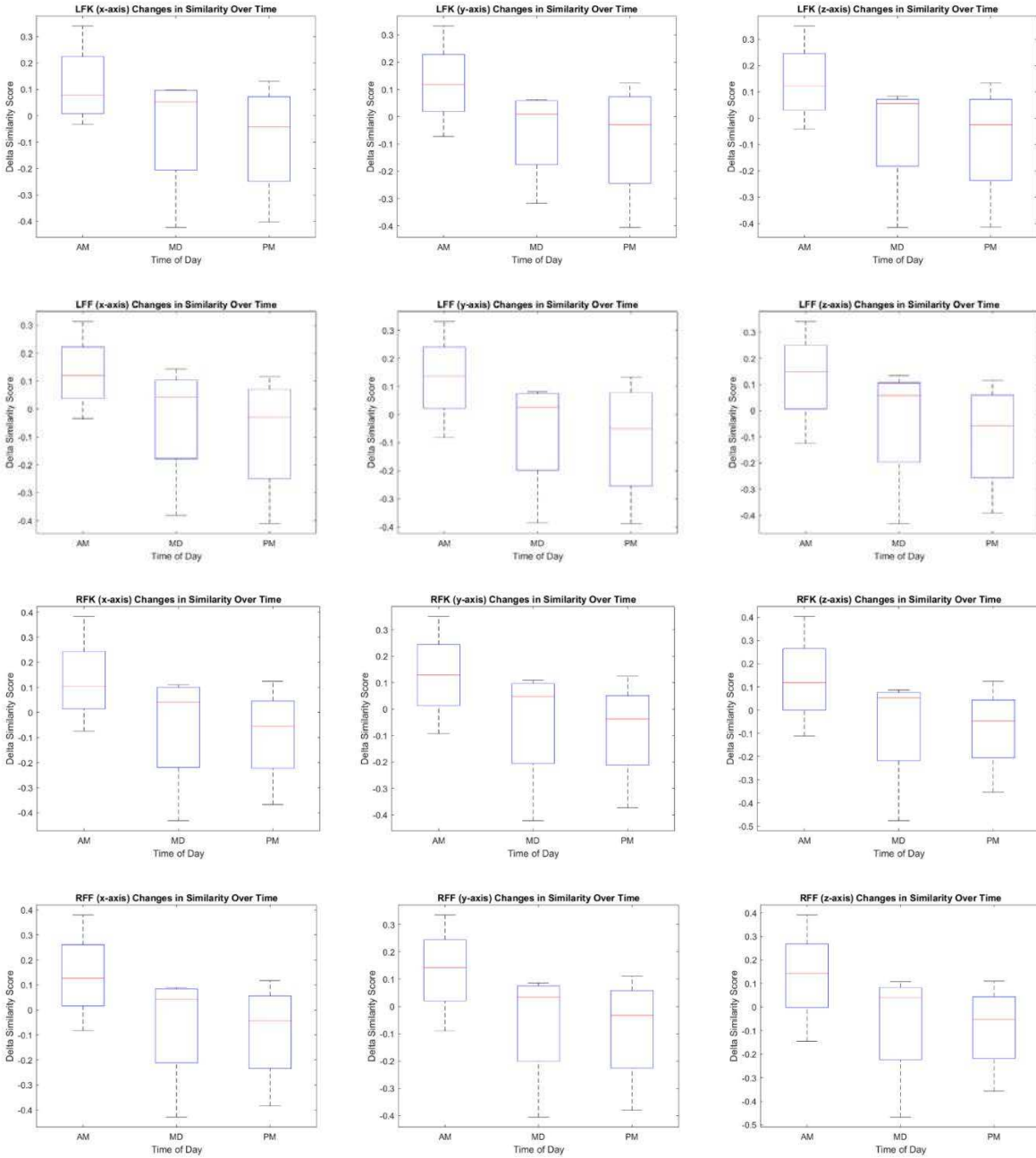
Figure A.24: Change in similarity score of right and left forelimb fetlock and left and right forelimb knee sensors.
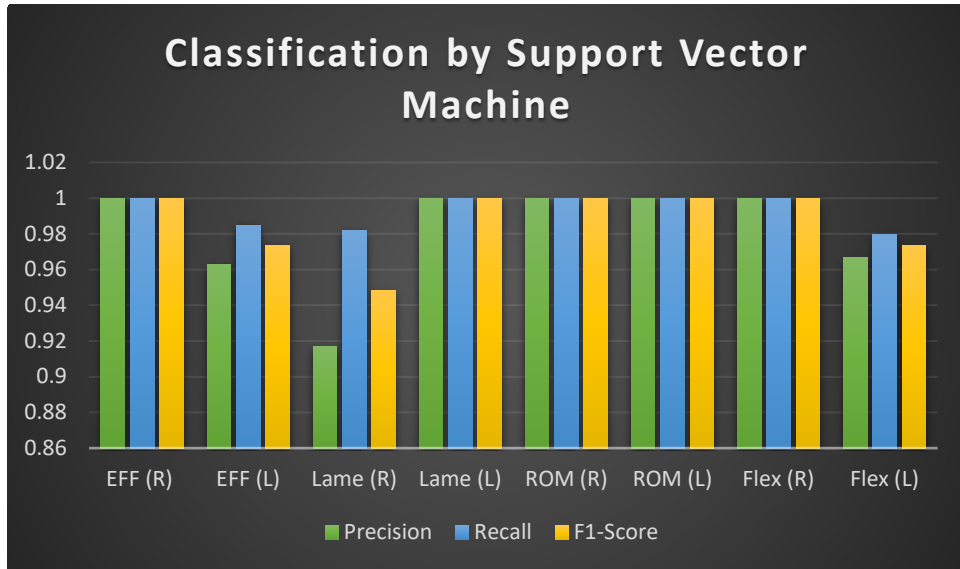
Figure A.25: Classification results from models developed using individual limbs for each of the four metrics of lameness using SVM.
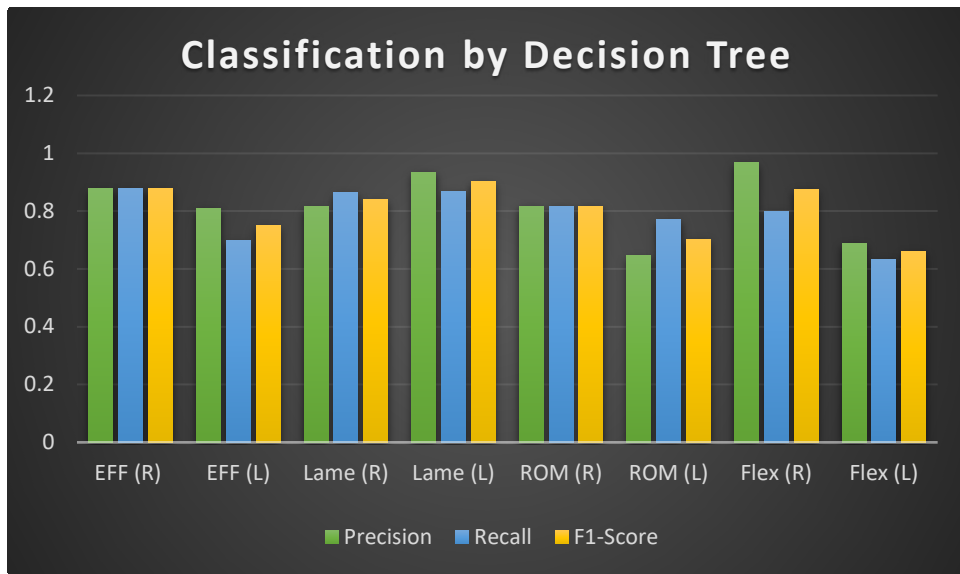
Figure A.26: Classification results from models developed using individual limbs for each of the four metrics of lameness using Decision Tree.
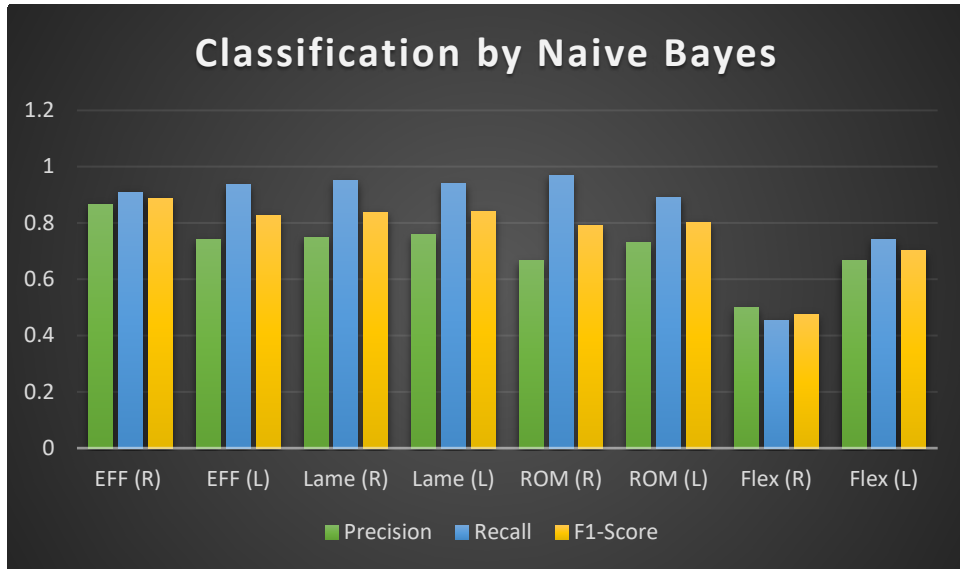
Figure A.27: Classification results from models developed using individual limbs for each of the four metrics of lameness using Naïve Bayes.
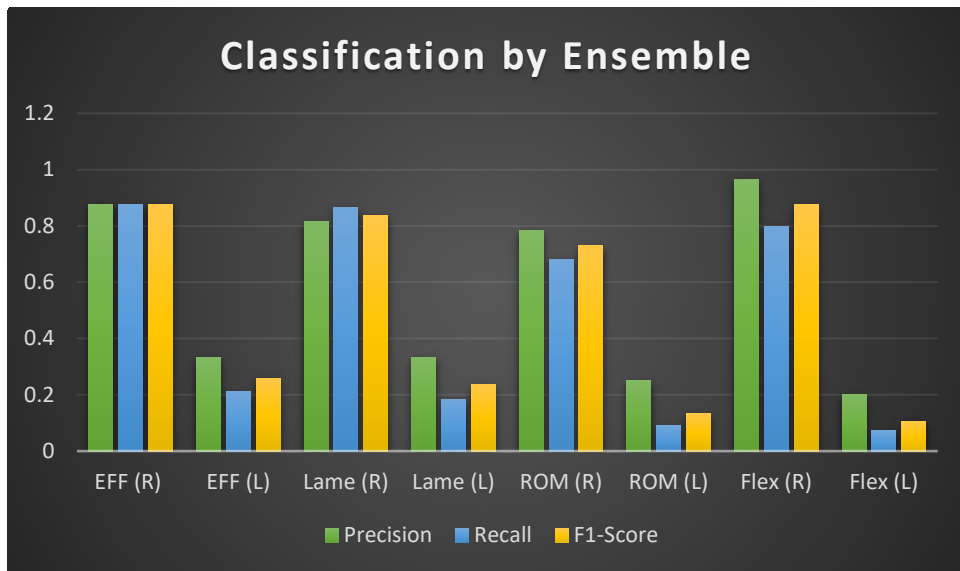
Figure A.28: Classification results from models developed using individual limbs for each of the four metrics of lameness using Ensemble.
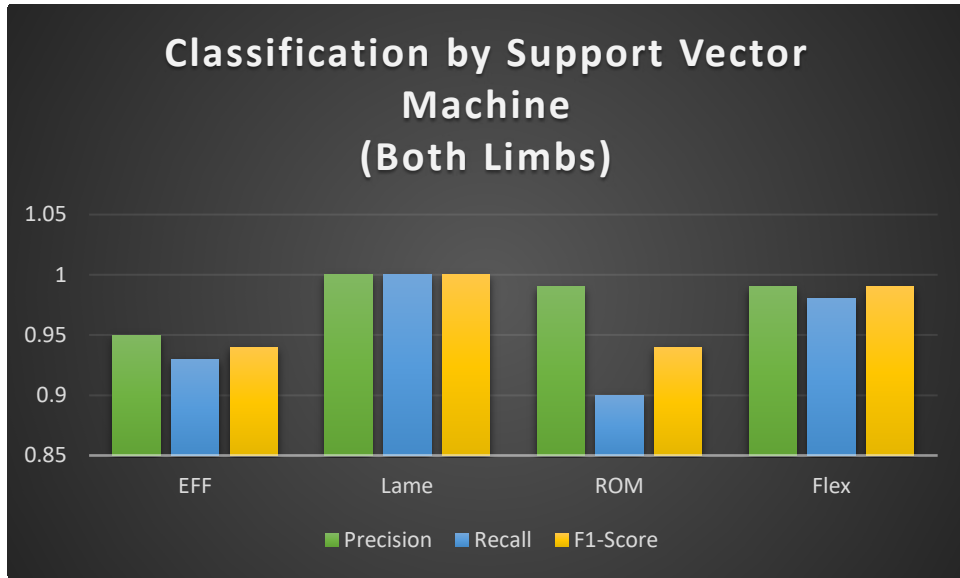
Figure A.29: Classification results from models developed using both limbs for each of the four metrics of lameness using SVM.
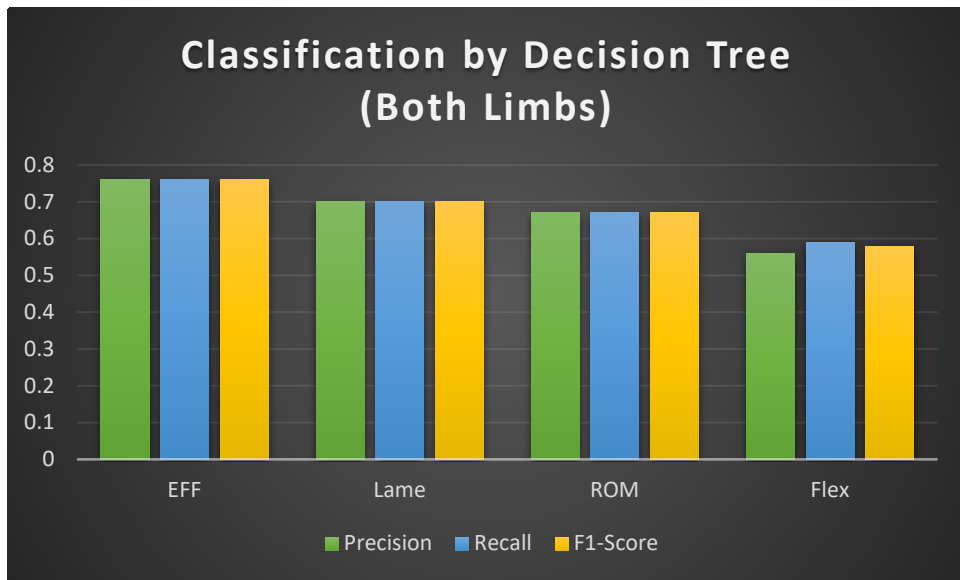
Figure A.30: Classification results from models developed using both limbs for each of the four metrics of lameness using Decision Tree.
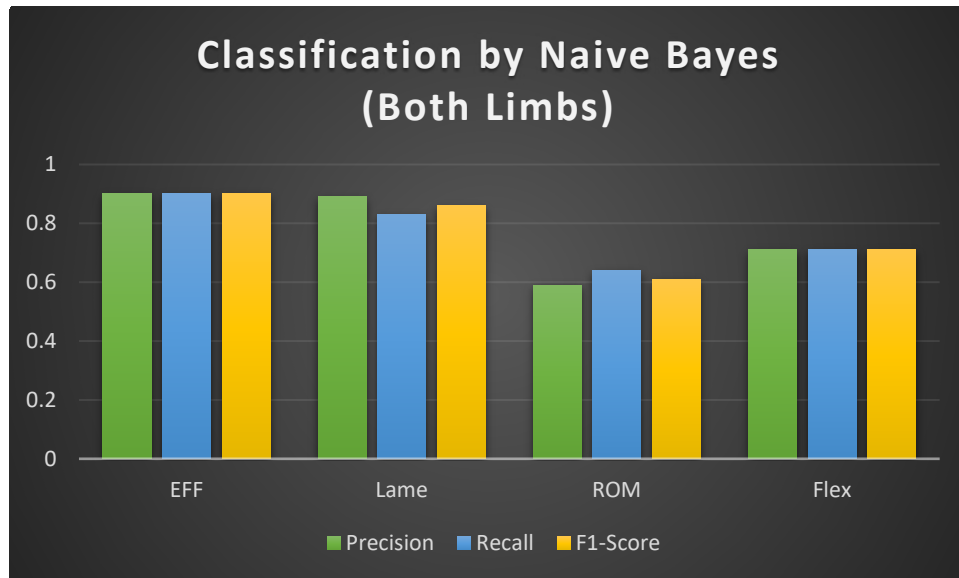
Figure A.31: Classification results from models developed using both limbs for each of the four metrics of lameness using Naïve Bayes.

	MQ-5	MQ-7	MQ-135
MQ-5	0	0.78395	4.94072
MQ-7	0.78395	0	11.0245
MQ-135	4.94072	11.0245	0

(a) 20°C, 33% RH

	MQ-5	MQ-7	MQ-135
MQ-5	0	1.0352	6.38428
MQ-7	1.0352	0	8.89186
MQ-135	6.38428	8.89186	0

(b) 25°C, 33% RH

	MQ-5	MQ-7	MQ-135
MQ-5	0	1.24042	4.28076
MQ-7	1.24042	0	7.61727
MQ-135	4.28076	7.61727	0

(c) 30°C, 33% RH

	MQ-5	MQ-7	MQ-135
MQ-5	0	1.1895	3.96794
MQ-7	1.1895	0	7.37707
MQ-135	3.96794	7.37707	0

(d) 35°C, 33% RH

	MQ-5	MQ-7	MQ-135
MQ-5	0	0.81995	4.09798
MQ-7	0.81995	0	6.56959
MQ-135	4.09798	6.56959	0

(e) 40°C, 33% RH

	MQ-5	MQ-7	MQ-135
MQ-5	0	0.77044	3.48864
MQ-7	0.77044	0	5.74267
MQ-135	3.48864	5.74267	0

(f) 45°C, 33% RH

	MQ-5	MQ-7	MQ-135
MQ-5	0	0.73392	2.49251
MQ-7	0.73392	0	4.81914
MQ-135	2.49251	4.81914	0

(g) 50°C, 33% RH

Figure A.32: ANOVA f-statistics for comparisons between sensor groups (33% RH measurements).

	MQ-5	MQ-7	MQ-135
MQ-5	0	3.05666	2.21937
MQ-7	3.05666	0	8.70033
MQ-135	2.21937	8.70033	0

(a) 10°C, 85% RH

	MQ-5	MQ-7	MQ-135
MQ-5	0	2.89905	2.11631
MQ-7	2.89905	0	8.32502
MQ-135	2.11631	8.32502	0

(b) 15°C, 85% RH

	MQ-5	MQ-7	MQ-135
MQ-5	0	2.56208	2.61355
MQ-7	2.56208	0	8.46176
MQ-135	2.61355	8.46176	0

(c) 20°C, 85% RH

	MQ-5	MQ-7	MQ-135
MQ-5	0	2.21681	2.69543
MQ-7	2.21681	0	7.92917
MQ-135	2.69543	7.92917	0

(d) 25°C, 85% RH

	MQ-5	MQ-7	MQ-135
MQ-5	0	1.82725	2.54755
MQ-7	1.82725	0	6.97643
MQ-135	2.54755	6.97643	0

(e) 30°C, 85% RH

	MQ-5	MQ-7	MQ-135
MQ-5	0	2.05674	2.37359
MQ-7	2.05674	0	7.25875
MQ-135	2.37359	7.25875	0

(f) 35°C, 85% RH

	MQ-5	MQ-7	MQ-135
MQ-5	0	1.79756	2.1619
MQ-7	1.79756	0	6.42458
MQ-135	2.1619	6.42458	0

(g) 40°C, 85% RH

	MQ-5	MQ-7	MQ-135
MQ-5	0	1.62158	1.8606
MQ-7	1.62158	0	5.60012
MQ-135	1.8606	5.60012	0

(h) 45°C, 85% RH

	MQ-5	MQ-7	MQ-135
MQ-5	0	1.52395	1.84447
MQ-7	1.52395	0	5.25869
MQ-135	1.84447	5.25869	0

(i) 50°C, 85% RH

Figure A.33: ANOVA f-statistics for comparisons between sensor groups (85% RH measurements).

	Sensor 1	Sensor 2	Sensor 3	Sensor 4	Sensor 5	Sensor 6	Sensor 7	Sensor 8	Sensor 9	Sensor 10
Sensor 1	0	20855.62	3856.88	2162.387	14412.66	6104.979	7648.438	4841.299	10191.94	367.5167
Sensor 2	20855.62	0	27333.69	1072.715	638.5113	775.3307	889.6102	729.9649	4525.826	826.3033
Sensor 3	3856.88	27333.69	0	6731.62	21764.18	13112.5	15144.67	11240.23	17632.83	2007.327
Sensor 4	2162.387	1072.715	6731.62	0	347.7667	110.2542	132.3128	80.25061	**0.028074**	62.29333
Sensor 5	14412.66	638.5113	21764.18	347.7667	0	83.39094	84.85234	98.10591	1496.913	406.0781
Sensor 6	6104.979	775.3307	13112.5	110.2542	83.39094	0	**0.485418**	**1.773865**	277.6702	233.3065
Sensor 7	7648.438	889.6102	15144.67	132.3128	84.85234	**0.485418**	0	4.237849	387.8087	252.5361
Sensor 8	4841.299	729.9649	11240.23	80.25061	98.10591	**1.773865**	4.237849	0	178.163	203.3405
Sensor 9	10191.94	4525.826	17632.83	**0.028074**	1496.913	277.6702	387.8087	178.163	0	82.30988
Sensor 10	367.5167	826.3033	2007.327	62.29333	406.0781	233.3065	252.5361	203.3405	82.30988	0

Figure A.34: MQ-5 ANOVA f-statistics (20°C, 33% RH).

	Sensor 1	Sensor 2	Sensor 3	Sensor 4	Sensor 5	Sensor 6	Sensor 7	Sensor 8	Sensor 9	Sensor 10
Sensor 1	0	260109.1	80355.07	11529.19	17226.92	7.232367	30432.52	7874.698	598.3441	1925.719
Sensor 2	260109.1	0	911455.3	7581.504	843.4445	17.56806	2653.73	2739.842	670.7435	3391.974
Sensor 3	80355.07	911455.3	0	54346.08	55577.51	50.12902	105112.4	32277.55	3205.56	11913.86
Sensor 4	11529.19	7581.504	54346.08	0	1119.166	**1.387693**	1160.974	71.09178	13.76719	141.9914
Sensor 5	17226.92	843.4445	55577.51	1119.166	0	8.82297	31.76263	423.2267	264.1111	1168.973
Sensor 6	7.232367	17.56806	50.12902	**1.387693**	8.82297	0	7.227348	**2.791257**	**0.424316**	**0.081412**
Sensor 7	30432.52	2653.73	105112.4	1160.974	31.76263	7.227348	0	335.2244	212.9597	1097.086
Sensor 8	7874.698	2739.842	32277.55	71.09178	423.2267	**2.791257**	335.2244	0	49.41715	285.6514
Sensor 9	598.3441	670.7435	3205.56	13.76719	264.1111	**0.424316**	212.9597	49.41715	0	5.989645
Sensor 10	1925.719	3391.974	11913.86	141.9914	1168.973	**0.081412**	1097.086	285.6514	5.989645	0

Figure A.35: MQ-5 ANOVA f-statistics (25°C, 33% RH).

	Sensor 1	Sensor 2	Sensor 3	Sensor 4	Sensor 5	Sensor 6	Sensor 7	Sensor 8	Sensor 9	Sensor 10
Sensor 1	0	49512.53	26467.86	10319.74	19858.6	23565.21	41012.16	3463.903	511.6448	111.8742
Sensor 2	49512.53	0	104485	5868.313	479.9885	1909.279	867.4428	2097.432	509.5672	529.6193
Sensor 3	26467.86	104485	0	42250.47	53502.27	66286.76	95998.82	15654.66	2725.29	1067.329
Sensor 4	10319.74	5868.313	42250.47	0	1897.82	1131.275	2850.318	**2.839034**	**2.285018**	53.08226
Sensor 5	19858.6	479.9885	53502.27	1897.82	0	217.2446	**0.552898**	804.2407	243.6577	318.5357
Sensor 6	23565.21	1909.279	66286.76	1131.275	217.2446	0	318.7007	389.1055	124.2216	210.0209
Sensor 7	41012.16	867.4428	95998.82	2850.318	**0.552898**	318.7007	0	935.2515	246.0738	319.4388
Sensor 8	3463.903	2097.432	15654.66	**2.839034**	804.2407	389.1055	935.2515	0	4.643705	57.92944
Sensor 9	511.6448	509.5672	2725.29	**2.285018**	243.6577	124.2216	246.0738	4.643705	0	25.08826
Sensor 10	111.8742	529.6193	1067.329	53.08226	318.5357	210.0209	319.4388	57.92944	25.08826	0

Figure A.36: MQ-5 ANOVA f-statistics (30°C, 33% RH).

	Sensor 1	Sensor 2	Sensor 3	Sensor 4	Sensor 5	Sensor 6	Sensor 7	Sensor 8	Sensor 9	Sensor 10
Sensor 1	0	429178.5	75704.15	9099.776	19945.86	67879.76	4566.738	5173.774	2468.503	494.4758
Sensor 2	429178.5	0	600481.1	8725.674	343.8748	9895.763	494.4983	306.8171	1544.074	2338.661
Sensor 3	75704.15	600481.1	0	44593.25	57716.02	190511.4	15871.51	16919.62	11592.36	4708.887
Sensor 4	9099.776	8725.674	44593.25	0	2181.326	1581.131	394.2372	576.0409	15.74786	167.8302
Sensor 5	19945.86	343.8748	57716.02	2181.326	0	485.3775	109.2222	40.34903	653.4141	1368.942
Sensor 6	67879.76	9895.763	190511.4	1581.131	485.3775	0	**1.446844**	32.8257	246.9409	872.8601
Sensor 7	4566.738	494.4983	15871.51	394.2372	109.2222	**1.446844**	0	10.83021	151.6427	594.5594
Sensor 8	5173.774	306.8171	16919.62	576.0409	40.34903	32.8257	10.83021	0	242.2455	740.8293
Sensor 9	2468.503	1544.074	11592.36	15.74786	653.4141	246.9409	151.6427	242.2455	0	183.2047
Sensor 10	494.4758	2338.661	4708.887	167.8302	1368.942	872.8601	594.5594	740.8293	183.2047	0

Figure A.37: MQ-5 ANOVA f-statistics (35°C, 33% RH).

	Sensor 1	Sensor 2	Sensor 3	Sensor 4	Sensor 5	Sensor 6	Sensor 7	Sensor 8	Sensor 9	Sensor 10
Sensor 1	0	1041645	75398.84	7567.693	77602.38	13409.45	5968.259	3715.206	1018.603	41.05394
Sensor 2	1041645	0	461875	9731.685	788.1713	2077.767	831.9884	443.7369	458.2548	1536.133
Sensor 3	75398.84	461875	0	38597.55	159820.2	44840.39	21092.89	13165.52	4579.639	1384.586
Sensor 4	7567.693	9731.685	38597.55	0	5000.946	932.3861	575.9781	426.3617	44.40197	211.6106
Sensor 5	77602.38	788.1713	159820.2	5000.946	0	758.4991	330.2877	172.6932	265.8995	1202.365
Sensor 6	13409.45	2077.767	44840.39	932.3861	758.4991	0	0.882951	3.514923	36.4253	642.5023
Sensor 7	5968.259	831.9884	21092.89	575.9781	330.2877	0.882951	0	0.953356	38.21887	607.1488
Sensor 8	3715.206	443.7369	13165.52	426.3617	172.6932	3.514923	0.953356	0	41.88689	577.8021
Sensor 9	1018.603	458.2548	4579.639	44.40197	265.8995	36.4253	38.21887	41.88689	0	252.264
Sensor 10	41.05394	1536.133	1384.586	211.6106	1202.365	642.5023	607.1488	577.8021	252.264	0

Figure A.38: MQ-5 ANOVA f-statistics (40°C, 33% RH).

	Sensor 1	Sensor 2	Sensor 3	Sensor 4	Sensor 5	Sensor 6	Sensor 7	Sensor 8	Sensor 9	Sensor 10
Sensor 1	0	230289	91789.87	5695.817	31687.86	15775.73	13459.51	29231	144.8778	243.7407
Sensor 2	230289	0	372313.5	8176.61	104.1797	2865.078	502.6869	3139.412	407.8	1162.481
Sensor 3	91789.87	372313.5	0	33975.69	85352.41	57003.13	42454.99	93055.63	1184.066	2504.622
Sensor 4	5695.817	8176.61	33975.69	0	4035.562	955.6095	1776.072	1676.362	5.418827	40.63097
Sensor 5	31687.86	104.1797	85352.41	4035.562	0	1108.387	151.5131	906.0828	329.5761	925.0957
Sensor 6	15775.73	2865.078	57003.13	955.6095	1108.387	0	250.5368	49.87403	103.3763	333.8299
Sensor 7	13459.51	502.6869	42454.99	1776.072	151.5131	250.5368	0	126.6016	210.8723	600.3247
Sensor 8	29231	3139.412	93055.63	1676.362	906.0828	49.87403	126.6016	0	138.812	436.5579
Sensor 9	144.8778	407.8	1184.066	5.418827	329.5761	103.3763	210.8723	138.812	0	**2.618332**
Sensor 10	243.7407	1162.481	2504.622	40.63097	925.0957	333.8299	600.3247	436.5579	**2.618332**	0

Figure A.39: MQ-5 ANOVA f-statistics (45°C, 33% RH).

	Sensor 1	Sensor 2	Sensor 3	Sensor 4	Sensor 5	Sensor 6	Sensor 7	Sensor 8	Sensor 9	Sensor 10
Sensor 1	0	358578.8	137434	3142.016	33154.57	24214.23	113074.7	3529.577	2735.401	207.978
Sensor 2	358578.8	0	756939.1	7994.561	104.9532	4971.429	1211.947	113.2721	1535.647	1181.83
Sensor 3	137434	756939.1	0	24937.29	97845.03	95080.16	313947.3	11878.15	13668.74	2410.593
Sensor 4	3142.016	7994.561	24937.29	0	4408.458	1426.877	5226.204	863.9208	212.4086	17.21053
Sensor 5	33154.57	104.9532	97845.03	4408.458	0	1531.98	54.26644	42.56319	978.2553	954.2759
Sensor 6	24214.23	4971.429	95080.16	1426.877	1531.98	0	1967.508	117.2609	98.19706	351.315
Sensor 7	113074.7	1211.947	313947.3	5226.204	54.26644	1967.508	0	15.64244	897.3986	875.6183
Sensor 8	3529.577	113.2721	11878.15	863.9208	42.56319	117.2609	15.64244	0	238.5772	491.6671
Sensor 9	2735.401	1535.647	13668.74	212.4086	978.2553	98.19706	897.3986	238.5772	0	141.963
Sensor 10	207.978	1181.83	2410.593	17.21053	954.2759	351.315	875.6183	491.6671	141.963	0

Figure A.40: MQ-5 ANOVA f-statistics (50°C, 33% RH).

	Sensor 1	Sensor 2	Sensor 3	Sensor 4	Sensor 5	Sensor 6	Sensor 7	Sensor 8	Sensor 9	Sensor 10
Sensor 1	0	32509.97	3959.605	3190.832	26507.01	59494.74	12685.69	15873.55	1145.908	242.4081
Sensor 2	32509.97	0	22511.83	1438.668	227.5594	972.6681	342.7509	1707.037	251.7948	2032.57
Sensor 3	3959.605	22511.83	0	7703.426	22766.7	21734.35	15232.52	15219.64	3576.003	2298.94
Sensor 4	3190.832	1438.668	7703.426	0	2090.816	641.992	466.5446	145.479	18.20821	311.8427
Sensor 5	26507.01	227.5594	22766.7	2090.816	0	1817.059	863.9758	2548.065	453.2838	2575.945
Sensor 6	59494.74	972.6681	21734.35	641.992	1817.059	0	0.532442	531.2029	66.13399	1342.988
Sensor 7	12685.69	342.7509	15232.52	466.5446	863.9758	0.532442	0	225.2243	63.41171	1165.95
Sensor 8	15873.55	1707.037	15219.64	145.479	2548.065	531.2029	225.2243	0	3.68452	778.5697
Sensor 9	1145.908	251.7948	3576.003	18.20821	453.2838	66.13399	63.41171	3.68452	0	280.7271
Sensor 10	242.4081	2032.57	2298.94	311.8427	2575.945	1342.988	1165.95	778.5697	280.7271	0

Figure A.41: MQ-5 ANOVA f-statistics (10°C, 85% RH).

	Sensor 1	Sensor 2	Sensor 3	Sensor 4	Sensor 5	Sensor 6	Sensor 7	Sensor 8	Sensor 9	Sensor 10
Sensor 1	0	226263.5	468818.6	4492.808	470093.9	15219.37	15628.05	3387.404	8095.094	2605.643
Sensor 2	226263.5	0	643363.9	1074.813	850.9557	1179.922	466.9438	621.1937	2402.057	6077.573
Sensor 3	468818.6	643363.9	0	17578.42	1313240	51820.61	49080.95	12691.89	33105.58	18716.42
Sensor 4	4492.808	1074.813	17578.42	0	1607.325	83.66709	225.3449	3.686726	5.209926	497.5486
Sensor 5	470093.9	850.9557	1313240	1607.325	0	2128.937	1039.226	955.5322	3559.288	7803.782
Sensor 6	15219.37	1179.922	51820.61	83.66709	2128.937	0	63.03258	32.94933	205.2885	1545.702
Sensor 7	15628.05	466.9438	49080.95	225.3449	1039.226	63.03258	0	119.9207	453.3306	2046.047
Sensor 8	3387.404	621.1937	12691.89	3.686726	955.5322	32.94933	119.9207	0	17.2334	474.8155
Sensor 9	8095.094	2402.057	33105.58	5.209926	3559.288	205.2885	453.3306	17.2334	0	585.5329
Sensor 10	2605.643	6077.573	18716.42	497.5486	7803.782	1545.702	2046.047	474.8155	585.5329	0

Figure A.42: MQ-5 ANOVA f-statistics (15°C, 85% RH).

	Sensor 1	Sensor 2	Sensor 3	Sensor 4	Sensor 5	Sensor 6	Sensor 7	Sensor 8	Sensor 9	Sensor 10
Sensor 1	0	375838.4	772747.9	13661.62	108255.4	44704.19	41523.36	611.7903	6483.519	10595.03
Sensor 2	375838.4	0	1033788	5023.208	509.5576	3753.362	2006.077	92.03999	3190.091	14969.86
Sensor 3	772747.9	1033788	0	61112.73	286939.6	160448.5	140874.3	2333.188	30692.13	68458.3
Sensor 4	13661.62	5023.208	61112.73	0	5775.002	547.7249	901.3137	12.98196	11.95441	636.0183
Sensor 5	108255.4	509.5576	286939.6	5775.002	0	4387.072	2814.35	151.7791	3961.874	14108.63
Sensor 6	44704.19	3753.362	160448.5	547.7249	4387.072	0	83.10638	2.000358	493.3708	3268.11
Sensor 7	41523.36	2006.077	140874.3	901.3137	2814.35	83.10638	0	9.374244	763.6497	3976.246
Sensor 8	611.7903	92.03999	2333.188	12.98196	151.7791	2.000358	9.374244	0	20.97944	88.52757
Sensor 9	6483.519	3190.091	30692.13	11.95441	3961.874	493.3708	763.6497	20.97944	0	276.236
Sensor 10	10595.03	14969.86	68458.3	636.0183	14108.63	3268.11	3976.246	88.52757	276.236	0

Figure A.43: MQ-5 ANOVA f-statistics (20°C, 85% RH).

	Sensor 1	Sensor 2	Sensor 3	Sensor 4	Sensor 5	Sensor 6	Sensor 7	Sensor 8	Sensor 9	Sensor 10
Sensor 1	0	959726	371097.1	9954.477	91615.35	27401.97	15369.65	5987.727	18488.97	1088.8
Sensor 2	959726	0	1473300	3969.799	677.2068	3365.434	316.5257	1464.581	4449.842	2187.128
Sensor 3	371097.1	1473300	0	44268.5	228236.4	98592.55	48520.82	24545.6	73965.32	7756.287
Sensor 4	9954.477	3969.799	44268.5	0	4697.161	280.9873	796.5079	29.34543	53.14292	201.5905
Sensor 5	91615.35	677.2068	228236.4	4697.161	0	3960.875	795.4123	2103.232	4984.518	2754.967
Sensor 6	27401.97	3365.434	98592.55	280.9873	3960.875	0	269.1783	51.01476	110.6651	596.3328
Sensor 7	15369.65	316.5257	48520.82	796.5079	795.4123	269.1783	0	341.5477	577.2314	1029.484
Sensor 8	5987.727	1464.581	24545.6	29.34543	2103.232	51.01476	341.5477	0	0.000397	281.4247
Sensor 9	18488.97	4449.842	73965.32	53.14292	4984.518	110.6651	577.2314	0.000397	0	359.4665
Sensor 10	1088.8	2187.128	7756.287	201.5905	2754.967	596.3328	1029.484	281.4247	359.4665	0

Figure A.44: MQ-5 ANOVA f-statistics (25°C, 85% RH).

	Sensor 1	Sensor 2	Sensor 3	Sensor 4	Sensor 5	Sensor 6	Sensor 7	Sensor 8	Sensor 9	Sensor 10
Sensor 1	0	1594432	134630.9	4559.677	10159.32	28493.89	260605	6358.094	67983.58	474.0128
Sensor 2	1594432	0	807551.2	2174.441	12.48557	5931.659	18234.19	1414.994	18040.84	3225.581
Sensor 3	134630.9	807551.2	0	21459.74	28274.44	100564.3	419735.9	25776.79	200709.6	5986.147
Sensor 4	4559.677	2174.441	21459.74	0	1087.385	99.52072	535.1858	52.0073	61.42561	415.5164
Sensor 5	10159.32	12.48557	28274.44	1087.385	0	999.5753	534.8843	716.0444	1251.463	2157.749
Sensor 6	28493.89	5931.659	100564.3	99.52072	999.5753	0	650.0274	0.736313	27.67757	947.3474
Sensor 7	260605	18234.19	419735.9	535.1858	534.8843	650.0274	0	184.113	2206.2	1647.692
Sensor 8	6358.094	1414.994	25776.79	52.0073	716.0444	0.736313	184.113	0	3.584409	692.3279
Sensor 9	67983.58	18040.84	200709.6	61.42561	1251.463	27.67757	2206.2	3.584409	0	886.7541
Sensor 10	474.0128	3225.581	5986.147	415.5164	2157.749	947.3474	1647.692	692.3279	886.7541	0

Figure A.45: MQ-5 ANOVA f-statistics (30°C, 85% RH).

	Sensor 1	Sensor 2	Sensor 3	Sensor 4	Sensor 5	Sensor 6	Sensor 7	Sensor 8	Sensor 9	Sensor 10
Sensor 1	0	142341.8	167890.3	9000.192	39666.57	32942.34	15237.76	15977.95	14916.16	166.0833
Sensor 2	142341.8	0	307330.2	4297.847	219.8644	4717.967	186.0308	1214.319	3746.825	1225.734
Sensor 3	167890.3	307330.2	0	43570.02	101581.7	118100.9	47860.3	56636.6	62165.44	2303.103
Sensor 4	9000.192	4297.847	43570.02	0	4091.387	264.8639	1188.195	541.747	79.35075	197.3078
Sensor 5	39666.57	219.8644	101581.7	4091.387	0	3716.751	460.945	1536.778	3507.713	1467.123
Sensor 6	32942.34	4717.967	118100.9	264.8639	3716.751	0	656.732	136.9625	47.17091	393.9701
Sensor 7	15237.76	186.0308	47860.3	1188.195	460.945	656.732	0	176.1046	803.0807	814.9488
Sensor 8	15977.95	1214.319	56636.6	541.747	1536.778	136.9625	176.1046	0	253.9422	539.203
Sensor 9	14916.16	3746.825	62165.44	79.35075	3507.713	47.17091	803.0807	253.9422	0	305.9539
Sensor 10	166.0833	1225.734	2303.103	197.3078	1467.123	393.9701	814.9488	539.203	305.9539	0

Figure A.46: MQ-5 ANOVA f-statistics (35°C, 85% RH).

	Sensor 1	Sensor 2	Sensor 3	Sensor 4	Sensor 5	Sensor 6	Sensor 7	Sensor 8	Sensor 9	Sensor 10
Sensor 1	0	58417.89	63687.75	3505.391	17416.35	8966.789	6029.361	2230.862	3369.855	1211.446
Sensor 2	58417.89	0	143383.7	2172.81	138.4559	2362.154	69.28623	325.8922	847.0113	5244.387
Sensor 3	63687.75	143383.7	0	18792.81	45996.05	38876.61	19528.28	9080.959	14872.49	13384.96
Sensor 4	3505.391	2172.81	18792.81	0	2131.549	65.78447	596.9232	99.6238	62.0397	345.7546
Sensor 5	17416.35	138.4559	45996.05	2131.549	0	2039.653	216.2921	509.4321	1054.781	4415.457
Sensor 6	8966.789	2362.154	38876.61	65.78447	2039.653	0	408.2246	27.00718	3.153544	884.5105
Sensor 7	6029.361	69.28623	19528.28	596.9232	216.2921	408.2246	0	90.85824	230.9219	1675.792
Sensor 8	2230.862	325.8922	9080.959	99.6238	509.4321	27.00718	90.85824	0	11.06546	549.5278
Sensor 9	3369.855	847.0113	14872.49	62.0397	1054.781	3.153544	230.9219	11.06546	0	597.2023
Sensor 10	1211.446	5244.387	13384.96	345.7546	4415.457	884.5105	1675.792	549.5278	597.2023	0

Figure A.47: MQ-5 ANOVA f-statistics (40°C, 85% RH).

153

	Sensor 1	Sensor 2	Sensor 3	Sensor 4	Sensor 5	Sensor 6	Sensor 7	Sensor 8	Sensor 9	Sensor 10
Sensor 1	0	176611.9	246911.4	4689.446	17235.58	4664.284	9837.027	9869.382	557.412	129.615
Sensor 2	176611.9	0	489556.5	4645.239	103.8519	1048.317	272.5672	505.9411	259.9098	3843.89
Sensor 3	246911.4	489556.5	0	34041.76	53698.98	23531.01	38476.57	40597.36	3290.967	5487.827
Sensor 4	4689.446	4645.239	34041.76	0	2989.099	225.357	1057.73	873.8941	15.18789	491.9552
Sensor 5	17235.58	103.8519	53698.98	2989.099	0	1037.725	384.2612	570.1235	348.3489	3494.128
Sensor 6	4664.284	1048.317	23531.01	225.357	1037.725	0	190.8776	115.5343	8.895733	973.3264
Sensor 7	9837.027	272.5672	38476.57	1057.73	384.2612	190.8776	0	13.357	96.37183	1924.681
Sensor 8	9869.382	505.9411	40597.36	873.8941	570.1235	115.5343	13.357	0	67.8396	1746.505
Sensor 9	557.412	259.9098	3290.967	15.18789	348.3489	8.895733	96.37183	67.8396	0	238.0138
Sensor 10	129.615	3843.89	5487.827	491.9552	3494.128	973.3264	1924.681	1746.505	238.0138	0

Figure A.48: MQ-5 ANOVA f-statistics (45°C, 85% RH).

	Sensor 1	Sensor 2	Sensor 3	Sensor 4	Sensor 5	Sensor 6	Sensor 7	Sensor 8	Sensor 9	Sensor 10
Sensor 1	0	95970.58	474632.7	2557.803	3605.878	4546.16	3736.817	6595.067	1342.78	9.251627
Sensor 2	95970.58	0	363394.3	4702.111	**0.008858**	1188.212	50.20776	187.968	676.8225	2038.045
Sensor 3	474632.7	363394.3	0	30396.3	14479.07	29287.22	16854.74	31289.43	10025.36	2708.792
Sensor 4	2557.803	4702.111	30396.3	0	1026.937	374.0494	847.6744	1124.136	93.59378	246.7596
Sensor 5	3605.878	**0.008858**	14479.07	1026.937	0	331.4203	23.50199	58.95921	335.9247	1261.581
Sensor 6	4546.16	1188.212	29287.22	374.0494	331.4203	0	192.7883	196.9757	14.63378	674.453
Sensor 7	3736.817	50.20776	16854.74	847.6744	23.50199	192.7883	0	5.887761	212.2507	1089.662
Sensor 8	6595.067	187.968	31289.43	1124.136	58.95921	196.9757	5.887761	0	203.0723	1170.812
Sensor 9	1342.78	676.8225	10025.36	93.59378	335.9247	14.63378	212.2507	203.0723	0	399.4614
Sensor 10	9.251627	2038.045	2708.792	246.7596	1261.581	674.453	1089.662	1170.812	399.4614	0

Figure A.49: MQ-5 ANOVA f-statistics (50°C, 85% RH).

	Sensor 1	Sensor 2	Sensor 3	Sensor 4	Sensor 5	Sensor 6	Sensor 7	Sensor 8	Sensor 9	Sensor 10
Sensor 1	0	1351.524	19.66333	14.0348	461.1635	3.860501	5.57635	73.21043	8.03949	8.03949
Sensor 2	1351.524	0	27288.46	158176.9	16260.4	112364	49588.73	43673.57	48360.57	48360.57
Sensor 3	19.66333	27288.46	0	1159.61	10195.57	101.3832	56.19818	2447.764	719.9599	719.9599
Sensor 4	14.0348	158176.9	1159.61	0	28731.83	3238.897	1358.868	1580.705	38.28113	38.28113
Sensor 5	461.1635	16260.4	10195.57	28731.83	0	31599	16320.13	7501.83	12493.76	12493.76
Sensor 6	3.860501	112364	101.3832	3238.897	31599	0	5.124328	5224.232	863.261	863.261
Sensor 7	5.57635	49588.73	56.19818	1358.868	16320.13	5.124328	0	3097.458	617.1517	617.1517
Sensor 8	73.21043	43673.57	2447.764	1580.705	7501.83	5224.232	3097.458	0	1035.759	1035.759
Sensor 9	8.03949	48360.57	719.9599	38.28113	12493.76	863.261	617.1517	1035.759	0	0
Sensor 10	8.03949	48360.57	719.9599	38.28113	12493.76	863.261	617.1517	1035.759	0	0

Figure A.50: MQ-7 ANOVA f-statistics (20°C, 33% RH).

	Sensor 1	Sensor 2	Sensor 3	Sensor 4	Sensor 5	Sensor 6	Sensor 7	Sensor 8	Sensor 9	Sensor 10
Sensor 1	0	3279.089	256.3707	5.53962	979.2309	162.6781	151.5037	8.267143	15.91587	7384.576
Sensor 2	3279.089	0	1451442	509472.9	91912.6	204671.4	33198.78	889276.3	500130.9	37900947
Sensor 3	256.3707	1451442	0	17650.73	206569.9	354.8465	52.81019	51520.49	13018.66	1173890
Sensor 4	5.53962	509472.9	17650.73	0	80446.25	3591.996	750.3975	2687.228	187.2983	939225.6
Sensor 5	979.2309	91912.6	206569.9	80446.25	0	62827.61	12691.98	77338.17	85289.33	1780269
Sensor 6	162.6781	204671.4	354.8465	3591.996	62827.61	0	0.484565	9127.53	2517.247	217622.8
Sensor 7	151.5037	33198.78	52.81019	750.3975	12691.98	0.484565	0	1691.576	538.3128	35289.74
Sensor 8	8.267143	889276.3	51520.49	2687.228	77338.17	9127.53	1691.576	0	4407.855	2083574
Sensor 9	15.91587	500130.9	13018.66	187.2983	85289.33	2517.247	538.3128	4407.855	0	842925.9
Sensor 10	7384.576	37900947	1173890	939225.6	1780269	217622.8	35289.74	2083574	842925.9	0

Figure A.51: MQ-7 ANOVA f-statistics (25°C, 33% RH).

	Sensor 1	Sensor 2	Sensor 3	Sensor 4	Sensor 5	Sensor 6	Sensor 7	Sensor 8	Sensor 9	Sensor 10
Sensor 1	0	9746.998	848.7372	127.6004	2649.465	1723.633	321.8166	114.9765	23.06735	24241.02
Sensor 2	9746.998	0	2378900	217319	100953.7	197840.2	2795553	559135.6	136191.4	25786418
Sensor 3	848.7372	2378900	0	5332.01	277353.6	1970.079	18397.27	14368.49	7225.731	3560029
Sensor 4	127.6004	217319	5332.01	0	55354.6	6640.771	722.3474	8.169434	335.2754	386482.4
Sensor 5	2649.465	100953.7	277353.6	55354.6	0	76438.02	224921.6	102752.9	33778.59	2226075
Sensor 6	1723.633	197840.2	1970.079	6640.771	76438.02	0	6387.907	8989.718	8413.015	125681.3
Sensor 7	321.8166	2795553	18397.27	722.3474	224921.6	6387.907	0	2370.775	2128.242	7638510
Sensor 8	114.9765	559135.6	14368.49	8.169434	102752.9	8989.718	2370.775	0	356.2384	1098041
Sensor 9	23.06735	136191.4	7225.731	335.2754	33778.59	8413.015	2128.242	356.2384	0	295912.6
Sensor 10	24241.02	25786418	3560029	386482.4	2226075	125681.3	7638510	1098041	295912.6	0

Figure A.52: MQ-7 ANOVA f-statistics (30°C, 33% RH).

	Sensor 1	Sensor 2	Sensor 3	Sensor 4	Sensor 5	Sensor 6	Sensor 7	Sensor 8	Sensor 9	Sensor 10
Sensor 1	0	30121.22	6562.347	1686.079	4979.253	6840.904	2261.271	585.3541	361.3104	95388.06
Sensor 2	30121.22	0	1522212	392172.3	74831.32	348830	188314.7	565266.5	60922.08	18300637
Sensor 3	6562.347	1522212	0	10882.13	161829	285.2347	2809.684	36850.29	5021.088	1621540
Sensor 4	1686.079	392172.3	10882.13	0	60508.75	7404.831	280.435	2016.414	479.4814	645562.2
Sensor 5	4979.253	74831.32	161829	60508.75	0	87733.95	42658.08	55322.15	12931.28	1209469
Sensor 6	6840.904	348830	285.2347	7404.831	87733.95	0	2977.335	17260.9	5249.678	252744
Sensor 7	2261.271	188314.7	2809.684	280.435	42658.08	2977.335	0	2534.166	942.0252	246689.3
Sensor 8	585.3541	565266.5	36850.29	2016.414	55322.15	17260.9	2534.166	0	0.459251	1373326
Sensor 9	361.3104	60922.08	5021.088	479.4814	12931.28	5249.678	942.0252	0.459251	0	126978.2
Sensor 10	95388.06	18300637	1621540	645562.2	1209469	252744	246689.3	1373326	126978.2	0

Figure A.53: MQ-7 ANOVA f-statistics (35°C, 33% RH).

	Sensor 1	Sensor 2	Sensor 3	Sensor 4	Sensor 5	Sensor 6	Sensor 7	Sensor 8	Sensor 9	Sensor 10
Sensor 1	0	155486.5	2027.902	6783.721	24355.97	33439.03	3813.536	203.5319	1663.046	457771.9
Sensor 2	155486.5	0	28740.67	250637.4	126385.2	341059.2	69342.1	18425.73	3328236	16450610
Sensor 3	2027.902	28740.67	0	104.4821	10322.08	1358.157	10.73013	506.0929	1165.73	28272.3
Sensor 4	6783.721	250637.4	104.4821	0	64066.81	10954.88	94.78339	402.9839	5283.994	303595.1
Sensor 5	24355.97	126385.2	10322.08	64066.81	0	126138.7	23037.79	4792.108	123669.5	1847220
Sensor 6	33439.03	341059.2	1358.157	10954.88	126138.7	0	3539.543	4388.925	40890.8	126158.7
Sensor 7	3813.536	69342.1	10.73013	94.78339	23037.79	3539.543	0	557.5811	2303.651	74157.06
Sensor 8	203.5319	18425.73	506.0929	402.9839	4792.108	4388.925	557.5811	0	4.686109	39004.68
Sensor 9	1663.046	3328236	1165.73	5283.994	123669.5	40890.8	2303.651	4.686109	0	3820945
Sensor 10	457771.9	16450610	28272.3	303595.1	1847220	126158.7	74157.06	39004.68	3820945	0

Figure A.54: MQ-7 ANOVA f-statistics (40°C, 33% RH).

	Sensor 1	Sensor 2	Sensor 3	Sensor 4	Sensor 5	Sensor 6	Sensor 7	Sensor 8	Sensor 9	Sensor 10
Sensor 1	0	67920	9556.239	6606.62	8682.14	814.5923	1109.827	2133.943	436.2398	233842.5
Sensor 2	67920	0	833309.7	211714.7	38120.61	3595.168	13484.26	743270.6	87802.81	10676901
Sensor 3	9556.239	833309.7	0	**1.240359**	71064.76	270.4968	7.995046	13235.49	5164.583	959548.4
Sensor 4	6606.62	211714.7	**1.240359**	0	41482.41	272.424	9.322979	4205.39	3498.977	236399.4
Sensor 5	8682.14	38120.61	71064.76	41482.41	0	1786.339	4730.434	41613.65	14035.58	640754.6
Sensor 6	814.5923	3595.168	270.4968	272.424	1786.339	0	205.9613	529.086	631.4453	839.0346
Sensor 7	1109.827	13484.26	7.995046	9.322979	4730.434	205.9613	0	393.8027	614.1376	13338.02
Sensor 8	2133.943	743270.6	13235.49	4205.39	41613.65	529.086	393.8027	0	353.2737	1574529
Sensor 9	436.2398	87802.81	5164.583	3498.977	14035.58	631.4453	614.1376	353.2737	0	216916.1
Sensor 10	233842.5	10676901	959548.4	236399.4	640754.6	839.0346	13338.02	1574529	216916.1	0

Figure A.55: MQ-7 ANOVA f-statistics (45°C, 33% RH).

	Sensor 1	Sensor 2	Sensor 3	Sensor 4	Sensor 5	Sensor 6	Sensor 7	Sensor 8	Sensor 9	Sensor 10
Sensor 1	0	88171.77	16496.13	16299.34	10233.79	53012.51	1880.254	561.1902	1353.471	61955.38
Sensor 2	88171.77	0	634384.1	305155.3	28235.73	366757.4	15559.87	17848.05	174590.6	164686
Sensor 3	16496.13	634384.1	0	1011.905	70060.89	35060.75	153.6304	356.5355	12029.62	45053.75
Sensor 4	16299.34	305155.3	1011.905	0	58827.89	17868.29	40.83392	692.2356	11527.85	37578.23
Sensor 5	10233.79	28235.73	70060.89	58827.89	0	111005.6	5953.857	4721.272	22793.54	93312.32
Sensor 6	53012.51	366757.4	35060.75	17868.29	111005.6	0	964.7594	5741.867	50601.45	15555.23
Sensor 7	1880.254	15559.87	153.6304	40.83392	5953.857	964.7594	0	450.5412	1086.52	8752.937
Sensor 8	561.1902	17848.05	356.5355	692.2356	4721.272	5741.867	450.5412	0	90.27617	20951.55
Sensor 9	1353.471	174590.6	12029.62	11527.85	22793.54	50601.45	1086.52	90.27617	0	57196.25
Sensor 10	61955.38	164686	45053.75	37578.23	93312.32	15555.23	8752.937	20951.55	57196.25	0

Figure A.56: MQ-7 ANOVA f-statistics (50°C, 33% RH).

	Sensor 1	Sensor 2	Sensor 3	Sensor 4	Sensor 5	Sensor 6	Sensor 7	Sensor 8	Sensor 9	Sensor 10
Sensor 1	0	209436.6	26002.28	116.9614	10827.69	2176.103	1939.958	34888.44	268.4358	247154.8
Sensor 2	209436.6	0	544566.6	15374.19	8993.225	26520.48	39290.69	202806.7	13956.88	1106224
Sensor 3	26002.28	544566.6	0	1522.133	37511.79	14.90859	474.348	8139.008	813.3312	137925.8
Sensor 4	116.9614	15374.19	1522.133	0	4071.191	659.5942	345.0035	6032.627	25.38634	25640.58
Sensor 5	10827.69	8993.225	37511.79	4071.191	0	9375.601	10885.04	49515.28	4183.295	156180.1
Sensor 6	2176.103	26520.48	14.90859	659.5942	9375.601	0	109.7654	2085.183	367.1459	16262.33
Sensor 7	1939.958	39290.69	474.348	345.0035	10885.04	109.7654	0	5124.432	135.502	32867.08
Sensor 8	34888.44	202806.7	8139.008	6032.627	49515.28	2085.183	5124.432	0	4184.597	22774.2
Sensor 9	268.4358	13956.88	813.3312	25.38634	4183.295	367.1459	135.502	4184.597	0	19074.23
Sensor 10	247154.8	1106224	137925.8	25640.58	156180.1	16262.33	32867.08	22774.2	19074.23	0

Figure A.57: MQ-7 ANOVA f-statistics (10°C, 85% RH).

	Sensor 1	Sensor 2	Sensor 3	Sensor 4	Sensor 5	Sensor 6	Sensor 7	Sensor 8	Sensor 9	Sensor 10
Sensor 1	0	3303796	40165.81	21739.4	268024.3	11074.04	2053.714	28514.43	1910.064	579375
Sensor 2	3303796	0	530275.8	3090611	241058.6	112347.5	58431.47	135424	61969.5	1636326
Sensor 3	40165.81	530275.8	0	23112.71	185506.3	284.6853	742.5669	7745.478	1008.246	167650.7
Sensor 4	21739.4	3090611	23112.71	0	340324.3	7191.257	783.0882	22826.37	654.9704	500496.2
Sensor 5	268024.3	241058.6	185506.3	340324.3	0	47788.74	20622.14	71200.5	21398.95	887744.2
Sensor 6	11074.04	112347.5	284.6853	7191.257	47788.74	0	1153.976	3474.87	1411.409	44840.02
Sensor 7	2053.714	58431.47	742.5669	783.0882	20622.14	1153.976	0	7485.563	6.411107	51309.65
Sensor 8	28514.43	135424	7745.478	22826.37	71200.5	3474.87	7485.563	0	8279.138	12991.21
Sensor 9	1910.064	61969.5	1008.246	654.9704	21398.95	1411.409	6.411107	8279.138	0	57060.22
Sensor 10	579375	1636326	167650.7	500496.2	887744.2	44840.02	51309.65	12991.21	57060.22	0

Figure A.58: MQ-7 ANOVA f-statistics (15°C, 85% RH).

	Sensor 1	Sensor 2	Sensor 3	Sensor 4	Sensor 5	Sensor 6	Sensor 7	Sensor 8	Sensor 9	Sensor 10
Sensor 1	0	79903419	436659.7	5379.326	98445.14	18404.54	2824.732	1616376	8645.748	2067169
Sensor 2	79903419	0	4308578	206539.3	146459.3	102265	61866.57	6316603	144702.6	5228060
Sensor 3	436659.7	4308578	0	9647.878	325318.2	2579.502	1312.667	269218.3	1455.326	804112.2
Sensor 4	5379.326	206539.3	9647.878	0	46184.92	8151.232	191.1835	87923.2	905.9734	266860.3
Sensor 5	98445.14	146459.3	325318.2	46184.92	0	44634.43	18468.63	789063.2	42254.17	1322464
Sensor 6	18404.54	102265	2579.502	8151.232	44634.43	0	3886.625	2375.331	4108.434	28490.8
Sensor 7	2824.732	61866.57	1312.667	191.1835	18468.63	3886.625	0	20044.67	69.76085	71533.19
Sensor 8	1616376	6316603	269218.3	87923.2	789063.2	2375.331	20044.67	0	36440.1	226785.6
Sensor 9	8645.748	144702.6	1455.326	905.9734	42254.17	4108.434	69.76085	36440.1	0	135652.2
Sensor 10	2067169	5228060	804112.2	266860.3	1322464	28490.8	71533.19	226785.6	135652.2	0

Figure A.59: MQ-7 ANOVA f-statistics (20°C, 85% RH).

	Sensor 1	Sensor 2	Sensor 3	Sensor 4	Sensor 5	Sensor 6	Sensor 7	Sensor 8	Sensor 9	Sensor 10
Sensor 1	0	566258.3	106497.4	24557.31	28999.38	19773.38	1817.736	85484.28	16247.65	1549143
Sensor 2	566258.3	0	5578261	1028932	79740.41	111234.3	28292.35	353437.1	238395	13082697
Sensor 3	106497.4	5578261	0	17215.03	163064.8	3774.288	132.7086	33831.65	217.7803	2889585
Sensor 4	24557.31	1028932	17215.03	0	82847.44	8256.213	83.13499	48701.17	1625.133	1229457
Sensor 5	28999.38	79740.41	163064.8	82847.44	0	42971.62	8377.266	136559	53099.56	1023631
Sensor 6	19773.38	111234.3	3774.288	8256.213	42971.62	0	1898.695	2572.854	3768.493	35592.68
Sensor 7	1817.736	28292.35	132.7086	83.13499	8377.266	1898.695	0	7158.367	34.71459	31314.6
Sensor 8	85484.28	353437.1	33831.65	48701.17	136559	2572.854	7158.367	0	23504.07	37069.89
Sensor 9	16247.65	238395	217.7803	1625.133	53099.56	3768.493	34.71459	23504.07	0	222708.3
Sensor 10	1549143	13082697	2889585	1229457	1023631	35592.68	31314.6	37069.89	222708.3	0

Figure A.60: MQ-7 ANOVA f-statistics (25°C, 85% RH).

	Sensor 1	Sensor 2	Sensor 3	Sensor 4	Sensor 5	Sensor 6	Sensor 7	Sensor 8	Sensor 9	Sensor 10
Sensor 1	0	12912.39	2378.154	1445.024	2121.244	3898.757	774.0525	16585.39	2253.959	40997.2
Sensor 2	12912.39	0	2113664	448051.7	65669.86	27067.37	26172.81	2418243	324344.2	6349034
Sensor 3	2378.154	2113664	0	2185.616	150193.1	1704.405	130.8885	356889.4	**1.445304**	2480100
Sensor 4	1445.024	448051.7	2185.616	0	73344.54	2336.153	**0.542525**	142562.5	927.188	548038.3
Sensor 5	2121.244	65669.86	150193.1	73344.54	0	12641.79	7817.382	425860.1	70989.09	966410.9
Sensor 6	3898.757	27067.37	1704.405	2336.153	12641.79	0	1626.249	398.6547	1618.938	5710.159
Sensor 7	774.0525	26172.81	130.8885	**0.542525**	7817.382	1626.249	0	9418.4	128.8887	30837.82
Sensor 8	16585.39	2418243	356889.4	142562.5	425860.1	398.6547	9418.4	0	73765.21	248866
Sensor 9	2253.959	324344.2	**1.445304**	927.188	70989.09	1618.938	128.8887	73765.21	0	298942.8
Sensor 10	40997.2	6349034	2480100	548038.3	966410.9	5710.159	30837.82	248866	298942.8	0

Figure A.61: MQ-7 ANOVA f-statistics (30°C, 85% RH).

	Sensor 1	Sensor 2	Sensor 3	Sensor 4	Sensor 5	Sensor 6	Sensor 7	Sensor 8	Sensor 9	Sensor 10
Sensor 1	0	104931.2	29687.73	14457.08	16857.23	1714.917	12045.8	26787.4	14305.73	413711.9
Sensor 2	104931.2	0	561267.1	192561.2	91729.11	5519.047	107114.8	92589.1	153941.6	1645293
Sensor 3	29687.73	561267.1	0	17.41433	290722.9	669.5982	385.8318	11365.49	126.9061	629216.4
Sensor 4	14457.08	192561.2	17.41433	0	71609.32	686.0013	373.6768	10327.11	140.5574	202356.7
Sensor 5	16857.23	91729.11	290722.9	71609.32	0	2879.599	40813.03	49306.99	58160.24	1392918
Sensor 6	1714.917	5519.047	669.5982	686.0013	2879.599	0	514.6286	**0.159568**	595.0112	473.7229
Sensor 7	12045.8	107114.8	385.8318	373.6768	40813.03	514.6286	0	6529.146	75.85549	82792.16
Sensor 8	26787.4	92589.1	11365.49	10327.11	49306.99	0.159568	6529.146	0	8436.893	8419.063
Sensor 9	14305.73	153941.6	126.9061	140.5574	58160.24	595.0112	75.85549	8436.893	0	137984.7
Sensor 10	413711.9	1645293	629216.4	202356.7	1392918	473.7229	82792.16	8419.063	137984.7	0

Figure A.62: MQ-7 ANOVA f-statistics (35°C, 85% RH).

	Sensor 1	Sensor 2	Sensor 3	Sensor 4	Sensor 5	Sensor 6	Sensor 7	Sensor 8	Sensor 9	Sensor 10
Sensor 1	0	5297.561	1662.529	1935.606	607.6476	9107.282	1615.795	3539.479	2081.903	25234.16
Sensor 2	5297.561	0	220228.4	86097.68	28687.96	271635.6	17243.29	14343.96	122655.5	780836.5
Sensor 3	1662.529	220228.4	0	263.4584	128055.6	56866.04	241.3302	1956.538	563.9642	787388.7
Sensor 4	1935.606	86097.68	263.4584	0	35480.17	15852.57	85.5161	1565.881	**2.279035**	100651.7
Sensor 5	607.6476	28687.96	128055.6	35480.17	0	182145.6	6791.625	7662.93	55133.65	782656.8
Sensor 6	9107.282	271635.6	56866.04	15852.57	182145.6	0	1788.806	38.57138	21984.16	57297.03
Sensor 7	1615.795	17243.29	241.3302	85.5161	6791.625	1788.806	0	830.0041	78.07757	11416.05
Sensor 8	3539.479	14343.96	1956.538	1565.881	7662.93	38.57138	830.0041	0	1566.042	1216.904
Sensor 9	2081.903	122655.5	563.9642	**2.279035**	55133.65	21984.16	78.07757	1566.042	0	162537.1
Sensor 10	25234.16	780836.5	787388.7	100651.7	782656.8	57297.03	11416.05	1216.904	162537.1	0

Figure A.63: MQ-7 ANOVA f-statistics (40°C, 85% RH).

	Sensor 1	Sensor 2	Sensor 3	Sensor 4	Sensor 5	Sensor 6	Sensor 7	Sensor 8	Sensor 9	Sensor 10
Sensor 1	0	11928.19	4037.038	4313.349	834.6824	26245.7	6037.555	34561.8	5910.015	68701.6
Sensor 2	11928.19	0	387037.2	96290.8	61074.02	385887.4	51183.96	1272556	198925.6	2188462
Sensor 3	4037.038	387037.2	0	370.4798	133443.6	72672.18	2008.59	649328.9	2150.143	2315119
Sensor 4	4313.349	96290.8	370.4798	0	31168.76	21649.69	840.4382	40443.73	103.2252	116185.6
Sensor 5	834.6824	61074.02	133443.6	31168.76	0	209167.7	20039.69	843363.9	70736.73	1728798
Sensor 6	26245.7	385887.4	72672.18	21649.69	209167.7	0	4430.057	1073.338	30915.58	52735.36
Sensor 7	6037.555	51183.96	2008.59	840.4382	20039.69	4430.057	0	7306.181	614.7507	27795.5
Sensor 8	34561.8	1272556	649328.9	40443.73	843363.9	1073.338	7306.181	0	83407.95	869562.6
Sensor 9	5910.015	198925.6	2150.143	103.2252	70736.73	30915.58	614.7507	83407.95	0	259038.7
Sensor 10	68701.6	2188462	2315119	116185.6	1728798	52735.36	27795.5	869562.6	259038.7	0

Figure A.64: MQ-7 ANOVA f-statistics (45°C, 85% RH).

	Sensor 1	Sensor 2	Sensor 3	Sensor 4	Sensor 5	Sensor 6	Sensor 7	Sensor 8	Sensor 9	Sensor 10
Sensor 1	0	9871.733	4291.875	9586.032	602.9012	29408.21	8705.246	36698.92	7429.504	73333.81
Sensor 2	9871.733	0	347633.5	207107	45350.3	129665.3	68285.54	738977.1	221348.5	1479944
Sensor 3	4291.875	347633.5	0	11049.35	137482.9	34150.42	4491.325	359553.6	6268.19	1967474
Sensor 4	9586.032	207107	11049.35	0	90146.8	17125.58	320.7144	48673.34	894.6174	194335.4
Sensor 5	602.9012	45350.3	137482.9	90146.8	0	77840.43	29800.32	493167.8	90549.3	1206538
Sensor 6	29408.21	129665.3	34150.42	17125.58	77840.43	0	8246.177	1292.984	22179.14	2598.652
Sensor 7	8705.246	68285.54	4491.325	320.7144	29800.32	8246.177	0	8279.773	1201.991	35182.06
Sensor 8	36698.92	738977.1	359553.6	48673.34	493167.8	1292.984	8279.773	0	83489.02	99049.34
Sensor 9	7429.504	221348.5	6268.19	894.6174	90549.3	22179.14	1201.991	83489.02	0	309239.6
Sensor 10	73333.81	1479944	1967474	194335.4	1206538	2598.652	35182.06	99049.34	309239.6	0

Figure A.65: MQ-7 ANOVA f-statistics (50°C, 85% RH).

	Sensor 1	Sensor 2	Sensor 3	Sensor 4	Sensor 5	Sensor 6	Sensor 7	Sensor 8	Sensor 9	Sensor 10
Sensor 1	0	7273.92	16479.6	324.3653	1062.741	11366.39	20899.62	39494.84	27235.75	26612.16
Sensor 2	7273.92	0	215.4789	7854.917	1051.378	822.7895	2882.51	7797.799	4475.592	3173.091
Sensor 3	16479.6	215.4789	0	35724.95	2207.579	606.0906	4245.392	142748.8	9947.087	11783.29
Sensor 4	324.3653	7854.917	35724.95	0	572.174	12595.47	29546.54	103934.6	45860.56	54610.42
Sensor 5	1062.741	1051.378	2207.579	572.174	0	2806.421	5212.785	8568.253	6539.93	5366.152
Sensor 6	11366.39	822.7895	606.0906	12595.47	2806.421	0	305.0091	1425.822	666.7007	167.4133
Sensor 7	20899.62	2882.51	4245.392	29546.54	5212.785	305.0091	0	577.5519	83.09687	102.0514
Sensor 8	39494.84	7797.799	142748.8	103934.6	8568.253	1425.822	577.5519	0	285.5768	5946.437
Sensor 9	27235.75	4475.592	9947.087	45860.56	6539.93	666.7007	83.09687	285.5768	0	658.8141
Sensor 10	26612.16	3173.091	11783.29	54610.42	5366.152	167.4133	102.0514	5946.437	658.8141	0

Figure A.66: MQ-135 ANOVA f-statistics (20°C, 33% RH).

	Sensor 1	Sensor 2	Sensor 3	Sensor 4	Sensor 5	Sensor 6	Sensor 7	Sensor 8	Sensor 9	Sensor 10
Sensor 1	0	152130.2	1393.123	500.7338	26409.44	54599.18	67923.41	565802.4	395817	317611.2
Sensor 2	152130.2	0	14.629	67570.79	95488.07	977.6196	4605.44	188060.9	82746.57	45366.63
Sensor 3	1393.123	14.629	0	1129.245	426.3165	93.13335	291.7896	924.2481	637.9094	426.6184
Sensor 4	500.7338	67570.79	1129.245	0	8514.461	37610.22	48567.51	229754.7	176858.5	145308.8
Sensor 5	26409.44	95488.07	426.3165	8514.461	0	25804.11	36792.26	810270.2	420220.6	298786.9
Sensor 6	54599.18	977.6196	93.13335	37610.22	25804.11	0	825.2989	12670.79	6785.899	3286.219
Sensor 7	67923.41	4605.44	291.7896	48567.51	36792.26	825.2989	0	4596.925	1611.543	275.5592
Sensor 8	565802.4	188060.9	924.2481	229754.7	810270.2	12670.79	4596.925	0	10530.72	29626.51
Sensor 9	395817	82746.57	637.9094	176858.5	420220.6	6785.899	1611.543	10530.72	0	4234.3
Sensor 10	317611.2	45366.63	426.6184	145308.8	298786.9	3286.219	275.5592	29626.51	4234.3	0

Figure A.67: MQ-135 ANOVA f-statistics (25°C, 33% RH).

	Sensor 1	Sensor 2	Sensor 3	Sensor 4	Sensor 5	Sensor 6	Sensor 7	Sensor 8	Sensor 9	Sensor 10
Sensor 1	0	9710.418	2616.67	63.21842	3855.914	25058.05	2890.347	84640.78	62008.72	61699.56
Sensor 2	9710.418	0	215.028	11473.62	5243.566	46.24234	377.4981	6119.633	2829.095	2385.51
Sensor 3	2616.67	215.028	0	2566.088	784.7346	440.754	6.95735	4242.28	2491.419	2216.416
Sensor 4	63.21842	11473.62	2566.088	0	8954.647	49427.24	2899.882	309936.6	200043.2	230116.2
Sensor 5	3855.914	5243.566	784.7346	8954.647	0	27597.29	787.9554	338195.7	183209.5	235264.2
Sensor 6	25058.05	46.24234	440.754	49427.24	27597.29	0	766.3307	25672.89	9948.403	8955.308
Sensor 7	2890.347	377.4981	6.95735	2899.882	787.9554	766.3307	0	6188.06	3736.88	3362.567
Sensor 8	84640.78	6119.633	4242.28	309936.6	338195.7	25672.89	6188.06	0	13379.99	43898.46
Sensor 9	62008.72	2829.095	2491.419	200043.2	183209.5	9948.403	3736.88	13379.99	0	619.7425
Sensor 10	61699.56	2385.51	2216.416	230116.2	235264.2	8955.308	3362.567	43898.46	619.7425	0

Figure A.68: MQ-135 ANOVA f-statistics (30°C, 33% RH).

	Sensor 1	Sensor 2	Sensor 3	Sensor 4	Sensor 5	Sensor 6	Sensor 7	Sensor 8	Sensor 9	Sensor 10
Sensor 1	0	7063.341	5930.338	29.23968	2748.206	20082.15	4295.37	104342.6	66737.49	50206.32
Sensor 2	7063.341	0	1225.177	8742.951	4185.568	62.88993	2.521436	3950.759	1108.642	1056.782
Sensor 3	5930.338	1225.177	0	10211.3	2366.384	2444.213	694.015	39309.14	19416.2	15152.02
Sensor 4	29.23968	8742.951	10211.3	0	9544.641	41794.3	5030.363	421788.7	252140.8	114073.6
Sensor 5	2748.206	4185.568	2366.384	9544.641	0	19543.46	2335.282	362180.1	188482.7	74517.38
Sensor 6	20082.15	62.88993	2444.213	41794.3	19543.46	0	18.76998	37815.98	12415.17	8063.7
Sensor 7	4295.37	2.521436	694.015	5030.363	2335.282	18.76998	0	2555.268	770.0066	755.0803
Sensor 8	104342.6	3950.759	39309.14	421788.7	362180.1	37815.98	2555.268	0	48326.78	8455.7
Sensor 9	66737.49	1108.642	19416.2	252140.8	188482.7	12415.17	770.0066	48326.78	0	2.357847
Sensor 10	50206.32	1056.782	15152.02	114073.6	74517.38	8063.7	755.0803	8455.7	2.357847	0

Figure A.69: MQ-135 ANOVA f-statistics (35°C, 33% RH).

	Sensor 1	Sensor 2	Sensor 3	Sensor 4	Sensor 5	Sensor 6	Sensor 7	Sensor 8	Sensor 9	Sensor 10
Sensor 1	0	18356.22	1641.85	74.69721	866.4375	4645.299	12431.77	58391.91	28417.78	36108.77
Sensor 2	18356.22	0	6563.805	81398.61	17207.13	1846.279	**0.026896**	46616.39	3341.017	9818.536
Sensor 3	1641.85	6563.805	0	3881.193	291.8483	782.405	4483.582	32745.42	12702.86	16995.47
Sensor 4	74.69721	81398.61	3881.193	0	3193.171	9566.3	28392.28	474265.8	136099.9	292637.5
Sensor 5	866.4375	17207.13	291.8483	3193.171	0	2379.665	9621.737	78244.44	30589.44	43782.55
Sensor 6	4645.299	1846.279	782.405	9566.3	2379.665	0	1276.244	18847.63	5372.41	7770.268
Sensor 7	12431.77	**0.026896**	4483.582	28392.28	9621.737	1276.244	0	12261.07	1246.831	2624.842
Sensor 8	58391.91	46616.39	32745.42	474265.8	78244.44	18847.63	12261.07	0	24601.29	73837.65
Sensor 9	28417.78	3341.017	12702.86	136099.9	30589.44	5372.41	1246.831	24601.29	0	791.5326
Sensor 10	36108.77	9818.536	16995.47	292637.5	43782.55	7770.268	2624.842	73837.65	791.5326	0

Figure A.70: MQ-135 ANOVA f-statistics (40°C, 33% RH).

	Sensor 1	Sensor 2	Sensor 3	Sensor 4	Sensor 5	Sensor 6	Sensor 7	Sensor 8	Sensor 9	Sensor 10
Sensor 1	0	8918.768	445.5435	163.95	490.0243	2560.316	5333.295	39523.57	16348.25	22365.68
Sensor 2	8918.768	0	11396.1	22500.63	12405.21	4185.032	554.5712	8299.603	239.455	1115.334
Sensor 3	445.5435	11396.1	0	4313.649	**0.361168**	2489.799	5930.904	159407.2	38887.6	78789.44
Sensor 4	163.95	22500.63	4313.649	0	5842.9	11564.51	14246.33	311337.1	79527.59	170771.2
Sensor 5	490.0243	12405.21	**0.361168**	5842.9	0	2895.824	6439.826	259886.9	50071.85	123458.2
Sensor 6	2560.316	4185.032	2489.799	11564.51	2895.824	0	1368.284	61243.04	13419.87	25534.15
Sensor 7	5333.295	554.5712	5930.904	14246.33	6439.826	1368.284	0	15364.57	2075.591	4352.885
Sensor 8	39523.57	8299.603	159407.2	311337.1	259886.9	61243.04	15364.57	0	22544.08	48674.48
Sensor 9	16348.25	239.455	38887.6	79527.59	50071.85	13419.87	2075.591	22544.08	0	1074.671
Sensor 10	22365.68	1115.334	78789.44	170771.2	123458.2	25534.15	4352.885	48674.48	1074.671	0

Figure A.71: MQ-135 ANOVA f-statistics (45°C, 33% RH).

	Sensor 1	Sensor 2	Sensor 3	Sensor 4	Sensor 5	Sensor 6	Sensor 7	Sensor 8	Sensor 9	Sensor 10
Sensor 1	0	26576.16	630.0469	1204.554	111.5745	668.8918	2486.273	70830.37	16176.9	36876.47
Sensor 2	26576.16	0	126598.1	151724.8	117648.9	12517.77	2598.129	219843.5	78.07811	8251.074
Sensor 3	630.0469	126598.1	0	221.2774	3732.581	2963.974	5576.169	334378.9	42449.05	140063.3
Sensor 4	1204.554	151724.8	221.2774	0	6293.259	4016.634	6666.427	391752.8	48589.44	162241.3
Sensor 5	111.5745	117648.9	3732.581	6293.259	0	531.7394	2558.509	394605.1	29860.14	127926.3
Sensor 6	668.8918	12517.77	2963.974	4016.634	531.7394	0	738.4344	41111.5	7951.031	19665.12
Sensor 7	2486.273	2598.129	5576.169	6666.427	2558.509	738.4344	0	14020.81	1743.474	5544.528
Sensor 8	70830.37	219843.5	334378.9	391752.8	394605.1	41111.5	14020.81	0	19888.23	29901.91
Sensor 9	16176.9	78.07811	42449.05	48589.44	29860.14	7951.031	1743.474	19888.23	0	2816.717
Sensor 10	36876.47	8251.074	140063.3	162241.3	127926.3	19665.12	5544.528	29901.91	2816.717	0

Figure A.72: MQ-135 ANOVA f-statistics (50°C, 33% RH).

	Sensor 1	Sensor 2	Sensor 3	Sensor 4	Sensor 5	Sensor 6	Sensor 7	Sensor 8	Sensor 9	Sensor 10
Sensor 1	0	149142.9	41674.05	7986.218	31876.53	66946.34	50382.57	176812.2	109335.5	161773.5
Sensor 2	149142.9	0	86668.54	16992.04	45685.11	468.934	15.22208	20637.96	1771.55	14099.09
Sensor 3	41674.05	86668.54	0	961.9498	24.93283	19453.54	11316.87	108782.4	42186.89	90811.34
Sensor 4	7986.218	16992.04	961.9498	0	730.145	13810.35	9579.311	30744.1	18823.42	28252.84
Sensor 5	31876.53	45685.11	24.93283	730.145	0	17510.75	10500.09	73798.96	33246.31	63849.29
Sensor 6	66946.34	468.934	19453.54	13810.35	17510.75	0	315.8662	1899.196	29.0261	1305.831
Sensor 7	50382.57	15.22208	11316.87	9579.311	10500.09	315.8662	0	3931.169	663.0587	3087.204
Sensor 8	176812.2	20637.96	108782.4	30744.1	73798.96	1899.196	3931.169	0	2730.53	127.1334
Sensor 9	109335.5	1771.55	42186.89	18823.42	33246.31	29.0261	663.0587	2730.53	0	1720.36
Sensor 10	161773.5	14099.09	90811.34	28252.84	63849.29	1305.831	3087.204	127.1334	1720.36	0

Figure A.73: MQ-135 ANOVA f-statistics (10°C, 85% RH).

	Sensor 1	Sensor 2	Sensor 3	Sensor 4	Sensor 5	Sensor 6	Sensor 7	Sensor 8	Sensor 9	Sensor 10
Sensor 1	0	53207.83	15132.12	11017.58	20000.59	67808.15	64731.83	108422.2	80827.42	93600.78
Sensor 2	53207.83	0	43753.65	53516.82	33260.56	237.9375	441.5324	5514.048	397.4287	3698.551
Sensor 3	15132.12	43753.65	0	2772.849	3256.42	81608.51	127001.1	381829.2	184980.6	173226.2
Sensor 4	11017.58	53516.82	2772.849	0	11272.87	97258.15	152702.1	417093	213523.4	197336.8
Sensor 5	20000.59	33260.56	3256.42	11272.87	0	63050.19	90694.15	299432.2	140230.4	138927.4
Sensor 6	67808.15	237.9375	81608.51	97258.15	63050.19	0	2269.679	4865.671	7.379424	2763.298
Sensor 7	64731.83	441.5324	127001.1	152702.1	90694.15	2269.679	0	31735.42	4932.587	15319.47
Sensor 8	108422.2	5514.048	381829.2	417093	299432.2	4865.671	31735.42	0	9591.157	103.933
Sensor 9	80827.42	397.4287	184980.6	213523.4	140230.4	7.379424	4932.587	9591.157	0	4141.66
Sensor 10	93600.78	3698.551	173226.2	197336.8	138927.4	2763.298	15319.47	103.933	4141.66	0

Figure A.74: MQ-135 ANOVA f-statistics (15°C, 85% RH).

	Sensor 1	Sensor 2	Sensor 3	Sensor 4	Sensor 5	Sensor 6	Sensor 7	Sensor 8	Sensor 9	Sensor 10
Sensor 1	0	383815.7	23807.13	76861.25	143418.6	306198.1	79726.8	1174414	360838.9	832991.3
Sensor 2	383815.7	0	13949.5	206939.4	135709.4	211.3084	974.8846	18044.27	5.201642	14560.92
Sensor 3	23807.13	13949.5	0	3724.43	671.0142	11829.49	5319.615	30576.26	14023.5	29721.9
Sensor 4	76861.25	206939.4	3724.43	0	15544.67	154127.2	32024.81	1060902	192118.7	609769.3
Sensor 5	143418.6	135709.4	671.0142	15544.67	0	98950.64	19190.97	770018.3	126346.5	442098.6
Sensor 6	306198.1	211.3084	11829.49	154127.2	98950.64	0	494.7386	18873.87	265.8198	15930.07
Sensor 7	79726.8	974.8846	5319.615	32024.81	19190.97	494.7386	0	8379.176	1037.793	8145.045
Sensor 8	1174414	18044.27	30576.26	1060902	770018.3	18873.87	8379.176	0	15497.79	13.88958
Sensor 9	360838.9	5.201642	14023.5	192118.7	126346.5	265.8198	1037.793	15497.79	0	12799.1
Sensor 10	832991.3	14560.92	29721.9	609769.3	442098.6	15930.07	8145.045	13.88958	12799.1	0

Figure A.75: MQ-135 ANOVA f-statistics (20°C, 85% RH).

	Sensor 1	Sensor 2	Sensor 3	Sensor 4	Sensor 5	Sensor 6	Sensor 7	Sensor 8	Sensor 9	Sensor 10
Sensor 1	0	184621.8	50880.59	15867.47	40879.94	85065.39	59266.31	373571.7	215835.6	385016.6
Sensor 2	184621.8	0	72174.67	101111.6	105790.4	798.2086	3621.273	11486.24	47.15167	14667.32
Sensor 3	50880.59	72174.67	0	8432.59	1937.283	22131.03	10757.98	259997.4	92315.56	273217.5
Sensor 4	15867.47	101111.6	8432.59	0	3639.081	40155.13	24180.35	249757.1	120494.6	260442.1
Sensor 5	40879.94	105790.4	1937.283	3639.081	0	31730.86	16822.45	415864.5	142429.1	432273.3
Sensor 6	85065.39	798.2086	22131.03	40155.13	31730.86	0	781.5017	8804.174	647.3377	10425.17
Sensor 7	59266.31	3621.273	10757.98	24180.35	16822.45	781.5017	0	15298.79	3485.701	17229.86
Sensor 8	373571.7	11486.24	259997.4	249757.1	415864.5	8804.174	15298.79	0	22073.31	1026.865
Sensor 9	215835.6	47.15167	92315.56	120494.6	142429.1	647.3377	3485.701	22073.31	0	27498.13
Sensor 10	385016.6	14667.32	273217.5	260442.1	432273.3	10425.17	17229.86	1026.865	27498.13	0

Figure A.76: MQ-135 ANOVA f-statistics (25°C, 85% RH).

	Sensor 1	Sensor 2	Sensor 3	Sensor 4	Sensor 5	Sensor 6	Sensor 7	Sensor 8	Sensor 9	Sensor 10
Sensor 1	0	2985397	161812.5	28014.84	41641.83	16844.27	151567.6	1327728	1466791	3485644
Sensor 2	2985397	0	327304.3	187098.2	91307.16	1397.967	41731.32	23529.09	1198.595	80200.32
Sensor 3	161812.5	327304.3	0	4816.963	5.567898	3744.576	17163.33	322701.2	230293.3	537896.8
Sensor 4	28014.84	187098.2	4816.963	0	2445.712	6519.401	26881.73	223896.1	155308.9	292525.9
Sensor 5	41641.83	91307.16	5.567898	2445.712	0	3569.455	9930.373	124565.5	76678.73	156675.9
Sensor 6	16844.27	1397.967	3744.576	6519.401	3569.455	0	392.046	4001.228	1050.866	4834.675
Sensor 7	151567.6	41731.32	17163.33	26881.73	9930.373	392.046	0	71755.06	31659.42	98616.57
Sensor 8	1327728	23529.09	322701.2	223896.1	124565.5	4001.228	71755.06	0	25534.2	1041.138
Sensor 9	1466791	1198.595	230293.3	155308.9	76678.73	1050.866	31659.42	25534.2	0	63734.04
Sensor 10	3485644	80200.32	537896.8	292525.9	156675.9	4834.675	98616.57	1041.138	63734.04	0

Figure A.77: MQ-135 ANOVA f-statistics (30°C, 85% RH).

	Sensor 1	Sensor 2	Sensor 3	Sensor 4	Sensor 5	Sensor 6	Sensor 7	Sensor 8	Sensor 9	Sensor 10
Sensor 1	0	53979.27	2564.644	2556.274	5668.917	22358.98	18066.13	76504.6	49974.15	87206.7
Sensor 2	53979.27	0	25731.81	78674.22	45340.37	2978.299	10774.54	3375.044	1991.502	8145.905
Sensor 3	2564.644	25731.81	0	177.5164	174.3437	8634.316	5382.459	39279.43	21750.04	45858.3
Sensor 4	2556.274	78674.22	177.5164	0	1448.875	18788.5	14418.27	146682.7	83259.41	189722.6
Sensor 5	5668.917	45340.37	174.3437	1448.875	0	10329.56	6374.761	82726.03	42709.74	104544
Sensor 6	22358.98	2978.299	8634.316	18788.5	10329.56	0	886.0087	8338.527	1113.679	11537.59
Sensor 7	18066.13	10774.54	5382.459	14418.27	6374.761	886.0087	0	23948.19	7113.037	31724.07
Sensor 8	76504.6	3375.044	39279.43	146682.7	82726.03	8338.527	23948.19	0	21328.28	1964.015
Sensor 9	49974.15	1991.502	21750.04	83259.41	42709.74	1113.679	7113.037	21328.28	0	51315.57
Sensor 10	87206.7	8145.905	45858.3	189722.6	104544	11537.59	31724.07	1964.015	51315.57	0

Figure A.78: MQ-135 ANOVA f-statistics (35°C, 85% RH).

	Sensor 1	Sensor 2	Sensor 3	Sensor 4	Sensor 5	Sensor 6	Sensor 7	Sensor 8	Sensor 9	Sensor 10
Sensor 1	0	7820.226	219.8323	303.9908	824.5873	4498.526	2729.676	10725.73	6220.85	12195.26
Sensor 2	7820.226	0	37839.28	25493.73	21281.35	3553.097	11859.64	586.5	1677.414	1716.701
Sensor 3	219.8323	37839.28	0	94.02197	2748.464	42256.93	50862.43	213619.3	170846.1	324248.9
Sensor 4	303.9908	25493.73	94.02197	0	928.4599	19595.31	13118.09	74888.37	43082.8	95177.8
Sensor 5	824.5873	21281.35	2748.464	928.4599	0	15318.85	8838.493	80965.42	43849.22	109870.1
Sensor 6	4498.526	3553.097	42256.93	19595.31	15318.85	0	5158.768	21034.44	2263.082	34408.68
Sensor 7	2729.676	11859.64	50862.43	13118.09	8838.493	5158.768	0	133022.2	102831.8	304022.3
Sensor 8	10725.73	586.5	213619.3	74888.37	80965.42	21034.44	133022.2	0	38548.7	1953.354
Sensor 9	6220.85	1677.414	170846.1	43082.8	43849.22	2263.082	102831.8	38548.7	0	132266.7
Sensor 10	12195.26	1716.701	324248.9	95177.8	109870.1	34408.68	304022.3	1953.354	132266.7	0

Figure A.79: MQ-135 ANOVA f-statistics (40°C, 85% RH).

	Sensor 1	Sensor 2	Sensor 3	Sensor 4	Sensor 5	Sensor 6	Sensor 7	Sensor 8	Sensor 9	Sensor 10
Sensor 1	0	162293	1806.858	5501.815	9648.814	12052.9	17453.77	185291.2	17552.35	579061.2
Sensor 2	162293	0	177101.2	70160.45	41791.03	2737.957	11143.55	1455.825	2836.705	5513.641
Sensor 3	1806.858	177101.2	0	3084.017	6987.22	10283.91	14769.78	200809.4	15282.53	1039791
Sensor 4	5501.815	70160.45	3084.017	0	918.9403	5718.849	6125.928	86713.21	8434.652	172580
Sensor 5	9648.814	41791.03	6987.22	918.9403	0	3269.877	2620.085	54332.92	4922.846	94615.82
Sensor 6	12052.9	2737.957	10283.91	5718.849	3269.877	0	353.264	4979.034	18.82037	6949.269
Sensor 7	17453.77	11143.55	14769.78	6125.928	2620.085	353.264	0	17045.46	678.351	25928.81
Sensor 8	185291.2	1455.825	200809.4	86713.21	54332.92	4979.034	17045.46	0	5453.738	461.297
Sensor 9	17552.35	2836.705	15282.53	8434.652	4922.846	18.82037	678.351	5453.738	0	8016.692
Sensor 10	579061.2	5513.641	1039791	172580	94615.82	6949.269	25928.81	461.297	8016.692	0

Figure A.80: MQ-135 ANOVA f-statistics (45°C, 85% RH).

	Sensor 1	Sensor 2	Sensor 3	Sensor 4	Sensor 5	Sensor 6	Sensor 7	Sensor 8	Sensor 9	Sensor 10
Sensor 1	0	676666.1	1535.745	2835.898	12223.61	7325.617	12964.23	154086.2	39731.54	1451817
Sensor 2	676666.1	0	311602.6	87612.48	101099.7	5434.407	24606.46	816.0667	3252.117	10084.34
Sensor 3	1535.745	311602.6	0	4723.121	13848.42	8820.268	15096.78	135250.3	41094.17	464743.2
Sensor 4	2835.898	87612.48	4723.121	0	836.171	3274.637	3559.941	60578.8	17927.89	123781.2
Sensor 5	12223.61	101099.7	13848.42	836.171	0	1924.44	1623.737	59456.59	14467.45	153441
Sensor 6	7325.617	5434.407	8820.268	3274.637	1924.44	0	280.8908	6516.194	1068.319	8823.641
Sensor 7	12964.23	24606.46	15096.78	3559.941	1623.737	280.8908	0	22210.63	4685.924	37679.28
Sensor 8	154086.2	816.0667	135250.3	60578.8	59456.59	6516.194	22210.63	0	4344.752	220.19
Sensor 9	39731.54	3252.117	41094.17	17927.89	14467.45	1068.319	4685.924	4344.752	0	8062.76
Sensor 10	1451817	10084.34	464743.2	123781.2	153441	8823.641	37679.28	220.19	8062.76	0

Figure A.81: MQ-135 ANOVA f-statistics (50°C, 85% RH).

	Sensor 1	Sensor 2	Sensor 3	Sensor 4	Sensor 5	Sensor 6	Sensor 7	Sensor 8	Sensor 9	Sensor 10
Sensor 1	1399.015	17021.73	41223.45	4642.77	3887.006	22130.5	40289.26	81829.97	53374.3	56614.68
Sensor 2	9765.08	221.1924	36.75305	11087.3	1877.781	217.4567	1345.556	4317.1	2301.68	1276.777
Sensor 3	7600.674	24046.76	36275.48	12369.04	10321.8	28855.36	40620.97	56357.77	46826.88	45934.62
Sensor 4	610.4166	598.3303	1085.457	294.4033	**0.002214**	1660.525	2828.583	4175.46	3399.49	2683.193
Sensor 5	5691.29	109.4362	860.0182	5817.549	611.1192	1471.847	4278.178	10745.87	6380.034	4976.215
Sensor 6	2285.311	284.1115	829.8776	1685.043	166.8917	1453.703	3112.158	5507.662	4055.469	3066.334
Sensor 7	2847.632	314.435	1027.743	2245.125	210.1056	1667.785	3765.374	7129.045	5037.294	3876.738
Sensor 8	1788.26	287.6937	747.3988	1235.924	116.301	1339.685	2719.878	4563.057	3466.506	2608.935
Sensor 9	2495.018	2570.268	11486.42	2098.674	**0.024002**	6066.735	15187.53	47617.3	23351.37	24365.75
Sensor 10	39.8301	560.8738	787.1992	**1.11833**	71.9043	1150.105	1650.98	2135.686	1867.877	1525.654

Figure A.82: MQ-5 vs. MQ-135 ANOVA f-statistics (20°C, 33% RH).

	Sensor 1	Sensor 2	Sensor 3	Sensor 4	Sensor 5	Sensor 6	Sensor 7	Sensor 8	Sensor 9	Sensor 10
Sensor 1	16318.62	236450.9	3003.964	15555.62	83756.65	94890.55	110001.6	629123	481243.4	406602.7
Sensor 2	173910	970.3797	40.50499	77572.94	119351.9	324.109	3051.929	160585.4	66181.01	33558.92
Sensor 3	206399.8	853815.3	8833.619	143140.7	504679.4	264524.1	281320.4	1893271	1427388	1233774
Sensor 4	2858.533	6206.449	386.5644	1620.083	**0.171967**	7343.644	11169.76	28008.87	22227.29	17857.64
Sensor 5	7481.887	494.9144	17.92581	5570.319	1862.705	1203.526	2760.142	8856.934	6365.579	4529.368
Sensor 6	**0.51085**	15.26323	11.94807	**0.099364**	**1.355695**	20.92959	29.40898	47.34428	39.78345	33.55492
Sensor 7	12775.46	1739.272	46.66147	8760.848	2751.011	2906.191	5904.708	21587.83	15651.5	11395.65
Sensor 8	2402.126	2153.822	220.3189	1583.083	111.7695	3133.33	5151.399	11900.2	9332.154	7346.543
Sensor 9	100.8101	566.9995	255.8232	50.32099	13.80487	808.3136	1193.585	2083.986	1715.663	1416.636
Sensor 10	219.9196	2914.328	600.1942	77.2817	171.7624	3777.979	5373.538	9750.392	8087.985	6751.154

Figure A.83: MQ-5 vs. MQ-135 ANOVA f-statistics (25°C, 33% RH).

	Sensor 1	Sensor 2	Sensor 3	Sensor 4	Sensor 5	Sensor 6	Sensor 7	Sensor 8	Sensor 9	Sensor 10
Sensor 1	4365.715	25001.8	7083.971	12633.7	43415.38	92894.23	8440	375678.9	270595.2	299577.8
Sensor 2	16375.15	4.113121	298.9283	23974.01	11738.58	38.99479	530.6242	12676.29	5555.782	4777.934
Sensor 3	34655.25	60086.25	21584.34	66101.43	111408.9	162469.3	26223.95	378359.9	309944.2	323081.8
Sensor 4	1473.426	3678.989	749.884	1552.33	19.13862	8652.871	728.3273	36583.82	25211.93	24214.35
Sensor 5	6602.894	280.3171	6.585799	7727.864	2660.74	843.5388	37.91487	11052.73	6217.647	5581.801
Sensor 6	6009.299	1093.769	52.70853	7799.043	1827.37	3209.644	20.71138	25589.35	15572.29	14605.64
Sensor 7	10982.08	425.2904	5.331148	16650.67	6007.183	1801.459	39.6403	28006.43	15342.53	14343.45
Sensor 8	654.0981	1649.929	434.0556	553.6333	0.223278	2611.374	383.1261	9710.416	6791.521	6338.36
Sensor 9	81.53076	463.7006	184.77	57.35808	6.37146	580.1287	154.721	1860.946	1337.876	1244.343
Sensor 10	0.306768	497.5301	268.3487	0.362377	65.56142	580.8198	239.8011	1458.1	1110.963	1047.113

Figure A.84: MQ-5 vs. MQ-135 ANOVA f-statistics (30°C, 33% RH).

	Sensor 1	Sensor 2	Sensor 3	Sensor 4	Sensor 5	Sensor 6	Sensor 7	Sensor 8	Sensor 9	Sensor 10
Sensor 1	8425.672	18982.4	34532.57	22174.35	74658.77	106569.5	11026.11	1057022	660989	238130.9
Sensor 2	34076.38	8.80715	4863.852	133690.9	78259.74	212.0055	0.087056	268085.2	58362.6	13095.12
Sensor 3	62547.42	49607.01	109171.1	139924.8	234228.2	241272.4	29715.21	1056456	791584.4	413095.9
Sensor 4	726.3482	3260.951	1235.339	1203.787	30.42896	5987.267	2082.383	34675.6	20727.52	18075.9
Sensor 5	5940.27	204.4602	440.4751	7873.278	3002.222	125.7651	108.2995	9388.659	3793.019	3471.223
Sensor 6	8570.612	1337.049	1.06448	19073.59	4712.365	3695.025	723.3176	83474	39920.65	24895.49
Sensor 7	1254.858	410.088	2.451253	1488.334	363.864	331.0633	293.6821	4319.73	2135.755	2092.437
Sensor 8	1578.475	266.0976	35.57209	1850.981	557.294	185.151	183.9015	3700.149	1714.094	1682.432
Sensor 9	344.048	1198.15	221.6034	443.5189	2.897693	1216.892	915.8702	6781.507	3971.306	3878.397
Sensor 10	3.354958	1971.334	823.5643	0.160489	250.2043	2011.565	1633.106	6797.569	4509.473	4447.716

Figure A.85: MQ-5 vs. MQ-135 ANOVA f-statistics (35°C, 33% RH).

	Sensor 1	Sensor 2	Sensor 3	Sensor 4	Sensor 5	Sensor 6	Sensor 7	Sensor 8	Sensor 9	Sensor 10
Sensor 1	5399.865	241072.3	16480.93	30399.98	22142.19	26740.68	64222.26	2686498	388475.5	1727216
Sensor 2	17515.84	917.9867	5437.599	147171	17117.48	1093.958	238.5127	329037	13163.63	84439.05
Sensor 3	37380.25	308991.7	58359.22	117732	81871.19	73655.35	133475.3	810298.3	402586.2	629828.7
Sensor 4	240.9935	10877.43	528.1422	773.5467	99.14346	2445.411	7776.513	38854.82	17920.18	22697.33
Sensor 5	9138.441	1717.654	2187.16	27516.36	6302.942	165.5947	894.7959	36536.67	7403.245	13008.26
Sensor 6	2129.07	2874.591	109.5208	4024.244	683.5321	206.105	2189.359	17179.69	6233.169	8241.357
Sensor 7	1235.059	1230.159	76.82131	1890.852	381.0036	94.47781	1074.383	7222.244	2689.985	3428.306
Sensor 8	870.1077	682.2259	67.64343	1225.366	277.0288	45.27435	625.8537	4153.474	1531.148	1938.457
Sensor 9	155.7144	613.7487	3.59238	230.1028	12.06194	144.4923	590.259	2460.555	1106.31	1320.219
Sensor 10	93.16695	1765.856	485.2603	61.69	311.5669	944.8349	1717.095	4007.849	2430.461	2699.809

Figure A.86: MQ-5 vs. MQ-135 ANOVA f-statistics (40°C, 33% RH).

	Sensor 1	Sensor 2	Sensor 3	Sensor 4	Sensor 5	Sensor 6	Sensor 7	Sensor 8	Sensor 9	Sensor 10
Sensor 1	4204.073	48909.81	37927.8	17343.26	60792.06	44868.39	35498.13	1574356	223229.3	816255.8
Sensor 2	9785.515	480.4682	23470.7	60591.67	32226.27	5059.908	86.37895	81497.26	4516.201	18121.77
Sensor 3	29953.23	113782.4	140131.5	113874.8	188220.1	133142.9	93953.5	1039276	365511.1	726041
Sensor 4	49.65027	7646.512	146.5894	499.8372	164.8462	1791.992	4341.261	36547.87	14366.32	19991.85
Sensor 5	4975.799	574.0342	5279.853	12769.82	5689.359	1190.919	1.032001	14240.73	2021.996	4122.544
Sensor 6	1444.776	3309.734	803.559	4365.35	849.5042	34.88034	1231.001	25680.34	7358.973	11451.79
Sensor 7	2329.363	1047.271	1697.931	5020.87	1760.126	176.0915	178.5668	10572.46	2373.2	3897.667
Sensor 8	2370.154	3303.796	1970.832	8412.048	2179.108	4.231841	1033.05	37330.43	9009.426	15568.7
Sensor 9	0.22299	560.1029	23.37503	4.442155	24.03283	131.5464	338.9704	1497.219	708.9741	864.47
Sensor 10	12.74219	1509.09	108.0138	0.08099	110.6925	421.2704	952.4891	3936.535	1930.858	2339.956

Figure A.87: MQ-5 vs. MQ-135 ANOVA f-statistics (45°C, 33% RH).

	Sensor 1	Sensor 2	Sensor 3	Sensor 4	Sensor 5	Sensor 6	Sensor 7	Sensor 8	Sensor 9	Sensor 10
Sensor 1	11152.68	672640	20119.61	16386.94	62629.26	16517.26	17194	1917919	112270.2	494225.8
Sensor 2	14113.21	14999.66	68191.54	83347.63	51836.79	5350.84	496.7864	244663.6	1985.983	31046.53
Sensor 3	66944.4	1134992	157890.5	153624.1	281658.1	70991.45	56335.8	2216643	268829.6	891875.8
Sensor 4	111.2291	13715.14	26.0767	131.1124	364.9094	916.1426	2534.387	32947.97	10506.29	19150.29
Sensor 5	5152.485	2136.939	11740.7	13749.17	6386.281	1965.478	126.8698	17313.07	1194.38	5671.877
Sensor 6	1293.121	13032.79	4999.056	6524.916	1344.891	62.1951	471.4234	47118.62	7599.104	21090.31
Sensor 7	7778.396	11608.77	29004.06	35203.24	16747.02	2475.762	54.49151	83901.56	3773.576	23371.42
Sensor 8	648.7759	557.317	1204.068	1432.517	528.9899	198.4219	**0.169778**	2902.272	441.76	1209.274
Sensor 9	76.24232	3161.843	404.5806	585.4283	23.30168	29.83625	502.7931	9210.219	2644.309	4976.004
Sensor 10	69.26127	1885.279	6.656579	**0.162518**	117.8613	263.1428	679.733	4157.588	1720.902	2620.614

Figure A.88: MQ-5 vs. MQ-135 ANOVA f-statistics (50°C, 33% RH).

	Sensor 1	Sensor 2	Sensor 3	Sensor 4	Sensor 5	Sensor 6	Sensor 7	Sensor 8	Sensor 9	Sensor 10
Sensor 1	1323.137	147715.7	31860.11	4456.111	23043.23	57574.62	41925.59	173649.1	99886.25	156614.8
Sensor 2	40235.76	607.6648	6805.437	6743.65	6456.714	1107.278	233.4047	6426.284	1878.252	5340.704
Sensor 3	2233.889	31775.54	15057.64	8747.566	14222.93	29983.29	25757.83	41908.29	33841.26	40358.36
Sensor 4	5005.647	2913.583	**0.000495**	240.7146	**2.044561**	3414.281	2254.457	6752.958	4068.873	6207.022
Sensor 5	32704.6	**0.003374**	6837.191	7386.615	6690.386	150.8705	5.22868	2003.36	305.928	1569.974
Sensor 6	69408.31	17538.09	9838.551	5610.804	7338.65	6468.262	2764.783	43888.29	14070.11	35902.28
Sensor 7	17051.05	1554.068	1339.418	2461.871	1403.996	2054.166	955.8838	6232.007	2797.324	5486.006
Sensor 8	21871.9	6514.829	655.9248	1778.37	721.2878	5850.692	3267.297	17325.91	8575.677	15411.78
Sensor 9	1721.596	498.8705	22.51382	172.8134	29.90729	698.4333	436.1108	1367.182	790.203	1250.11
Sensor 10	628.4865	2972.37	429.1033	85.87306	386.4695	3409.305	2636.796	5254.168	3743.824	4958.921

Figure A.89: MQ-5 vs. MQ-135 ANOVA f-statistics (10°C, 85% RH).

	Sensor 1	Sensor 2	Sensor 3	Sensor 4	Sensor 5	Sensor 6	Sensor 7	Sensor 8	Sensor 9	Sensor 10
Sensor 1	498.9521	126538.4	131854.2	80806.12	171939.6	227550.4	463069	1088502	568297	435421.8
Sensor 2	51001.74	1901.564	58331.44	74378.64	40062.52	5115.935	1373.13	33224.87	9048.105	19682.96
Sensor 3	14993.27	313334.6	860277	657253.1	916465.9	548885.1	1270699	2571571	1422481	978214.7
Sensor 4	4982.899	2254.176	423.3474	818.6384	142.3239	2966.285	1768.352	5573.559	3168.192	5099.01
Sensor 5	62956.02	722.0044	124266.7	150166.5	87662.19	3035.985	101.4808	37210.6	6608.275	17804.12
Sensor 6	13048.68	3068.13	2446.275	3850.391	1278.828	4504.337	2418.885	10159.06	5106.437	8859.639
Sensor 7	13779.07	1785.142	3197.086	4653.086	1921.552	2761.248	1230.986	6857.586	3113.176	5973.323
Sensor 8	3912.063	1413.694	384.2326	691.2684	154.036	1865.834	1059.66	3556.685	1973.089	3270.709
Sensor 9	7849.581	4547.586	617.6366	1299.762	163.0331	6106.402	3887.259	11681.15	6740.934	10459.44
Sensor 10	3100.816	8856.651	91.61217	**0.899235**	433.4765	10999.89	8249.353	17875.95	11942.03	16350.12

Figure A.90: MQ-5 vs. MQ-135 ANOVA f-statistics (15°C, 85% RH).

	Sensor 1	Sensor 2	Sensor 3	Sensor 4	Sensor 5	Sensor 6	Sensor 7	Sensor 8	Sensor 9	Sensor 10
Sensor 1	1965.879	521858.7	21275.84	130655.2	266456.5	384971.3	78077.36	4133914	474717.7	1599494
Sensor 2	277380.7	8714.742	5521.956	121499.1	67697.65	5194.637	357.6921	70426.68	8632.296	55211.36
Sensor 3	194238.6	1243689	89391.58	966166.5	1283927	943930	207895.3	7655658	1131250	3266424
Sensor 4	15734.58	11811.05	29.60977	2028.555	227.0625	10189.28	5141.973	24247.19	11900.94	23811.46
Sensor 5	107023.3	1217.828	6129.224	43942.64	26405.39	598.4341	**0.397233**	11350.93	1291.928	10828.23
Sensor 6	47120.76	13017.3	379.0004	11059.66	3841.093	10510.54	3658.006	34559.49	13067.25	32976.94
Sensor 7	44147.7	8721.707	720.2883	11583.11	4671.294	6948.4	2376.78	24404.59	8807.206	23552.97
Sensor 8	719.4347	279.0501	5.535186	140.6217	40.98382	240.0221	148.425	595.5497	285.0374	602.0293
Sensor 9	7716.203	7133.128	64.60972	817.2307	45.50026	6264.07	3672.347	13730.76	7214.236	13660.11
Sensor 10	12770.74	28022.61	1135.513	245.8491	427.7925	24588.01	12235.15	52626.49	28002.57	50897.73

Figure A.91: MQ-5 vs. MQ-135 ANOVA f-statistics (20°C, 85% RH).

	Sensor 1	Sensor 2	Sensor 3	Sensor 4	Sensor 5	Sensor 6	Sensor 7	Sensor 8	Sensor 9	Sensor 10
Sensor 1	19.83894	457096	150036.4	32571.41	146810.5	124663.3	82178.37	3880154	764062.6	3738948
Sensor 2	161062.4	16740.44	43976.03	73003.4	84145.73	2192.622	42.09137	181671.1	22832.28	197005.2
Sensor 3	70583.16	870688.4	496194	213273.4	529287.5	293753.3	215755.6	3201881	1280558	3190929
Sensor 4	9027.595	10488.59	3.54207	1231.233	154.2984	6258.721	3419.316	19525.18	10365.4	20797.92
Sensor 5	66535.7	1714.076	14656.19	29358.07	21627.21	161.4477	208.1472	10396.92	1547.709	11983.95
Sensor 6	22253.84	12058.49	596.316	5191.373	1947.534	5861.143	2546.516	26704.01	12123.62	28727.97
Sensor 7	14227.85	2875.764	1215.015	4448.417	2263.573	1346.993	362.5183	7092.064	2725.629	7769.373
Sensor 8	5769.547	4562.826	26.8382	1022.389	238.9576	2827.989	1455.125	8570.001	4409.865	9175.213
Sensor 9	15645.65	13020.15	77.56545	2841.465	706.1384	6966.808	3469.514	26369.36	13044.81	28197.27
Sensor 10	1108.064	4520.548	276.2167	5.122183	91.08775	3320.233	2203.845	7093.06	4396.502	7472.62

Figure A.92: MQ-5 vs. MQ-135 ANOVA f-statistics (25°C, 85% RH).

	Sensor 1	Sensor 2	Sensor 3	Sensor 4	Sensor 5	Sensor 6	Sensor 7	Sensor 8	Sensor 9	Sensor 10
Sensor 1	1038.277	2277920	159411.4	30919.53	44579.98	17681.99	154493.1	1226696	1284992	2775480
Sensor 2	2151391	126016.8	143331	96121.13	39140.81	6.206371	6675.324	131986.5	49504.78	384669.3
Sensor 3	151609.4	1048596	324671.5	159359.4	168404.7	50166.73	319826.4	992302.5	898129.6	1277915
Sensor 4	4190.215	5776.035	55.62767	631.7254	63.17691	1164.597	708.874	9531.929	5142.579	10619.95
Sensor 5	9688.86	462.8836	2441.559	4106.503	2404.18	18.74447	386.7468	1624.828	324.2195	1990.096
Sensor 6	26745.55	19663.59	1491.765	5123.449	1290.895	1228.235	1006.484	33370.26	16803.3	39223.6
Sensor 7	264545.9	90941.44	21701.19	30929.06	9957.521	609.4	188.7519	128026.1	64493.85	199420.3
Sensor 8	5911.065	4598.934	320.9331	1287.388	328.25	721.3723	298.3468	8116.159	4022.948	9145.641
Sensor 9	64778.33	55528.16	2532.316	8778.32	1747.797	1687.929	2773.744	84369.67	45709.63	106917.3
Sensor 10	392.302	5929.588	379.6052	48.09049	351.472	2299.069	1847.191	8472.083	5490.291	9146.23

Figure A.93: MQ-5 vs. MQ-135 ANOVA f-statistics (30°C, 85% RH).

	Sensor 1	Sensor 2	Sensor 3	Sensor 4	Sensor 5	Sensor 6	Sensor 7	Sensor 8	Sensor 9	Sensor 10
Sensor 1	322.5997	347496.7	7605.64	18924.02	27899.9	59199	63072.5	1285405	755997.3	4786552
Sensor 2	27937.31	8411.578	9965.731	30059	14651.54	95.66148	702.2629	25217.49	4649.142	37264.7
Sensor 3	25753.59	543359.9	49011.58	123736.5	127059.7	148747.1	172593.3	1091470	803950.8	1567679
Sensor 4	3972.406	13451.52	292.4804	1017.368	69.96553	4201.976	2039.435	20884.75	10444.97	24441.26
Sensor 5	19063.25	1427.576	7779.666	14511.65	8477.325	34.16316	1003.655	4295.467	377.6528	5970.625
Sensor 6	9682.124	20791.96	1585.244	5039.491	1259.527	4058.974	1498.536	38179.21	16666.99	47677.25
Sensor 7	8666.246	3034.436	2708.287	4800.475	2347.047	335.1914	**1.720725**	5834.104	1703.088	7245.522
Sensor 8	7787.471	7052.399	1785.677	3804.675	1409.311	1412.693	268.7843	12274.72	4769.391	14865.39
Sensor 9	6111.036	13941.54	798.5072	2288.104	441.297	3620.095	1486.221	22940.82	10647.33	27396.86
Sensor 10	72.09163	2500.745	63.39419	20.63051	138.8655	1359.513	859.2485	3262.858	2003.318	3594.796

Figure A.94: MQ-5 vs. MQ-135 ANOVA f-statistics (35°C, 85% RH).

	Sensor 1	Sensor 2	Sensor 3	Sensor 4	Sensor 5	Sensor 6	Sensor 7	Sensor 8	Sensor 9	Sensor 10
Sensor 1	109.7459	69299.36	17835.52	8373.363	23423.71	104397.7	203102.1	449204.3	502166.7	724966.3
Sensor 2	4272.305	2919.392	24840.4	14271.23	10305.01	**0.560403**	2605.147	12107.67	1204.337	18361.44
Sensor 3	4603.829	145023	114340	61619.71	103773.9	222309.4	329199.4	549702.5	530735.6	708679.5
Sensor 4	688.4324	5969.972	560.0089	334.2167	13.28939	2391.749	793.4377	9956.881	4288.259	12017.07
Sensor 5	4139.196	562.4256	8560.458	6767.434	4680.362	142.3233	1386.28	1735.658	11.18729	2693.254
Sensor 6	1224.797	7486.147	2075.572	1291.614	305.8443	2769.822	634.1907	15184.46	5921.077	18950.09
Sensor 7	2002.183	1217.83	2444.708	1971.016	1091.115	78.2015	77.15745	2317.499	420.2059	3076.852
Sensor 8	876.3126	1502.96	668.691	517.4463	186.5213	344.6606	27.76614	2359.451	757.3855	2926.553
Sensor 9	951.8117	3096.424	854.0145	612.6898	163.357	913.1493	160.9927	5030.541	1829.802	6175.145
Sensor 10	128.9036	10543.87	2.91613	34.12302	465.8735	5771.08	3104.203	16744.51	8911.501	19565.72

Figure A.95: MQ-5 vs. MQ-135 ANOVA f-statistics (40°C, 85% RH).

	Sensor 1	Sensor 2	Sensor 3	Sensor 4	Sensor 5	Sensor 6	Sensor 7	Sensor 8	Sensor 9	Sensor 10
Sensor 1	2832.089	230369.8	20509.1	13248.94	17585.4	15472.25	24540.88	254055.3	22528.79	1251985
Sensor 2	108914.8	11021.21	122149.4	34722.22	16709.55	46.50328	1729.482	20349.4	**2.24984**	55985.26
Sensor 3	190016.8	520786.8	371573.9	142189.8	124985.4	54501.11	102059.3	539442.2	75541.63	1777237
Sensor 4	2902.305	13171.36	1943.47	407.4354	6.467364	1916.646	1093.549	17803.17	2653.932	22910.06
Sensor 5	13896.65	1040.041	12136.87	7439.875	4756.597	158.1584	1046.654	2431.691	85.52078	3567.575
Sensor 6	3342.453	4613.793	2554.244	1086.053	377.6047	482.9861	88.74495	6775.856	715.9768	8448.062
Sensor 7	7522.384	3253.015	6218.265	3291.419	1716.75	65.36087	60.58936	5382.105	158.6248	7124.353
Sensor 8	7423.348	4216.718	6069.243	3047.426	1482.256	149.2575	12.60264	6724.614	294.5567	8888.484
Sensor 9	387.154	935.4183	276.5801	102.7511	23.1069	180.9539	51.59644	1333.298	232.9997	1547.985
Sensor 10	16.75672	7788.046	**2.597879**	178.0303	522.706	2633.704	1894.174	9792.081	3117.809	11179.83

Figure A.96: MQ-5 vs. MQ-135 ANOVA f-statistics (45°C, 85% RH).

	Sensor 1	Sensor 2	Sensor 3	Sensor 4	Sensor 5	Sensor 6	Sensor 7	Sensor 8	Sensor 9	Sensor 10
Sensor 1	8450	796139.6	89.1257	7029.214	22053.14	9827.221	18796.52	179154.4	48902.58	1679086
Sensor 2	75797.36	15725.32	67451.05	21760.66	18143.14	448.9663	3698.774	12872.25	470.9751	32943.69
Sensor 3	585241.9	1835145	179263.4	123893.5	224570.7	48697.14	117347.4	468095	170854.5	3096799
Sensor 4	1354.858	15550.33	2169.421	139.7202	9.84844	1252.987	706.5944	16409.44	5756.483	21219.38
Sensor 5	2849.05	642.9716	3405.81	1673.06	1122.69	101.4747	397.2412	974.3254	53.08284	1230.981
Sensor 6	3125.369	6344.746	4084.496	1141.129	463.4665	167.2993	0.234305	7404.078	1929.77	9372.811
Sensor 7	2864.52	1311.842	3496.777	1537.479	951.1846	22.57951	239.847	1808.689	229.8692	2241.679
Sensor 8	4982.229	2980.931	6056.096	2450.076	1474.194	7.357187	287.1253	3836.552	574.374	4938.253
Sensor 9	877.2908	2831.264	1226.264	288.8169	81.39685	172.8958	21.21001	3454.103	1089.071	4033.874
Sensor 10	5.63686	4387.066	3.92599	135.5401	324.1399	1158.508	795.2715	4983.223	2542.34	5501.929

Figure A.97: MQ-5 vs. MQ-135 ANOVA f-statistics (50°C, 85% RH).

	Sensor 1	Sensor 2	Sensor 3	Sensor 4	Sensor 5	Sensor 6	Sensor 7	Sensor 8	Sensor 9	Sensor 10
Sensor 1	9.839027	62580.31	24.76616	2147.086	20593.13	49.67652	12.99728	4127.14	926.3367	926.3367
Sensor 2	736.9077	2965.389	12472.54	21356.67	1031.19	26401.72	17667.62	9440.248	13984.06	13984.06
Sensor 3	411.9113	50392.68	2248.325	9664.17	25654.85	5165.802	3938.258	11736.77	7072.942	7072.942
Sensor 4	191.9784	3701.746	2006.459	930.2169	344.6988	2051.902	1908.048	264.7431	960.7941	960.7941
Sensor 5	470.8339	7820.692	8672.416	13193.65	4.349677	18113.35	12032.86	4881.282	8659.825	8659.825
Sensor 6	350.0563	4596.824	4744.193	3776.019	73.65272	6419.11	5336.555	1513.261	3334.466	3334.466
Sensor 7	363.693	5797.841	5544.248	5113.523	75.90779	8381.269	6597.394	1982.492	4228.912	4228.912
Sensor 8	326.9049	3882.325	3983.32	2794.728	88.31602	4931.876	4270.204	1121.745	2590.871	2590.871
Sensor 9	215.8708	30057.53	5429.532	9408.88	2271.903	14452.16	7952.629	1565.302	4748.184	4748.184
Sensor 10	59.16274	1975.476	417.6948	72.57402	396.3265	308.3745	318.0183	**0.492445**	94.74745	94.74745

Figure A.98: MQ-5 vs. MQ-7 ANOVA f-statistics (20°C, 33% RH).

	Sensor 1	Sensor 2	Sensor 3	Sensor 4	Sensor 5	Sensor 6	Sensor 7	Sensor 8	Sensor 9	Sensor 10
Sensor 1	137.0429	611674.6	1612.295	6003.811	124313.6	41.99589	13.27752	19403.38	3945.403	667502.7
Sensor 2	1533.36	143484.2	517548.9	188336	6418.624	103431.1	18094.03	238991.4	192450.5	5726378
Sensor 3	1949.049	1891620	87819.13	142209.5	452849.7	33419.66	6231.564	255618.3	125902.6	293991.8
Sensor 4	268.3223	25685.94	16168.52	5269.072	2981.479	10155.73	4251.898	2943.436	6160.254	165485.5
Sensor 5	832.2301	7776.19	21804.27	10457.99	14.84049	15687.93	7716.376	7635.503	11480.63	142251.8
Sensor 6	**1.193696**	43.96705	10.68377	**2.020203**	9.850014	8.09317	8.298476	**0.509131**	**2.699886**	161.5488
Sensor 7	754.9346	19173.7	40514.03	18055.29	214.3613	24558.21	8786.881	13320.56	19852.32	289707.8
Sensor 8	375.4428	10802.22	10426.25	3986.133	892.9701	7523.96	4152.34	2438.466	4559.904	90564.36
Sensor 9	84.12524	1920.306	826.6524	231.0197	329.0208	645.1868	588.8353	100.8351	282.8049	9612.777
Sensor 10	84.94986	9032.476	2793.7	636.1314	1773.72	2003.589	1399.566	221.2185	810.4537	37825.43

Figure A.99: MQ-5 vs. MQ-7 ANOVA f-statistics (25°C, 33% RH).

	Sensor 1	Sensor 2	Sensor 3	Sensor 4	Sensor 5	Sensor 6	Sensor 7	Sensor 8	Sensor 9	Sensor 10
Sensor 1	681.2144	356685.8	141.9606	2373	101280.9	2016.478	1706.785	4116.709	3960.665	398957.4
Sensor 2	3595.876	9978.487	67727.66	32033.28	943.0287	51517.12	53150.35	39051.33	23563.14	392079.2
Sensor 3	6779.179	363608.6	33643.62	38146.37	171767.6	9419.092	49298.05	51128.98	39033.5	53004.64
Sensor 4	384.744	32736.21	13748.95	4612.846	4685.907	14961.31	8403.67	5159.914	2682.615	172912
Sensor 5	1998.749	9250.466	24254.56	12335.36	13.03746	24710.83	18005.84	13550.14	9148.925	166232.5
Sensor 6	1439.097	22082.9	31488.21	13378.48	747.657	28301.85	22468.48	15635.31	9175.071	255854.8
Sensor 7	2239.322	23602.63	59415	24371.52	45.5544	43370.47	44540.81	30661.4	16867.01	420713
Sensor 8	313.9286	8637.77	4044.198	1650.679	1235.808	5758.629	2494.446	1657.4	1044.652	47882.54
Sensor 9	68.09136	1664.408	577.0799	225.5624	289.8943	955.2688	336.3506	215.9582	135.9399	7761.603
Sensor 10	0.333971	1328.562	133.7304	24.47635	355.2354	283.2575	54.05525	21.81494	6.115836	3482.439

Figure A.100: MQ-5 vs. MQ-7 ANOVA f-statistics (30°C, 33% RH).

	Sensor 1	Sensor 2	Sensor 3	Sensor 4	Sensor 5	Sensor 6	Sensor 7	Sensor 8	Sensor 9	Sensor 10
Sensor 1	4712.705	922983.5	1663.773	4577.671	121105.4	1612.681	909.6044	18687.35	3081.245	1065147
Sensor 2	10295.13	180846.9	712391.6	168813.3	5523.888	180325.4	86443.02	216061.2	24516.32	9805321
Sensor 3	30575	972172.9	69602.69	87647.56	278956.9	29110.06	45036.86	143370.4	34100.19	126210.9
Sensor 4	175.2711	30200.2	12006.65	4085.638	3511.305	11758.8	4759.053	2115.086	1230.897	132950.2
Sensor 5	3212.576	7485.675	23583.77	12869.27	49.23707	22785.56	13359.78	9791.11	6495.999	136714.5
Sensor 6	2768.006	68801.14	89059.08	34118.05	977.99	57803.93	27178.96	27497.55	8082.17	712679.6
Sensor 7	765.4362	3600.576	5465.996	2814.654	59.74198	5843.063	3266.912	1926.466	1644.351	37168.15
Sensor 8	1004.943	3039.699	6126.343	3298.152	9.794166	6510.192	3774.284	2335.9	1998.46	38683.3
Sensor 9	145.3156	5880.208	3127.042	1256.11	610.213	3455.544	1588.925	689.1915	584.6937	30092.17
Sensor 10	36.39057	6078.566	734.749	123.0277	1350.786	897.0345	226.539	13.38184	10.71774	14405.91

Figure A.101: MQ-5 vs. MQ-7 ANOVA f-statistics (35°C, 33% RH).

	Sensor 1	Sensor 2	Sensor 3	Sensor 4	Sensor 5	Sensor 6	Sensor 7	Sensor 8	Sensor 9	Sensor 10
Sensor 1	27843.81	3770294	40.82971	2737.177	291470.3	7968.11	262.5959	1429.173	137214.2	1952348
Sensor 2	46480.96	360245.2	13412.35	104081.6	4067.542	180140.4	31373.6	6859.399	573338.3	6159402
Sensor 3	103904.6	785432.6	7431.259	54694.08	313982.8	12124.67	18270.31	13352.69	171861.3	68411.49
Sensor 4	29.40089	32676.25	1824.501	3076.56	5893.559	14626.78	2701.626	249.0517	653.8024	110909.8
Sensor 5	13491.05	27198.09	9565.859	35209.89	15.41398	74322.33	18668.84	4517.277	31858.63	471890.3
Sensor 6	1782.884	13566.31	4239.521	7495.754	780.8107	20903.79	6256.613	1538.712	3903.102	108669.4
Sensor 7	897.2076	5656.253	2950.027	3645.348	306.1119	10226.36	3621.472	1098.336	1775.923	47402.4
Sensor 8	607.9849	3231.718	2223.524	2352.324	152.6261	6512.25	2491.836	853.3293	1142.188	28732.67
Sensor 9	73.28863	1993.155	714.3295	588.2929	248.1256	2081.616	701.7447	193.7878	203.0794	10500.56
Sensor 10	180.1714	3489.148	14.22854	0.001316	1178.416	339.2231	6.336417	54.49875	75.76381	4454.457

Figure A.102: MQ-5 vs. MQ-7 ANOVA f-statistics (40°C, 33% RH).

	Sensor 1	Sensor 2	Sensor 3	Sensor 4	Sensor 5	Sensor 6	Sensor 7	Sensor 8	Sensor 9	Sensor 10
Sensor 1	16837.15	1562504	4511.037	1436.831	101052.7	165.9777	41.56892	42843.71	10796.62	1349978
Sensor 2	15526.19	54726.42	153364	68268.76	694.1505	2037.074	5911.918	99411.16	23597.25	1425970
Sensor 3	79633.75	977781.5	106740.3	52737.81	222456.1	91.5912	4109.893	179483.2	68437.96	77775.15
Sensor 4	40.43336	29589.86	3151.914	2622.577	5274.949	720.947	782.1065	501.1565	84.29664	88269.2
Sensor 5	5074.378	9547.181	24002.35	19521.2	25.80539	1830.788	4474.308	13938.14	7864.78	182567.5
Sensor 6	959.0715	19493.43	10854.25	8916.099	1323.727	1208.19	2230.236	4673.559	2266.44	132649.6
Sensor 7	1849.857	7541.159	9974.754	8816.183	106.9894	1509.929	2999.366	5212.107	3202.871	88708.99
Sensor 8	2023.573	27960.72	20287.74	15166.09	1176.627	1333.881	2786.166	9545.181	4189.413	228321.4
Sensor 9	14.10435	1221.997	71.70908	69.35472	302.0829	310.786	79.79599	3.721046	0.115861	2897.316
Sensor 10	75.32816	3246.612	101.952	96.94576	880.2774	373.1797	103.1797	2.09E-05	11.92808	6429.157

Figure A.103: MQ-5 vs. MQ-7 ANOVA f-statistics (45°C, 33% RH).

	Sensor 1	Sensor 2	Sensor 3	Sensor 4	Sensor 5	Sensor 6	Sensor 7	Sensor 8	Sensor 9	Sensor 10
Sensor 1	32686.73	640019.3	16280.78	2070.848	96789.15	13885.58	6.950812	1533.101	30786.73	33831.9
Sensor 2	22026.13	64800.09	332371.2	143387	268.3082	212990.5	6945.719	6020.422	57751.25	112410.7
Sensor 3	154873.5	1065803	266273.1	103195	265446.6	15037.58	4047.445	14744.77	188836.8	5591.027
Sensor 4	487.8282	25222.57	955.3417	1561.058	5919.853	9899.193	698.5055	21.03178	21.99301	28960.66
Sensor 5	4763.547	10405.1	22686.79	23716.8	0.258428	50541.77	5258.918	3828.127	9278.256	68703.88
Sensor 6	757.6238	31293.51	14017.5	15169.36	2625.809	41830.52	2835.72	1375.009	3206.704	59818.28
Sensor 7	9318.356	41588.27	82069.58	63691.07	141.2941	120136.5	5472.177	4171.475	22983.22	93382.52
Sensor 8	431.738	1983.462	2235.734	2668.144	48.95142	6716.592	1986.96	958.788	893.6313	17324.49
Sensor 9	4.873652	6941.185	1329.37	1775.77	1133.27	6614.006	1161.235	294.0162	192.0709	19822.47
Sensor 10	148.0376	3363.991	35.03166	85.2459	1002.934	942.7375	126.9946	3.201171	35.56113	4919.98

Figure A.104: MQ-5 vs. MQ-7 ANOVA f-statistics (50°C, 33% RH).

	Sensor 1	Sensor 2	Sensor 3	Sensor 4	Sensor 5	Sensor 6	Sensor 7	Sensor 8	Sensor 9	Sensor 10
Sensor 1	5542.89	227654.4	4337.927	251.6751	21174.17	363.3378	69.37469	16223.6	60.68874	146054.3
Sensor 2	18781.07	6340.263	55762.33	5869.068	301.7595	12235.22	14954.8	65025.46	5821.681	205035.9
Sensor 3	8182.536	42082.02	1702.482	3364.048	18406.31	1082.524	2243.444	8.96153	2478.165	6462.661
Sensor 4	930.7985	6513.208	6425.739	904.5411	679.3334	3127.116	2768.523	13376.69	1118.746	39924.59
Sensor 5	16054.2	1775.732	41725.56	6727.296	874.4943	12960.17	15183.8	54026.22	6670.248	144881.7
Sensor 6	34522.97	67282.97	139487.9	4545.777	42.71657	10929.36	14349.46	94371.18	4546.421	494619.9
Sensor 7	6107.746	6004.556	21957.74	3205.312	13.23973	7581.877	8161.178	33734.38	3395.817	96992.81
Sensor 8	6630.837	17963.6	31212.99	2531.766	484.0798	7005.7	7882.753	43346.02	2730.857	152646.4
Sensor 9	413.4539	1277.868	2074.975	541.929	94.14348	1555.017	1237.054	4455.182	677.1728	11529.34
Sensor 10	1.571577	5071.491	900.6231	22.73218	1386.336	567.325	327.3483	3164.223	71.53733	11374.1

Figure A.105: MQ-5 vs. MQ-7 ANOVA f-statistics (10°C, 85% RH).

	Sensor 1	Sensor 2	Sensor 3	Sensor 4	Sensor 5	Sensor 6	Sensor 7	Sensor 8	Sensor 9	Sensor 10
Sensor 1	121778	2617067	3157.272	48208.61	471535.3	1878.967	51.45984	13195.44	123.6642	355940.6
Sensor 2	123331	37854.5	157144.9	155680.3	4359.684	55111.77	26324.62	78585.94	27320.52	654291.2
Sensor 3	1684134	7417623	62719.96	1147755	1656390	8548.696	15233.19	7.132445	17576.52	92767.22
Sensor 4	1414.974	5311.54	6055.825	2238.743	347.6441	6330.34	3032.707	13206.96	2905.695	37851.33
Sensor 5	292519.6	49776.55	235873.7	353291.7	16092.53	66677.94	32131.82	90734.14	33606.35	918805.9
Sensor 6	5926.255	9744.669	18665.3	8524.645	155.7742	15721.13	7709.083	28839.95	7589.904	100326.6
Sensor 7	6731.756	6492.813	18946.84	9265.062	0.75724	16396.02	8519.613	29138.91	8401.294	93338.57
Sensor 8	1138.421	3369.513	4554.995	1747.436	169.543	4954.87	2479.61	10277.2	2370.192	27248.34
Sensor 9	2386.99	11274.55	10699.36	3898.718	897.2793	9908.781	4430.58	20318.36	4285.584	69764.67
Sensor 10	157.2208	17450.43	4224.791	637.3608	3694.347	4455.908	1371.449	11999.59	1259.44	46526.93

Figure A.106: MQ-5 vs. MQ-7 ANOVA f-statistics (15°C, 85% RH).

	Sensor 1	Sensor 2	Sensor 3	Sensor 4	Sensor 5	Sensor 6	Sensor 7	Sensor 8	Sensor 9	Sensor 10
Sensor 1	598793.1	7405073	7591.559	5179.447	302261.6	4176.18	480.3948	441525.5	300.9157	1038366
Sensor 2	152702.2	73473.11	398308.2	66856	4525.137	55400.69	26126.48	875462	58031.34	1410340
Sensor 3	3336477	12235355	434107.4	102828	945907.7	3355.508	23060.82	2500.054	42843.11	228554
Sensor 4	1759.823	23864.07	17116.74	5023.125	1996.072	16297.73	4524.11	55866.21	7584.317	130650
Sensor 5	44747.93	10952.16	121294	43960.91	3983.22	50038.66	24488.16	263450.5	44569.6	483379.8
Sensor 6	10604.71	34144.79	53096.51	15972.22	599.664	28823.92	10371.97	146090.3	19199.89	307448.7
Sensor 7	11116.01	23980.89	48946.71	16494.24	119.4975	29461.17	11199.27	129093.5	19758.66	268260.9
Sensor 8	125.2124	579.4485	748.0779	320.1323	21.753	1332.138	417.7863	2168.919	502.7437	4921.048
Sensor 9	680.7487	13473.65	8253.359	2506.085	1376.095	10722.72	2740.713	28148.78	4172.622	67872.71
Sensor 10	130.7689	52218.09	14364.26	2375.18	8330.576	13130.54	2344.709	61499.62	4672.814	158359

Figure A.107: MQ-5 vs. MQ-7 ANOVA f-statistics (20°C, 85% RH).

	Sensor 1	Sensor 2	Sensor 3	Sensor 4	Sensor 5	Sensor 6	Sensor 7	Sensor 8	Sensor 9	Sensor 10
Sensor 1	118399	5863137	1351.231	22395.46	172267.7	3261.339	206.9127	31487.83	518.5471	2821548
Sensor 2	115532.9	222010.3	909816.6	287564.9	2822.305	58311.29	11816.86	200797.4	96747.03	4239516
Sensor 3	491162.6	3691724	394249.2	308769.3	458357.3	5097.539	9870.346	302.497	62083.02	257045.6
Sensor 4	546.964	20006.02	9212.147	4557.29	1735.319	12781.17	2385.415	30953.67	6533.218	98599.8
Sensor 5	27397.23	11022.97	87739.88	57132.44	2735.166	47581.27	12293.38	117695.4	50342.67	436514.1
Sensor 6	3487.27	27572.54	25698.46	14173.83	844.0211	22638.24	4543.801	58311.62	16208.48	210411.4
Sensor 7	3269.849	7320.231	14563.5	9162.574	0.613734	17855.54	5001.283	36512.21	11321.56	96223
Sensor 8	543.1293	8771.873	5579.199	3006.409	568.2315	9222.639	2181.11	19399.75	4394.966	52725.38
Sensor 9	1611.198	27129.16	17223.86	8975.364	1586.126	18106.24	3412.049	46330.77	11289.58	161853
Sensor 10	16.95294	7214.534	970.0913	312.9499	1351.699	2790.163	397.1851	6427.561	732.0635	19074.99

Figure A.108: MQ-5 vs. MQ-7 ANOVA f-statistics (25°C, 85% RH).

	Sensor 1	Sensor 2	Sensor 3	Sensor 4	Sensor 5	Sensor 6	Sensor 7	Sensor 8	Sensor 9	Sensor 10
Sensor 1	3219.905	1981268	7619.45	6783.195	170310.8	1236.207	400.0472	258427.8	762.395	1812837
Sensor 2	3485.134	242284.6	1866769	208960.6	2238.465	15155.73	10748.83	1951989	154467.3	7216944
Sensor 3	18761.73	1165386	169187.3	115396.9	336166.8	757.8593	11271.93	1743.515	69519.8	75688.32
Sensor 4	68.2209	10102.96	3560.413	2388.214	1167.281	4787.229	1305.786	19189.73	3371.709	44618.61
Sensor 5	1659.369	1810.471	8857.727	7145.918	172.411	8801.587	4486.238	26023.72	8493.534	49861.57
Sensor 6	430.5964	36605.14	23262.03	14598.9	2166.841	8144.408	3400.773	99888.8	17854.53	227506
Sensor 7	1229.118	167801.4	232781.2	78699.36	1633.815	10920.97	6000.143	641084.3	71563.53	1681674
Sensor 8	244.5783	8654.839	5137.466	3637.964	626.5145	5790.244	1951.703	23300.21	4840.068	51741.7
Sensor 9	370.606	97304.67	55905.95	27810.67	5341.7	8360.059	3526.864	231612.4	30988.13	565137.1
Sensor 10	192.5335	8823.727	266.6398	89.38674	2326.446	1577.494	58.6283	5031.595	265.5332	14575.33

Figure A.109: MQ-5 vs. MQ-7 ANOVA f-statistics (30°C, 85% RH).

	Sensor 1	Sensor 2	Sensor 3	Sensor 4	Sensor 5	Sensor 6	Sensor 7	Sensor 8	Sensor 9	Sensor 10
Sensor 1	51742.08	814379.1	11529.07	2101.5	546047.4	480.0364	47.16442	8210.217	522.5223	681335
Sensor 2	15389.6	26258.51	102360.5	54590.34	1115.833	3226.162	38749.7	49776.88	49247.08	569670
Sensor 3	189876.8	904922.1	185665.6	72120.18	632731.8	14.37064	28244.68	296.7005	48127.24	52411.09
Sensor 4	3.282973	22134.42	5681.508	4600.064	2992.841	1686.681	5489.009	17194.74	5280.648	86607.48
Sensor 5	7914.698	5089.11	31165.47	25190.83	1098.684	3494.015	23814.4	38551.88	25553.54	171584.4
Sensor 6	809.5691	39394.48	21958.04	14787.8	3122.568	2081.409	13670.28	28341.39	15157.25	231318.4
Sensor 7	1937.736	6547.901	11482.41	9951.197	1.867394	2673.796	10734.48	23237.04	10685.28	84142.54
Sensor 8	1037.315	13340.46	11420.07	9427.106	480.4448	2291.895	10089.61	23212.07	10173.69	104277.5
Sensor 9	205.6233	24288.26	9883.046	7715.177	2413.623	1912.312	8363.049	21600.26	8462.061	120823
Sensor 10	194.9737	3473.503	55.16082	46.3134	940.5757	640.127	126.9943	1625.045	83.90439	5280.191

Figure A.110: MQ-5 vs. MQ-7 ANOVA f-statistics (35°C, 85% RH).

	Sensor 1	Sensor 2	Sensor 3	Sensor 4	Sensor 5	Sensor 6	Sensor 7	Sensor 8	Sensor 9	Sensor 10
Sensor 1	2896.761	227293.4	8672.244	468.8888	135359.6	27303.51	2.825302	1240.322	637.6596	365426.3
Sensor 2	858.1416	11802.84	46127.42	26962	246.2773	103297	7221.458	8076.644	35328.86	300238.9
Sensor 3	13204.84	359659.5	116889.4	31532.73	267373.2	3864.087	3873.486	44.79452	44857.5	29921.13
Sensor 4	41.46553	10624.08	1801.28	2082.621	1769.278	12525.63	1497.102	3458.728	2315.588	38120.11
Sensor 5	1068.601	2213.001	13134.54	12291.07	426.2436	34807.92	6436.434	7890.564	13583.91	78831.99
Sensor 6	0.14734	15595.14	5259.899	5030.668	1926.589	26427.69	2479.447	4460.117	5863.057	79412.4
Sensor 7	253.2817	2733.276	4154.871	4415.385	7.77425	14335.85	3233.99	5231.427	4716.893	34284.15
Sensor 8	17.62682	2695.557	1369.486	1602.536	195.694	6418.212	1519.27	3332.503	1688.447	16646.21
Sensor 9	1.207406	5576.595	1971.223	2252.545	589.5043	10303.15	1790.958	3747.399	2431.065	28317.38
Sensor 10	505.145	17351.39	296.659	509.5319	4826.443	8071.886	523.4997	2241.811	589.2786	30728.74

Figure A.111: MQ-5 vs. MQ-7 ANOVA f-statistics (40°C, 85% RH).

	Sensor 1	Sensor 2	Sensor 3	Sensor 4	Sensor 5	Sensor 6	Sensor 7	Sensor 8	Sensor 9	Sensor 10
Sensor 1	7798.385	526352.8	20585.44	619.8649	225630.2	44414.7	343.6696	486935.4	386.4835	2235309
Sensor 2	1459.383	36851.44	110845.7	34410.49	790.93	198861.9	22371.63	589581.6	71362.56	1129702
Sensor 3	37949.71	974562.8	346582.3	45147.12	616295.2	3294.939	9291.502	3298.408	84584.03	115432.4
Sensor 4	357.9132	21177.16	1723.153	2127.478	3435.838	22160.36	3801.518	30587.57	3238.624	66605.72
Sensor 5	1220.775	3223.365	11620.92	11132.04	387.4753	39725.31	12400.73	50018.11	14079.17	87450.89
Sensor 6	**1.90812**	7945.673	2369.807	2783.804	614.9842	16828.3	4388.582	21177.83	3653.877	42294.43
Sensor 7	198.0203	6588.841	5875.861	6067.76	59.3933	27802.63	7765.834	35290.66	7848.579	66053.65
Sensor 8	113.3839	8208.562	5711.693	5867.766	177.2932	28877.25	7554.111	37224.19	7741.29	70739.62
Sensor 9	13.82139	1493.552	253.6917	362.0822	169.5482	2450.195	777.5151	2896.951	450.6835	5968.16
Sensor 10	1194.248	10781.24	8.475204	10.18606	3194.965	3466.529	357.5535	4581.057	49.49353	12413.36

Figure A.112: MQ-5 vs. MQ-7 ANOVA f-statistics (45°C, 85% RH).

	Sensor 1	Sensor 2	Sensor 3	Sensor 4	Sensor 5	Sensor 6	Sensor 7	Sensor 8	Sensor 9	Sensor 10
Sensor 1	8413.011	431130	47957.79	1001.27	206985.2	23689.26	1156.995	199727.6	47.35912	1151072
Sensor 2	700.6044	25665.54	60961.7	64841.82	46.89634	72294.44	27738.67	273170.4	60492.55	573681.1
Sensor 3	44726.76	1020754	893863.2	80144.83	746604.1	262.3319	13105.59	5113.631	137520.6	92772.45
Sensor 4	951.7913	21011.07	546.7884	3497.497	4676.521	20076.52	3724.347	23766.1	2153.629	55465.33
Sensor 5	161.115	1358.93	2196.642	4224.082	**2.552614**	13717.26	4703.022	12337.68	3408.57	22495.35
Sensor 6	80.44929	9608.25	1999.086	5536.267	1084.419	21741.69	5647.646	23857.53	4056.191	49436.52
Sensor 7	58.8357	2420.073	2125.724	4433.907	29.91805	15353.07	4893.609	14208.54	3496.272	26778.61
Sensor 8	40.88882	5197.294	3634.297	7637.595	136.5912	24164.62	7586.778	26095.04	6013.825	50233.89
Sensor 9	107.0213	4239.403	517.4537	1777.991	611.6464	9620.164	2224.068	8177.9	1232.892	17250.29
Sensor 10	1007.25	5693.451	59.16278	60.06247	1956.383	2983.381	182.909	1998.112	4.591871	5791.74

Figure A.113: MQ-5 vs. MQ-7 ANOVA f-statistics (50°C, 85% RH).

	Sensor 1	Sensor 2	Sensor 3	Sensor 4	Sensor 5	Sensor 6	Sensor 7	Sensor 8	Sensor 9	Sensor 10
Sensor 1	24.322	572.8497	702.1769	69.83966	204.3706	930.4783	1192.784	1426.78	1299.899	1113.82
Sensor 2	31410.16	5570.965	17828.57	60370.46	7298.086	920.6769	207.2527	163.7537	30.75327	1418.938
Sensor 3	1075.746	10182.84	16466.03	2539.998	3109.476	14045.29	21209.79	31034.22	25064.52	23688.46
Sensor 4	53.75146	16500.52	192076.3	2130.42	1891.439	21789.41	56344.45	638307.6	101500	176686
Sensor 5	7539.351	212.5272	2405.145	9901.592	657.4134	2137.571	7126.53	28372.11	12021.66	11312
Sensor 6	1369.172	21517.74	88317.74	6470.082	3971.985	26799.48	57298.09	190269.9	86419.54	109218.2
Sensor 7	1027.73	14296.15	31131.48	3395.176	3335.826	19150.62	33535.56	62168.07	43168.26	44058.03
Sensor 8	323.7541	6629.629	22825.85	**2.271459**	498.644	11032.57	24106.68	64661.92	35066.56	37726.51
Sensor 9	99.28332	10766.21	28439.58	1129.104	1745.226	15507.36	29931.97	64894.18	40661.45	42556.99
Sensor 10	99.28332	10766.21	28439.58	1129.104	1745.226	15507.36	29931.97	64894.18	40661.45	42556.99

Figure A.114: MQ-7 vs. MQ-135 ANOVA f-statistics (20°C, 33% RH).

	Sensor 1	Sensor 2	Sensor 3	Sensor 4	Sensor 5	Sensor 6	Sensor 7	Sensor 8	Sensor 9	Sensor 10
Sensor 1	8.198574	1372.772	682.1537	33.5747	281.2114	1728.678	2278.684	3493.814	3006.353	2601.941
Sensor 2	548356.9	170724.1	793.6648	217512.5	812849.9	10157.95	3179.033	12451.96	3781.314	19299.82
Sensor 3	39659.46	470109.2	3615.945	30300.35	191114.3	127729.3	144219.8	1449112	978645	801434.2
Sensor 4	2227.197	167724.5	1897.93	3519.916	41127.59	66418.68	80283.71	526829.5	389286.8	320866.7
Sensor 5	64667.18	3378.462	9.108178	33791.31	23203.67	3776.352	8866.937	102778.7	63207.98	42026.52
Sensor 6	8474.764	94839.41	3085.521	9713.091	33917.33	64566.8	76394.04	213872.8	180190.9	157529.6
Sensor 7	1667.099	16655.8	2655.018	2239.642	5934.388	17716.91	21684.31	34920.25	30686.7	27259.57
Sensor 8	**0.009398**	207949.2	1396.491	564.5304	36748.42	58911.2	72852.06	898030.1	567648.6	442849.7
Sensor 9	3686.71	172195.5	2072.092	4936.54	45778.03	70176.28	84183.65	517325.7	387654.4	321818.4
Sensor 10	1347091	5322724	20913.04	667306.8	4260811	704525.7	705214.7	28564090	10030972	7641107

Figure A.115: MQ-7 vs. MQ-135 ANOVA f-statistics (25°C, 33% RH).

	Sensor 1	Sensor 2	Sensor 3	Sensor 4	Sensor 5	Sensor 6	Sensor 7	Sensor 8	Sensor 9	Sensor 10
Sensor 1	**0.02173**	3041.304	1301.996	10.28978	532.6223	4161.658	1272.199	10672.72	8129.748	7716.678
Sensor 2	77785.74	4837.004	3573.055	290185.3	315527.4	20036	5261.955	3684.208	5936.097	25971.41
Sensor 3	6774.019	29997.97	7963.38	31461.18	136959.5	164058.4	9657.533	2252943	1061311	2089865
Sensor 4	782.7008	16625.6	4433.198	2665.958	17522.54	57743.98	5146.138	232130.8	166343.4	177538.1
Sensor 5	18894.2	360.3836	26.1747	49078.86	23569.95	2855.828	95.87673	116951.8	52489.72	60339.07
Sensor 6	8571.609	29897.07	9935.051	16968.35	38575.67	79670.39	11780.77	209049.8	164858.9	169224.4
Sensor 7	2621.924	23246.97	5817.42	14305.42	93976.09	132472.9	6962.83	2541796	1023878	2462591
Sensor 8	850.1945	18200.97	4516.659	4121.211	33466.54	84590.08	5305.846	582440.1	365421.1	460419.1
Sensor 9	132.4426	12877.82	3397.826	641.7411	8636.043	39617.49	3859.775	146911.6	106442.5	109526.9
Sensor 10	197778.5	173103.1	56206.18	868438.8	2038370	964596.1	71793.99	19559276	6637879	27154388

Figure A.116: MQ-7 vs. MQ-135 ANOVA f-statistics (30°C, 33% RH).

	Sensor 1	Sensor 2	Sensor 3	Sensor 4	Sensor 5	Sensor 6	Sensor 7	Sensor 8	Sensor 9	Sensor 10
Sensor 1	93.89108	4346.457	2260.445	205.21	493.2333	7557.868	2879.999	34103.55	21568.32	19297.51
Sensor 2	92337.51	2935.25	32706.71	365331.8	302471.2	28801.76	1923.945	5565.526	21819.32	4088.497
Sensor 3	12800.65	21899.59	43273.47	38664.69	116423.4	133525.8	12683.3	1780827	1049088	296328.4
Sensor 4	2164.793	13134.67	19039.97	4111.423	25338.92	61219.33	7677.389	443708.5	285839	143107
Sensor 5	15312.85	574.9863	617.5085	38774.03	14508.18	1316.255	282.5376	94233.36	38479.24	20366.26
Sensor 6	11291.39	21670.75	35707.63	20598.74	50617.7	87419.71	13031.28	384034.6	272983.8	169134.9
Sensor 7	2837.932	13738.82	17844.84	4240.806	17788.08	47240.42	8324.952	209080.5	143552.1	99117.23
Sensor 8	438.6946	10415.08	14039.42	687.2543	18715.06	54940.19	5978.072	657523.7	385835	145645.3
Sensor 9	169.4456	7638.53	6218.431	121.9631	3180.99	17021.21	4887.25	68105.15	45355.61	38155.16
Sensor 10	244235.6	108389.9	322161.1	997253.2	1709188	794063.5	63505.87	25221697	10403063	1399564

Figure A.117: MQ-7 vs. MQ-135 ANOVA f-statistics (35°C, 33% RH).

	Sensor 1	Sensor 2	Sensor 3	Sensor 4	Sensor 5	Sensor 6	Sensor 7	Sensor 8	Sensor 9	Sensor 10
Sensor 1	214.6414	37397.19	1299.397	1677.412	490.3209	4919.242	16775.82	176997	63855.28	104330.6
Sensor 2	50144.96	31958.88	26611.41	451026.8	65947.07	14314.72	7968.101	20006.19	12915.94	46916.35
Sensor 3	1036.712	14520.64	3755.626	982.9296	2924.173	6613.664	12255.3	32594.22	19679.85	22510.19
Sensor 4	1587.706	78933.08	8015.453	3208.335	8135.047	14957.03	35951.52	274795.6	117608.3	183136.1
Sensor 5	11385.91	4510.558	2563.951	67749.17	9016.475	143.0411	1490.726	152486.4	19370.47	54673.97
Sensor 6	12329.15	140239.6	25083.94	30094.5	30776.8	35679.64	69251.69	365586.1	188397	268907.3
Sensor 7	1511.276	31598.83	6047.348	1812.009	5211.966	10827.98	22149.56	78293.79	43903.33	53498.98
Sensor 8	20.87548	7807.081	1122.788	**0.001085**	594.7871	2869.93	6610.465	21518.72	11598.94	13595.75
Sensor 9	28.29397	119010.8	3799.741	108.778	3200.97	9747.468	30786.31	2078791	216841.3	1171233
Sensor 10	119949.6	1233228	157147.5	852007.2	270743.5	180029.4	324479	10346911	1718196	7836507

Figure A.118: MQ-7 vs. MQ-135 ANOVA f-statistics (40°C, 33% RH).

	Sensor 1	Sensor 2	Sensor 3	Sensor 4	Sensor 5	Sensor 6	Sensor 7	Sensor 8	Sensor 9	Sensor 10
Sensor 1	217.0152	10337.51	55.94419	1869.034	72.41681	2376.669	5602.635	83899.46	26768.16	43792
Sensor 2	32358.41	4660.003	130129.7	267973.2	216440.5	46389.67	10254.26	12957.54	11063.13	19836.83
Sensor 3	2102.52	38467.11	21206.54	6195.448	32126.95	30244.47	26865.08	895394.9	163366	485728.6
Sensor 4	1747.467	30773.97	11657.78	2973.606	14466.14	19953.46	21465.45	243767.9	86728.5	149331.6
Sensor 5	6550.772	1282.482	11204.77	31048.83	13826.72	1837.173	43.28825	54640.71	6412.58	16394.7
Sensor 6	624.0976	2336.934	882.839	519.0129	888.9354	1317.523	1855.714	4057.667	2657.336	2957.93
Sensor 7	551.6635	6531.447	1356.836	367.0487	1393.775	2817.253	4622.3	15821.83	8633.127	10286.1
Sensor 8	154.1102	24905.13	5790.033	5.442014	9097.588	14157.48	15710.81	804317	114791.9	389483.8
Sensor 9	**0.384905**	14402.84	1028.313	336.3307	1230.38	5086.323	8640.785	106085.1	36643.68	58938.5
Sensor 10	80543.74	234293.9	502884.6	534007.7	851600.8	364811.7	203202	8918489	1072251	4845858

Figure A.119: MQ-7 vs. MQ-135 ANOVA f-statistics (45°C, 33% RH).

	Sensor 1	Sensor 2	Sensor 3	Sensor 4	Sensor 5	Sensor 6	Sensor 7	Sensor 8	Sensor 9	Sensor 10
Sensor 1	226.958	47166.11	3121.377	4849.024	74.17084	259.0774	1932.695	144377.4	20075.9	62559.17
Sensor 2	50063.87	30837.1	187722.1	215576.8	182082	28394.2	9182.66	7631.957	8574.903	4310.169
Sensor 3	4578.792	756851.6	5727.265	3424.536	33317.34	8978.141	11086.64	3336857	86292.11	468864.9
Sensor 4	5868.223	238752.3	6682.307	4660.102	24056.28	10313.92	12389.93	548862.5	75040.11	238268.1
Sensor 5	8706.322	6280.132	28326.72	33786.15	16897.43	3138.888	183.8022	54817.77	2266.598	15127.24
Sensor 6	25681.74	300981.1	40428.45	36604.25	74010.2	31494.88	29567.49	546655.8	127363.2	305463.6
Sensor 7	1264.624	9893.715	729.5619	540.0659	1738.987	2337.034	3878.945	18744.33	8752.793	12700.51
Sensor 8	199.6388	9921.453	**2.360922**	12.8719	448.189	954.0062	2384.685	22738.36	8141.813	13743.77
Sensor 9	115.416	113838.9	530.8259	1501.777	1364.756	1726.963	4181.137	322918.8	36294.95	127685.8
Sensor 10	46672.87	134143.2	52008.4	49493.5	66449.67	52295.01	51264.52	189894.7	106437.4	147363.2

Figure A.120: MQ-7 vs. MQ-135 ANOVA f-statistics (50°C, 33% RH).

	Sensor 1	Sensor 2	Sensor 3	Sensor 4	Sensor 5	Sensor 6	Sensor 7	Sensor 8	Sensor 9	Sensor 10
Sensor 1	11592.83	120281.3	11874.83	529.4784	7640.599	38437.16	26055.16	144914.4	72763.01	127276.2
Sensor 2	218915.3	64352.83	197010.8	32090.7	101138.6	1658.9	3738.909	180.2044	2687.317	4.045249
Sensor 3	380.7936	375731.5	94072.12	12090.07	61451.46	95043.64	70060.57	343597.6	183957	303936.9
Sensor 4	942.0573	9414.013	1776.118	475.5859	1599.3	9632.78	7487.603	15575.4	11120.55	14697.83
Sensor 5	27516.67	2053.714	2766.68	3813.904	2757.726	2457.595	1030.346	9021.905	3681.02	7822.724
Sensor 6	12.79887	18325.61	6247.282	2926.651	5808.241	17772.44	14632.93	26575.57	20321.55	25359.68
Sensor 7	128.7444	26185.28	7524.089	2708.705	6777.647	23090.66	18376.73	38572.84	28115.3	36498.72
Sensor 8	8892.765	153541.6	68486.42	23687.49	58484.72	93852.21	76337.45	181716.3	131600.5	171381.3
Sensor 9	454.5687	8820.627	1992.293	681.598	1824.926	9175.32	7279.012	14187.91	10386.48	13444.62
Sensor 10	100358.2	902873.6	438531.4	97273.95	320598.8	293788.8	236851.9	796265.7	512460	730752

Figure A.121: MQ-7 vs. MQ-135 ANOVA f-statistics (10°C, 85% RH).

	Sensor 1	Sensor 2	Sensor 3	Sensor 4	Sensor 5	Sensor 6	Sensor 7	Sensor 8	Sensor 9	Sensor 10
Sensor 1	7769.703	73271.68	22808.35	5420.823	47235.7	139463.9	289477.8	858831.7	383639.6	295965.8
Sensor 2	111082.2	5087.375	677566.8	699944.9	506396.5	4478.21	41254.69	316.9895	10919.41	0.531165
Sensor 3	17.3668	115600.3	65475.66	47001.34	84173.35	178151.8	238680.1	435207.2	293184.4	285030.5
Sensor 4	4408.193	89630.36	52405.07	22364.28	83957.38	167306.8	348611.7	950373.6	447792.9	342252.8
Sensor 5	43657	8570.232	73667.42	98447.61	42167.3	19525.63	18376.96	136525.5	45790.73	58801.56
Sensor 6	272.7788	57419.81	18989.28	14591.07	24056.8	71692.82	68410.9	110130.2	83954.17	96483.16
Sensor 7	391.6472	30565.48	5532.174	3601.116	7994.332	37791.28	33257.19	58285.12	42808.1	52134.3
Sensor 8	5738.09	80278.64	38613.33	32970.67	44727.4	95608.13	92491.53	133530.3	108094	120551.7
Sensor 9	535.1021	31523.5	5480.11	3484.187	8047.367	39343.89	34797.1	61651.22	44981.61	54756.9
Sensor 10	60206.12	423442.5	586743.4	516825.4	630091	621763	914945.3	1334142	1009804	892260

Figure A.122: MQ-7 vs. MQ-135 ANOVA f-statistics (15°C, 85% RH).

	Sensor 1	Sensor 2	Sensor 3	Sensor 4	Sensor 5	Sensor 6	Sensor 7	Sensor 8	Sensor 9	Sensor 10
Sensor 1	125145.3	260794.3	3347.004	472.416	23968.4	182759.5	31949.04	4556615	235867	1053357
Sensor 2	1313213	17944.48	30152.78	1321044	957153.7	18646.43	8042.325	383.4745	15246.08	187.0405
Sensor 3	101.9569	541862.1	26230.24	153835.5	282621.9	408385.9	88057.2	3057495	496633	1487889
Sensor 4	7509.363	104415.1	7658.237	3920.828	14080.05	90122.7	35490.38	203601.2	102324.7	185345.2
Sensor 5	220076.2	26235.15	1930.491	77728.46	34944.72	18235.59	2929.724	137519.5	25386.94	104916.5
Sensor 6	2754.652	73269.12	20216.8	17014.69	25155.48	68443.45	45364.33	102653.2	73101.53	100587.6
Sensor 7	1072.989	39638.99	6073.945	2370.864	6170.089	36194.51	21970.33	62292.23	39622.76	60950.94
Sensor 8	142533.4	1065223	81558	694111.1	933344.8	824473	192296	4786881	978051.9	2546275
Sensor 9	1067.448	85793.98	10686.37	7192.927	16385.77	76711.05	37679.85	144272.9	84896.74	136805.7
Sensor 10	515964	1617241	184962	1286018	1542096	1315062	359390.8	4561055	1508154	3099183

Figure A.123: MQ-7 vs. MQ-135 ANOVA f-statistics (20°C, 85% RH).

	Sensor 1	Sensor 2	Sensor 3	Sensor 4	Sensor 5	Sensor 6	Sensor 7	Sensor 8	Sensor 9	Sensor 10
Sensor 1	31744.36	129361.8	6190.995	1084.879	1383.222	39401.96	22004.92	505542.7	176426.7	522824
Sensor 2	390052.9	13102.18	284155.4	263940.7	463882.8	9444.836	16109.63	130.5188	25945.05	664.4433
Sensor 3	200.4277	439627.5	138715.3	28721.41	133861	119650.3	78459.41	3713079	733499.7	3583237
Sensor 4	5858.547	243373.2	48843.82	6497.021	36975.37	78017.66	49598.44	911384.9	341364.7	929373.1
Sensor 5	80937.5	19406.12	9864.029	28371.56	19858.5	5225.1	1234.156	74460.86	22095.75	80963.29
Sensor 6	2562.767	77702.17	27995.92	14541.12	23349.62	55004.86	43153.82	109486.6	79833.41	112802.9
Sensor 7	227.9614	19198.76	3792.191	1033.244	2595.473	14320.13	10584.68	27866.84	19086.15	29014.47
Sensor 8	21404.22	228597	106165.6	61458.18	95733.09	139269.9	109580.4	345570.7	247858.1	353663.3
Sensor 9	428.1527	125030.4	29359.97	8110.219	22035.24	63676.83	44259.22	230501.5	139484.2	238593.7
Sensor 10	288750.5	1792119	1339842	608136.1	1584354	557933.6	422340.3	9943308	2908366	9612293

Figure A.124: MQ-7 vs. MQ-135 ANOVA f-statistics (25°C, 85% RH).

	Sensor 1	Sensor 2	Sensor 3	Sensor 4	Sensor 5	Sensor 6	Sensor 7	Sensor 8	Sensor 9	Sensor 10
Sensor 1	2905.102	7887.716	16.78655	196.2509	10.80148	1879.668	1477.381	12243.61	7126.901	13510.91
Sensor 2	2303605	47288.91	441448.9	264231.7	143241.8	4430.96	86929.31	236.1702	43620.43	382.8398
Sensor 3	4380.638	2658869	132591.7	21110.53	34395.89	15315.86	134677.1	1228929	1330099	3165629
Sensor 4	5029.469	348967.4	30328.58	6227.337	14979.54	11906.31	62818.51	373399	288022.4	499748.4
Sensor 5	167454.2	27701.87	24450.63	34175.13	14354.44	117.4054	552.4145	54100.25	20412.08	74778.4
Sensor 6	1398.606	21229.3	6575.041	4416.626	6278.568	10420.88	11373.25	26313.78	20252.83	27727.49
Sensor 7	286.1464	18346.18	1995.069	606.0224	1809.493	5636.541	6463.662	25071.38	17049.79	27120.56
Sensor 8	318230	2495102	539978.8	194901.4	193996.3	46914.31	409436	1766389	1808232	2934544
Sensor 9	304.5184	248454.1	31278.52	9613.493	18549.25	14071.21	61586.84	285280.4	216100.4	350650.9
Sensor 10	2392287	8181160	1756795	598184.7	516032.6	92101.52	961669.4	4087170	4958945	8568542

Figure A.125: MQ-7 vs. MQ-135 ANOVA f-statistics (30°C, 85% RH).

	Sensor 1	Sensor 2	Sensor 3	Sensor 4	Sensor 5	Sensor 6	Sensor 7	Sensor 8	Sensor 9	Sensor 10
Sensor 1	7736.556	53642.73	482.2392	3088.183	131.6229	9916.867	5876.426	110869.1	54520.74	149678.3
Sensor 2	77493.48	4640.907	40681.02	138750.6	81439.56	9503.644	25319.95	392.345	20936.91	116.839
Sensor 3	29.49354	256082.9	4071.863	8175.914	15877.12	45500.24	45545.41	781619	460664.4	1725753
Sensor 4	48.83672	117797.6	3034.318	4044.01	9205.496	33364.04	29727.15	204690.5	129506.1	257544.4
Sensor 5	27527.46	27527.91	8337.976	36830.2	14449.67	1055.373	31.38098	112418.4	29223.63	242326.9
Sensor 6	605.6355	4593.105	1348.43	1190.64	1581.479	3376.269	2765.584	5323.401	4088.419	5628.77
Sensor 7	82.09599	73878.92	3930.245	4589.197	8805.306	28987.58	24637.16	107309.7	71201.63	123732.7
Sensor 8	7132.142	73788.15	15660.9	18224.37	23223.62	43269.01	38895.96	91252.81	69618	98845.76
Sensor 9	3.97007	99922.11	3698.499	4779.021	9742.14	32782.83	28800.07	158828.8	103056.3	190900
Sensor 10	70564.02	965479.5	104806.2	294637.8	273476.4	257735.6	318666.3	2103784	1605628	3312297

Figure A.126: MQ-7 vs. MQ-135 ANOVA f-statistics (35°C, 85% RH).

	Sensor 1	Sensor 2	Sensor 3	Sensor 4	Sensor 5	Sensor 6	Sensor 7	Sensor 8	Sensor 9	Sensor 10
Sensor 1	849.647	3001.469	695.2142	494.2134	115.2718	919.8645	184.9391	4775.552	1785.448	5832.446
Sensor 2	11345.77	1073.859	124768.3	62265.6	61632.73	17375.3	59666.13	351.4876	18053.1	51.96707
Sensor 3	3.511112	57794.16	6666.505	3023.631	13221.1	90434.76	292521.7	564284.9	1149307	1245393
Sensor 4	9.884316	39409.98	2779.826	2526.175	7062.249	35958.04	30036.82	102449.8	67858.77	125084.8
Sensor 5	3860.57	5884.581	47995.14	18272.22	14029.09	449.891	3608.601	42174.77	9414.678	72442.24
Sensor 6	2489.42	111044.4	64105.91	36866.37	64926.69	156543.6	210070.9	397108.9	356725.7	506286.2
Sensor 7	80.82008	12013.73	887.8635	1030.3	2015.6	7669.827	5143.098	16575.88	10299.61	18661.84
Sensor 8	1215.591	11439.53	2849.945	3001.555	3996.973	8301.651	6469.895	13783.76	9914.618	14952.73
Sensor 9	14.30571	48356.88	4588.771	3482.586	10168.82	51969.33	52266.87	166240.9	120299.1	214164.9
Sensor 10	11631.94	262264.6	445357.8	166973.2	288091.6	543927.8	1508051	1674757	2581431	2676393

Figure A.127: MQ-7 vs. MQ-135 ANOVA f-statistics (40°C, 85% RH).

	Sensor 1	Sensor 2	Sensor 3	Sensor 4	Sensor 5	Sensor 6	Sensor 7	Sensor 8	Sensor 9	Sensor 10
Sensor 1	5576.38	6722.279	4348.691	1835.637	667.1204	553.635	87.85454	9915.043	863.4979	12888.1
Sensor 2	333477.1	3618.463	423836.2	129813	76389.84	6325.524	22539.15	210.7688	7167.62	47.40318
Sensor 3	2489.182	165524.9	180.1636	2364.48	6034.04	9768.195	13746.69	189061.7	14526.55	872461.8
Sensor 4	5.228432	61944.18	236.105	2009.78	4380.712	9318.701	10633.72	74865.07	12745.73	111841
Sensor 5	121708.4	19276.44	151756.7	31733.9	13656.87	10.4159	774.7173	31594.53	102.327	105021.1
Sensor 6	49493.4	251928.5	71930.76	59197.37	61369.32	39004.44	62888.65	274694.1	52613.09	493783.8
Sensor 7	987.3939	37535.61	1809.998	3692.712	5705.502	10655.99	10880.12	44726.52	13265.85	54693.28
Sensor 8	245873	587476.8	803407.1	147086.3	123804.9	50607.39	97511.88	599373.3	71013.92	3455923
Sensor 9	166.35	115023.8	1691.333	5106.475	8840.039	12228.87	16514.13	134399.1	17303.41	264527.4
Sensor 10	798221.9	1006252	3239287	363789.4	278903.8	92133.06	189377.8	991856.5	127924.4	7061911

Figure A.128: MQ-7 vs. MQ-135 ANOVA f-statistics (45°C, 85% RH).

	Sensor 1	Sensor 2	Sensor 3	Sensor 4	Sensor 5	Sensor 6	Sensor 7	Sensor 8	Sensor 9	Sensor 10
Sensor 1	6144.168	6160.052	7536.442	2602.882	1416.614	17.926	129.9351	7250.351	1398.927	9687.216
Sensor 2	373980.7	5357.716	259332.2	96975.19	106257.3	9021.074	33780.17	441.6075	7931.125	196.6171
Sensor 3	11761.58	691401.1	8264.755	559.4133	5676.443	5263.03	8458.766	136015.9	32218.21	1782317
Sensor 4	4552.458	216259.6	1071.119	7594.531	16979.53	11007.83	18311.84	124932.2	43972.82	293273.8
Sensor 5	162419.6	35761.09	108644.7	27410.16	24788.57	362.7979	3886.207	19184.85	808.8018	81000.91
Sensor 6	28597.91	119063.1	22989.44	31362.24	40186.93	31501.46	42365.59	108390.9	65053.44	137242.2
Sensor 7	2550.776	58728.67	1279.107	4986.271	8397.485	9769.28	11716.88	54312.68	26298.16	72381.77
Sensor 8	254869.7	1092105	103801.2	87551.13	154658.6	40129.35	91238.29	372782.1	139688.6	1605767
Sensor 9	1241.855	245455	1.089633	4388.158	12340	8684.254	14324.84	123151.7	39063.96	350772.1
Sensor 10	1327936	2813233	405102.4	237845.1	412749	78910.39	198932.7	676800.5	260848.5	4784469

Figure A.129: MQ-7 vs. MQ-135 ANOVA f-statistics (50°C, 85% RH).

(a)   (b)   (c)

(d)   (e)   (f)
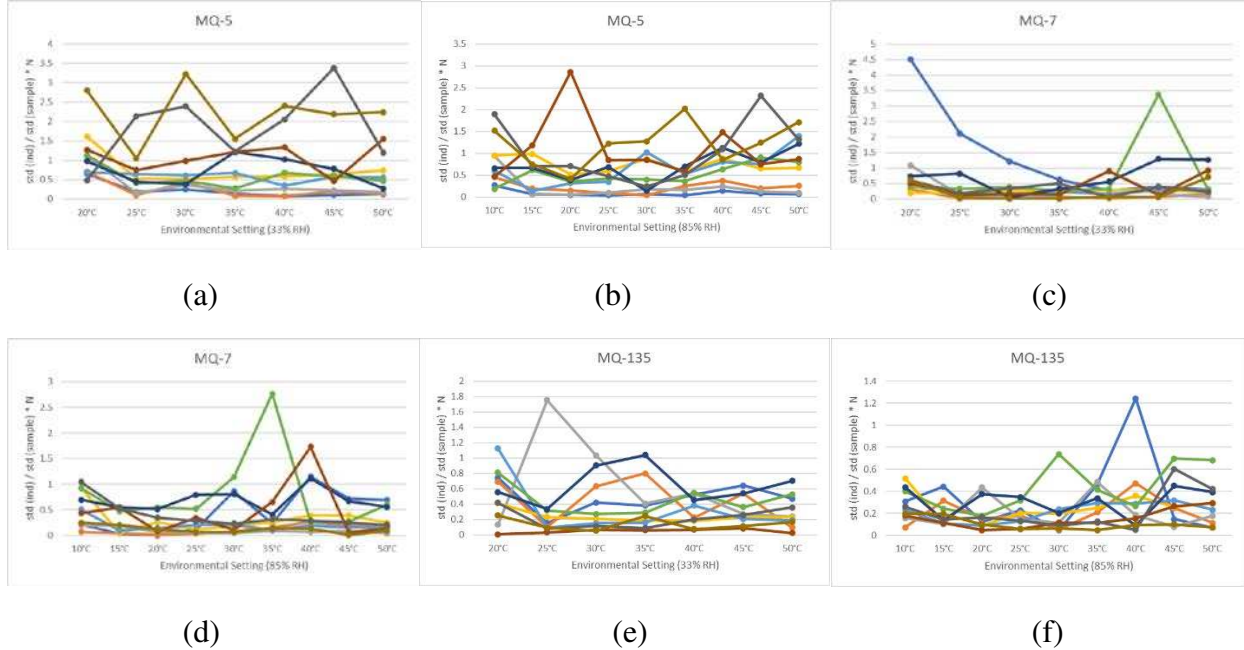
Figure A.130: Ratio of standard deviation of individual sensor measurements to the standard deviation of the full sample size at each environmental setting; (a) MQ-5 Sensors (33% RH), (b) MQ-5 Sensors (85% RH), (c) MQ-7 Sensors (33% RH), (d) MQ-7 Sensors (85% RH), (e) MQ-135 Sensors (33% RH), and (f) MQ-135 Sensors (85% RH).
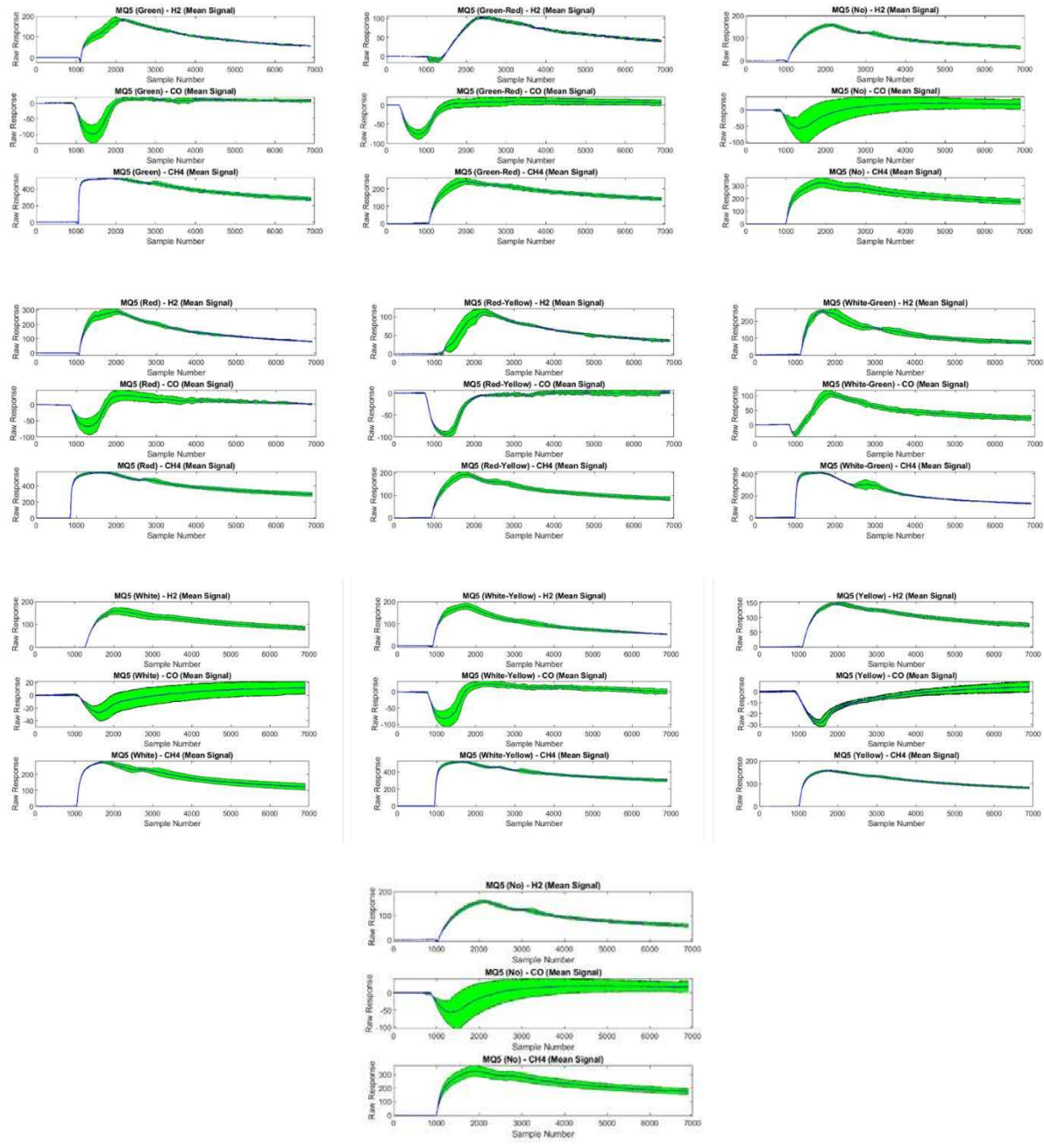
Figure A.131: MQ-5 Sensor Response to H_2, CO, and CH_4.
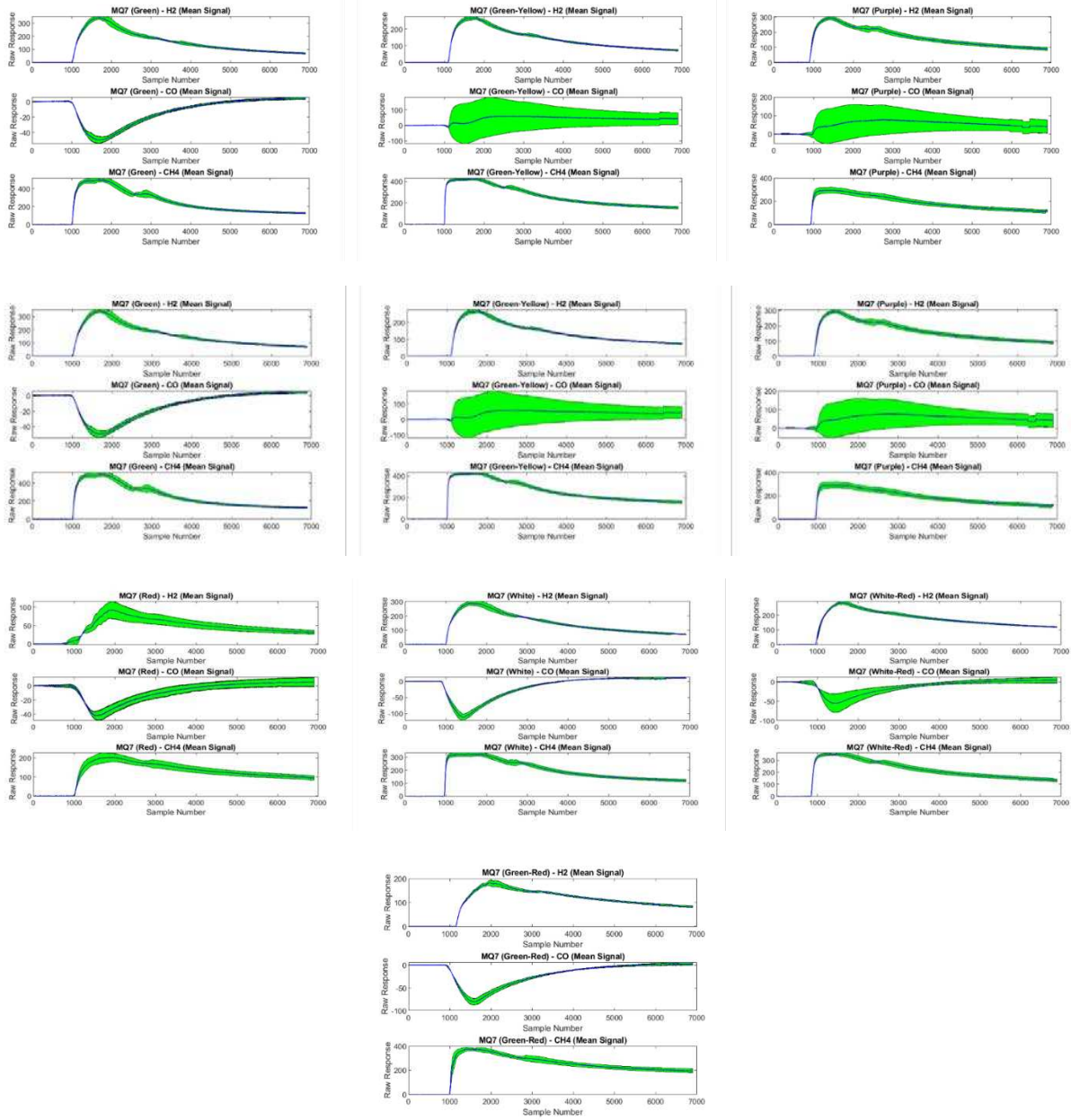
Figure A.132: MQ-7 Sensor Response to H_2, CO, and CH_4.
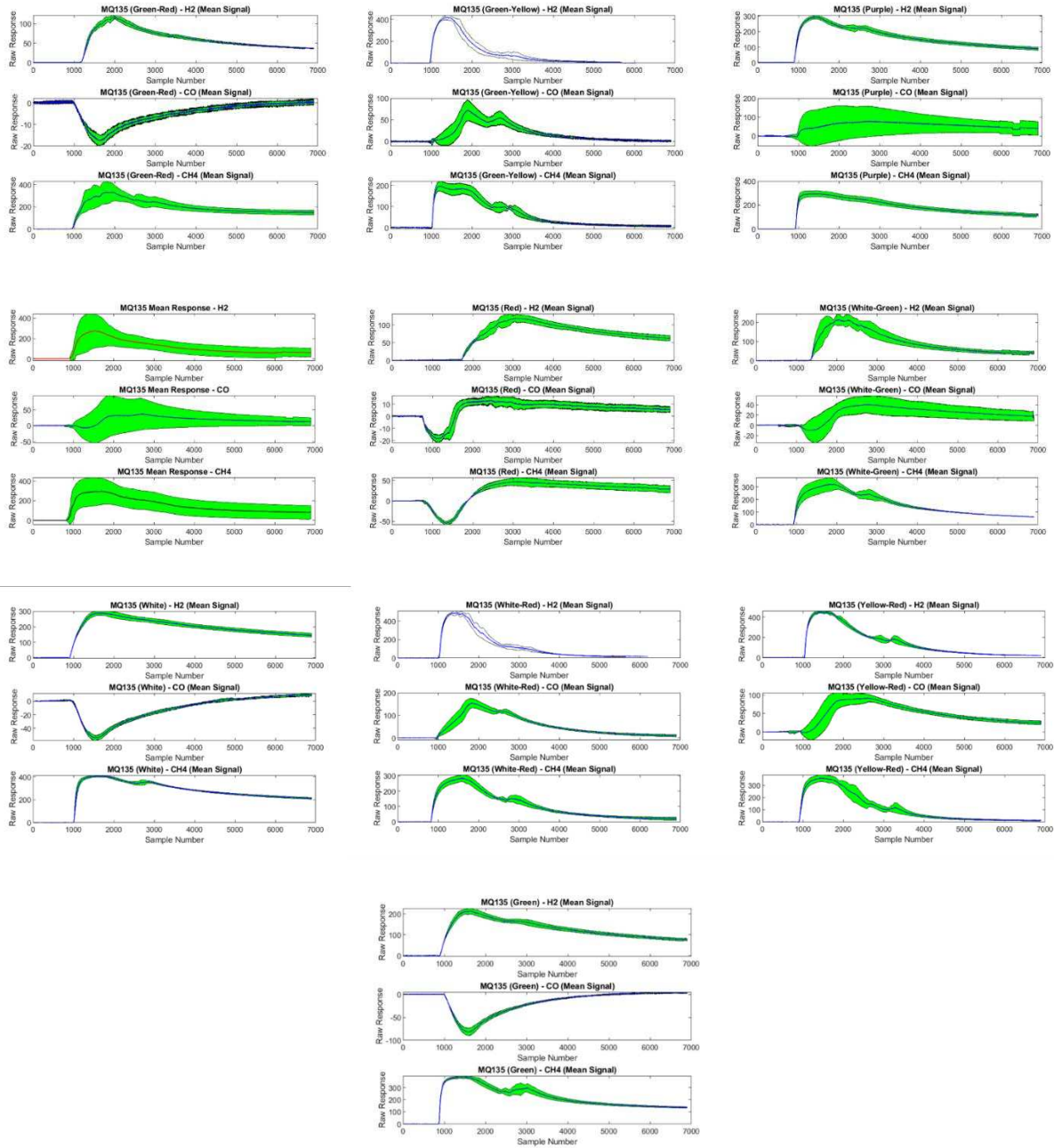
Figure A.133: MQ-135 Sensor Response to H_2, CO, and CH_4.